CRYSTAL PLASTICITY ANALYSIS OF SEVERE PLASTIC DEFORMATION
PROCESSES

A THESIS SUBMITTED TO
THE GRADUATE SCHOOL OF NATURAL AND APPLIED SCIENCES
OF
MIDDLE EAST TECHNICAL UNIVERSITY

BY

ÜLKE ŞİMŞEK

IN PARTIAL FULFILLMENT OF THE REQUIREMENTS
FOR
THE DEGREE OF DOCTOR OF PHILOSOPHY
IN
AEROSPACE ENGINEERING

MARCH 2024

Approval of the thesis:

CRYSTAL PLASTICITY ANALYSIS OF SEVERE PLASTIC DEFORMATION PROCESSES

submitted by **ÜLKE ŞİMŞEK** in partial fulfillment of the requirements for the degree of **Doctor of Philosophy in Aerospace Engineering Department, Middle East Technical University** by,

Prof. Dr. Naci Emre Altun
Dean, Graduate School of **Natural and Applied Sciences** ⸻

Prof. Dr. Serkan Özgen
Head of Department, **Aerospace Engineering** ⸻

Assoc. Prof. Dr. Tuncay Yalçınkaya
Supervisor, **Aerospace Engineering, METU** ⸻

Examining Committee Members:

Assoc. Prof. Dr. Ercan Gürses
Aerospace Engineering, METU ⸻

Assoc. Prof. Dr. Tuncay Yalçınkaya
Aerospace Engineering, METU ⸻

Assoc. Prof. Dr. Hüsnü Dal
Mechanical Engineering, METU ⸻

Prof. Dr. Özgür Aslan
Mechanical Engineering, Atılım University ⸻

Assist. Prof. Dr. Kemal Davut
Materials Science and Engineering, IZTECH ⸻

Date:08.03.2024

I hereby declare that all information in this document has been obtained and presented in accordance with academic rules and ethical conduct. I also declare that, as required by these rules and conduct, I have fully cited and referenced all material and results that are not original to this work.

Name, Surname: ÜLKE ŞİMŞEK

Signature   :

ABSTRACT

CRYSTAL PLASTICITY ANALYSIS OF SEVERE PLASTIC DEFORMATION PROCESSES

ŞİMŞEK, ÜLKE

Ph.D., Department of Aerospace Engineering

Supervisor: Assoc. Prof. Dr. Tuncay Yalçınkaya

March 2024, 188 pages

Advancements in technology for the creation, characterization, modeling, design, and application of nanostructured materials are essential for maintaining competitiveness in the global industrial design and manufacturing market. Recently, processing extremely fine-grained metals through severe plastic deformation (SPD) techniques has reached a critical phase in development. Sufficient laboratory findings are available to demonstrate the overall viability of this approach, and it is widely acknowledged that these materials hold significant innovation potential. The present work aims to conduct numerical investigations into the severe plastic deformation behaviors of metallic materials using both classical continuum and microscale approaches based on finite element method (FEM) simulations. Microscale analysis bridges the gap between continuum plasticity theory and the textural characteristics of metallic materials. By controlling the microstructural features and texture of metallic materials, it becomes possible to improve properties such as strength, fatigue resistance, resilience, and machinability. Finite Element simulations typically utilize two types of algorithms for simulating metal forming processes: implicit and explicit. These processes involve geometric nonlinearities, material nonlinearities, and variable contact problems. The

explicit solution technique offers particular advantages when analyzing large three-dimensional contact problems, making it applicable to metal forming simulations and providing simplicity in solving dynamic contact frictions. An explicit crystal plasticity finite element method (CPFEM) model is developed to systematically understand the deformation behavior and texture evolution of single crystals and polycrystalline materials during full-scale SPD processes.

Keywords: Severe Plastic Deformations, Finite Element Method, Continuum Mechanics, Microscale Mechanics, Crystal Plasticity, Texture Analysis

ÖZ

ŞİDDETLİ PLASTİK DEFORMASYON SÜREÇLERİNİN KRİSTAL PLASTİSİTE ANALİZİ

ŞİMŞEK, ÜLKE

Doktora, Havacılık ve Uzay Mühendisliği Bölümü

Tez Yöneticisi: Doç. Dr. Tuncay Yalçınkaya

Mart 2024 , 188 sayfa

Nano yapıya sahip malzemelerin üretiminde, karakterizasyonunda, modellenmesinde ve uygulamasında ki teknolojik ilerlemeler, küresel pazarda endüstriyel tasarım ve üretkenlik açısından çok önemlidir. Son yıllarda, aşırı ince taneli metallerin üretiminde, şiddetli plastik deformasyon (ŞPD) tekniklerinin kullanımı kritik bir aşamaya ulaşmıştır. Bu yaklaşımın genel olarak uygulanabilirliğini göstermek için yeterli laboratuvar bulguları mevcuttur ve bu üretim yöntemi ile elde edilen malzemelerin yüksek yenilik potansiyeline sahip olduğu kabul edilmektedir. Mevcut çalışma, metal malzemelerin şiddetli plastik deformasyon davranışlarını klasik sürekli ve mikro ölçekli yaklaşımları kullanarak sonlu elemanlar yöntemi (SEY) simülasyonlarıyla sayısal olarak incelemeyi amaçlamaktadır. Mikro ölçekli analiz, plastisite teorisi kullanılarak elde edilen sonuçlar ile metalik malzemelerin doku özellikleri arasındaki ilişkiyi açıklamakta kullanılabilir. Bununla birlikte, metal malzemelerin mikroyapısal özellikleri ve doku yapısını kontrol ederek dayanıklılık, yorgunluk direnci, esneklik ve işlenebilirlik gibi çeşitli mekanik özelliklerini geliştirmek mümkün hale gelebilir. Sonlu eleman simülasyonları genellikle metal şekillendirme işlemlerini simüle etmek için

örtük ve açık algoritma olmak üzere iki farklı türde algoritma kullanır. Metal şekillendirme işlemlerinin simülasyonu, doğrusal olmayan geometrileri, doğrusal olmayan malzeme mekanik özelliklerini ve değişken temas problemlerini içerir. Açık çözüm tekniği, büyük üç boyutlu temas problemlerini analiz etme konusunda belirli avantajlar sunar. Açık çözüm tekniğinin sağladığı üstünlükler, bu çalışmada metal şekillendirme simülasyonlarında dinamik temas sürtünmelerinden kaynaklanan problemleri çözmekte basitlik sağlamıştır. Açık algoritmaya sahip kristal plastisite sonlu eleman yöntemi modeli, tek kristalli ve çok kristalli malzemelerin ŞPD işlemleri sırasındaki deformasyon davranışlarını ve doku evrimlerini sistematik bir şekilde analiz etmek amacıyla geliştirilmiştir.

Anahtar Kelimeler: Şiddetli Plastik Deformasyonlar, Sonlu Eleman Analizi, Sürekli Ortamlar Mekaniği, Mikro-ölçekli Mekanik, Kristal Plastisite, Doku Analizi

To my family...

ACKNOWLEDGMENTS

TABLE OF CONTENTS

LIST OF FIGURES

FIGURES

xvii

xxi

LIST OF ABBREVIATIONS

SPD	Severe plastic deformation
NCM	Nanocrystalline materials
UFG	Ultrafine-grained
FEM	Finite element method
CP	Crystal plasticity
CPFEM	Crystal plasticity finite element method
ECAP	Equal channel angular pressing
TE	Twist extrusion
HPT	High pressure torsion
ARB	Accumulated roll bonding
MDF	Multi-directional forging
NLTE	Non-linear twist extrusion
LTE	Linear twist extrusion
3D	Three dimensional
2D	Two dimensional
SC	Single Crystal
FCC	Face centered cubic
BCC	Body centered cubic
HCP	Hexagonal closed packed
Nb	Niobium
Cu	Copper
Al	Aluminum
SFE	Staking fault energy
PK2	Piola-second Kirchoff stress

CRSS	Critical resolved shear stress
CTE	Coefficient of thermal expansion
APF	Atomic packing factor
DIC	Digital image correlation
EBSD	Electron backscatter diffraction
PEEQ	Plastic equivalent strain
SEM	Scanning electron microscopy
TEM	Transmission electron microscope
SAC	Selected area channeling
CPU	Central Process Unit
VUMAT	Explicit user-defined material model
UMAT	Implicit user-defined material model
RVE	Representative Volume Element
KE	Kinetic energy
IE	Internal energy
PD	Plastic dissipation
SE	Strain energy
ETOTAL	Total energy
FEA	Finite element analysis
SH	Inhomogeneity

CHAPTER 1

INTRODUCTION

The development of materials possessing superior strength, heightened rigidity, and reduced weight compared to existing substances has been pursued over centuries. Furthermore, these materials must be engineered to withstand elevated temperatures. The technology sectors of highly developed nations have ascribed particular significance to these pursuits. In the recent decade, innovative processing techniques have been meticulously formulated, all aimed at augmenting the performance attributes of conventional materials. Nanocrystalline materials, which refer to polycrystalline materials characterized by grain sizes not exceeding 100 nm ([1]), have emerged as a central focus of inquiry. Because of their extremely small dimensions, a significant portion of atoms is located at the interfaces of these grains, imparting unique characteristics to these materials ([2]). Gleiter's pioneering publication in 1981 established the seminal significance of nanocrystalline materials. Gleiter ingeniously employed an inert gas condensation technique to synthesize ultrafine metallic particles at the nanoscale. Subsequent consolidation of these particles into compact discs occurred in situ under ultra-high vacuum conditions ([3]). Research related to nanocrystalline materials has experienced exponential growth in the past few decades, especially in recent years, resulting in a deeper comprehension of their metallurgical and mechanical characteristics. These materials encompass single or multi-phase polycrystals harboring grain dimensions within the nanoscale regime ($1 \times 10^{-9} - 250 \times 10^{-9} m$). The upper echelons of this scale have given rise to the term "ultrafine grain size," denoting dimensions ranging from 250 to 1000 nm ([4]). Ultrafine-grained (UFG) metallic materials have assumed a significant place within contemporary materials science, attributable to their conspicuous attributes confer substantial value for impending structural and functional engineering applications. Nanocrystalline materi-

als, characterized by exceptional properties, hold the potential to exhibit augmented tensile strength, elevated hardness, enhanced fracture toughness, reduced ductility, heightened diffusivity, elevated specific heat capacity, improved coefficient of thermal expansion (CTE), superior machinability, and outstanding soft magnetic properties when compared to conventional polycrystalline materials ([5], [6], [7]). These advantages have induced extensive research within this domain, especially with the advent of sophisticated tools for processing and characterization, sparking heightened activity. UFG materials present a remarkable avenue for probing the characteristics of solid interfaces and advancing our comprehension of the structure-property interplay in solid materials on the nanoscale. They also bear considerable promise for technological applications due to their distinctive attributes. Reducing the grain size of conventional superplastic alloys has increased both the elongation to failure and an optimal strain rate ([8]). The acquisition of superplasticity necessitates a delicate interplay of minute and thermally robust grain sizes, complying with well-established criteria. Conventionally, superplastic materials possess below 10μm grain dimensions ([9]). Advanced materials, particularly those of the ultrafine-grained category, are used in various diverse fields, including aerospace, automotive, biomaterials, chemical sensors, construction, electronics, metal forming, information storage, and optics ([10], [11], [12]). While various techniques have emerged for crafting nanostructured materials over time, many remain confined in their capacity for broader industrial adoption. Foremost among these methodologies are inert gas condensation [13], mechanical alloying [14], electro-deposition [14], amorphous material crystallization [15], severe plastic deformation processes [16], cryomilling [17], plasma synthesis [18], chemical vapor deposition [19], pulse electron deposition sputtering [20], physical vapor deposition [21], and spark erosion [22]. The pursuit of manipulating metallic materials into ultrafine-grained structures through severe plastic deformations (SPD) has reached a critical juncture. The empirical findings highlight the viability of this trajectory, underpinned by the innovative potential embedded in these materials. As a result, we will witness substantial progress and innovative production approaches in this field. One of the most essential foundations of the scientific understanding of how metals respond to external forces on a macroscopic scale while undergoing permanent deformation is based on the mathematical framework of plasticity theory. This framework encompasses a set of differential equations that mani-

fest as mechanical models. This knowledge structure, synergistically combined with advanced computational techniques and state-of-the-art hardware, yields practical solutions encompassing a wide range of small and large plastic strains, all while considering appropriate boundary conditions. Continually refining material models to integrate physical and empirical realities using phenomenological representations constitutes a thriving focal point of academic pursuit. Meanwhile, noteworthy progress in traditional metal-forming endeavors is largely anchored in optimization paradigms and engineering enhancements. Plastic deformation establishes a symbiotic relationship with the crystallographic foundations at the micrometer scale, thereby providing pure knowledge of the overall structure of metals. The current research set sails numerical investigations, meticulously scrutinizing the behavior of metallic materials undergoing severe plastic deformation. This analytical journey takes place at the convergence of classical continuum plasticity theory and microscale analysis, executed through finite element method (FEM) simulations integrated with SPD processes. Microscale analysis fills the gap and sews the information deficiency between the continuum plasticity theory and textural characteristics of metallic materials. The crystal plasticity finite element method (CPFEM) is an effective tool for simulating the change in microstructural properties and texture evolution during plastic deformations ([23], [24], [25], [26]). The ability to predict changes in texture within metals during SPD processes holds strategic significance. It plays an important role in the design of new production methodologies and the determination of process parameters.

1.1 Processes and Methodologies of Severe Plastic Deformations

The most promising strategy for producing ultrafine-grained (UFG) metals revolves around severe plastic deformation (SPD), an emerging facet within metal forming technology. SPD involves inducing significant plastic deformation in materials while minimizing changes to their shape and dimensions. The application of SPD to metal processing to generate UFG metals characterized by submicron-scale grain sizes has matured over more than two decades. This scientific field has evolved into one of the most thoroughly investigated domains, encompassing physical metallurgy and

extending widely across the field of materials science. Initially, research primarily revolved around the projected changes in specific material properties as grain size decreases, such as enhanced strength or superplasticity at lower temperatures ([27]). However, with time, this scientific field has significantly diversified, incorporating a range of diverse subjects. This expansion includes the development of innovative SPD techniques, material modeling, and the creation of tailor-made materials. Foremost among the SPD methodologies stand out equal channel angular pressing (ECAP), high-pressure torsion (HPT), accumulated roll bonding (ARB), multidirectional forging (MDF), and twist extrusion (TE). These pathways have garnered significant attention and occupy the forefront of SPD research. This section briefly outlines these processes and introduces the computational methodology underlying severe plastic deformations.

1.1.1 Equal-Channel Angular Pressing (ECAP)

In the 1970s, researchers at the Institute of Technical Physics in Minsk, USSR, embarked on significant theoretical and empirical endeavors to devise a method capable of inducing consistent and repetitive simple shear within a substantial billet. The culmination of these efforts, initially documented in the institute's internal records, resulted in a patent granted in 1977. This patent, credited to Segal, laid the groundwork for what is now known as the equal-channel angular pressing (ECAE or ECAP) method ([28]). A schematic illustration of the ECAP principle is presented in Figure 1.1. The internal channel of the mold is bent at an abrupt angle ϕ, accompanied by an additional angle ψ that represents the outer curvature where the two channels intersect. The conventional values for these angles are $90°$ and $20°$, respectively. The specimen, often in the form of a rod or rectangular bar, is pressed through the mold using a punch. The procedure unfolds as follows: initially, the billet undergoes deformation as it traverses the mold (Route A), incurring a predetermined plastic strain. Subsequently, the billet is extracted from the mold, rotated around the vertical direction to a sectional view by $90°$, and pressed through the mold again (Route B_A). Once more, the billet is removed from the mold, rotated by $180°$, and subjected to pressing through the mold (Route C). The deformation mechanism involved is simple shear, which occurs as the billet moves through the mold. A fundamental aspect of SPD

processing, setting it apart from conventional metalworking techniques like rolling, extrusion, and drawing, is its ability to maintain the billet's cross-sectional area despite introducing significant strains. This characteristic allows for repeated pressing of the same billet, leading to exceptionally high strain levels. In the initial pass, grains exhibit a spherical, cell-like morphology. After a $90°$ rotation of the billet, the cell shape elongates, taking on an ellipsoidal configuration ([29]). This transformation occurs due to the change in the shear plane. Upon a $180°$ rotation, the strain acts on the same plane as a pure strain but in the opposite direction. This process induces the recrystallization of grains into a more distinct structure, reducing grain size.

With each successive iteration of the billet through the mold, the magnitude of strain increases, consequently enhancing the grains' resistance to deformation. As the number of passes increases, a finer grain structure can be achieved.

Moreover, An additional measure involves applying backpressure to the opposite end
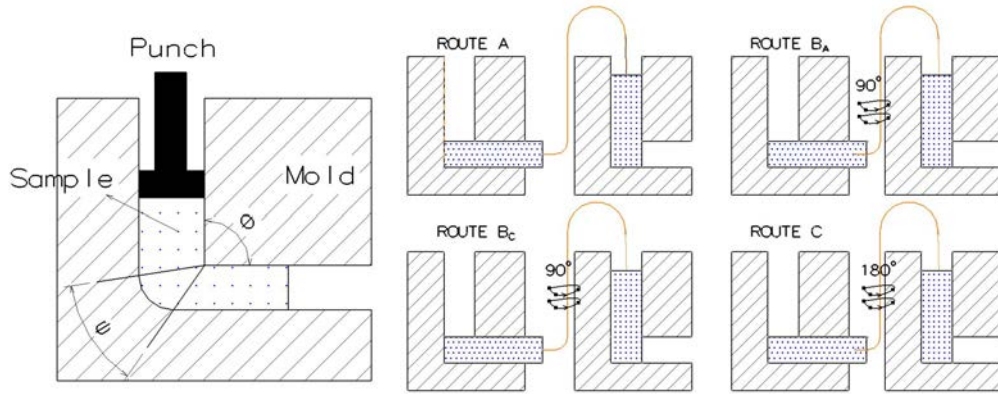
Figure 1.1: Shematic diagram (**left**) and processing routes for ECAP (**right**)

of the workpiece. This increases workability and facilitates a more even stress distribution across the billet, allowing the workpiece to fill the cavity of the die better throughout the process.

The Equation 1.1 can be used to calculate the equivalent plastic shear strain value, as discussed by Segal ([28]).

$$\gamma_N = 2cot\left(\frac{\psi}{2} + \frac{\phi}{2}\right) + \psi\ cosec\left(\frac{\psi}{2} + \frac{\phi}{2}\right) \tag{1.1}$$

The cumulative equivalent strain value can be computed using the die-channel and

inner and outer angles, as derived from Equation 1.2.

$$\epsilon_N = N \frac{1}{\sqrt{3}} \left[2cot \left(\frac{\psi}{2} + \frac{\phi}{2} \right) + \psi \, cosec \left(\frac{\psi}{2} + \frac{\phi}{2} \right) \right] \tag{1.2}$$

Consequently, numerous subsequent models have been developed, including the Segal strain model. This model was established to express the independent strain relationship for a sharp corner where $\psi = 0°$. The overall strain is depicted as follows:

$$\epsilon_N = 2N \frac{1}{\sqrt{3}} cot \left(\frac{\phi}{2} \right) \tag{1.3}$$

Hence, for a single extrusion pass with $\phi = 90°$, Equation 1.3 transforms into:

$$\epsilon_N = 2N \frac{1}{\sqrt{3}} = 1.155 \tag{1.4}$$

As a result, the extrusion stress or pressure, as postulated by Segal ([28]), is depicted in Equation 1.5:

$$P_N = \frac{2}{\sqrt{3}} \sigma_0 cot \left(\frac{\phi}{2} \right) \tag{1.5}$$

Where N = number of passes, γ_N = equivalent plastic shear strain, ϕ = angle between the channels (inner arc angle), ψ = outer arc angle, ϵ_N = effective strain, P_N = plunger pressure or required stress to push the sample material through the mold, σ_0 is the yield strength of the material under test. Notably, the necessary pressure for deformation primarily depends on the material's ECAP angle and yield strength. It should be noted that the incorporation of ψ in the pressure equation introduces variations. Moreover, the geometric analysis described earlier does not encompass the influence of friction, strain hardening, and strain rate sensitivity. Additionally, it does not account for strain distribution. ECAP has limitations, including its inability to efficiently process materials with substantial length due to the instability introduced by the pressing punch. Furthermore, challenges arise from the short service life of the die and the intricate nature of the process, which limit the widespread applicability of ECAP. Many modern SPD techniques also have drawbacks in terms of efficiency and cost-effectiveness. Many efforts of the ECAP process to translate fundamental experimental setups into production have faced challenges. The primary reason for ECAP's limitation to a laboratory tool is the absence of robust engineering advancements, particularly appropriate processing technology tailored to various products.

1.1.2 High Pressure Torsion

The inception of high-pressure torsion (HPT) processing can be attributed to a seminal work conducted by Bridgman ([30]). In this seminal publication, Bridgman succinctly delineated the foundational principles of this experimental technique, demonstrating that subjecting a specimen to torsional deformation while simultaneously applying longitudinal compression enhances its flexibility. Figure 1.2 depicts a schematic representation illustrating these principles. The specimen, configured in a disc shape, is positioned between two anvils, where it is subjected to an applied compressive pressure, denoted as P, reaching several gigapascals (GPa). This pressure is achieved at ambient temperature or by applying elevated thermal conditions. Concurrently, the specimen experiences torsional strain due to the rotation of the lower anvil. The disc undergoes shear deformation due to surface frictional forces, effectively creating a quasi-hydrostatic pressure environment, thereby facilitating the progression of deformation. HPT possesses a noteworthy attribute and advantage compared to other
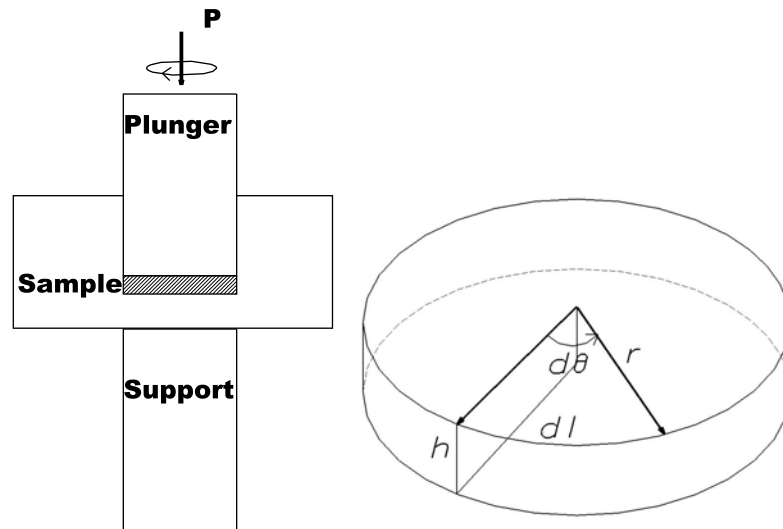
Figure 1.2: Shematic diagram (**left**) and parameters used in estimating the total strain in HPT process (**right**)

techniques. Primarily, it can subject material to nearly limitless deformation strains without causing substantial damage to either the specimen or the tool. This capability stems from the significant hydrostatic pressure component inherent in the process, which effectively shields materials from catastrophic failure ([31]). Equally impor-

tant is the fact that material deformation, for the most part, occurs without altering its outer dimensions. Although HPT typically involves smaller sample sizes than other SPD methodologies like ECAP, it facilitates various microstructure characterizations. It holds the potential to improve various mechanical properties. Importantly, from an engineering perspective, although it requires high pressure, there are minimal impediments to scaling up the process for larger specimens if such scaling is deemed necessary ([32]). A detailed analysis of these resulting microstructures reveals several notable characteristics of HPT processing. Firstly, the average grain sizes in the central regions of the disk tend to be larger than those at the periphery. This difference in grain morphology arises from the equiaxed nature of grains around the perimeter, while the central region exhibits elongated grains resembling conventional rolling microstructures ([33]). These elongated grains at the disk's center highlight that the prevailing processing conditions are insufficient to achieve an utterly homogenized microstructure throughout the specimen ([34]). Achieving a lower grain size limit within HPT-deformed materials primarily depends on factors such as metal purity, alloying elements, punch pressure, process temperature, and strain rate. By applying a sufficiently high number of rotations, even disks with very low radii can reach the lower limit of grain fragmentation in HPT-deformed materials. As a result, harmonizing the microstructure and mechanical properties across nearly the entire disk becomes feasible despite the linear relationship between applied strain and radius ([35]). For an infinitely small rotation, $d\theta$, and a displacement, dl, it follows from Figure 1.2 that $dl = rd\theta$, where r is the radius of the disk, and the incremental shear strain, $d\gamma$, is then given by:

$$d\gamma = \frac{dl}{h} = \frac{rd\theta}{h} \tag{1.6}$$

where h is the disk thickness; by further assuming that the thickness of the disk is independent of the rotation angle, θ, it follows from formal integration that, since $\theta = 2\pi N$, the shear strain, γ, is given by

$$\gamma = \frac{dl}{h} = \frac{2\pi\,Nr}{h} \tag{1.7}$$

where N is the number of revolutions. Finally, in many investigations, the equivalent von Mises strain is then calculated using the relationship

$$\epsilon = \frac{\gamma}{\sqrt{3}} \tag{1.8}$$

HPT process does offer significant advantages, such as consistent deformation, low deformation resistance, minimal porosity, and the absence of contamination. However, incorporating HPT into industrial applications faces specific limitations, primarily related to the size and shape of the samples subjected to the process. Furthermore, the complexities of manipulating process parameters and the inherent uncertainty in predicting the resulting results make it difficult to use HPT effectively for engineering purposes.

1.1.3 Accumulated Roll Bonding

The Accumulative Roll Bonding (ARB) technique represents an innovative approach to material processing, enabling the continuous production of plates, sheets, and bars. This significant development can produce substantial materials while enhancing their properties.[36]. The ARB technique involves a multi-stage, solid-state process. It consists of several intricately coordinated steps. These steps include meticulous surface preparation, precise cutting, deliberate stacking, subsequent rolling, and, in some cases, a post-rolling heat treatment phase to improve the bonding quality among the stacked sheets. The process flow of ARB is briefly illustrated in Figure 1.3, where two or more sheets undergo a careful stacking procedure before undergoing substantial plastic deformation through rolls. This deformation is precisely controlled to facilitate effective solid-state bonding between the individual layers, ultimately resulting in the desired composite structure.
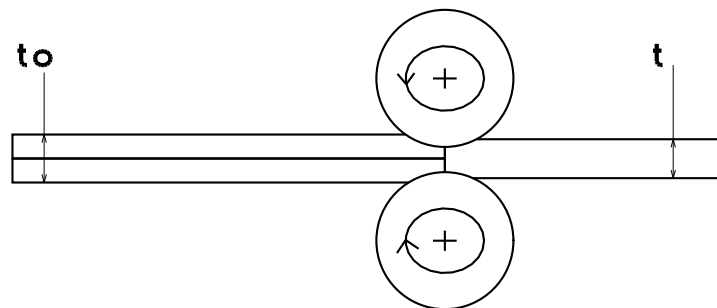
Figure 1.3: Schematic presentation of accumulated roll bonding (ARB) process

ARB technique represents a promising avenue with substantial industrial potential due to its inherent advantages, such as high production rates and seamless continuous

operation. A complex interplay of process parameters and underlying mechanisms significantly influences the bonding quality achieved through ARB. Recent research efforts have been dedicated to unraveling the intricate bonding mechanisms inherent in the roll bonding process. Current research efforts have been dedicated to unraveling the complicated bonding mechanisms inherent in the roll bonding process. Within the scientific discourse, four prominent theories have emerged to elucidate these mechanisms: the film theory, energy barrier theory, recrystallization theory, and diffusion bonding theory ([37]). Collectively, these theories contribute to our comprehensive understanding of the ARB process, providing insights into optimizing bonding quality and overall performance. The film theory postulates that bonding occurs when two clean metal surfaces are brought into proximity. This theory is particularly prominent in low-temperature ARB processes, where bonding is achieved as metal surfaces are exposed to substantial deformation. In this scenario, the fracture of surface layers and the extrusion of fresh metal through cracks play crucial roles in establishing direct contact between the surfaces. This mechanism becomes operative as the metal surfaces undergo significant plastic deformation, facilitating the intimate interaction required for adequate bonding. On the contrary, the energy barrier theory postulates that even if pristine surfaces come into firm contact, bonding will not occur unless an energy barrier is surmounted. Numerous parameters influence ARB, with material type, surface characteristics, and rolling conditions considered the most influential. UFG microstructures are primarily engendered through grain subdivision during SPD. Consequently, the elongated UFG structures observed in ARB-processed materials resemble the lamellar boundary structures that emerge in materials subjected to intense deformation via conventional rolling. This phenomenon suggests that UFG structures are formed by stacking 50 % rolled sheets between cycles and incorporating severely shear-deformed surface regions into the center. Thus, unlike conventional rolling, the sheared regions are not confined solely to subsurface layers; they intricately distribute throughout the sheet's thickness as each ARB cycle progresses (Hansen [38]). The thickness reduction by the ARB process in most literature is selected as 50% so that sheet material has the initial thickness after every forming cycle ([39]). The final thickness of the strip (t), total reduction (t_r), where t_0 is the initial thickness of the strip and equivalent Von Mises strain (ϵ_{vm}) after the N cycles can be

calculated using eqn. 1.9-eqn. 1.11

$$t = \frac{t_0}{2^N} \tag{1.9}$$

$$t_r = \frac{t_0 - t}{t_0} = 1 - \frac{t}{t_0} \tag{1.10}$$

$$\epsilon_{vm} = \left(-\frac{2}{\sqrt{3}} ln \left(\frac{t}{t_0} \right) \right) N \tag{1.11}$$

One of the challenges associated with the ARB process is the potential for material fracture. This fracture risk can be mitigated by reducing the number of ARB passes, using thicker material sheets, selecting less prone to fracture, optimizing processing conditions, or introducing defects that can act as crack stoppers. Researchers are actively developing new methods to enhance the fracture toughness of ARB-processed materials.

This challenge arises from the accumulation of total plastic strain within the materials during the process, exacerbated by the non-hydrostatic nature of the rolling process. As a result, edge cracks may appear in the sheets significantly as the number of cycles increases. This phenomenon limits the broader application of the ARB technique in industrial-scale sheet metal operations. Additionally, the confinement of shear strain, a crucial factor for grain refinement in sheet metal operations, becomes particularly pronounced on the surfaces of sheet metals subjected to ARB processing. The distinct mechanical properties of UFG metals compared to conventional metals can pose difficulties when applying ARB in practical industrial settings.

1.1.4 Multi Directional Forging

The utilization of Multi-Directional Forging (MDF), acknowledged as one of the earliest and most fundamental metal forming techniques for SPD processing, was spearheaded by Imaev [40]. The methodology encompasses consecutive upsetting stages in two (plane) or three mutually perpendicular directions. In the latter scenario, an initial material with a rectangular geometry $A \times B \times C$, where $A > B > C$, undergoes forging along the first axis X until the aspect ratio transforms to $B \times A \times C$ with a 90^0 rotation determined by the punch force surface area. Subsequently, forging occurs along the second axis Y, causing the ratio to change to $C \times B \times A$ following another

90^0 rotation. Finally, forging along the third axis Z concludes the process, restoring the original shape $A \times B \times C$ (see Fig. 1.4). This iterative, non-monotonic, and cyclic loading sequence is repeated multiple times to accumulate significant strain levels in the material.
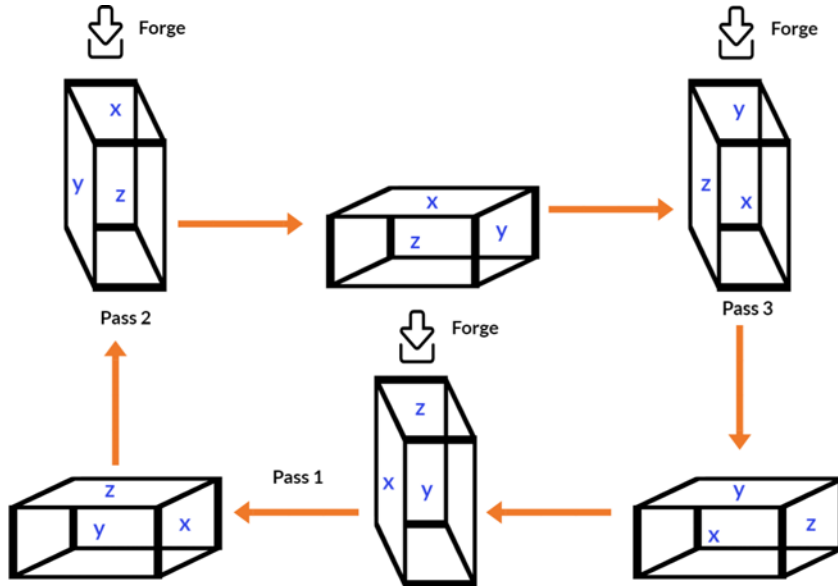
Figure 1.4: Schematic presentation of multi-directional forging (MDF) process

A notable advantage of the MDF technique is its seamless compatibility with the existing large hydrostatic presses commonly used in industrial settings. This compatibility makes the method highly attractive for commercial applications, particularly for producing large bulk samples ([41]). Implementing the MDF process leads to a significant improvement in hardness and a simultaneous reduction in wear rate. However, it's important to note that the rate of this enhancement tends to decrease as the number of forging passes increases.

Furthermore, the MDF process induces a noticeable change in the wear mechanism, attributed to the decrease in the friction coefficient of the deformed specimen. An important observation is the development of a microstructure in the final pass specimen characterized by a fusion of ultrafine grains and micro shear bands. The analysis of these results highlights that conventional mechanisms such as dislocation subdivisions, twinning, and shear banding play a primary role in grain refinement. It is also relevant to mention that the prevalence of deformation twinning and shear banding intensifies as the stacking fault energy decreases, ultimately reducing the final grain

size ([42]).

The effective plastic strain ensuing from the forging process can be quantified through equation 1.12. In this formulation, H and W symbolize the height and width of the deformed sample, respectively.

$$\epsilon_{eq} = \frac{2}{\sqrt{3}} ln \left(\frac{H}{W} \right) \tag{1.12}$$

The non-uniformity parameters of forging deformation are determined using equation 1.13, where ϵ_{max} represents the maximum effective plastic strain within the section, ϵ_{min} signifies the minimum effective plastic strain within the section, and ϵ_{avg} denotes the average effective plastic strain across the section.

$$c = \frac{\epsilon_{max} - \epsilon_{min}}{\epsilon_{avg}} \tag{1.13}$$

The MDF process is not without its limitations, with the most significant being the development of tensile stresses at the free surfaces and high hydrostatic pressures. These factors significantly contribute to crack formation and restrict the number of passes that can be effectively utilized, especially at lower temperatures ([43]). Additionally, like other forging methods, MDF faces challenges related to microstructural heterogeneity.

MDF is particularly well-suited for brittle materials when performed at room temperature, primarily due to lower strain rates than techniques such as ECAP and HPT. However, it's essential to acknowledge that the grain refinement potential of the MDF process is relatively less pronounced compared to alternative SPD approaches. Furthermore, the achieved reduction in grain size is not uniform throughout the entire sample, a concern that can be mitigated by increasing the number of processing passes ([44]).

1.1.5 Twist Extrusion

Twist extrusion (TE) was first introduced in 2002 by Beygelzimer ([45]). Unique features characterize this method, including the distinctive arrangement of cross-sectional planes within the channel. These cross-sections remain orthogonal to the

extrusion axis and unchanged along the entire axis. The slope angle α of the twist line varies along the height of the channel, being zero at both the initial and final sections. This specific channel geometry leads to an intriguing consequence: the overall shape of the specimen remains constant throughout the TE process. The operational principles of this method are schematically depicted in Figure 1.5.
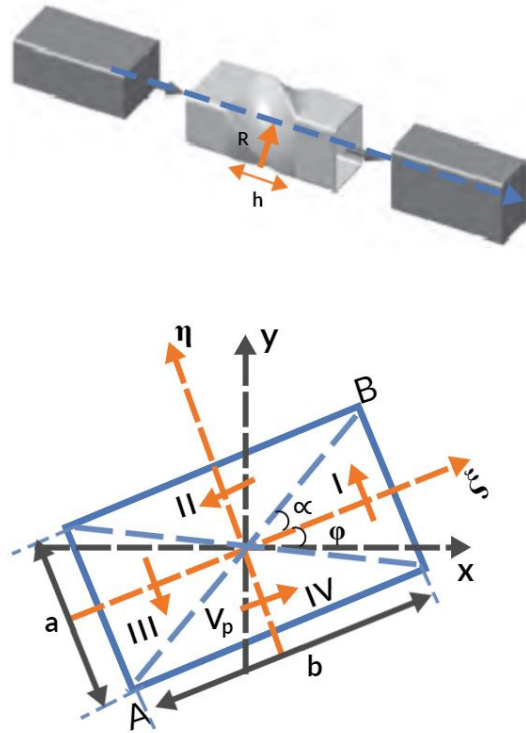
Figure 1.5: Schematic presentation of twist extrusion (TE) process (**top**) and kinematically possible velocities during process (**bottom**)

This technique enables multiple extrusions of the specimen, accumulating significant levels of severe plastic deformation. Notably, one of the distinctive features of TE is its suitability for processing bars with rectangular cross-sectional profiles. Unlike ECAE, where the simple shear plane is typically inclined at an angle of 45-60 degrees relative to the longitudinal axis of the specimen, TE introduces a shear plane perpendicular to the specimen's longitudinal axis. This configuration allows for the creation of unique structures and textures. Moreover, using various combinations and regimes, the strategic integration of ECAE and TE processes leads to an expanded range of potential deformation paths. These paths encompass not only those achiev-

14

able through ECAE alone but also distinct paths derived from TE, thus further diversifying the capabilities of the method. TE demonstrates a steep deformation gradient within the cross-sectional area, similar to the HPT process. Although limited data exists on the effects of this deformation gradient on structure and properties, existing evidence suggests that increasing the gradient can enhance grain refinement in metals and subsequently improve their ductility ([46]).

In contrast to the ECAE process, TE exhibits a distinct characteristic of vigorous material flows undergoing deformation within the cross-sectional dimensions of a billet. This phenomenon contributes to the homogenization of the material's structure and properties. Homogenization is a process that can be used to improve the properties of powder materials by reducing the variation in composition and microstructure. This can make it easier to consolidate the powder into a solid material with uniform properties ([47]). TE also introduces a substantial nonmonotonic change in the specimen's surface as it passes through the die. Upon entering the twisted region, the billet's surface expands (by 70-80%), returning to its original size upon exiting the region. These changes impact the metal's structure and provide an avenue for introducing various alloying elements into the billet's surface layers. Compared to ECAE, the distorted areas at the billet's terminations, particularly the head and rear parts, are notably smaller under the TE process ([48]). This aspect holds increased significance in repeated processing runs. Additionally, TE possesses the distinctive feature of preserving the billet's movement direction, setting it apart from ECAE. This characteristic enables the seamless integration of TE into pre-existing industrial production lines ([49]). During the TE process, it is commonly observed that high-angular dislocation walls tend to become paired. Two distinct types of paired high-angular dislocation walls have been noted in some cases. After three TE passes, the deformation structure becomes more uniform, although single cells are still observed. The overall structure predominantly consists of shear bands oriented in two planes of the subgrains alongside well-shaped grains. The average size of these structural elements measures $0.3\mu m$ ([50]). The following equations can outline the potential range of velocities for the TE process ([51]) within the regions labeled as I and III in Figure 1.5.

$$V_x = -V_0\frac{y}{R}tan\alpha - \frac{V_p(z)}{b}\left(xsin\left(\frac{z}{h}2\psi_{max}\right) + y - ycos\left(\frac{z}{h}2\psi_{max}\right)\right)$$
$$V_y = V_0\frac{y}{R}tan\alpha + \frac{V_p(z)}{b}\left(xsin\left(\frac{z}{h}2\psi_{max}\right) + y + ycos\left(\frac{z}{h}2\psi_{max}\right)\right) \quad (1.14)$$
$$V_z = V_0$$

In the II and IV areas in Fig. 1.5

$$V_x = -V_0\frac{y}{R}tan\alpha - V_p(z)\frac{b}{a^2}\left(-xsin\left(\frac{z}{h}2\psi_{max}\right) + y + ycos\left(\frac{z}{h}2\psi_{max}\right)\right)$$
$$V_y = V_0\frac{y}{R}tan\alpha - V_p(z)\frac{b}{a^2}\left(xsin\left(\frac{z}{h}2\psi_{max}\right) - y + ycos\left(\frac{z}{h}2\psi_{max}\right)\right) \quad (1.15)$$
$$V_z = V_0$$

Where x,y, and z represent the coordinate positions of the particle, with the z-axis directed along the twist die axis. V_x, V_y and V_z denote the components of the velocity vector, while V_0 signifies the extrusion speed. α represents the slope angle of the twist line on the extrusion axis, and V_p corresponds to the velocity of material moving within the cross-section of the die channel. R represents the distance between the extrusion axis and the mold, ψ_{max} is the angle of cross-section rotation as an outcome from the twisting channel relative to the entrance, and h denotes the height of the twisting channel. The average degree of accumulated strain can be calculated using the following equation:

$$\dot{\epsilon} = tan\alpha_{max} \quad (1.16)$$

In TE, a notable phenomenon is the significant grain refinement that occurs during the initial passes. However, depending on the specific material and processing conditions, the effectiveness of grain refinement decreases considerably after the third or fourth pass. Eventually, the mean grain size stabilizes at the lowest achievable level for the given material and temperature.

However, this method's limitation is the non-uniform strain distribution across the specimen, leading to heterogeneous mechanical properties. To address this challenge, one strategy is to increase the number of passes, which can help alleviate the non-uniformity in strain distribution and potentially lead to more consistent mechanical properties throughout the specimen.

1.2 The Structure of Metallic Crystalline Solids

The discovery of X-ray diffraction by metallic crystals ([52]) and the recognition that metals consist fundamentally of atoms organized in specific geometric lattices ([53]) initiated numerous inquiries into the correlation between atomic arrangement and the plastic deformation of metals. Much of the fundamental research on the plastic deformation of metals has been conducted using single crystal specimens. This methodology removes the complicating influences of grain boundaries and the limitations imposed by adjacent grains and second-phase particles. X-ray diffraction analysis has revealed that atoms within a metal crystal are arranged in a consistent, repetitive three-dimensional pattern. When explaining crystalline structures, atoms are visualized as solid spheres with precisely defined diameters ([54]). This concept called the atomic hard sphere model, envisions these spheres as representing nearest-neighbor atoms in contact. As per the hard sphere model, the atomic configurations of certain common elemental metals are depicted in Figure (1.6). The simplest crystalline
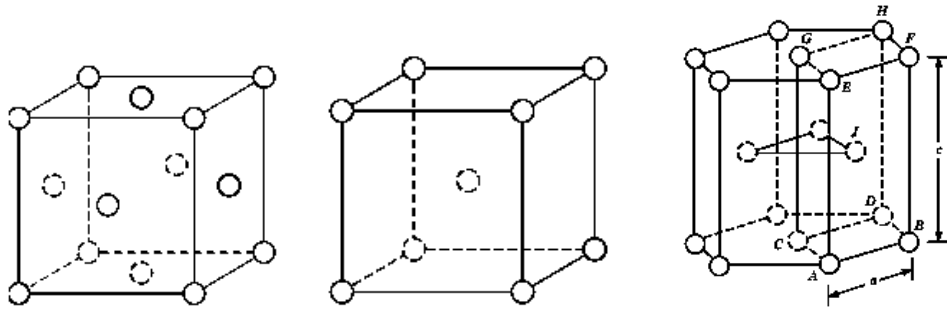
Figure 1.6: Atomic hard sphere model of the common elemental metals face-centered cubic (**left**), body-centered cubic (**mid**), and hexagonal closed packed (**right**), respectively.

structure is the simple cubic lattice. Crystallographic planes and directions are identified using Miller indices concerning these lattice axes. A crystallographic plane or direction is determined by the measurements of its intersections with the three axes, originating from the coordinate system's origin. In cases where a plane intersects an axis in the negative direction, an overline is employed to signify the associated integer. For example, there are six crystallographically equivalent planes of the type (100), each with varying indices like (100), (010), ($\bar{1}$00), (0$\bar{1}$0), or (00$\bar{1}$), contingent

upon the chosen axes. The symbol 100 represents a set or set of planes. Crystallographic directions are indicated by integers enclosed in square brackets [uvw] without the necessity for reciprocals to define directions. A family of crystallographically equivalent directions is denoted as <uvw>. In cubic lattice symmetry situations, a direction is always perpendicular to the plane with corresponding indices. Nevertheless, specific crystallographic directions may not share the same index in crystals with hexagonal symmetry. This inconsistency is resolved by using a four-axis, or Miller-Bravais coordinate system. The three axes, designated as a_1, a_2, and a_3, are situated in a common plane and create angles of $120°$ with each other. The z-axis is perpendicular to this basal plane. As explained previously, the directional indices are denoted with four indices as [uvtw]. Following the convention, the first three indices correspond to projections along the respective a_1, a_2, and a_3 axes in the basal plane. The conversion from the three-index system to the four-index system, from $[u'v'w']$ to $[uvtw]$, is achieved using the following formulas:

$$
\begin{aligned}
u &= \frac{n}{3}(2u' - v') \\
v &= \frac{n}{3}(2v' - u') \\
t &= -(u + v) \\
w &= nw'
\end{aligned}
\tag{1.17}
$$

The transition between the two indexing systems involves primed indices for the three-index scheme and unprimed indices for the new Miller-Bravais four-index system. A factor "n" may be required to reduce the indices u, v, t, and w to their smallest integers. Furthermore, converting planes from Miller-Bravais indices to Miller indices is straightforward: the "i" value in [hkil] is omitted, yielding [hkl]. In the case of ideal hexagonal close packing (hcp) structures, the ratio of the c-axis length to the a-axis length, denoted as c/a, is approximately 1.633. Two other critical characteristics of a metallic crystal structure are the atomic packing factor (APF) and the stacking fault energy (SFE). The APF represents the ratio of the volume occupied by solid spheres within a unit cell, considering the atomic hard sphere model. The APFs for various metallic structures are detailed in Table 1.1.

18

$$APF = \frac{volume \quad of \quad atoms \quad in \quad a \quad unit \quad cell}{total \quad unit \quad cell \quad volume} \tag{1.18}$$

Table 1.1: Unit cell length and atomic packing factor (APF) of some metallic structures

Crystal Structure	unit cell length	APF
FCC	$a = 2R\sqrt{2}$	0.74
BCC	$a = \frac{4R}{\sqrt{3}}$	0.68
HCP	$a = 2R, c = \frac{4\sqrt{6}R}{3}$	0.74

Differences in the deformation behavior of metals can be attributed to variations in stacking fault behavior. Nearly parallel partial dislocations experience a repulsive force, which is counteracted by the surface tension of the stacking fault, pulling them closer together. A lower stacking fault energy results in greater separation between partial dislocations and wider stacking faults ([55]). Typical stacking fault energy (SFE) values are provided in Table 1.2. Stacking faults have several effects on plastic deformation. Metals with broader SFE exhibit faster strain hardening, are prone to twinning during annealing and show distinct temperature-dependent flow stress behaviors compared to metals with narrower stacking faults ([56]). Metals with higher SFE tend to form deformation substructures like dislocation tangles and cells, while those with lower SFE display banded, linear arrays of dislocations.

1.2.1 Deformation with Slip

Deformation of metals through plasticity primarily occurs via the displacement of crystal planes sliding over one another along specific crystallographic planes, known as slip planes. This mechanism upholds the crystal structure's integrity owing to the lattice's translational symmetry, guaranteeing that the crystal is flawlessly restored after a uniform slip. During this process, every atom within the deformed region of the crystal advances by a whole number of lattice spacings. Slip is most favorable along specific directions on distinct crystallographic planes. Typically, the slip plane aligns

Table 1.2: Staking fault energy (SFE) of some metallic materials ([57])

Metarial	Stacking fault energy (SFE) $Mj \times m^{-2}$
Brass	$< \approx 10$
310 stainless Steel	≈ 45
Silver	≈ 25
Gold	≈ 50
Copper	≈ 80
Nickel	≈ 150
Aliminum	≈ 200

with the plane with the highest atomic density, and the slip direction is located within that plane. Because high atomic density planes usually have greater spacing within the crystal structure, they tend to offer less resistance to slip than other planes. This pairing of the particular slip plane and direction constitutes what is referred to as the slip system. Within the face-centered cubic (fcc) crystal structure, the densely packed systems correspond to the 111 octahedral planes and the <110> directions. Inside the FCC unit cell, there are eight 111 planes. However, the planes on opposite faces of the octahedron are parallel, resulting in four distinct sets of octahedral planes. Each 111 plane includes three <110> directions. Consequently, the fcc lattice encompasses a total of twelve potential slip systems. The fcc structure's different slip planes and directions are visually illustrated in Figure 1.7, and their specific details are presented in Table 1.3.
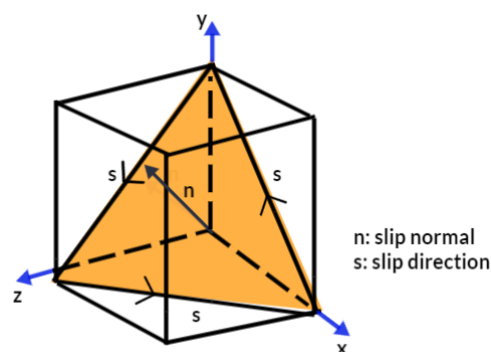
Figure 1.7: Slip Systems of FCC Single Crystals.

Table 1.3: Slip systems of FCC single crystals [58].

| Slip System | Slip Plane Normal | Slip Direction |
number	n	s
1	(111)	$[1\bar{1}0]$
2	(111)	$[01\bar{1}]$
3	(111)	$[10\bar{1}]$
4	$(\bar{1}11)$	$[110]$
5	$(\bar{1}11)$	$[01\bar{1}]$
6	$(\bar{1}11)$	$[101]$
7	$(1\bar{1}1)$	$[110]$
8	$(1\bar{1}1)$	$[011]$
9	$(1\bar{1}1)$	$[10\bar{1}]$
10	$(11\bar{1})$	$[1\bar{1}0]$
11	$(11\bar{1})$	$[011]$
12	$(11\bar{1})$	$[101]$

In contrast to the face-centered cubic (fcc) arrangement, the body-centered cubic (bcc) structure does not exhibit close packing. Consequently, no single plane with a prevailing atomic density is similar to the 111 planes in the fcc structure. The 110 planes have the highest atomic density within the bcc structure, though they are not notably denser than several other planes. In contrast to the fcc structure, where the <110> directions are closely packed, the <111> direction is similarly closely packed in the bcc structure. As a result, bcc metals adhere to the general rule that the slip direction corresponds to the close-packed direction. However, bcc metals differ from most other metals because they lack a single well-defined slip plane. The bcc structure's different slip planes and directions are visually illustrated in Figure 1.8, and their specific details are presented in Table 1.4.
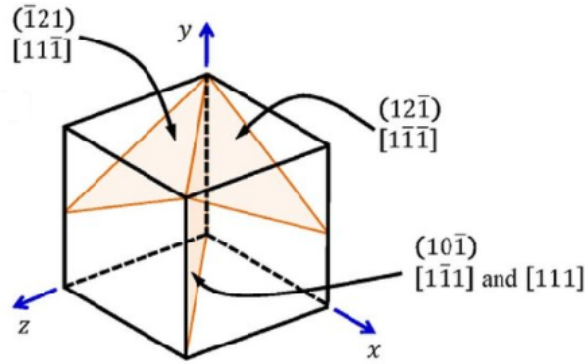
Figure 1.8: Slip systems of BCC single crystals.

1.2.2   Critical Resolved Shear Stress for Slip

The evolution of slip within a single crystal is contingent on numerous factors, including the extent of the shear stress imposed by external loads, the inherent geometric configuration of the crystal lattice, and the alignment of active slip planes concerning the applied shearing stresses. The slip initiation transpires when the shear stress applied to the slip plane, aligned with the selected slip direction, reaches a threshold known as the critical resolved shear stress (CRSS). This parameter is analogous to the yield stress in a conventional stress-strain curve, albeit within the context of an individual crystal. The specific value of CRSS depends on the material's chemical composition and temperature. Determining the exact stress threshold at which the initial slip bands become visible is considerably complex in practical situations. Usually, determining CRSS involves identifying the point where the extrapolated lines from the elastic and plastic regions intersect on the stress-strain curve. It is crucial to note that this determination process is inherently hindered by challenges arising from the intricate behavioral complexities displayed by the material under these conditions. The complex nature of these challenges, including factors like microstructural heterogeneities and structural imperfections, adds to the inherent complexity of accurately determining the CRSS value. Therefore, a thorough understanding of the material's behavior under different conditions is essential for a reliable determination of its CRSS. The variation in the magnitude of tensile loads required to initiate slip in single crystals with different crystallographic orientations can be understood by considering the concept of CRSS as introduced by Schmid [60]. Let's contemplate a

Table 1.4: Slip systems of BCC single crystals ([59]).

Slip System	Slip Plane Normal	Slip Direction
number	n	s
1	$(01\bar{1})$	$[111]$
2	$(10\bar{1})$	$[111]$
3	$(1\bar{1}0)$	$[111]$
4	$(01\bar{1})$	$[\bar{1}11]$
5	(101)	$[\bar{1}11]$
6	(110)	$[\bar{1}11]$
7	(011)	$[1\bar{1}1]$
8	$(10\bar{1})$	$[1\bar{1}1]$
9	(110)	$[1\bar{1}1]$
10	(011)	$[11\bar{1}]$
11	(101)	$[11\bar{1}]$
12	$(1\bar{1}0)$	$[11\bar{1}]$
13	$(\bar{2}11)$	$[111]$
14	$(1\bar{2}1)$	$[111]$
15	$(11\bar{2})$	$[111]$
16	(211)	$[\bar{1}11]$
17	$(12\bar{1})$	$[\bar{1}11]$
18	$(1\bar{1}2)$	$[\bar{1}11]$
19	$(21\bar{1})$	$[1\bar{1}1]$
20	(121)	$[1\bar{1}1]$
21	$(\bar{1}12)$	$[1\bar{1}1]$
22	$(2\bar{1}1)$	$[11\bar{1}]$
23	$(\bar{1}21)$	$[11\bar{1}]$
24	$(11\bar{2})$	$[11\bar{1}]$

cylindrical single crystal with a cross-sectional area represented as A (refer to Figure 1.9). In this situation, ϕ denotes the angle between the slip plane's normal vector and the tensile loading axis. At the same time, λ represents the angle between the slip's

direction and the tensile loading axis. The area of the slip plane, oriented at an angle ϕ to the crystal's geometry, is equal to $A/\cos\phi$. At the same time, the axial force component acting within the slip plane, particularly in the slip direction, is denoted as $F\cos\lambda$. Consequently, the critical resolved shear stress is defined by:
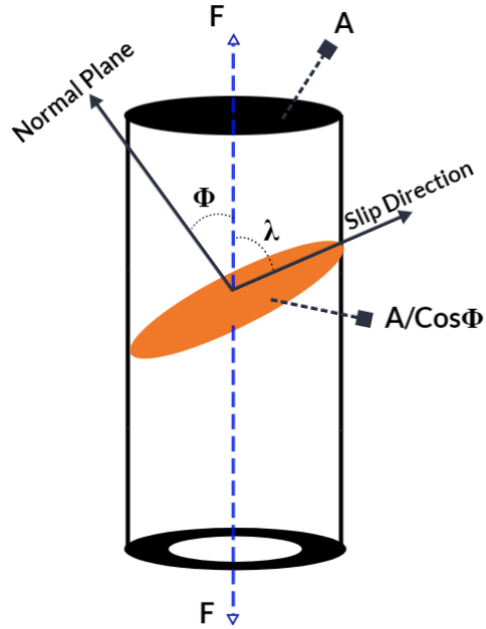
Figure 1.9: Calculation of critical resolved shear stress

$$\tau_R = \frac{F\cos\lambda}{A/\cos\phi} = \frac{F}{A}\cos\phi\cos\lambda \tag{1.19}$$

Equation 1.19 presents the formula for the shear stress resolved onto the slip plane in the direction of the slip. This shear stress reaches its maximum value when both ϕ and λ are set to $45°$, resulting in $\tau_R = \frac{1}{2}\frac{F}{A}$. When the tension axis is perpendicular to the slip plane ($\lambda = 90°$) or aligned parallel to it ($\phi = 90°$), the resolved shear stress becomes zero. The slip does not occur in these extreme orientations because there is no shear stress within the slip plane. Crystals that approach these orientations are more susceptible to fracture rather than undergoing slip. The Schmid factor, represented as m, is the ratio of CRSS to the axial stress. The Schmid factor is calculated as $m = \cos\phi\cos\lambda$ for a single crystal subjected to tension or compression along its axis. Experimental observations demonstrate that a single crystal undergoes slip

when the CRSS on the slip plane reaches a critical value. This phenomenon, known as Schmid's law, is particularly evident in HCP metals. The restricted number of slip systems in hcp metals leads to significant differences between the orientation of the slip plane and the axis of applied tensile forces. This contrast highlights the importance of Schmid's law in these crystalline systems. The determination of the CRSS magnitude within a crystal is intricately affected by the intricate interplay between its dislocation population and various defects, including vacancies, interstitials, and impurity atoms. While this stress inherently exceeds the force required to activate an isolated dislocation, it is still significantly lower than the stress necessary to initiate slip within a perfectly ordered lattice. Building upon this reasoning, the CRSS tends to decrease as the density of defects within the material decreases. This observation underscores the significant impact of defect concentrations on the material's mechanical behavior. It offers valuable insights into the intricate interplay between lattice imperfections and the initiation of plastic deformation.

1.3 Texture Analysis

Numerous crucial materials for technology, such as metals, ceramics, and certain plastics, consist of multiple crystalline structures. These materials' characteristics are determined by the properties of individual crystals and the parameters that define their polycrystalline nature. As specific crystal properties exhibit strong directional dependence, the crystallographic orientation of crystallites within the aggregate texture of polycrystalline materials becomes crucial among these parameters. When all potential orientations of the crystallites are equally probable, the reliance on orientation diminishes on average. As a result, the polycrystalline material exhibits isotropic behavior overall ([61]). It has long been recognized that the microstructure significantly influences the properties of materials. The majority of engineering materials are inherently polycrystalline, with few exceptions. In such instances, the microstructure can be defined as the amalgamation of morphology and orientation of the constituents. Morphology pertains to the shape of the constituents, while orientation is linked to their crystallography. Consequently, texture emerges as a fundamental aspect of microstructure. Understanding microstructure and crystallography is crucial

in examining fabricated and natural materials. Traditionally, separate investigations have been conducted in parallel: Optical microscopy, scanning electron microscopy (SEM), and image analysis are utilized to analyze microstructure, while crystallographic analysis relies on x-ray texture determination or diffraction in the transmission electron microscope (TEM), supplemented by contributions from Kossel diffraction and selected area channeling (SAC) in the SEM. Hence, a typical material profile might encompass the distribution of grain sizes alongside texture analysis determined through X-ray techniques ([62]). Electron backscatter diffraction (EBSD) is a powerful technique for characterizing and analyzing microstructures in crystalline materials ([63]). EBSD data can determine numerous structural parameters influencing materials' properties and performance, including grain size, phase constituents, mechanical anisotropy, and residual strain ([64]). This capability underscores EBSD as a valuable tool for controlling and developing the microstructures of commercial metallic materials ([65]). Electron Backscatter Diffraction (EBSD) is a technique that enables the retrieval of crystallographic information from samples using a scanning electron microscope (SEM) ([66]). In EBSD, a fixed electron beam hits a tilted crystalline sample, causing diffracted electrons to create a pattern on a fluorescent screen. This distinctive pattern reflects the crystal structure and orientation of the specific sample region from which it originates. The diffraction pattern enables the measurement of crystal orientation, grain boundary misorientations, and differentiation between various materials and offers insights into local crystalline perfection. By scanning the beam across a grid on a polycrystalline sample and measuring the crystal orientation at each point, the resultant map will unveil the morphology of constituent grains, their orientations, and their boundaries ([67]). Additionally, this data can illustrate the preferred crystal orientations, commonly known as texture, present within the material. EBSD enables a comprehensive and quantitative representation of the sample's microstructure ([68]).

1.3.1 Representation of Orientations and Textures

Pole figures and Orientation Distribution Functions (ODFs) are crucial in studying crystallography, materials science, and technology. These tools are utilized to ascertain the preferred orientation of crystals within a material. Pole figures are visual rep-

resentations depicting a material's distribution of crystallographic orientations. They illustrate the density of crystallographic planes perpendicular to a specific direction in space. Typically presented as polar plots, they depict the density of the crystallographic plane as a function of the angle between the crystallographic plane and the direction in question. ODFs serve as mathematical representations of the preferred orientation of crystals within a material. They characterize the likelihood of encountering a crystal in a specific orientation within a given volume of material. ODFs are commonly depicted as a function of Euler angles, which describe the crystal's orientation relative to a reference frame.

1.3.1.1 Pole figures

A pole figure represents the distribution of a chosen orientation or set of orientations within a crystal or group of crystals comprising a material. It is typically depicted as a histogram. A pole figure measurement acquired through X-ray diffraction encompasses a volume of reciprocal space corresponding to a half sphere. It enables the determination of the orientation of specific periodicities, often called planes, present in a material. Although a pole figure could be derived from an orientation distribution function to illustrate various crystal directions, only reflections that are not forbidden will be visible in a pole figure measurement. The term "pole figure" denotes the outcomes derived from an X-ray pole figure measurement. Figure.1.10 depicts a schematic pole figure derived from a single crystal with a constant direct projection. In this representation, the continuous direct projection's angle between the surface normal and a plane can be directly gauged as the radius on the pole figure. In contrast, Figure.1.10 illustrates the surface measured by this pole figure in the three-dimensional reciprocal space. High intensities, denoted by dots in Figure.1.10, are noticed on the pole figure when a reciprocal space point intersects a sphere of radius $|S| = 1/d$ centered on the origin of the reciprocal lattice ([69]).
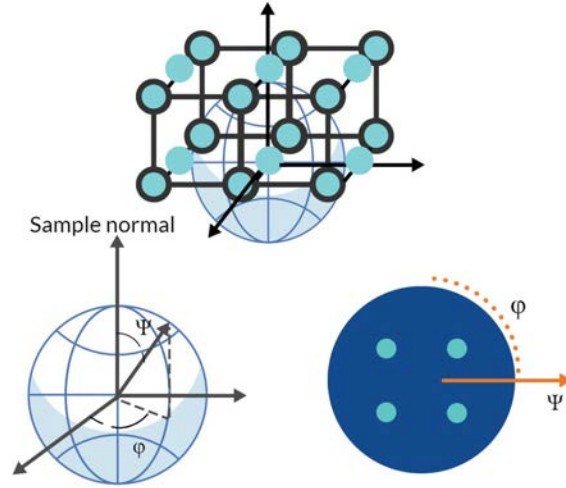
Figure 1.10: Reciprocal space representation of the single crystal reciprocal lattice and pole figure in 3D dimension (**top**), the sample reference frame defines the ϕ and ψ angles (**left**), and schematic representation of a single crystal pole figure (**right**).

1.3.1.2   Orientation distribution function

Quantitative texture analysis thoroughly examines the ODF, such as measuring the weight fractions of texture components or fibers. These components enable deductions about various processes affecting the microstructure, like deformation or recrystallization. Each of these processes generates distinctive texture components, allowing for the identification of changes during thermo-mechanical processing steps. A polycrystalline material's ODF quantitatively portrays its crystallographic texture, facilitating the computation of its anisotropic physical properties. The ODF sometimes called the orientation density function, is defined by the orientation space corresponding to each orientation. It represents attributes such as the volume percentage of crystals in a polycrystalline specimen oriented in a specific manner. This is often expressed by a formula Equation.1.20, ([70]).

$$odf(g) = \frac{1}{V}\frac{dV(g)}{dg} \tag{1.20}$$

Where V is the volume and g is the percentage of crystals in a polycrystalline specimen in this specific orientation.

28

1.4 Fundamentals of Continuum Mechanics

Continuum mechanics provides a robust and practical framework for understanding a wide range of physical phenomena, avoiding the necessity to delve into the intricate details of underlying microstructures. By conceptualizing materials as continuous media, continuum mechanics allows us to analyze and predict macroscopic behaviors, including deformation, stress, strain, and fluid flow. While predictions derived from macroscopic assessments may not yield precise outcomes, they are accurate enough to guide the engineering design of industrial products. To conclude, it is necessary to investigate micromechanical behavior by examining engineering materials in more depth under prescribed boundary conditions. Microscopic examination requires the reflection of kinetic and kinematic material behavior in the material model under certain assumptions. Deformation of materials can be examined from diverse viewpoints, and a fundamental factor in continuum mechanics for measuring deformation is the deformation gradient, symbolized by the tensor $\boldsymbol{F}$. The deformation gradient tensor, a second-order tensor, carries considerable significance in mathematically clarifying the transformation of line elements from their original state in the reference configuration to their present spatial condition. For visual clarity, imagine a line element $\mathbf{dX}$ positioned within the material body, where $\mathbf{X}$ represents the position of this element from the reference configuration, as depicted in Figure 1.11. As a result of either kinematic or kinetic alterations, the motion of the material body in space causes the line element to take on the shape of $\mathbf{dx}$, with the distance changing to $\mathbf{x}$ in the current configuration. The motion can be efficiently described using a vector function χ, while the gradient within the material can be expressed as $\frac{\partial \chi}{\partial \mathbf{X}}$.

$$\mathbf{dx} = \chi(\mathbf{X} + \mathbf{dX}) - \chi(\mathbf{X}) = (\mathbf{Grad}\chi)\mathbf{dX} \tag{1.21}$$

If we represent the vector function χ as $\mathbf{x} = \mathbf{x}(\mathbf{X}, \mathbf{t})$, we can denote the material gradient as:

$$\boldsymbol{F} = \frac{\partial \mathbf{x}}{\partial \mathbf{X}}, \qquad F_{ij} = \frac{\partial x_i}{\partial X_j} \tag{1.22}$$

The inverse deformation gradient $\boldsymbol{F}^{-1}$ maps the spatial line element $\mathbf{dx}$ to the material line element $\mathbf{dX}$.

$$\boldsymbol{F}^{-1} = \frac{\partial \mathbf{X}}{\partial \mathbf{x}}, \qquad {F^{-1}}_{ij} = \frac{\partial X_i}{\partial x_j} \tag{1.23}$$

The decomposition of the deformation gradient can consistently be achieved by multiplying two tensors: a stretch tensor and a rotation tensor. This decomposition appears in two distinct forms, known as the polar decomposition.

$$\boldsymbol{F} = \boldsymbol{RU} \qquad Polar \quad Decomposition \quad (Material)$$
$$\boldsymbol{F} = \boldsymbol{vR} \qquad Polar \quad Decomposition \quad (Spatial)$$

(1.24)

In this situation, the tensor $\boldsymbol{R}$ possesses the property of being a proper orthogonal tensor, indicating that $\boldsymbol{R}^T \boldsymbol{R} = \boldsymbol{I}$ and $\det(\boldsymbol{R}) = 1$, where $\boldsymbol{R}^T$ denotes the transpose of $\boldsymbol{R}$. This tensor is designated as the rotation tensor and represents the local rotational behavior at the point indicated by $\mathbf{X}$. Further, it defines the skew-symmetric angular velocity tensor $\boldsymbol{\Omega}$.

$$\boldsymbol{\Omega} = \dot{\boldsymbol{R}}\boldsymbol{R}^T$$

(1.25)

The tensor $\boldsymbol{U}$ takes on the shape of a unique symmetric tensor known as the right stretch tensor. It measures the local stretch the material undergoes at the point indicated by X. Moreover, $\boldsymbol{v}$ represents a symmetric, positively definite second-order tensor, often called the left stretch tensor. The velocity gradient serves as a measure
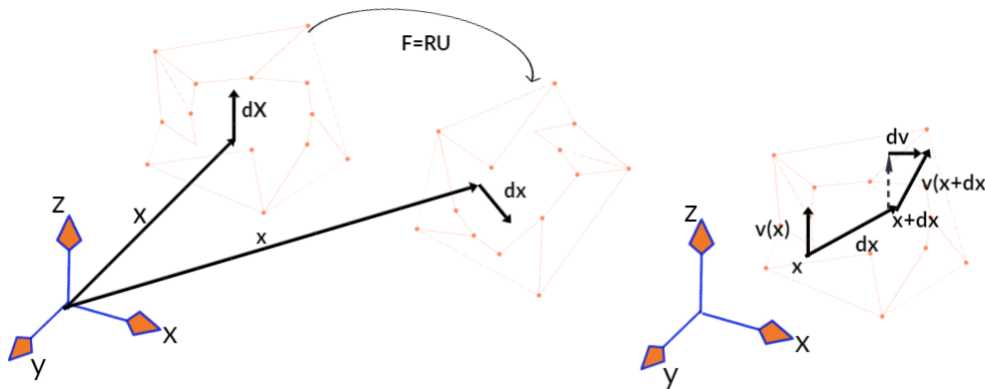
Figure 1.11: Kinematics of a line element in a material body with the deformation gradient (**left**) and kinematics of velocity gradient (**right**)

of the rate at which a material undergoes deformation. When we consider two stationary points, namely, $\mathbf{x}$ and $\mathbf{x} + \mathbf{dx}$, as shown in Fig. 1.11, the velocities of material particles at these positions at any given moment in time are represented as $\mathbf{v}(\mathbf{x})$ and $\mathbf{v}(\mathbf{x} + \mathbf{dx})$.

30

$$\mathbf{v}(\mathbf{x} + \mathbf{dx}) = \mathbf{v}(\mathbf{x}) + \frac{\partial \mathbf{v}}{\partial \mathbf{x}} \mathbf{dx} \tag{1.26}$$

The relative velocity between these points is given by:

$$\mathbf{dv} = \frac{\partial \mathbf{v}}{\partial \mathbf{x}} \mathbf{dx} \approx \mathbf{ldx} \tag{1.27}$$

With "l" is defined to be the spatial velocity gradient

$$\mathbf{l} = \frac{\partial \mathbf{v}}{\partial \mathbf{x}} = grad\mathbf{v} \quad l_{i,j} = \frac{\partial v_i}{\partial x_j} \tag{1.28}$$

The spatial velocity gradient can be expressed as

$$\frac{\partial \mathbf{v}}{\partial \mathbf{x}} = \frac{\partial \mathbf{v}}{\partial \mathbf{x}} \frac{\partial \mathbf{X}}{\partial \mathbf{x}} = \frac{\partial}{\partial \mathbf{X}} \left(\frac{\partial \mathbf{x}}{\partial t} \right) \frac{\partial \mathbf{X}}{\partial \mathbf{x}} = \frac{\partial}{\partial t} \left(\frac{\partial \mathbf{x}}{\partial \mathbf{X}} \right) \frac{\partial \mathbf{X}}{\partial \mathbf{x}} \tag{1.29}$$

Alternatively, equation 1.29 can be represented as $\mathbf{l} = \dot{\boldsymbol{F}} \boldsymbol{F}^{-1}$.

The velocity gradient can also be decomposed into symmetric and skew-symmetric tensor parts.

$$\mathbf{l} = \boldsymbol{d} + \boldsymbol{w} \tag{1.30}$$

Where $\boldsymbol{d}$ is the rate of deformation tensor (rate of stretch tensor) and $\boldsymbol{w}$ is the spin tensor (rate of rotation or vorticity tensor), defined by

$$
\begin{aligned}
\boldsymbol{d} &= \frac{1}{2}(\mathbf{l} + \mathbf{l}^{\mathbf{T}}), & d_{ij} &= \frac{1}{2} \left(\frac{\partial v_i}{\partial x_j} + \frac{\partial v_j}{\partial x_i} \right) \\
\boldsymbol{w} &= \frac{1}{2}(\mathbf{l} - \mathbf{l}^{\mathbf{T}}), & w_{ij} &= \frac{1}{2} \left(\frac{\partial v_i}{\partial x_j} - \frac{\partial v_j}{\partial x_i} \right)
\end{aligned} \tag{1.31}
$$

While considering two line elements in the reference configuration $d\mathbf{X}^{(\mathbf{1})}$ and $d\mathbf{X}^{(\mathbf{2})}$ which are mapped into line elements $d\mathbf{x}^{(\mathbf{1})}$ and $d\mathbf{x}^{(\mathbf{2})}$ in the current configuration we can write,

$$
\begin{aligned}
d\mathbf{x}^{(\mathbf{1})} \cdot d\mathbf{x}^{(\mathbf{2})} &= \boldsymbol{F} d\mathbf{X}^{(\mathbf{1})} \cdot \boldsymbol{F} d\mathbf{X}^{(\mathbf{2})} \\
&= d\mathbf{X}^{(\mathbf{1})} (\boldsymbol{F}^T \boldsymbol{F}) d\mathbf{X}^{(\mathbf{2})} \\
&= d\mathbf{X}^{(\mathbf{1})} \boldsymbol{G} d\mathbf{X}^{(\mathbf{2})}
\end{aligned} \tag{1.32}
$$

where by definition $\boldsymbol{G}$ is the Right Cauchy Green Strain denoted as $\boldsymbol{F}^T \boldsymbol{F}$ and also the same way Left Cauchy-Green Strain $\boldsymbol{b}$ (Finger tensor) defined as $\boldsymbol{F} \boldsymbol{F}^T$ in deformed configuration.

Whereas the left and right Cauchy-Green tensors give information about the change in angle between line elements and the stretch of line elements, the Green-Lagrange strain (E) and the Euler Almansi Strain (e) tensors directly give information about the change in the squared length of elements. Green Lagrange strain is defined as,

$$\begin{aligned} E &= \frac{1}{2}(G - I) = \frac{1}{2}(FF^T - I) \qquad Green \quad Lagrange \quad Strain \\ e &= \frac{1}{2}(I - b^{-1}) = \frac{1}{2}(I - F^{-T}F^{-1}) \qquad Euler \quad Almansi \quad Strain \end{aligned} \tag{1.33}$$

Whereas the Cauchy stress is the pushforward of the second Piola-Kirchhoff (PK2) stress with deformation gradient F Equation 1.34,

$$\sigma = \frac{1}{J}FSF^T \tag{1.34}$$

In equation J is the volume ratio ($det F$) and PK2 stress (S) can be found from the multiplication of rotated elastic modulus (Eq. 1.35) according to initial orientations $\tilde{C}=Q_0^C C Q_0^{CT}$ with material strain tensor Green-Lagrange strain from Eq. 1.33 and Eq. 1.36 where Q_0^C is the transformed fourth order initial rotational orientation tensor. ([71],[72]).

$$C = \begin{pmatrix} C_{11} & C_{12} & C_{12} & 0 & 0 & 0 \\ C_{12} & C_{11} & C_{12} & 0 & 0 & 0 \\ C_{12} & C_{12} & C_{11} & 0 & 0 & 0 \\ 0 & 0 & 0 & C_{44} & 0 & 0 \\ 0 & 0 & 0 & 0 & C_{44} & 0 \\ 0 & 0 & 0 & 0 & 0 & C_{44} \end{pmatrix} \tag{1.35}$$

$$S = \tilde{C} : E \tag{1.36}$$

The Kirchhoff stress tensor τ, which is a spatial tensor field parameterized by spatial coordinates, can be found in Equation. 1.37,

$$\tau = J\sigma \tag{1.37}$$

Cauchy stress and the rate of strain tensor exhibit incompatibility in the presence of rigid body rotations. It is perhaps easiest to comprehend this situation when the object has been stretched to a fixed amount held constant while it continues to rotate (Fig. 1.12). During this rotation, the stress transitions from being primarily influenced by the y-axis to being primarily influenced by the x-axis. Consequently, stress changes with time, leading to $\dot{\sigma} \neq 0$. However, the rate of deformation tensor is

32
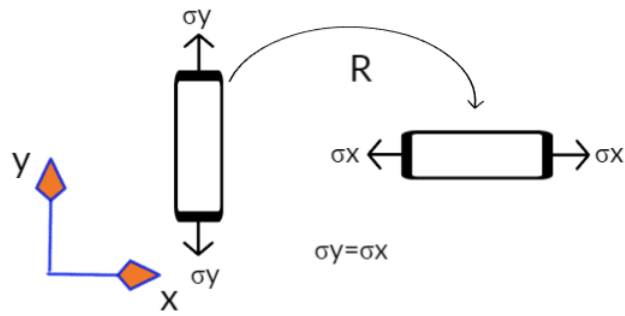
Figure 1.12: Rigid body rotation of stretched object

zero because no actual deformations occur while the material rotates under a constant stretch. In plasticity theory, two primary approaches are commonly utilized. The first category of methods relies on hyperelastic-plastic relationships and multiplicative elastic-plastic kinematics. It involves a Helmholtz free energy density governed by either elastoplastic deformation [73], [74], [75]. On the other hand, the second category of approaches relies on hyperelastic-plastic relationships, decomposing the deformation rate additively and employing objective stress.
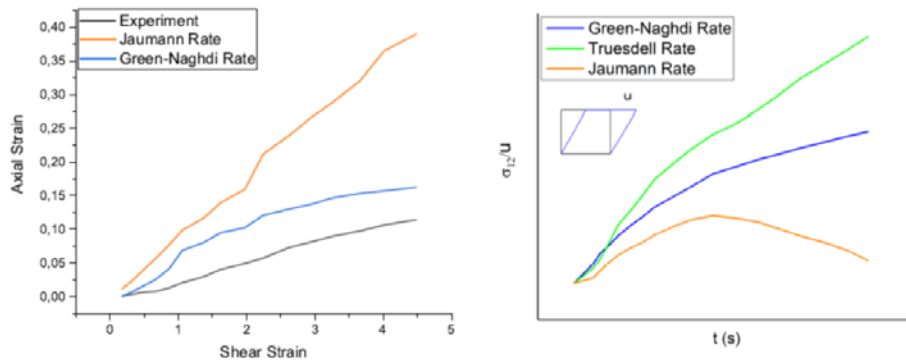
Figure 1.13: Axial strain versus shear strain curve under pure torsion (**left**) and predictions from three objective stress rates under simple shear (**right**) ([76])

When developing elastoplastic models to accommodate finite strain and rate-dependent deformation, including objective stress rates in the constitutive equations becomes crucial. Objective stress rates guarantee that the model's predictions remain consis-

tent regardless of coordinate systems or frames of reference. In the past, a commonly used stress rate was the Zaremba-Jaumann-Noll stress rate, also known as the Jaumann stress rate [77]. However, further investigations demonstrated that this stress rate could lead to unwanted oscillations, particularly in cases involving hyperelastic materials undergoing simple shear deformation [78], [79]. This drawback prompted the exploration of alternative objective stress rates that could effectively characterize metallic behavior under finite strain conditions. To address the oscillatory behavior associated with the Jaumann stress rate, Johnson introduced the Green-Naghdi stress rate [80]. The Green-Naghdi stress rate provides a notable advantage by ensuring a monotonically increasing shear stress. This feature effectively eliminates the oscillations associated with the Jaumann stress rate. The Green-Naghdi stress rate's capacity to produce a stable and monotonic response makes it especially suitable for precisely characterizing the behavior of metallic materials experiencing finite strain conditions. By employing the Green-Naghdi stress rate, researchers and engineers can improve the accuracy and stability of their elastoplastic models when dealing with materials undergoing complex deformation processes at finite strains. Choosing an appropriate stress rate is crucial to ensure the model's predictions align with experimental observations and accurately represent the material's mechanical behavior throughout its deformation history. These advancements prompted further investigations, leading to the proposal of objective stress rates specifically tailored for capturing the behavior of metallic materials under finite strain conditions. Notable among these are the Green-Naghdi rate [81], Cotter-Rivlin rate [82], Oldroyd rate [83], and Truesdell rate [84]. Each of these stress rates serves distinct purposes, as outlined in Table 1.5. The predictions generated by these different objective stress rates under shear loading are depicted in Figure 1.13.

1.5 The Aim and The Outline of This Thesis

This thesis aims to contribute to a more detailed characterization of severe plastic deformations at the microscale by applying the crystal plasticity within the finite-element method for numerical simulations of extrusion processes. This thesis investigates the deformation under SPD processes boundary conditions, the specimen's tex-

Table 1.5: Objective stress rates for constitutive equations

Stress Rates	Equations
Jaumann	$\boldsymbol{\sigma}^{\nabla J} = \dot{\boldsymbol{\sigma}} + \boldsymbol{\sigma}\boldsymbol{w} - \boldsymbol{w}\boldsymbol{\sigma}$
Jaumann	$\boldsymbol{\tau}^{\nabla J} = \dot{\boldsymbol{\tau}} + \boldsymbol{\tau}\boldsymbol{w} - \boldsymbol{w}\boldsymbol{\tau}$
Green-Naghdi	$\boldsymbol{\sigma}^{\nabla G} = \dot{\boldsymbol{\sigma}} + \boldsymbol{\sigma}\boldsymbol{\Omega} - \boldsymbol{\Omega}\boldsymbol{\sigma}$
Green-Naghdi	$\boldsymbol{\tau}^{\nabla G} = \dot{\boldsymbol{\tau}} + \boldsymbol{\tau}\boldsymbol{\Omega} - \boldsymbol{\Omega}\boldsymbol{\tau}$
Oldroyd	$\boldsymbol{\sigma}^{\nabla O} = \dot{\boldsymbol{\sigma}} - \mathbf{l}\boldsymbol{\sigma} - \boldsymbol{\sigma}\mathbf{l}^T$
Oldroyd	$\boldsymbol{\tau}^{\nabla O} = \dot{\boldsymbol{\tau}}\mathbf{l}\boldsymbol{\tau} - \boldsymbol{\tau}\mathbf{l}^T$
Truesdell	$\boldsymbol{\sigma}^{\nabla T} = \dot{\boldsymbol{\sigma}} - \mathbf{l}\boldsymbol{\sigma} - \boldsymbol{\sigma}\mathbf{l}^T + tr(\boldsymbol{d})\boldsymbol{\sigma}$
Cotter-Rivlin	$\boldsymbol{\sigma}^{\nabla CR} = \dot{\boldsymbol{\sigma}} + \mathbf{l}^T\boldsymbol{\sigma} + \boldsymbol{\sigma}\mathbf{l}$
Cotter-Rivlin	$\boldsymbol{\tau}^{\nabla CR} = \dot{\boldsymbol{\tau}} + \mathbf{l}^T\boldsymbol{\tau} + \boldsymbol{\tau}\mathbf{l}$

ture evolution, plastic deformation response, material mechanical characteristics after deformation, and the change in simulated microstructural properties. In the course of this thesis, the traditional SPD processes TE and ECAP are studied. The novel SPD process, namely non-linear twist extrusion (NLTE), is investigated with a novel explicit crystal plasticity algorithm and compared with the experimental results. Thus, the design of new production methodologies and process parameters are determined.

Chapter 2 introduces the initial computational study of the newly developed severe plastic deformation technique, the Non-Linear Twist extrusion process (NLTE). The results concerning a conventional extrusion process, linear twist extrusion (LTE), are discussed in detail. The method is expected to offer a great potential for industrial use.

Chapter 3 confers the study investigating the comparison and contrast of the texture evolutions during NLTE and TE processes, which are explored through the crystal plasticity finite element method. Single copper crystals have billet forms and are extruded separately through the TE and NLTE mold models. In addition to spatial stress and strain evolution investigations, extruded billets' orientation differences and texture evolution are examined for two different initial orientations of a single copper crystal. Moreover, the deformation histories at other locations of the sample are

analyzed with the crystal plasticity finite element method (CPFEM) to compare the performance of both techniques.

Chapter 4 describes a rate-dependent new crystal plasticity user subroutine to define material behavior (VUMAT) algorithm developed for use with the explicit solver of the Abaqus FE commercial program. The developed model is compared with experimental data under various loading conditions and digital image correlation experiments. The capability of the model to capture real material response is discussed.

Chapter 5 extends a comprehensive study of the newly developed severe plastic deformation NLTE process description by implementing the newly developed algorithm of 3D explicit Crystal plasticity finite element user material code (VUMAT). A new explicit CPFEM subroutine is employed to compare the experimental and predicted results of a single copper crystal Non-Linear Twist extrusion process. Moreover, the texture evolution and performance of newly developed severe plastic deformation mold are investigated.

Chapter 6 submits the results of three-dimensional explicit crystal plasticity finite element method (CPFEM) modeling of the equal channel angular pressing (ECAP) process of single crystal niobium (Nb).A study is conducted to analyze the behavior of single-crystalline Nb in the ECAP process to establish an approach to investigate the associated Taylor factor (M) and texture formation using different shear systems in body-centered cubic (BCC) structures. The developed model has been validated by comparison with experimental observations in the literature.

CHAPTER 2

NUMERICAL ANALYSIS OF A NEW TORSIONAL EXTRUSION PROCESS

2.1   Introduction

The classical twist extrusion process, which is referred to as linear twist extrusion (LTE) is based on pressing out a prism specimen through a die with a profile consisting of two prismatic regions separated by a twist part ([85], [86], [87], [88]). The original cross-section is maintained while it undergoes severe plastic deformation and the process can be applied repeatedly, which changes in the microstructure and properties of the specimen. High backpressure is applied when it exits the die. A disadvantage of LTE is strain localization at the inlet and outlet of the twisting part. Very high strain is imposed on the billet at both parts, while the billet is subjected to rigid body rotation inside the twisting part. This local strain causes high punching force and possibly inhomogeneous strain distribution.

The current study proposes a new SPD technique called Nonlinear Twist Extrusion (NLTE) to overcome the disadvantages of the LTE process. The initial numerical analysis is presented in comparison to classical twist extrusion processes. NLTE technique is devised based on TE, but an effective die geometry is designed here, resulting in higher and more homogeneous plastic strain evolution. The shear strain is imposed throughout the whole channel without rigid body rotation. The purpose is to spread the high plastic deformation to the larger regions of the cross-section.

The chapter is organized as follows. Firstly, in Section 2, the theoretical aspects of kinematics and the kinetics of the nonlinear twist extrusion process are discussed. Then, Section 3 introduces the mold geometry for linear and nonlinear twist extrusion, and the numerical procedure is summarized. The material response, boundary

conditions, and finite element analysis procedure are presented. The numerical results for both linear and nonlinear cases are illustrated in comparison in Section 4. The results are discussed in detail. Finally, the work is summarized, and concluding remarks are given in Section 5.

2.2   Kinetics and Kinematics of NLTE Process

Assume that the rotation angle of the twist channel and displacement can be expressed as $\theta = Cx^n \cdot \theta$ is the rotation angle by twisting, C is γ/r, x is the displacement along the longitudinal axis, n is the parameter, which is 1 for the linear torsion case (Fig. 2.1).
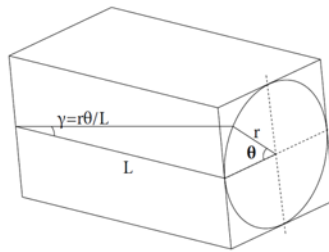
Figure 2.1: Linear twisting geometry

In the conventional TE, the rotation angle can be assumed to increase linearly with displacement. Therefore, it can be written as $\frac{d\theta}{dx} = C$, and for n=2, the rotation angle θ increases in a parabolic relation, and it can be found that $\frac{d\theta}{dx} = 2Cx$. It shows that the workpiece rotates more in the NLTE process than the LTE. As a consequence of a nonlinear design, it is expected that the specimen has to be faced with more severe and homogeneous plastic deformation if it is compared with the LTE process.

The currently designed channel of NLTE consists of three parts, as shown in Figure 2.2. In part I, the cross-section the channel changes gradually from a circular radius r to an elliptical shape with the major and minor axes of a and b, respectively. Since $ab = r^2$, the cross-sectional area of the channel is constant through this part. The bar is twisted in part II according to the parabolic relation $\theta = Cx^2$. In part III, the twisting continues with a constant rotation angle, but the cross-section changes from an elliptical to a circular shape again. The shape of the cross-section must be changed

38

back to the circle otherwise, the bar will be extruded out in an elliptical shape. FEM simulations illustrate that a backpressure is necessary for a proper extrusion process resulting in the original cross-section. Equivalent plastic strain values are used to show the advantage of the NLTE process with respect to the LTE one. Using the equivalent plastic strain relations and considering three parts of deformation of NLTE, the equivalent plastic strain part I from a circle (r) and to ellipse (a, b; $ab = r^2$). The design concept of NLTE was presented in a previous study and can be found as follows ([89]);

$$d\varepsilon_I^{eq} = \sqrt{\frac{2}{3}[(d\varepsilon_x^p)^2 + (d\varepsilon_y^p)^2 + (d\varepsilon_z^p)^2 + \frac{1}{3}((d\gamma_{xy}^p)^2 + (d\gamma_{zx}^p)^2 + (d\gamma_{yz}^p)^2)]} \quad (2.1)$$

In the first part of NLTE, when the following conditions of $d\varepsilon_z^p = d\gamma_{xy}^p = d\gamma_{yz}^p = d\gamma_{xz}^p = 0$, $d\varepsilon_x^p = \frac{dx}{r}$ and $d\varepsilon_y^p = \frac{d\gamma}{r}$ are applied, then the equivalent plastic strain in part I is;

$$d\varepsilon_I^{eq} = \sqrt{\frac{2}{3}[(\frac{dx}{r})^2 + (\frac{dy}{r})^2]} = \sqrt{\frac{2}{3}(\frac{dx}{r})^2 + (\frac{-dx}{r})^2} = \frac{2}{\sqrt{3}}\frac{dx}{r} \quad (2.2)$$

$$\varepsilon_I^{eq} = \int_r^a d\varepsilon_I^P = \frac{2}{\sqrt{3}}\ln\frac{a}{r} \quad (2.3)$$

Equivalent strain part II in NLTE can be described below;

$$d\varepsilon_{II}^{eq} = \sqrt{\frac{2}{3}[(d\varepsilon_r^p)^2 + (d\varepsilon_\theta^P)^2 + (d\varepsilon_x^p)^2 + \frac{1}{3}[(d\gamma_{r\theta}^p)^2 + (d\gamma_{xr}^p)^2 + (d\gamma_{\theta x}^p)^2]]} \quad (2.4)$$

Within the part II $d\varepsilon_r^{eq} = d\varepsilon_\theta^P = d\gamma_{\theta x}^p = d\gamma_{xr}^p = 0$ and $d\gamma_{r\theta}^p = rCdx$

$$\varepsilon_{II}^{eq} = \int \varepsilon_{II}^p = \sqrt{\frac{1}{3}} \int d\gamma_{r\theta}^p = \sqrt{\frac{1}{3}}\frac{r\theta_{max}}{L} \quad (2.5)$$

Since the deformations in part I and part III are similar, the equivalent strains are the same. Finally, the plastic equivalent strain (PEEQ) equation for NLTE is shown below;

$$\varepsilon^{eq} = 2\varepsilon_I^p + \varepsilon_{II}^P \quad (2.6)$$

$$\varepsilon^{eq} = 2(\frac{2}{\sqrt{3}}\ln\frac{a}{r}) + \sqrt{\frac{1}{3}}\frac{r\theta_{max}}{L} \quad (2.7)$$

According to Equation 2.7 for one pass of NLTE specimen, the equivalent plastic strain is approximately 1.4. As will be shown in the following section the value of the back pressure is identified according to this value, which will also depend on the material.
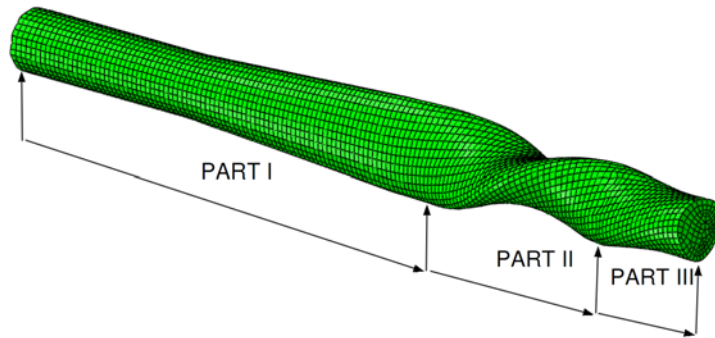
Figure 2.2: Schematic extrusion of the nonlinear twisting workpiece

2.3 Simulations of the Linear and the NonLinear Twist Extrusion

Commercial finite element software Abaqus is used to simulate LTE and NLTE processes. Copper specimens are modeled with rectangular and cylindrical shapes for LTE and NLTE, respectively. The von Mises plasticity model is the constitutive model used to simulate severe plastic deformations of workpieces. The true stress-strain curve of the copper specimen is illustrated in Figure 2.4. The dimensions of rectangular and cylindrical specimens are $20 \quad mm \times 20 \quad mm \times 50 \quad mm$ and $r = 10 \quad mm \times 30 \quad mm$ length. Explicit dynamic approaches are used due to the modeled molds' design complexity and severe plastic deformations. Mass scaling is employed to reduce calculation costs and speed up simulations by setting the value to 100 for the entire model in the analysis. The energy balance of the model alters for both LTE and NLTE processes as time progresses. Figure 2.3 illustrates this change by displaying the variations in kinetic energy (KE), internal energy (IE), and plastic dissipation energy (PD). It is worth noting that the model's total energy (Etotal) remains relatively constant throughout the simulation. To simulate the kinetics of the process, a velocity boundary condition is applied on the punch through its rigid body definition reference point. The punch speed is four mm/s, and the friction coefficient

between the molds and specimen surfaces is chosen to be 0.01. To ensure the removal of specimens from the mold, the dummy bodies were modeled with the same constitutive definition as the specimens and combined with their contact surfaces using tie constraints. The simulations modeled molds, specimens, and punches as rigid bodies. Mesh properties of the simulation models were given in Table-3.1 and FE model of the LTE and NLTE processes were shown in Figure 2.5. Boundary conditions were chosen to represent the real extrusion process. Molds and dummy molds' movement and rotation degree of freedoms are restricted through their rigid body definition reference point, and punch could only move through extrusion direction.
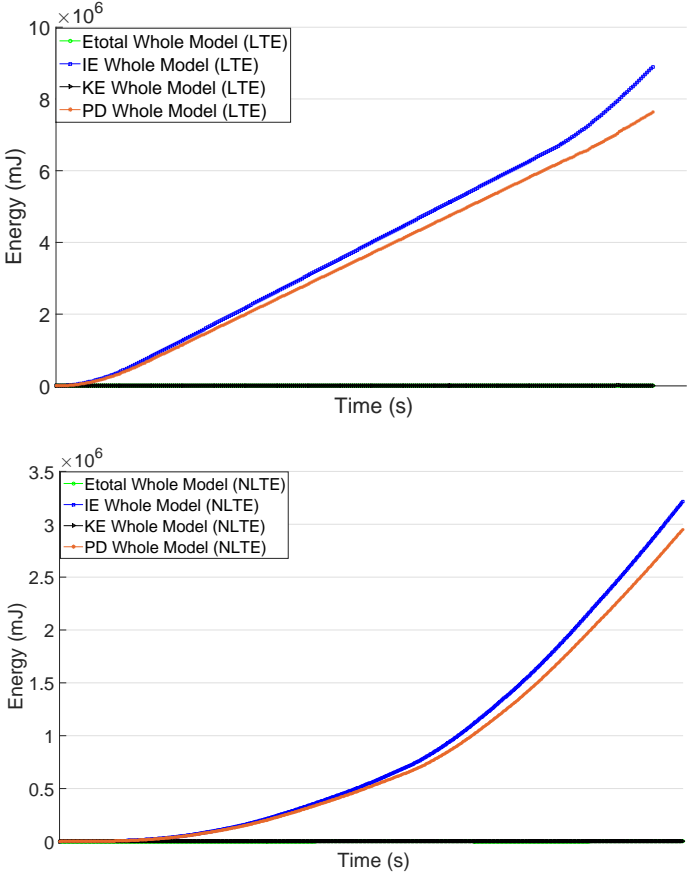
Figure 2.3: Comparison of whole model energies throughout the LTE (**top**) and NLTE (**bottom**) processes
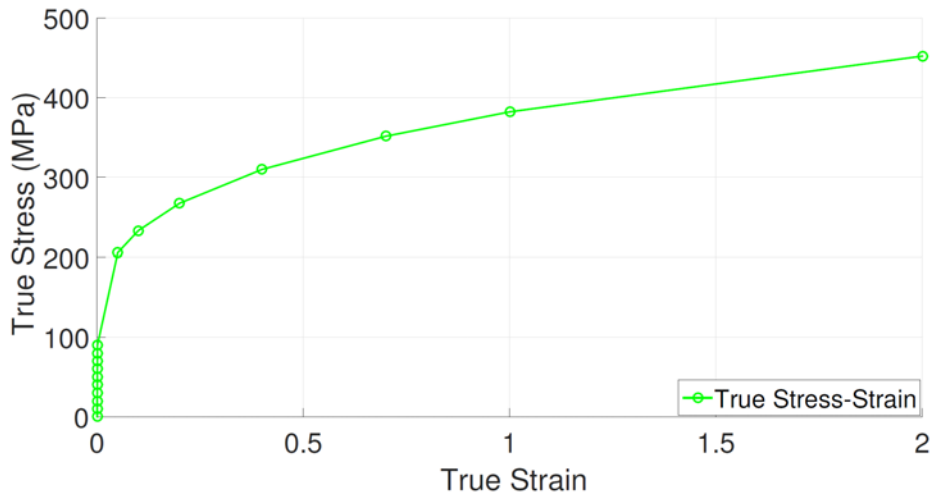
Figure 2.4: True stress vs true strain curve of copper specimen ([90])

(a) LTE Model

(b) LTE Mesh Model

(c) NLTE Model

(d) NLTE Mesh Model
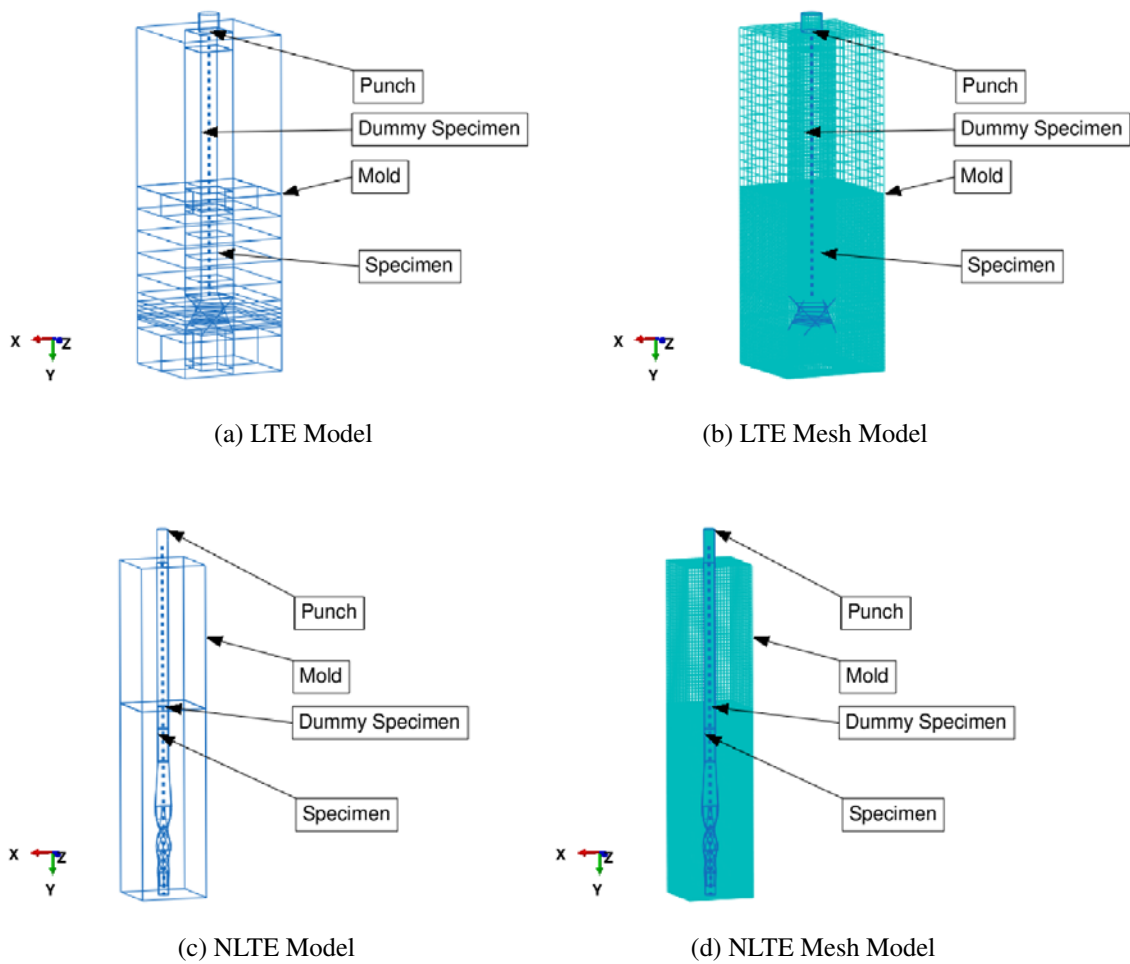
Figure 2.5: FEA Models of LTE and NLTE Processes

42

Table 2.1: FEM Model Mesh Parameters of simulated LTE and NLTE processes.

Model	Element Type	Element Family	Number of Elements
LTE Mold	Explicit-Tetrahedral-C3D4	3D Stress	305835
LTE Dummy Mold	Explicit-Hexahedral-C3D8R	3D Stress	2538
LTE Punch	Explicit-Hexahedral-C3D8R	3D Stress	925
LTE Specimen	Explicit-Hexahedral-C3D8R	3D Stress	20000
LTE Dummy Specimen	Explicit-Hexahedral-C3D8R	3D Stress	4500
NLTE Mold	Explicit-Tetrahedral-C3D4	3D Stress	419316
NLTE Dummy Mold	Explicit-Hexahedral-C3D8R	3D Stress	19866
NLTE Punch	Explicit-Hexahedral-C3D8R	3D Stress	1679
NLTE Specimen	Explicit-Hexahedral-C3D8R	3D Stress	3120
NLTE Dummy Specimen	Explicit-Hexahedral-C3D8R	3D Stress	15794

2.4 Results

To compare the deformation behavior of LTE and NLTE processes, two typical elements of the specimen were chosen at the inner and the outer sections of workpieces distinctively ([91],[92]). The selected elements are highlighted in Figure 2.6.
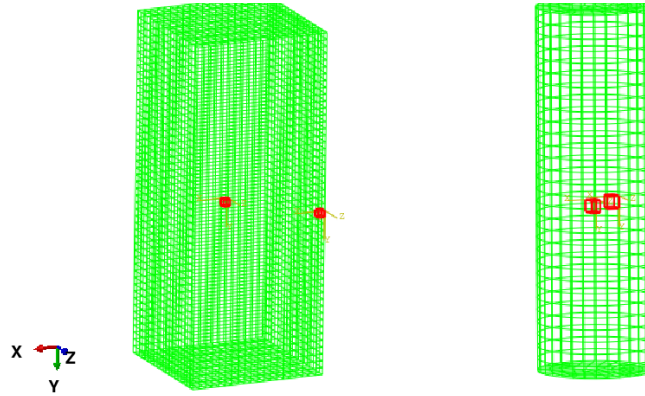
Figure 2.6: Investigated elements with their local coordinates at the center and the middle for the LTE process (**left**) and the NLTE process (**right**).

The simulations illustrate that there is an initial sudden increase of the load in LTE when the specimen head enters the twist zone (Fig.(2.7)). Then, the workpiece advances the twist zone without a significant load change. This behavior has also been discussed in the previous reports ([93]). On the contrary, in NLTE, the load increases throughout the process. This is one of the prominent advantages of NLTE. However, the punch force is dependent on the frictional coefficient. The cross-section of specimens differs between LTE and NLTE processes. To calculate punch pressure, the punch force is divided by their respective cross-sectional areas, enabling a more precise comparison of the results.

The deformed geometry of the specimen during processes and the equivalent plastic strain distribution are directly affected by the applied back pressure ([94]). Figure 2.8 and Figure 2.9 show the equivalent plastic strain distribution and the change in the geometry of the specimen depending on the back pressure values. It can be seen that an increase in back pressure yields more homogenous equivalent strain distribution for both processes. The specimens fill the mold better than the case without the applied back pressure. Moreover, the final cross-section shape resembles the initial
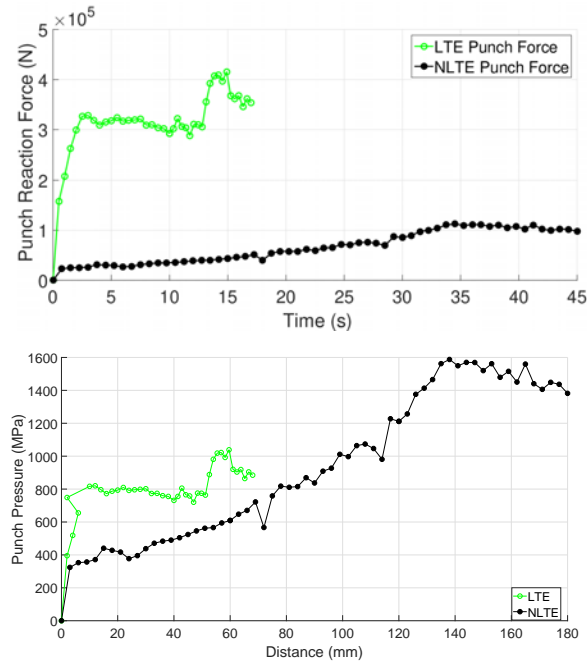
Figure 2.7: The Variation of punch reaction force (**top**) and punch pressure (**bottom**) according to process time and distance, respectively

geometry with the applied back pressure. An approximation to the calculated theoretical equivalent plastic strain value is used here to decide the amount of the applied back-pressure value in simulations. Figure 2.10 shows the equivalent plastic strain distribution of the inner and outer elements of LTE and NLTE specimens according to various back pressure values. It can be seen that plastic equivalent strain evolution in the NLTE process on the cross-section is more homogeneous compared to to traditional LTE processes for various back pressure values. 200MPa back pressure value is identified from Figure 2.10 to obtain the theoretical value of 1.4. Therefore, from now on, this value of back pressure is applied in all FEM simulations of LTE and NLTE processes.

Figure 2.11b and Figure 2.11a depict the Von Mises stress contours for both LTE and NLTE processes following a single pass.The stress values show an increase from the specimen center to the periphery, and maximum stresses can be observed at the edge of the surfaces. In the case of LTE, stress evolution is more heterogeneous, and higher stress values are obtained in certain regions. On the contrary, in the NLTE case, stress distribution is more homogenous throughout the specimen, and high-stress values are

45

(a) 0 MPa Back-Pressure

(b) 100 MPa Back-Pressure

(c) 200 MPa Back-Pressure

(d) 300 MPa Back-Pressure
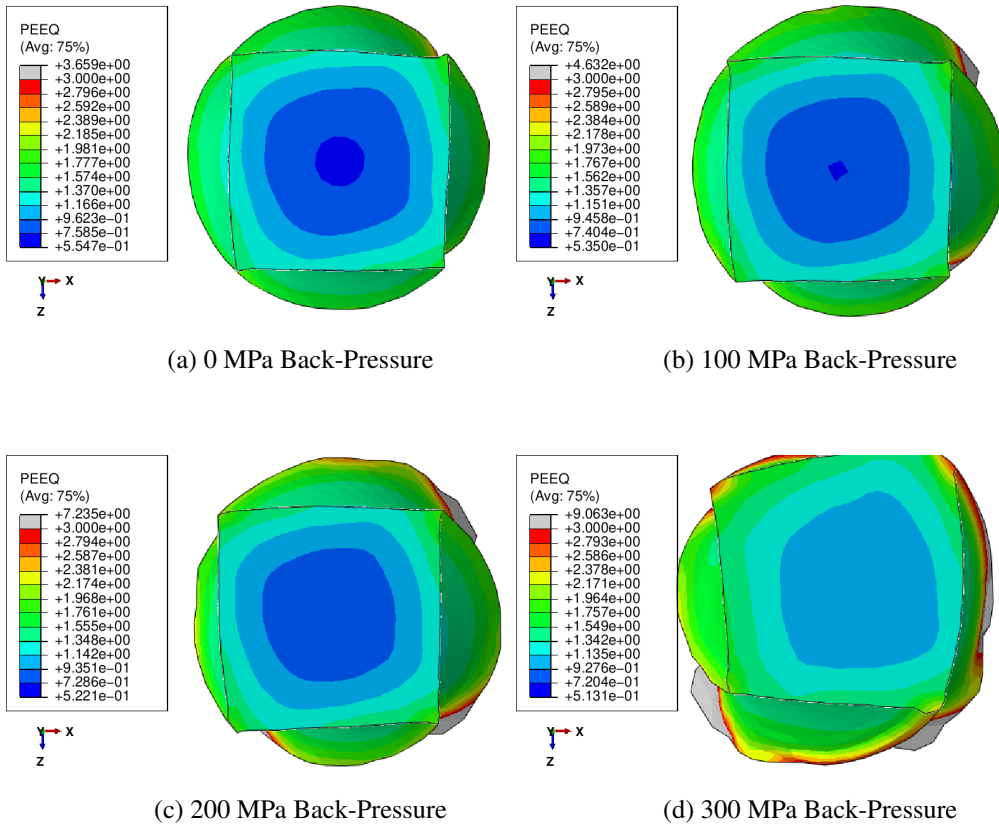
Figure 2.8: Section View of LTE specimen and variation of equivalent plastic strain values depending on the applied back-pressure in LTE process

(a) 0 MPa Back-Pressure   (b) 100 MPa Back-Pressure

(c) 200 MPa Back-Pressure   (d) 300 MPa Back-Pressure
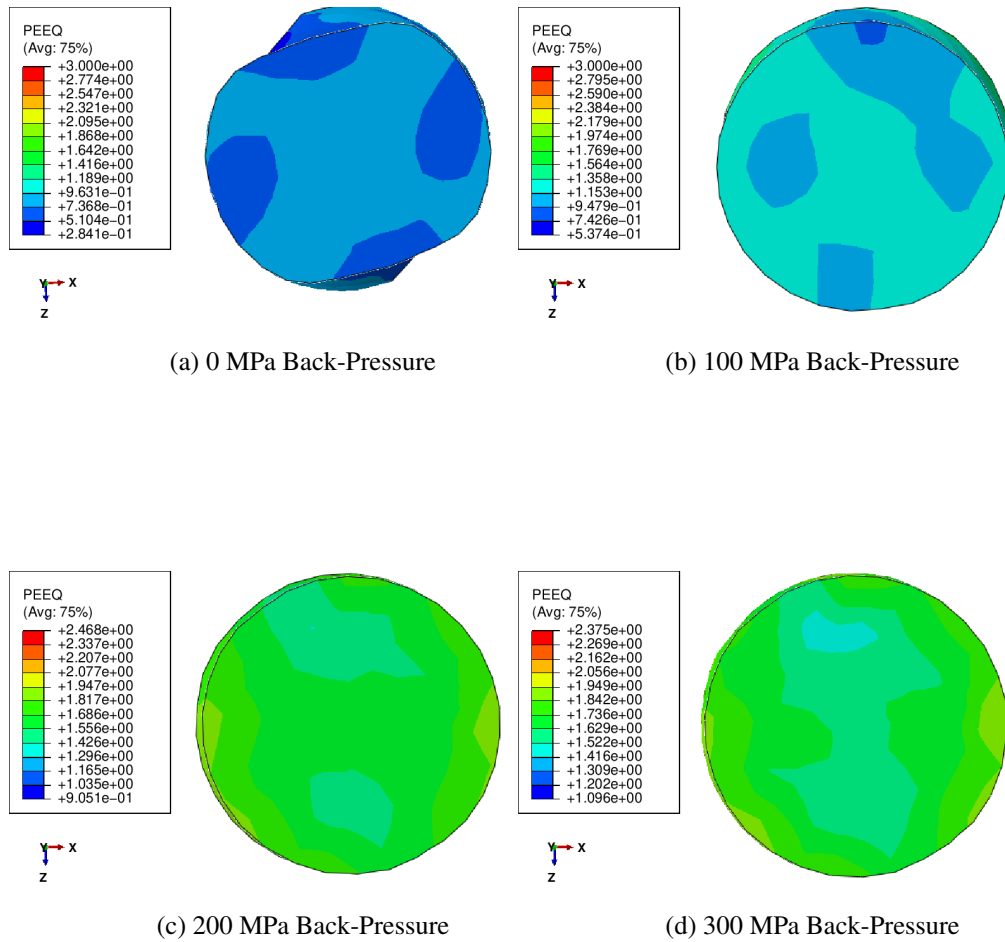
Figure 2.9: Section view of NLTE specimen and variation of equivalent plastic strain values depending on the applied back-pressure in NLTE process
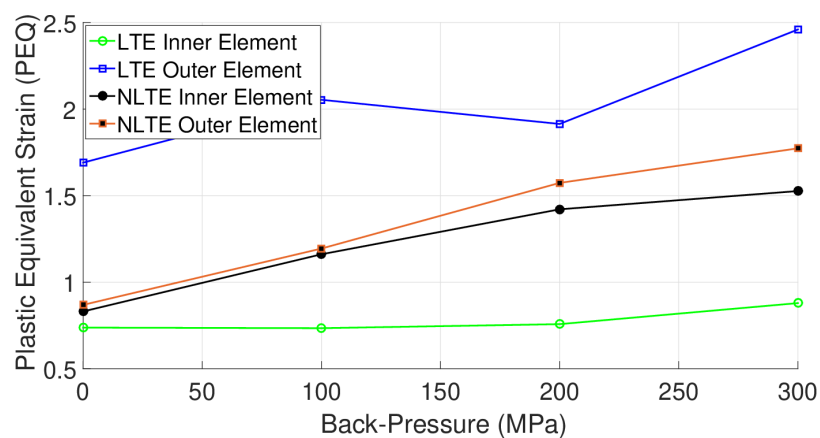
Figure 2.10: The variation of equivalent plastic strain under various back-pressure values

distributed more homogeneously.

(a) LTE Specimen von Mises Stress
Distribution

(b) NLTE Specimen von Mises Stress
Distribution
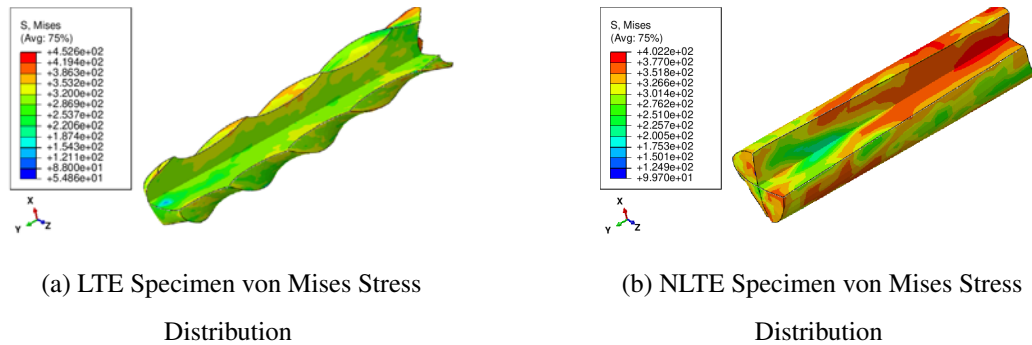
Figure 2.11: Von Mises stress distribution of LTE and NLTE specimens (MPa)

Figure 2.12 shows the equivalent plastic strain distribution in both LTE and NLTE specimens. In the case of the LTE process, a smaller magnitude of equivalent plastic strain evolves around the specimen center, and there is a gradual increase from the center to the surface of the specimen. Distinctively, in the case of the NLTE process, equivalent plastic strain evolves uniformly. This situation can also be illustrated by using volume fraction histograms in Figure 2.13. The volume fraction is computed as the number of elements with the same plastic deformation interval divided by the total element number of specimens. The histogram shows the volume fraction of each level of plastic strain values. The LTE process has a wider distribution of equivalent plastic strain distribution in the histogram. On the other hand, the NLTE process has a higher fraction at higher equivalent plastic strain value and a more uniform distribution of equivalent plastic strain.

Figure 2.14 shows the variation of nominal plastic strains during the LTE and NLTE deformation processes for outer and inner elements. The graphics were plotted according to the local coordinate systems for each typical element. In the LTE process, tensional normal plastic strain evolves at the outer element in 11 directions, while the inner element shows the compressive normal plastic strain. In the NLTE process, the deformation behavior of inner and outer elements is almost equivalent, and the elements tend to extend. Regarding the 22 plastic strain components, the LTE again shows distinct behavior and heterogeneous evolution for the inner and outer elements. Inner elements of the specimen are exposed to more nominal plastic strain than outer

48

(a) LTE Specimen

(b) LTE Specimen section view

(c) NLTE Specimen

(d) NLTE Specimen section view
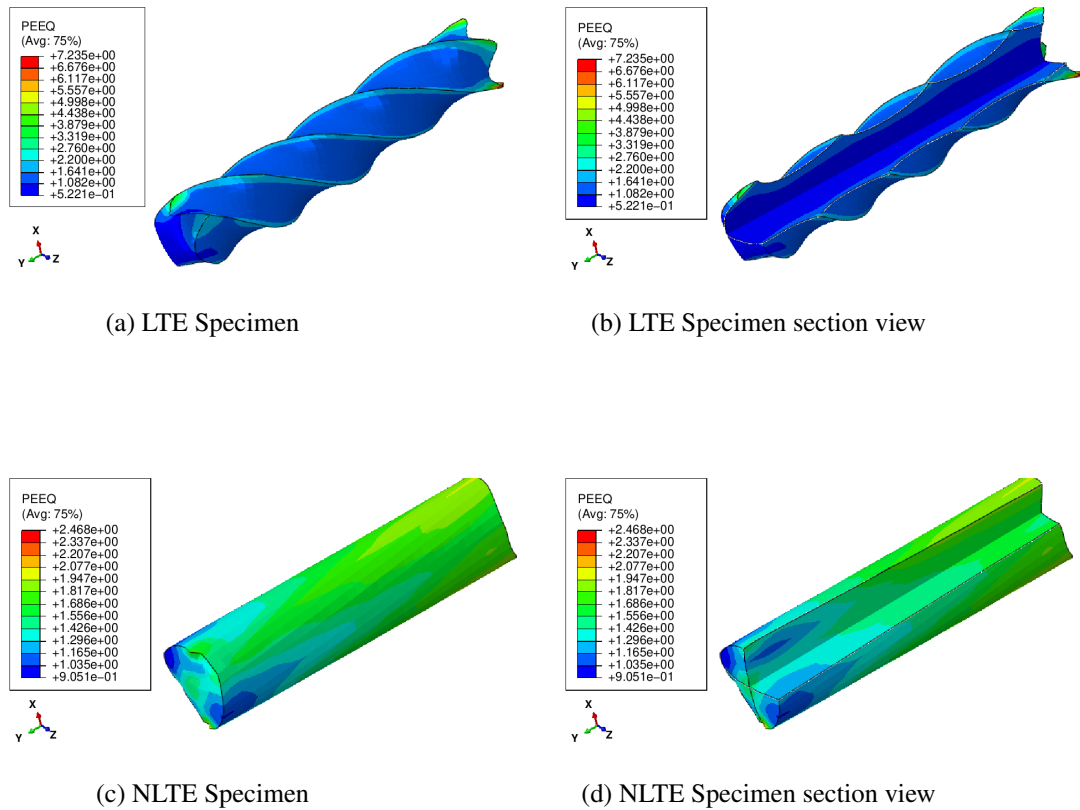
Figure 2.12: Distribution of equivalent plastic strain for LTE and NLTE process

elements. Tensional plastic strains become effective in the inner elements throughout the process, while the magnitude of the outer element changes from compression to tension in 22 extrusion directions. It is noticeable that a considerably high tensional normal plastic strain evolves in the inner element of the LTE process. For the NLTE, the deformation characteristics of outer and inner elements are quite similar and compressive plastic strains affect elements in 22 extrusion directions. For the 33 components of nominal plastic strain, the inner and outer elements are under compression throughout the process. A considerably high compressive nominal plastic strains are produced in the outer element during the LTE process.

Figure 2.15 shows the variation of shear plastic strain at various times during the LTE and NLTE deformation process for outer and inner elements according to each typical element's local coordinates. For the evolution of 12 and 23 components, there is a substantial difference in the LTE process's outer and inner element deformation characteristics. It is explicitly demonstrated that a high plastic strain of 1.5 is obtained
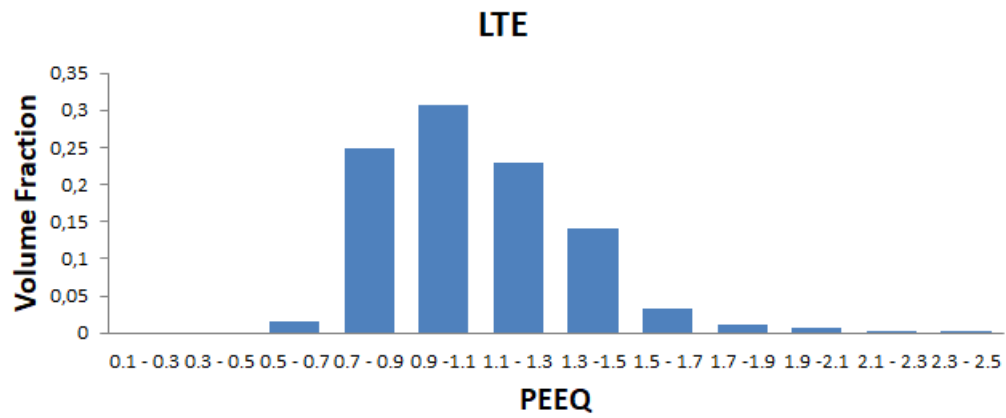
(a) LTE process
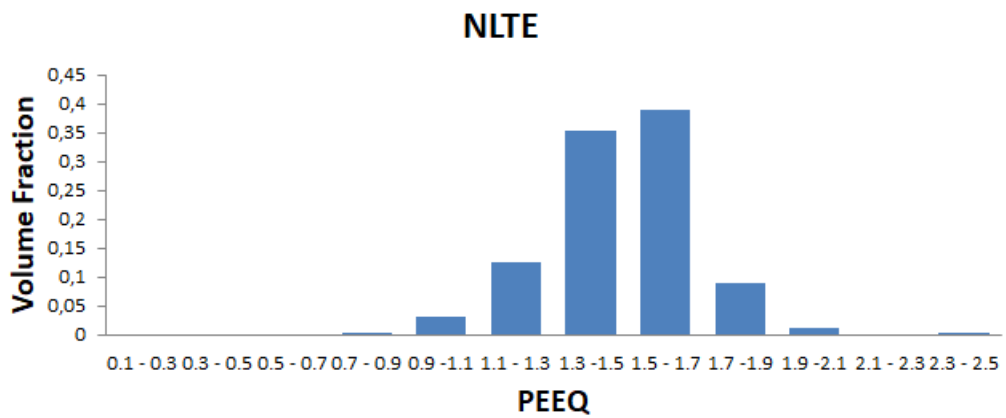
(b) NLTE process

Figure 2.13: Distribution of equivalent plastic strain according to volume fraction of LTE Specimen and NLTE Specimen
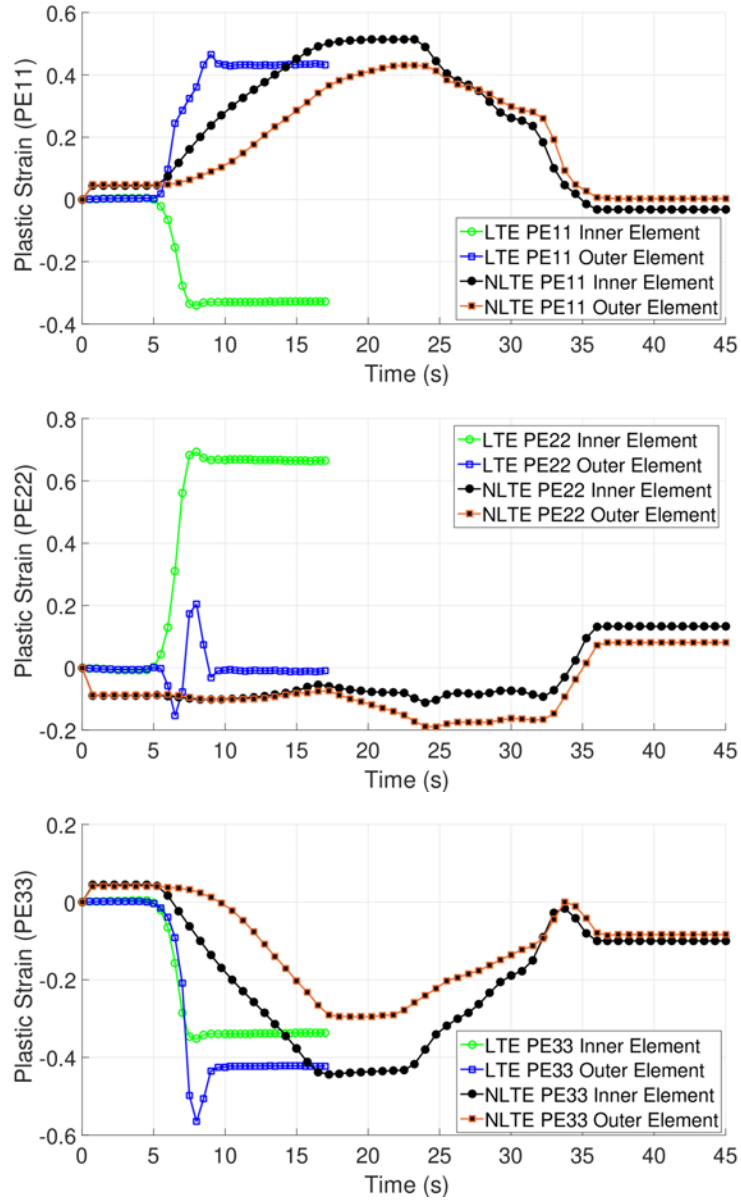
Figure 2.14: The variation of nominal plastic strains during the LTE and NLTE deformation processes for outer and inner elements.

in 12 directions in the outer element of LTE. In the case of NLTE, the outer element experiences more plastic shear strain than the inner element. The differences are less for the 23 components. Regarding the 13 components, the variation of plastic shear strain is considerably high in the NLTE process and the outer and the inner element deformation characteristics are quite similar. The outer elements experience more plastic strain for both processes. Note that the strain reversal reduces shear strain 13 of the outer element in LTE, while the amount of reversion is smaller in NLTE. Against the design concept of NLTE, strain reversion in NLTE occurs because of frictional force, which suppresses the complete rotation of the billet. The frictional force is a function of the pressure and contact area, and both are in a trade-off relation. To reduce strain reversal in NLTE, we must design a more optimum die channel for metal flow with a lower pressure and frictional force.

2.5   Conclusions

This study presents a new design for the twist extrusion process to obtain a more effective grain refinement procedure and overcome the disadvantages of classical processes. The performance of the design is addressed with the first numerical analysis, which is quite promising. The initial results illustrate the advantages of the process in terms of punching force and deformation distribution, where more effective strain evolution for grain refinement has been obtained with less punch force. Applied back pressure substantially influences the final geometry and evolution of plastic strain. The obtained equivalent plastic strain values show consistency with the theoretical calculations. While the LTE process induces strain evolution, increasing from inner elements to outer ones, more homogenous plastic strain distribution is captured by the NLTE process. This means the latter results in a more homogeneous grain refinement procedure. Moreover, the equivalent plastic strain volume fraction of NLTE reaches higher values than LTE, making it more effective than classical processes. As a next step, the experimental illustration of the design will be conducted, and the texture evolution will be analyzed through the crystal plasticity finite element method.
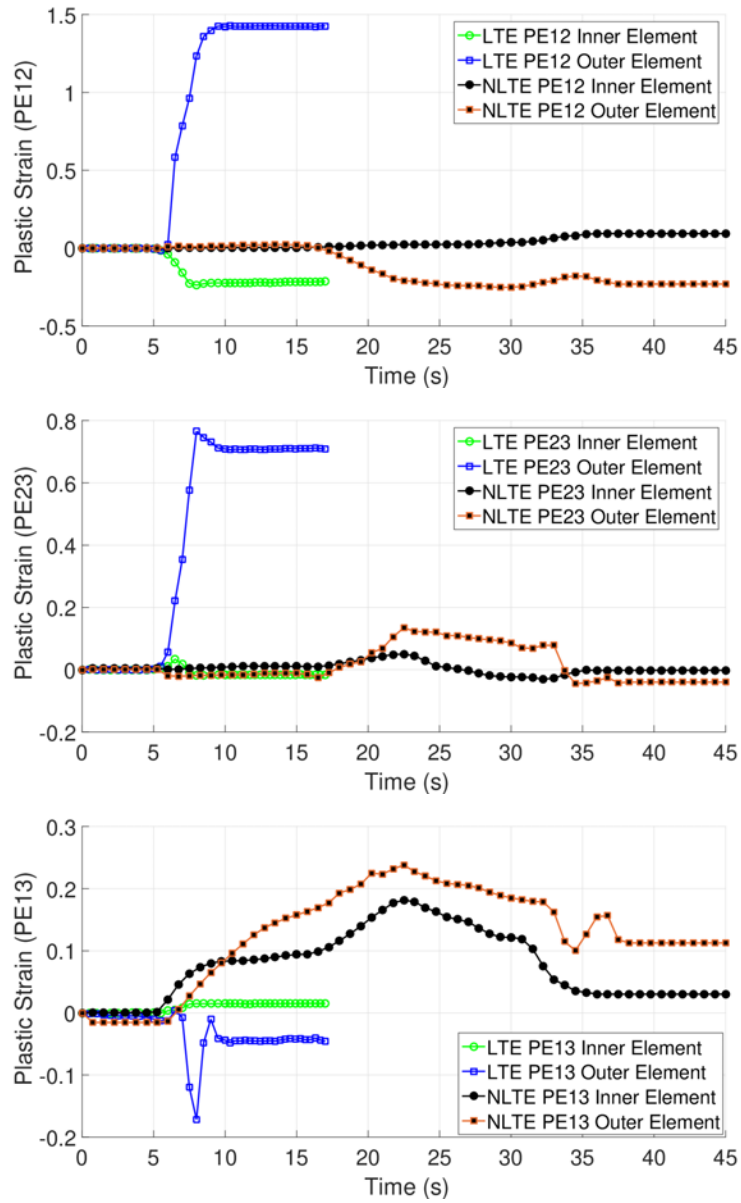
Figure 2.15: The variation of shear plastic strains at various times during the LTE and NLTE deformation processes for outer and inner elements

CHAPTER 3

COMPERATIVE CRYSTAL PLASTICITY FINITE ELEMENT ANALYSIS OF LINEAR AND NON-LINEAR TWIST EXTRUSION PROCESSES

3.1   Introduction

The size and uniform distribution of grains within polycrystalline metals play a pivotal role in their physical properties. In general, materials with smaller grain size exhibit increased strength and demonstrate enhanced properties at elevated temperatures compared to their coarser-grained counterparts (see, e.g., [95]). However, the presence of small grains can also generate certain problems such as a reduction in the ductility, and the material's ability to withstand cyclic loads, especially in low-cycle fatigue, can be affected (see, e.g., [96, 97]). The problem observed in the low-cycle regime is obviously linked to reduced ductility and a higher proportion of grain boundaries, which in turn leads to early initiation and propagation of cracks [98], and it is not observed in the high-cycle case. Numerical analyses of NLTE demonstrate advantages in the punch force, deformation distribution, strain evolution, and homogeneous plastic strain distribution compared to LTE [99]. Understanding the texture development and changes in material properties during the process can aid in optimizing the process parameters, which is the main purpose of the current work. To enhance and optimize the NLTE process, a deeper understanding of the development of texture and alterations in material properties during the procedure is pivotal. This comprehension is essential for refining the process parameters, including mold geometry, pass numbers, frictional interactions, process speed, and back-pressure values. Despite significant progress in investigating the kinetics and kinematics of SPD methods, research concerning the texture evolution characteristics of these processes remains relatively limited. However, the examination of the crys-

55

tallographic texture evolution arising from the ECAP process has been undertaken (see, e.g., [100].) This indicates a growing interest in exploring the textural aspects of SPD methods to enhance their efficiency and applicability. These investigations have demonstrated good agreement between the predicted texture evolution and the experimental observations. Furthermore, these studies have underscored the influence of the friction coefficient between the mold and the sample on the texture evolution [101]. In contrast, the crystallographic analysis of the LTE process has not aligned well with experimental results, with suggestions pointing towards grain thinning as a possible factor contributing to this disparity [102]. Studies of texture evolution during the design of the simple shear extrusion (SSE) process, achieved by varying the TE die and process, showed that consistent results were achieved between predicted and experimental textures. Additionally, the effect of back pressure on the texture evolution of SSE processes was demonstrated using CPFEM analysis [103]. In helical extrusion processes, a combination of FEM flow simulation and the crystal plasticity model has successfully predicted deformation textures, further highlighting the potential of these computational tools [104]. These studies collectively highlight the strides being made towards understanding and predicting texture evolution in various SPD processes, although challenges remain in certain cases.

In this context, the current work concentrates on the crystal plasticity analysis of the classical twist extrusion and the nonlinear twist extrusion processes in a comparative manner, focusing mainly on the texture evolution. In order to achieve this more clearly, a single-crystal copper specimen is extruded and the results are discussed in detail, which has not been done previously. The recently proposed nonlinear approach is studied using two different initial orientations and the results are analyzed in comparison to the classical process. Previous research indicates that NLTE offers advantages in the punch force, deformation distribution, and strain evolution for grain refinement, resulting in improved mechanical properties of the extruded materials. Modeling the texture evolution provides insights into the deformation behavior and helps to optimize the process parameters for the best NLTE extrusion outcome.

3.2 Extrusion Process Modeling and Constitutive Behavior

This section presents finite element models of LTE and NLTE processes with a crystal plasticity formulation. Calibration of the material parameters using the homogenization approach is also briefly discussed.

3.2.1 FE models of NLTE and LTE processes

A finite element methodology is employed to model both the LTE and NLTE processes, which is the most common technique in the modeling of both classical and additive manufacturing processes ([105],[106],[107]). The finite element representation of LTE and NLTE is depicted in Figure 3.1. In the LTE procedure, a billet is forced through a die featuring two linear channels separated by a section with spiral geometry. As the billet is steadily rotated within the spiral section of the die, the cross-sectional shape of the billet, perpendicular to the extrusion axis, remains unchanged during its translational movement. The primary difference in the NLTE process is that the billet is extruded while retaining its rotation around the longitudinal axis. This feature prevents strain reversal and the rigid body rotation of the specimen.
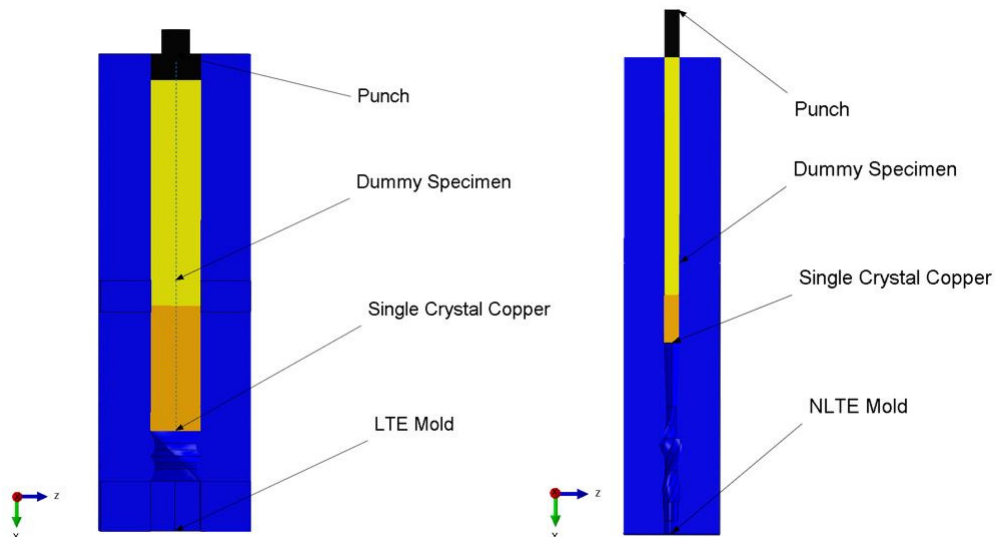
Figure 3.1: FE model of LTE (**left**) and NLTE (**right**) processes

In CPFEM simulations for the LTE and NLTE processes, the mold model and punch are treated as rigid bodies. Encastre boundary conditions (u1=u2=u3=R1=R2=R3=0) are applied to the rigid body reference point (center of mass) of the mold geometry and velocity boundary conditions (2 mm/s) are applied to the rigid body reference point of the punch geometry ([108],[109],[110]). Higher punch speeds cause convergence and singularity issues in the analysis. The friction coefficient taken into account with general contact algorithm between the mold and workpice is approximately μ=0.01 ([111],[112],[113]).

The models are built using individual SC copper samples, having square shapes for LTE and cylindrical shapes for NLTE. The rectangular prism with a square section has dimensions of 20 mm × 20 mm × 50 mm, while the cylindrical specimen has 20 mm in radius and 30 mm in height. Mesh properties for the SPD models are provided in Table 3.1. The completion times for the analyses are shown in Table 3.2.

3.2.2 Constitutive models for NLTE and LTE processes

In the analysis, samples subject to shear deformation in the twist region are modeled with a rate-dependent crystal plasticity model. The part called the dummy, which transmits the punch force to the sample to be examined throughout the process, is modeled with Von Mises Plasticity using the stress-strain values of the polycrystalline copper material (Figure 3.2). The CPFEM studies are based on a UMAT (user-defined material model) subroutine developed by Huang ([114]).

$$\mathbf{F} = \mathbf{F^e} \cdot \mathbf{F^p} \tag{3.1}$$

The deformation gradient $\mathbf{F}$ is decomposed multiplicatively into an elastic component $\mathbf{F^e}$ and a plastic components $\mathbf{F^P}$ as Equation 3.1 ([115],[116]). where $\mathbf{F^P}$ denotes the stress-free intermediate configuration where the orientation of the lattice does not change, and the plastic shearing occurs along well-defined slip planes. The symbol $\mathbf{F^e}$ represents lattice stretch and rotation. The elastic properties are assumed to remain unchanged in the presence of slip, meaning that stress is determined by $\mathbf{F^e}$. The

Table 3.1: FE model mesh parameters of simulated NLTE and LTE processes.

Model	Element Type	Element Family	Number of Elements
NLTE Mold	Implicit-Tetrahedral-C3D4	3D Stress	419316
NLTE Punch	Implicit-Hexahedral-C3D8R	3D Stress	1679
NLTE Specimen	Implicit-Hexahedral-C3D8R	3D Stress	48750
NLTE Dummy Specimen	Implicit-Hexahedral-C3D8R	3D Stress	15794
LTE Mold	Implicit-Tetrahedral-C3D4	3D Stress	33777765
LTE Punch	Implicit-Hexahedral-C3D8R	3D Stress	925
LTE Specimen	Implicit-Hexahedral-C3D8R	3D Stress	159989
LTE Dummy Specimen	Implicit-Hexahedral-C3D8R	3D Stress	36000
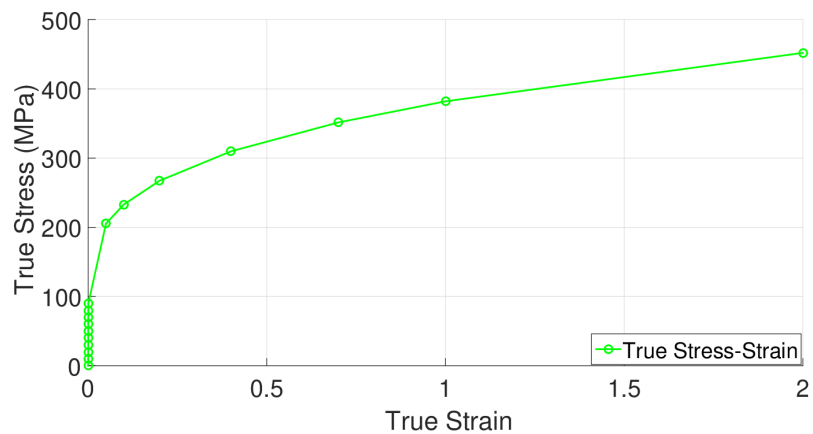
Figure 3.2: Stress-Strain curve of polycrystalline copper material ([99])

Table 3.2: LTE and NLTE processes analysis time

Model	Punch speed	CPU Time	Proximate analysis completion in days
UMAT CP LTE	2 mm/s	720 h:47 min:50 s	30 days
UMAT CP NLTE	2 mm/s	1078 h:17 min:21 s	45 days

plastic velocity gradient, denoted as $\mathbf{L^P}$, can be expressed in the following manner:

$$\mathbf{L^P} = \dot{\mathbf{F}}^{\mathbf{P}} \cdot \mathbf{F^{P-1}} = \sum_\alpha \dot{\gamma}^\alpha \mathbf{s}^\alpha \otimes \mathbf{m}^\alpha \tag{3.2}$$

Here, the unit vectors $\boldsymbol{s}^\alpha$ and $\boldsymbol{m}^\alpha$ represent the slip direction and the nominal direction to the slip plane in the reference configuration, respectively. which can be determined for the current configuration,

$$\mathbf{s}^{*\alpha} = \mathbf{F}^e \mathbf{s}^\alpha \tag{3.3}$$

$$\mathbf{m}^{*\alpha} = \mathbf{m}^\alpha \mathbf{F^{e-1}} \tag{3.4}$$

it is assumed that crystalline slip follows Schmid's law. The rate of slipping, denoted as $\dot{\gamma}^\alpha$, in a specific slip system α, depends exclusively on the Cauchy stress ($\boldsymbol{\sigma}$) through the resolved shear stress (τ^α). Resolved shear stress for each slip direction can be found as Equation 3.5;

$$\tau^\alpha = \mathbf{m}^{*\alpha} \cdot det(\mathbf{F}^e)\boldsymbol{\sigma} \cdot \mathbf{s}^{*\alpha} \tag{3.5}$$

According to Schmid's law, the rate of slipping, $\dot{\gamma}^\alpha$, for the αth slip system in a rate-dependent crystalline solid is governed by the corresponding resolved shear stress τ^α, as expressed in Equation 3.6.

$$\dot{\gamma}^\alpha = \dot{\gamma}_0 \Big|\frac{\tau^\alpha}{g^\alpha}\Big|^n sign(\tau^\alpha) \tag{3.6}$$

The constant $\dot{\gamma}_0$ represents the reference strain rate for slip system α, while g^α is a variable that signifies the current strength of that particular system. Additionally, the rate sensitivity exponent is denoted by n (as referenced in [117]). The evolution

of the strengths g^α, which characterizes strain hardening, is described through the incremental relation shown in Equation 3.7.

$$\dot{g}^\alpha = \sum_\beta h_{\alpha\beta} \dot{\gamma}^\beta \qquad (3.7)$$

The term $h_{\alpha\beta}$ represents the slip hardening moduli, and the summation encompasses all activated slip systems. Specifically, $h_{\alpha\alpha}$ (with no summation) is referred to as the self-hardening modulus, while $h_{\alpha\beta}$ (for $\alpha \neq \beta$) is known as the latent hardening modulus. A straightforward expression for the self-hardening moduli can be employed, as presented in Equation 3.8 (as mentioned in [118]).

$$h_{\alpha\alpha} = h(\gamma) = h_0 sech^2 \mid \frac{h_0 \gamma}{\tau_s - \tau_0} \mid (no\ sum\ on\ \alpha) \qquad (3.8)$$

Here, the parameter h_0 represents the initial hardening modulus, τ_0 stands for the critical resolved shear stress, equal to the initial value of the current strength g_0^α. Furthermore, τ_s denotes the stage I stress, often called the breakthrough stress, at which significant plastic flow begins. Finally, γ represents the Taylor cumulative shear strain on all slip systems, as follows:

$$\gamma = \sum_\alpha \int_0^t \mid \dot{\gamma}^\alpha \mid dt \qquad (3.9)$$

The latent hardening moduli are determined by the equation presented in Equation 3.10.

$$h_{\alpha\beta} = qh(\gamma)(\alpha \neq \beta) \qquad (3.10)$$

The provided expressions for the hardening moduli, with the constant q, do not consider the Bauschinger effect in a crystalline solid.

3.2.3 Calibration of Crystal Plasticity Model

In this part, the material parameters for single crystal (SC) copper are obtained following a homogenization scheme. The literature has inconsistent experimental data for tensile tests on SC copper. Hence, the stress-strain experimental data of polycrystal copper are utilized to calibrate the mechanical properties of SC copper (Fig. 3.3). To accomplish this, the tensile boundary conditions are enforced on a representative volume element (RVE) cube consisting of 500 grains with random orientations (Fig.

3.4). The boundary conditions applied to the RVE under tensile loading are depicted in Figure 3.5. Homogenization procedures are employed to calibrate the parameters of the CPFEM. During the application of these boundary conditions, it is ensured that the stress triaxiality value (T_r), which is calculated by dividing the hydrostatic pressure by the von Mises equivalent stress, remains constant at a ratio of 1/3 throughout the loading process and all the surfaces of the RVEs are kept straight.

Hydrostatic pressure is calculated by;

$$P_h = \frac{\sigma_1 + \sigma_2 + \sigma_3}{3} \tag{3.11}$$

Here, σ_1, σ_2 and σ_3 are the principal stresses in the three principal directions. It does not induce shear deformation. Equivalent von Mises stress can be defined as;

$$\sigma_{v_{eq}} = \frac{1}{2}\sqrt{(\sigma_1 - \sigma_2)^2 + (\sigma_1 - \sigma_3)^2 + (\sigma_3 - \sigma_2)^2} \tag{3.12}$$

And triaxiality can be found as;

$$T_r = \frac{P_h}{\sigma_{v_{eq}}} \tag{3.13}$$

To employ this boundary condition, firstly, the bottom surface of the RVE cube is constrained in y − direction (u_2). The master node is selected at the corner of the RVE cube. The coordinate of this node should be the (L_1, L_2, L_3) as it is located at the corner of the RVE, which enables us to couple the displacements of the surfaces and the master node. The unit cell's edges are aligned with the coordinate axes, ensuring their straightness throughout deformation ([119]). The displacements u_i, where $i \in 1, 2, 3$, of all other nodes located on the surface containing node M are linked with the displacement u_i of the node M. These couplings are established using the following linear Equations 3.14 ([120],[121]).

62

$$u_1(L_1, x_2, x_3) - (u_1)^M = 0,$$
$$u_1(0, x_2, x_3) + (u_1)^M = 0,$$
$$u_3(x_1, x_2, L_3) - (u_3)^M = 0,$$
$$u_3(x_1, x_2, 0) + (u_3)^M = 0, \quad\quad (3.14)$$
$$u_2(x_1, L_2, x_3,) - (u_2)^M = 0,$$
$$u_2(x_1, 0, x_3) = 0.$$

The overall responses of RVEs can be obtained with the fundamental theorem of homogenization,

$$\bar{\sigma_{ij}} = \frac{1}{V} \int_v \sigma_{ij} dv \quad with \quad i, j = 1, 2, 3 \quad\quad (3.15)$$

Where ($\bar{\sigma_{ij}}$) is the mesoscopic stress σ_{ij} is the microscopic Cauchy stress, and lastly, V is the volume of the RVE cube. As a result, $\bar{\sigma_{ij}}$ is determined for an RVE by summing the microscopic Cauchy stresses over each element with their associated integration points through the equation;

$$\bar{\sigma_{ij}} = \frac{\sum_{m=1}^{N} (\sum_{k=1}^{p} \sigma_{ij}{}^k v^k)^m}{V} \quad\quad (3.16)$$

where N is the number of elements, p is the total number of integration points, v is the integration volume, and V is the total volume. The material parameters of SC copper for the UMAT subroutine are illustrated in Table 3.3.
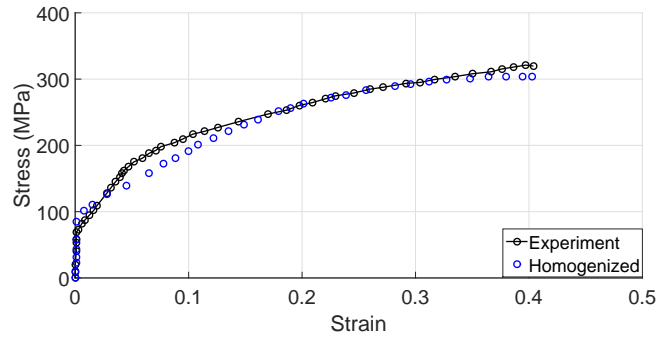
Figure 3.3: Homogenized Stress-Strain Curve vs. Experimental true stress-strain curve of polycrystal copper. ([99])
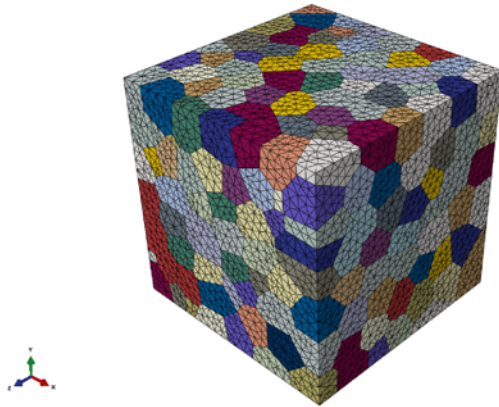
Figure 3.4: 500 grained calibration cube model
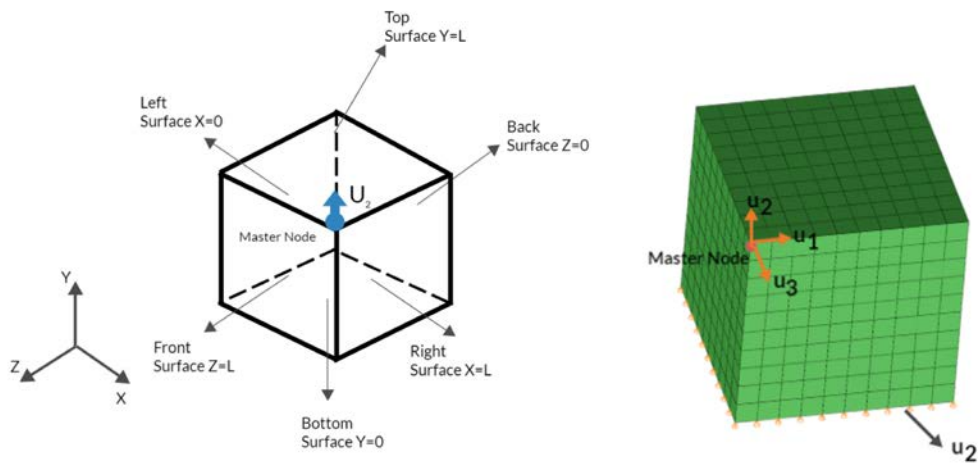
Figure 3.5: Boundary conditions of the representative volume element under axial loading to calibrate CPFEM parameters

Table 3.3: UMAT subroutine single crystal copper material parameters

Model	C_{11}	C_{12}	C_{44}	τ_0	τ_s	h_0	$\dot{\gamma}_0$	n	q
UMAT CP	168000 MPa	121400 MPa	75400 MPa	25 MPa	115 MPa	120 MPa	0.001 s^{-1}	17	1.4

3.3 Results and Discussion

CPFEM simulations are conducted for both LTE and NLTE processes, employing incipiently parallel to <100> and <111> directions SC copper specimens. The simulations demonstrate an initial quadratic increase in the load for both LTE and NLTE processes as the specimen head enters the twist zone. After this abrupt rise, the curve's gradient decreases, and the punch force slightly elevates throughout both processes. The previous reports have also discussed this behavior ([122]). Figure 3.6 illustrates the necessary punch force, in terms of punch pressure, by dividing the punch force from a crossectional area of the specimens because the specimens' cross sections are different. As it is shown, NLTE requires a lower punch force than LTE. This stands as a notable advantage of NLTE. The black curves represent results for incipiently parallel to<111> orientation SC copper, while the green lines represent incipiently parallel to <100> orientation SC copper.

In the LTE process, an incipiently <100> oriented SC copper experiences a higher punch force than an incipiently <111> oriented counterpart. Conversely, in the NLTE process, an incipiently <111> oriented SC copper requires more punch force throughout the process. Punch pressures should be evaluated considering the varying cross-sectional areas in both cases to present a more accurate comparison. However, the punch pressures are influenced by the frictional coefficient. A low friction coefficient (approximately 0.01) addresses convergence issues related to implicit solvers in contact nonlinearities and frictional discontinuities in these calculations. An increased friction coefficient would result in higher punch forces for both processes. The abrupt increase in punch pressure in the LTE process is attributed to the sudden cross-sectional change, a characteristic not observed in the proposed NLTE process.

Figure 3.7 depicts the Von Mises stress distribution for an incipiently parallel to <100> orientation SC copper during the LTE process. The stress values gradually rise from the specimen's center towards its periphery, with the maximum stress levels concentrated at the surface edges. Conversely, in the case of an initially <111> oriented single crystal subjected to the LTE process, the stress evolution becomes more heterogeneous, leading to elevated stress values in peripheral regions (Figure 3.8).
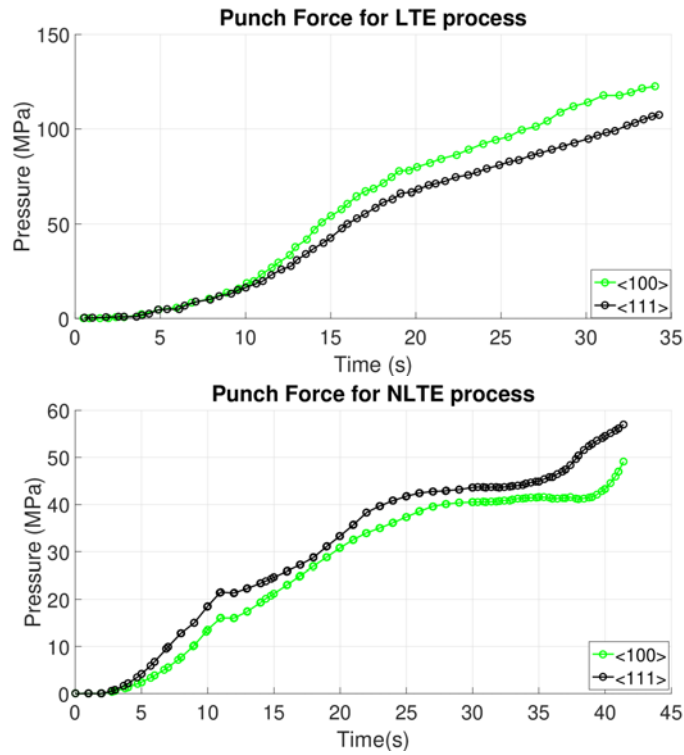
Figure 3.6: LTE and NLTE processes require different punch pressures based on the initial orientation of single crystal copper.
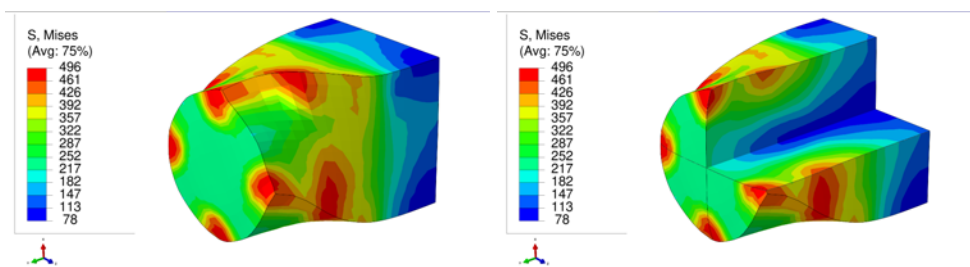
Figure 3.7: Von Mises stress distribution (in MPa) of an incipiently parallel to <100> orientation single crystal copper during a single pass of LTE (**left**) with a cross-sectional view (**right**).

Figures 3.9 and 3.10 display the Von Mises stress in the NLTE extrusion. Signifi-
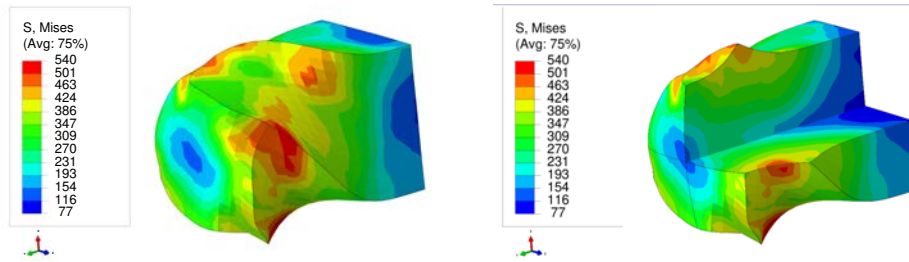
Figure 3.8: Von Mises stress distribution (in MPa) for an incipiently parallel to <111> orientation single crystal copper during a single pass of LTE (**left**) with a cross-sectional view (**right**).

cantly, after the NLTE process, stress becomes notably more uniform. High-stress values are found in the peripheral region and extend throughout the entire single copper specimen, differing from the LTE process. When comparing, incipiently parallel directed to <100> orientation SC copper specimens endure higher stress levels than their <111> oriented counterparts. In both processes, the outer surface of the specimens bears the maximum stress levels. This is attributed to the fact that these regions come into contact with the interior surface of the die during the extrusion process.

Figures 3.11 and 3.12 present the distribution of equivalent plastic strain resulting
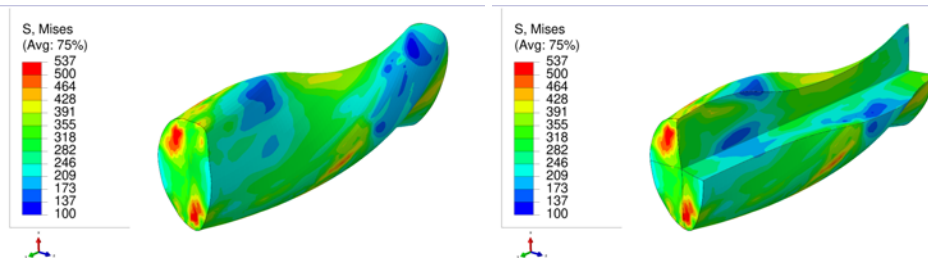
Figure 3.9: Von Mises stress distribution (in MPa) for an incipiently parallel to <100> orientation single crystal copper during a single pass of NLTE (**left**) with a cross-sectional view (**right**).

from LTE processes for incipiently parallel to <100> and <111> orientation single copper crystals, respectively. In LTE processes, the equivalent plastic strain displays a lower magnitude around the center of the specimen. From the center towards the surface of the specimen, there's a gradual increase in equivalent plastic strain for
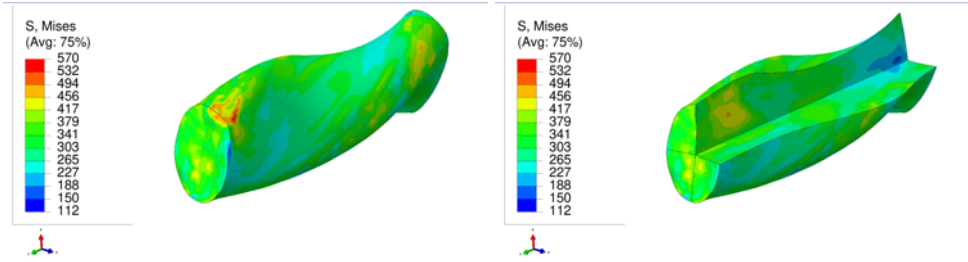
Figure 3.10: Von Mises stress distribution (in MPa) for an incipiently parallel to <111> orientation single crystal copper during a single pass of NLTE (**left**) with a cross-sectional view (**right**).

both initial orientations. Notably, the highest strain accumulates at the corners, while the lowest strain is observed at the center. This distribution pattern is linked to the inhomogeneous strain distribution characteristic of the LTE process ([123]).
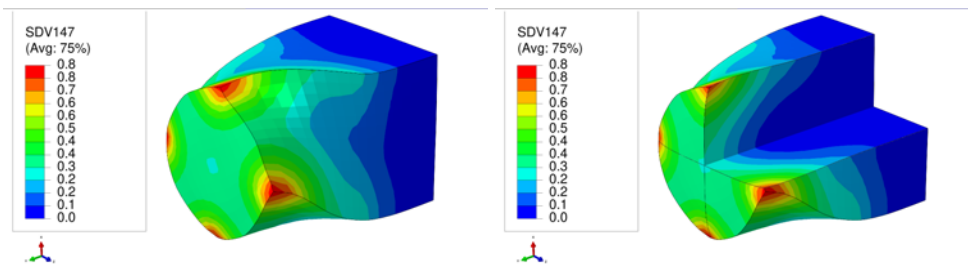
Figure 3.11: Plastic equivalent strain distribution of incipiently parallel to <100> orientation copper single crystal during one pass of LTE process (**left**) with a cross-sectional view (**right**).

Figures 3.13 and 3.14 highlight that, in NLTE processes, the evolution of equivalent plastic strain is notably uniform. The distribution of equivalent plastic strain is more consistent from the center to the periphery of the specimen. Similar to LTE processes, incipiently directed <111> orientation single copper specimens experience greater plastic deformation than incipiently directed to <111> orientation SC copper specimens for both processes.

Furthermore, during the NLTE process, the SC copper workpiece undergoes significantly higher plastic equivalent strain than the LTE process. This increased plastic deformation in NLTE processes will enhance grain refinement, further amplifying
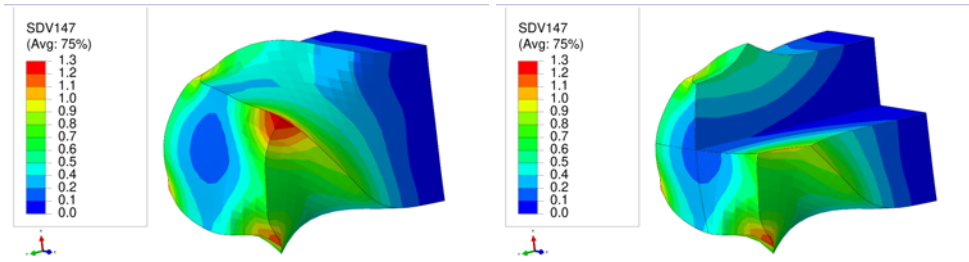
Figure 3.12: Plastic equivalent strain distribution of incipiently parallel to <111> orientation copper single crystal during one pass of LTE process (**left**) with a cross-sectional view (**right**).

plastic strains.
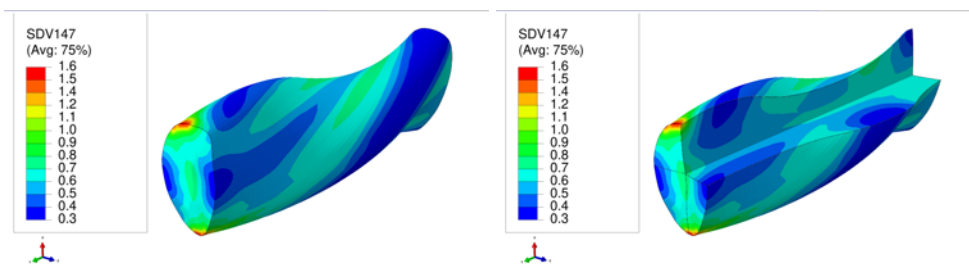
Figure 3.13: Plastic equivalent strain distribution of incipiently parallel to <100> orientation copper single crystal during one pass of NLTE process (**left**) with a cross-sectional view (**right**).

To demonstrate the kinetic and kinematic investigations of the LTE and NLTE processes, two representative elements from the workpieces have been chosen: one from the central section and another from the outer section of the specimen. Figure 3.15 visually emphasizes these selected elements.

The change of the reaction forces and boundary conditions according to the process time plays a vital role in SPD processes. During the process, loading directions, deformation modes, and the orientation of reaction forces on contact surfaces shift. Consequently, shear strain rates can vary due to these dynamic boundary conditions. Under the influence of dynamic strain rates, the anisotropic nature of a single crystal's flow stress can alter. While geometric factors tend to remain unaffected by strain rate changes, the motion of dislocations, interaction processes, and texture can exhibit
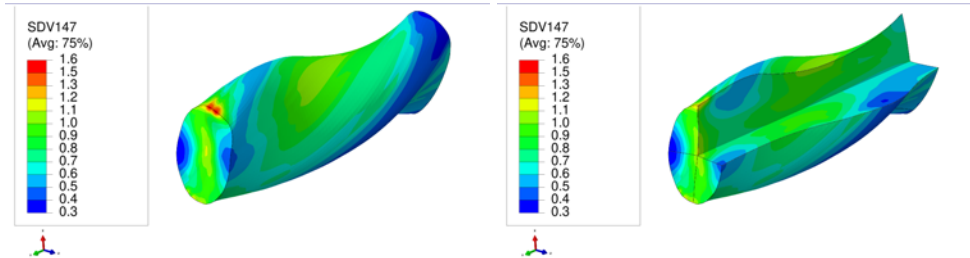
Figure 3.14: Plastic equivalent strain distribution of incipiently parallel to <111> orientation copper single crystal during one pass of NLTE process (**left**) with a cross-sectional view (**right**).
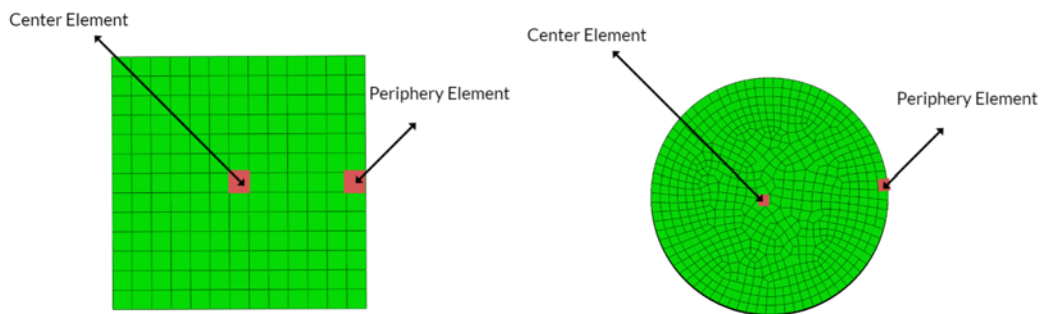
Figure 3.15: The analyzed elements, along with their local coordinates, are situated at the center and periphery for the LTE process (**left**) and the NLTE process (**right**).

heightened sensitivity to strain rate fluctuations. These factors ultimately influence slip activity and microstructural evolution. Exploring the behavior of plastic deformation under such conditions can be challenging due to the difficulty of observing isolated dislocation groups and measuring microstructure evolution.

In fcc metals, twelve distinct 111 slip systems play a role in plastic deformation. Nevertheless, The slip systems with identical Schmid factors do not always contribute equally to the deformation process. As dislocations form, aggregate, and arrange themselves into structures of lower energy, the internal stress state evolves. Local internal forces display heterogeneity and may either facilitate or impede dislocation glide on specific slip systems, regardless of their Schmid factors ([124]).

Rather than relying solely on Schmid factors and microstructural observations, anisotropy is best evaluated through the lens of slip activity. Slip activity refers to the count and distribution of active slip systems ([125]; [126]). These active slip systems are often indicated by dense slip lines and slip bands appearing on the most active planes. As strain rates increase, dislocation accumulation becomes more heterogeneous, and microstructures acquire a more directional character. This results in the formation of slip bands on the most active planes. The heightened heterogeneity amplifies changes in flow stress due to alterations in loading direction, especially as strain rate increases ([127];[128]). Figures 3.16 through 3.19 present shear strain variations over LTE process time, categorized by slip planes and the initial orientation of single copper crystals. These variations are analyzed for the workpieces' center and periphery elements, focusing on slip directions. Among the curves, the green, black, and red curves correspond to the center element, while the blue, pink, and yellow curves represent the periphery element.

In the case of an incipiently parallel to <100> orientation single copper crystal, the maximum shear strain values occur at <-111> and <111> slip planes, along with the [110] and [10-1] directions, respectively, with a magnitude of 0.2. Conversely, for an initially <111> oriented single copper crystal, the peak shear strain value is achieved on <1-11> and <11-1> slip planes.

Notably, the most active shear plane and direction during the LTE process for the incipiently parallel to <111> orientation SC copper, in the periphery element, is the
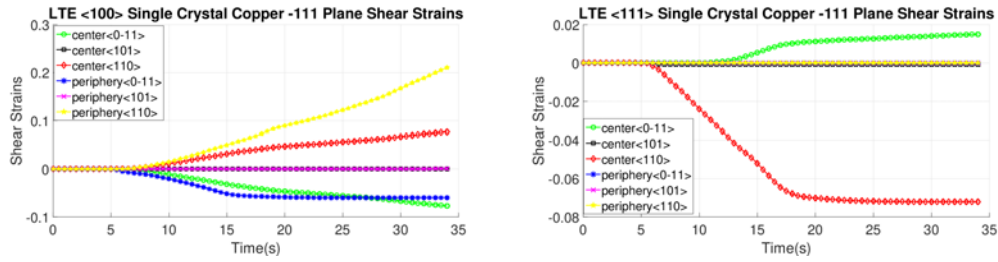
Figure 3.16: Shear Strain evolution of -111 slip plane according to slip directions of <100> and <111> oriented single copper crystal
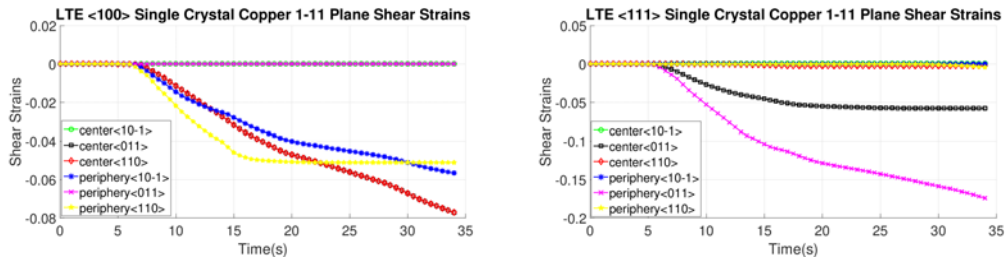
Figure 3.17: Shear Strain evolution of 1-11 slip plane according to slip directions of <100> and <111> oriented single copper crystal
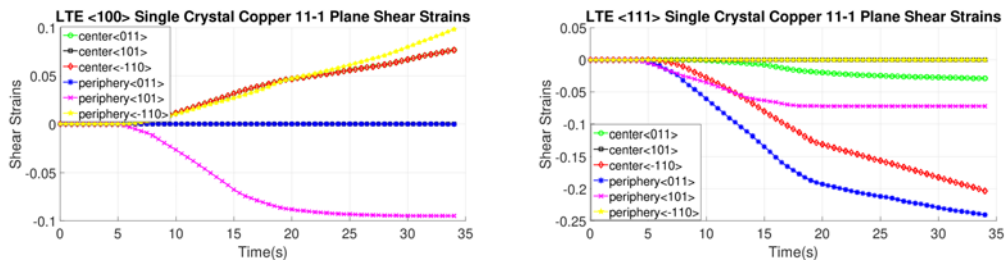
Figure 3.18: Shear Strain evolution of 11-1 slip plane according to slip directions of <100> and <111> oriented single copper crystal
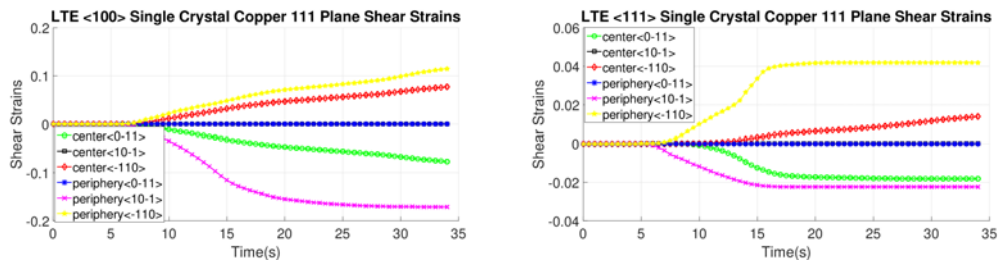
Figure 3.19: Shear Strain evolution of 111 slip plane according to slip directions of <100> and <111> oriented single copper crystal

shear plane <11-1> with the [10-1] shear direction, as illustrated in Figure 3.18. In contrast, less activated slip directions are evident for the initially <111> oriented single copper crystal's <-111> slip plane, as depicted in Figure 3.16.

Figures 3.20 to 3.23 depict the evolution of shear strains over the processing time of the NLTE process, categorized by shear plane, shear direction, and the initial orientations of a single copper crystal. These figures analyze the workpieces' center and periphery elements, focusing on shear directions similar to the LTE process.

For incipiently directed <100> orientation single copper crystal, the maximum shear strain value occurs at <11-1> and <111> slip planes, accompanied by the [101] and [10-1] directions, respectively, with a shear strain magnitude of 0.3. In the case of an initially <111> oriented single copper crystal, the maximum shear strain values are observed on <-111>, <1-11>, and <111> slip planes, along with [101], [110], and [101] directions, respectively.

These figures reveal that the most activated slip system belongs to the <-111> slip plane for the center element of an incipiently parallel to <111> orientation SC copper, as indicated in Figure 3.20. Conversely, the less activated slip system is associated with the 11-1 slip plane for the center element of an incipiently parallel to <111> orientation SC copper, as demonstrated in Figure 3.23. The NLTE process exhibits a more active shear system and higher shear strain values than the LTE process. Additionally, the phenomenon of strain reversal can be observed in the initially <111> oriented single copper crystal's <11-1> slip plane and [101] direction, as seen in Figure 3.22.

The stacking fault energy (SFE) significantly influences the resulting crystallographic texture in FCC materials and their alloys. The value of SFE is contingent on the material type and is influenced by the presence and ratio of alloying elements. For instance, pure nickel (Ni) and aluminum (Al) possess very high SFEs, exceeding 4200mJ/m^2, while pure copper (Cu) exhibits an intermediate SFE, typically around 50 to 60 mJ/m^2. Introducing alloying elements frequently reduces the SFE to values below 20 mJ/m^2. This characteristic of the SFE plays a crucial role in determining the primary deformation mechanism during plastic deformation. Specifically, materials with high to moderate SFE values tend to undergo deformation primarily through
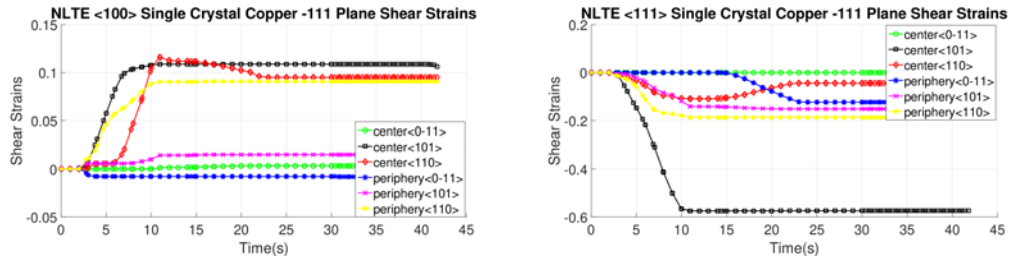
Figure 3.20: Shear Strain evolution of -111 slip plane according to slip directions of incipiently directed to <100> and <111> orientation single copper crystal
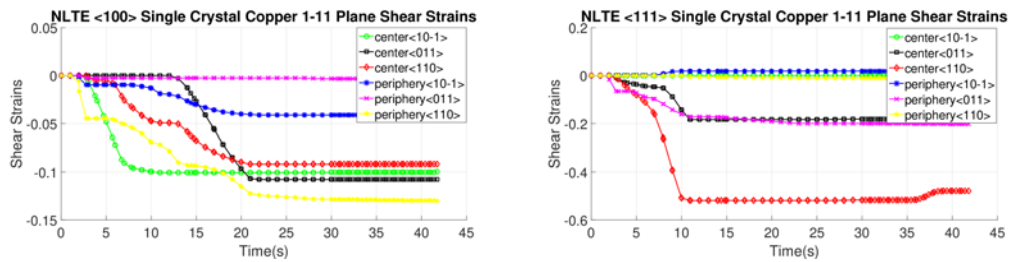
Figure 3.21: Shear Strain evolution of 1-11 slip plane according to slip directions of incipiently directed to <100> and <111> orientation single copper crystal
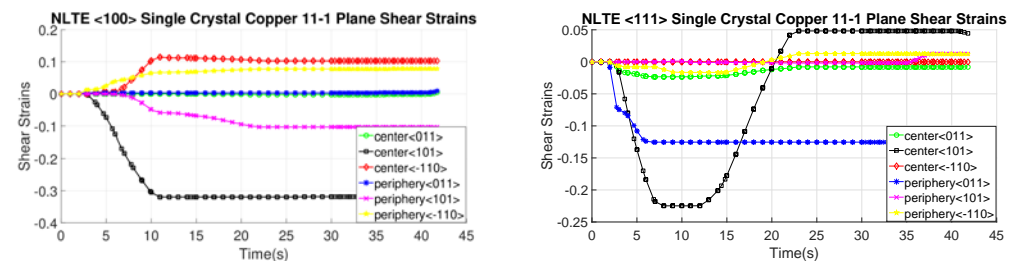
Figure 3.22: Shear Strain evolution of 11-1 slip plane according to slip directions of incipiently directed to <100> and <111> orientation oriented single copper crystal
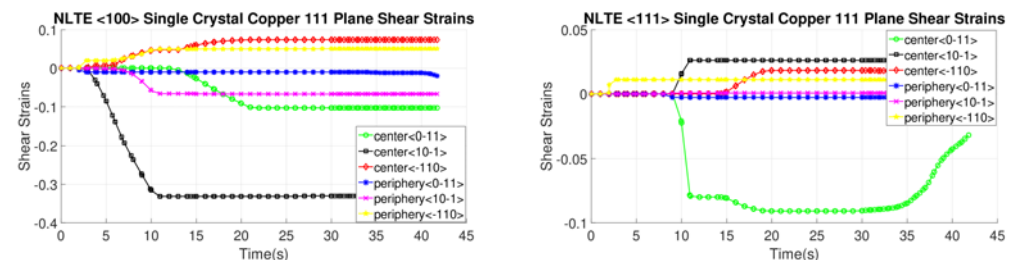
Figure 3.23: Shear Strain evolution of 111 slip plane according to slip directions of incipiently directed to <100> and <111> orientation oriented single copper crystal

74

Table 3.4: Texture components and pole figures for face-centered cubic (FCC) materials according to [111], [110], and [100] plane respectively and initial orientation of single copper crystal ([129])

Components Name	Directions	Bunge Euler Angles(φ_1 ϕ φ_2)	Pole Figures of Components [111] [110] [100]
Cube	[001]<100>	(0) (0) (0)	
Goss	[011]<100>	(0) (45) (0)	
Brass	[0$\bar{1}$1]<211>	(35) (45) (0)	
Copper	[$\bar{2}$11]<111>	(90) (35) (45)	
S	[12$\bar{3}$]<634>	(60) (32) (65)	

dislocation slip. In contrast, those with lower SFE values activate mechanisms such as twinning, leading to shear band formation. Both these mechanisms can significantly influence the deformation texture.

It is essential to recognize that using ideal components in inverse pole figures (IPFs) and orientation distribution functions (ODFs) to describe texture evolution may be insufficient. Instead, textures can be represented as a spread of orientations, forming continuous orientation tubes across orientation space. The elemental textures of FCC metals, such as Cube, Copper, Brass, Goss, and S orientations (Table 3.4), play a crucial role in comprehending the final texture of SC copper after deformation. These texture components provide insights into the mechanical behaviors, physical and chemical properties, and overall performance of materials in engineering applications.

The control and understanding of texture evolution are crucial for developing new materials ([130]). In FCC materials featuring a high to medium SFE, grains typically experience rotation towards copper-type textures as deformation intensifies, and the primary deformation mechanism that prevails throughout the entire deformation process is dislocation slip. The SFE value plays a pivotal role in determining the primary mechanisms of plastic deformation. In metals characterized by a high SFE, like aluminum and copper, slip remains the dominant deformation mode, developing a rolling texture consisting of copper, brass, and S texture components. In materials characterized by a low SFE, copper-oriented grains initially aggregate during the early stages of deformation. Nevertheless, as the loading process persists, these grains gradually undergo rotation toward brass-type textures, ultimately becoming the predominant texture after experiencing substantial deformations. The texture observed in low SFE metals, characterized by a significant brass component and a minor Goss orientation, is commonly called an alloy-type texture ([131]). In summary, the stacking fault energy profoundly influences deformation mechanisms and subsequent texture evolution in FCC materials, ultimately impacting their mechanical properties and applicability in engineering applications.

After the initial pass of both the LTE and NLTE processes, the outcomes for the central and peripheral elements are depicted in Figure 3.24 and Figure 3.25, respectively.
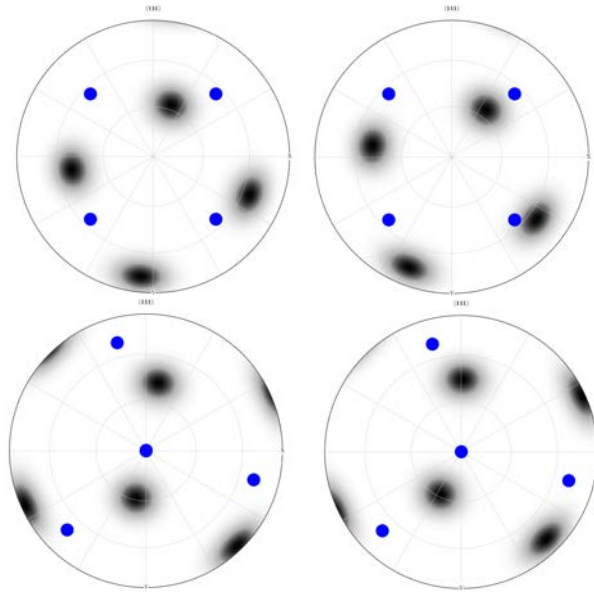
Figure 3.24: <111> Section pole figures of central elements (**left**) and peripheral elements (**right**) of a single crystal copper specimen after the LTE process. The blue points represent the incipiently directed <100> orientation (**top**) and <111> orientation (**bottom**).
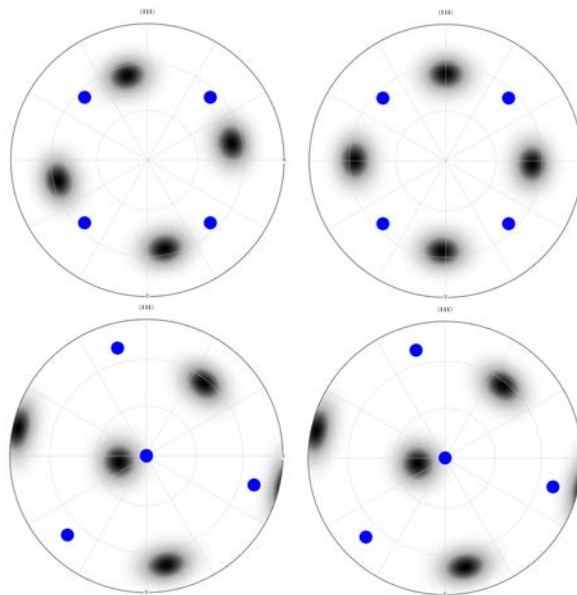
Figure 3.25: <111> Section pole figures of central elements (**left**) and peripheral elements (**right**) of a single crystal copper specimen after the NLTE process. The blue points represent the incipiently directed <100> orientation (**top**) and <111> orientation (**bottom**).

The initial orientation distributions exhibit significant variations after a single pass for each process. The orientation distribution in the pole figures after the LTE process is reminiscent of the main orientation pole figures associated with copper and S-textures. Similarly, the center and periphery elements of an incipiently directed to <100> orientation SC copper specimen show characteristics of the cube and S-texture after the NLTE process. Conversely, for incipiently directed to <111> orientation SC copper workpieces, the center and periphery elements exhibit orientation distributions resembling copper and S-textures after the NLTE process.

These pole figures indicate that both LTE and NLTE processes subject the elements of a single copper specimen to shear deformation, with dislocation slip being the dominant deformation mechanism in both cases. Moreover, following a single pass, the orientation distributions for central and peripheral elements exhibit greater alignment in the NLTE process compared to the LTE process. Comparing these results with the initial orientations reveals that both center and periphery elements rotate about 45 degrees along the extrusion axis.

ODF is characterized by defining the X and Y directions as the transverse direction (TD) and the extrusion direction (ED), respectively. In this study, a copper-type sample symmetry is employed. Five primary texture components (Cube, Brass, S, Goss, and Copper) are used in the analysis and presented in Figure 3.26. The texture evolution of the NLTE process is predicted and contrasted with that of the LTE process. Figures 3.27 and 3.28 illustrate the ODFs of ψ_2 angles at $0°$, $45°$, and $60°$ for the corresponding positions. Specifically, Figures (a) and (b) display the initially <100> oriented SC copper ODF results for center and periphery elements, while Figures (c) and (d) showcase the predicted ODF results for the initially <111> oriented single copper crystal's center and periphery elements, respectively.

ODFs offer a valuable means of enhancing our comprehension of the texture evolution following the first pass of LTE and NLTE processes. Since both LTE and NLTE processes are grounded in a shear deformation, analyzing ODF sections concerning the main textures can yield valuable insights. After a single pass of the LTE process, the ODFs for the center and periphery elements exhibit discernible distinctions when compared to each other, regardless of whether the initial orientation is <100> or
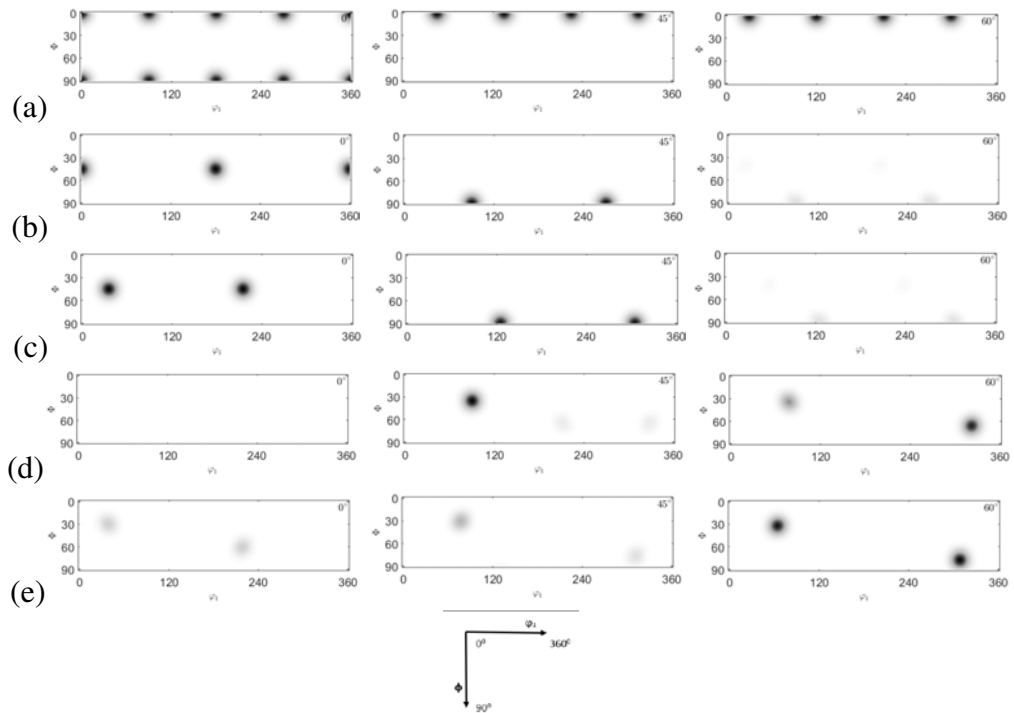
Figure 3.26: Comparison of ODF ($0^0, 45^0, 60^0$ section) obtained by texture components a) Cube, b) Goss, c) Brass, d) Copper and e) S-texture

<111>. Figure 3.27 presents a comparative view of the ODF results obtained from the LTE CPFEM analysis of a single copper specimen after a single pass. Comparing these ODF results with the primary texture components shown in Figure.3.27, the central and peripheral elements display significant Copper and S components in the case of an initially <100> oriented SC copper specimen. Conversely, for an initially <111> oriented SC copper specimen, the Copper and S component textures gradually weaken from the center to the periphery elements. In contrast, the Goss and Brass texture components gain strength.

Recent research has focused on understanding the influence of crystallographic texture on fatigue resistance. A significant fatigue performance was observed in Goss grains of an Al-Cu-Mg alloy, whereas Brass grains exhibited decreased resistance to fatigue crack propagation. The study demonstrated that a higher Goss/Brass volume fraction ratio enhanced fracture toughness in the Al-Cu-Mg alloy ([132]). The ODF CPFEM results for incipiently parallel directed to <100> and <111> orientation SC copper specimens are depicted in Figure 3.28. Upon comparing these results with the
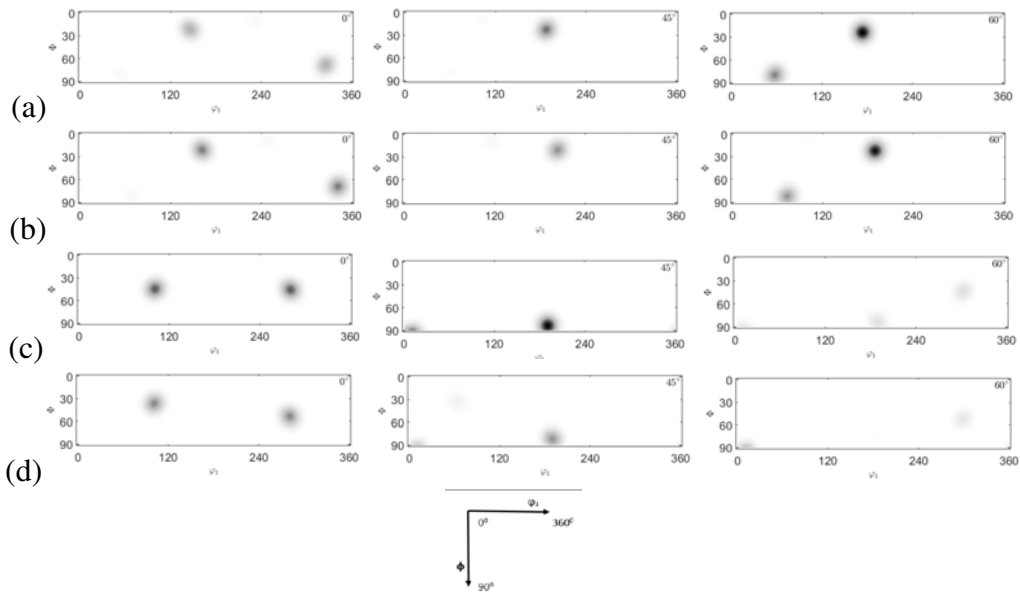
Figure 3.27: Comparison of ODF ($0^0, 45^0, 60^0$ section) obtained by CPFEM prediction of single crystal copper specimens a)center element initially oriented <100>, b) periphery elements initially oriented <100>, c)center element initially oriented <111> and d)periphery element initially oriented <111> after LTE process

main texture components displayed in Figure 3.26, it becomes evident that the major components for both center and periphery elements correspond to the cube texture components.

The evolution of cube texture in FCC materials is a subject of special attention due to its crucial role in preferential growth during recrystallization heat treatments of cold-rolled sheets. This texture anisotropy contributes to the formation of defects during deep-drawing processes ([133]). In the case of copper, the appearance of shear bands in the deformed structure provides alternative nuclei for recrystallization, exhibiting varying orientations with some inclination towards retained rolling texture components. These shear bands also disrupt the cube-oriented bands within the deformed structure, diminishing their favorability as nucleation sites. Consequently, the cube texture experiences significant weakening after recrystallization ([134]).

The propensity for shear banding is heavily reliant on the initial grain size of the material, thereby enabling the control of cube texture strength through this parameter. Fine initial grain sizes refine the spacing of oriented bands, leading to more closely

80
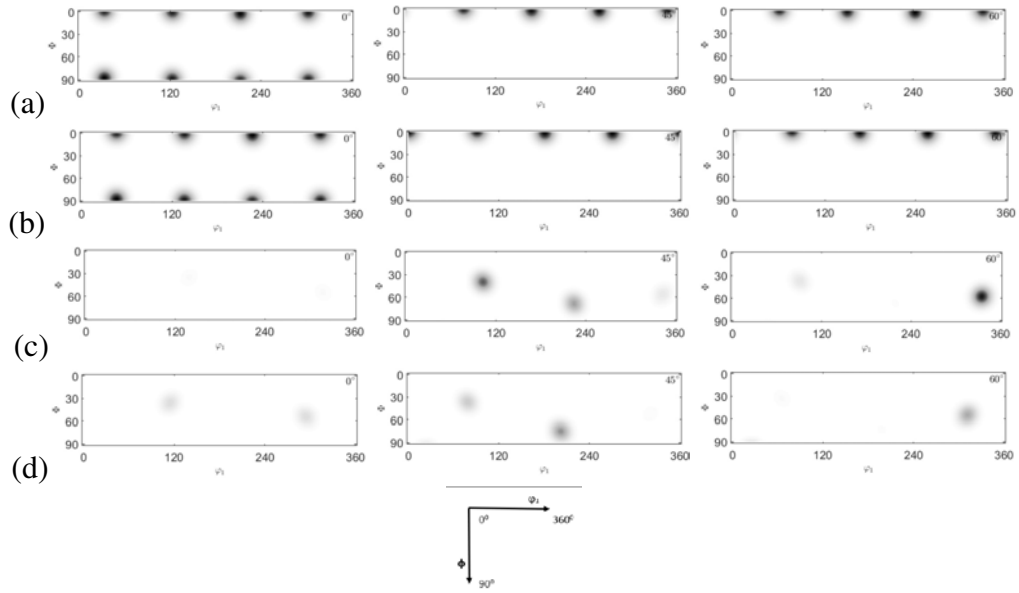
Figure 3.28: Comparison of ODF ($0^0, 45^0, 60^0$ section) obtained by CPFEM prediction of single crystal copper specimens a)center element initially oriented <100>, b) periphery elements initially oriented <100>, c)center element initially oriented <111> and d)periphery element initially oriented <111> after NLTE process

spaced cube bands. This not only facilitates the development of cube grains but also enhances the "orientation pinning" effect for other competing orientations, as exemplified in aluminum and discussed by Doherty et al. ([135]).

For initially <111> oriented SC copper specimens, both center and periphery elements exhibit strong S-textures following the NLTE process for a single pass. In metals with high SFE, such as aluminum and copper, slip is the dominant deformation mode, and the rolling texture comprises copper, brass, and S-texture components with nearly equal intensities.

3.4 Conclusion

In this study, numerical simulations are employed to explore the extrusion process of individual single-crystal copper workpieces, encompassing both the LTE and NLTE mechanisms, while considering two distinct initial orientations of the workpieces. By adopting this methodology, a thorough and intricate comparison of the effectiveness

of grain refinement, utilizing crystal plasticity finite element analysis, is conducted for these two severe plastic deformation techniques, marking the first instance of such an analysis in the literature.

This investigation's initial results underscore the NLTE process's benefits concerning punch force and deformation distribution. While the LTE process increases strain evolution from the central to the peripheral elements of the workpiece, the NLTE process experiences a more uniform distribution of plastic strain. Additionally, in shear deformation zones, the orientation distribution in the NLTE process appears more consistent than in the LTE process. The NLTE process demonstrates more active shear systems and elevated shear strain values than the LTE process. Consequently, the workpiece undergoes more extensive plastic deformation during the NLTE process. Therefore, it is expected that the NLTE process leads to greater grain refinement in the workpiece. Furthermore, strain reversal can be investigated specifically at the [11-1] slip plane and in the <101> direction. Moreover, the initial crystal orientation influences the ultimate orientation outcomes of the processes. The NLTE process exhibits more active shear systems and higher levels of shear strain than the LTE process. Additionally, the NLTE process changes crystal orientations through rotations along the extrusion direction.

The influence of back pressure and friction coefficient on severe plastic deformation processes and microstructure is well-established. However, due to computational limitations associated with using the implicit UMAT code in this study, considering the friction coefficient and back-pressure load might have been insufficient. We plan to perform more comprehensive analyses employing an explicit methodology within the crystal plasticity framework to mitigate this constraint. Subsequently, the acquired results will be further compared with experimental observations. This next phase of our research will yield a more precise comprehension of how these parameters affect the simulation results.

CHAPTER 4

EXPLICIT FINITE ELEMENT METHOD OF CRYSTAL PLASTICITY

4.1   Introduction

FEM provides researchers and engineers with the capability to simulate and visualize the behavior of materials undergoing deformation in SPD processes. It allows for manipulating process variables and parameters to study their effects and optimize the outcomes of SPD techniques. This level of control and understanding is crucial for enhancing the efficiency and effectiveness of these processes. There are two main types of solvers commonly used in FEM simulations for metal forming processes: implicit and explicit algorithms. Implicit solvers are well-suited for problems involving slow and steady deformation processes, while explicit solvers are more suitable for simulations involving rapid and dynamic changes. Researchers have utilized both types of solvers to investigate various aspects of SPD processes, from the mechanical response of materials to the microstructural changes that occur during deformation. The integration of FEM with computational techniques has opened up new avenues for studying and improving SPD processes, leading to enhanced material properties and optimized processing routes. By accurately simulating and analyzing these processes, researchers can gain insights into the underlying mechanisms and guide the development of advanced materials with tailored properties. Implicit solvers are suitable for problems with slow and steady deformations. They might struggle with highly discontinuous nonlinearities, such as frequent changes in contact and frictional sliding. As the size of the simulation model increases, memory usage and CPU costs per iteration also increase. Convergence difficulties can arise due to sudden changes in contact conditions. Explicit solvers are advantageous for analyzing large three-dimensional contact problems commonly encountered in metal forming simulations.

They can handle highly discontinuous nonlinearities. However, they have unstable algorithms. The time step must be smaller than a critical time step, as determined by stability considerations. This critical time step is usually small compared to the duration of the forming process. The Explicit Method is well-suited for short-duration processes. It can handle large and complex simulations with contact and friction and is particularly useful for dynamic and transient behaviors. It offers insights into short-time events. It can be used for simulations involving high velocities or artificially increased material density. In metal forming simulations, both methods have their merits and limitations. While implicit methods are more stable and better suited for long-term processes, explicit methods are more suitable for short-term, dynamic, and highly nonlinear processes. Researchers often choose the method that aligns best with the specific characteristics of the process they are simulating and the trade-offs between accuracy and computational efficiency. Industrial manufacturing needs to keep in check and predict the material mechanical properties of products throughout the material processing phase, requiring better predictive and physically-based models to intervene in the processing. The texture and anisotropy, and their impact on the mechanical properties of the products, are the key parameters for investigation. The CPFEM analysis provides a coherent explanation for deforming processes. Metal forming simulation with CPFEM can be performed using implicit and explicit algorithms. The implicit CPFEM method can experience numerical difficulties when simulating nonlinear, highly discontinuous, and high-speed dynamic processes. Most metal-forming simulations with CPFEM need explicit algorithms for stable analysis increments due to contact nonlinearities and frictional discontinuities. One of the main drawbacks of using crystal plasticity in large-scale finite element simulations is the high computational cost due to the stress update algorithm. Implicit and explicit CPFEM formulation advantages and disadvantages are discussed in previous works ([136],[137]). Additionally, the literature explores various explicit CPFEM formulations and algorithms. For example, crystal plasticity explicit formulation was derived using the Euler integration scheme (e.g., [138]). In another example, a framework for numerical integration of crystal elastoplastic constitutive equations compatible with explicit finite element codes presents the results of numerous calculations using a physics-based rate and temperature-dependent model of a copper and the effect of elastic unloading, elastic crystal anisotropy, and deformation-induced lattice ro-

84

tation were emphasized ([73]). Moreover, an effective computational algorithm for rate-independent crystal plasticity based on a single crystal yield surface was applied to tube hydroforming and cutting plane algorithm ([139]). Furthermore, severe numerical instability in the integration of rate-dependent crystal plasticity (RDCP) models is one of the main problems for implementing RDCP into the finite element method (FEM), especially for simulating dynamic/transient forming processes containing complicated contact conditions under considerable step lengths, large strains, and high strain rates. An implicit model was deduced with the primary unknowns of shear strain increments of slip systems under the corotational coordinate system. The subroutine VUMAT was developed for implementing the RDCP model in ABAQUS/-Explicit ([140]). Forby, a crystal plasticity scheme for explicit time integration codes was also developed based on a forward Euler algorithm ([141]). In addition, simulations of the deep drawing of cylindrical cups from as-rolled OFHC-copper blanks were carried out using an explicit finite element formulation ([142]). Besides, an explicit integration scheme for hypo-elastic viscoplastic crystal plasticity was proposed. It was found that the hypo-elastic implementation was only slightly faster and had similar accuracy as the hyper-elastic formulation ([143]). On the side, an efficient and robust constitutive explicit algorithm was proposed, and an implicit update algorithm into an explicit form was tested ([144]). Lastly, a hypoelastic–plastic formulation of porous crystal plasticity with a regularized version of Schmid's law was proposed. The equation describing the effect of the voids on plasticity was modified to allow for an explicit analytical solution for the effective resolved shear stress ([145]).

In this study, a rate-dependent new crystal plasticity user subroutine to define material behavior (VUMAT) algorithm is developed with the explicit solver of the Abaqus FE commercial program.
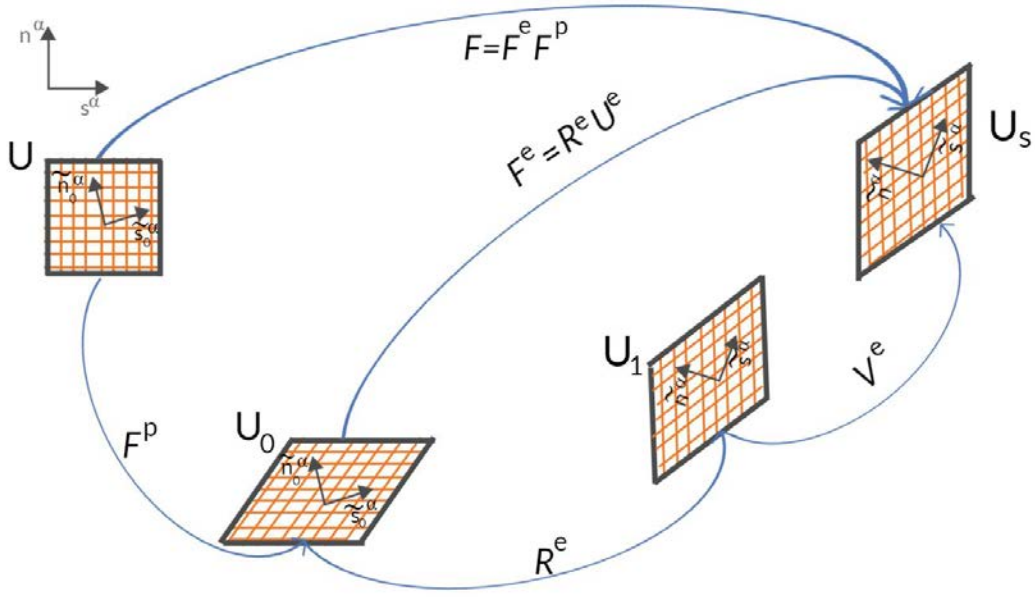
Figure 4.1: Kinematics of elastic and plastic deformation of single crystals

4.2 Explicit CPFEM Formulation

4.2.1 Kinematics

The material constitutive response of single crystals can be modeled by considering crystallographic slip mechanisms ([146],[147]). The total deformation gradient ($F = R^*U$), where R^* represents rigid body rotation and U represents the right stretch tensor, is multiplicatively decomposed into elastic (F^e) and plastic (F^P) components ([148]) (Eq.4.1). Additionally, the elastic part of the deformation (F^e) can be expressed as the multiplication of the left stretch tensor (V^e) and the rotation tensor (R^e).

$$F = F^e F^p \tag{4.1}$$

In the Abaqus explicit formulation, the total rotation tensor (R^*) represents rigid body rotation, which is formulated using the Green-McInnis-Naghdi rate ([149]). Under the assumption of plastic deformation, the plastic component of the deformation gradient does not affect the rigid body rotation of a single crystal. Thus, the elastic part of the rotation (R^e) can be considered equal to the total rotation (R^*) of the deformation.

$$F = R^*U = V^e R^* F^p \tag{4.2}$$

The resolved shear stress τ^α acting on the αth slip system in the undeformed lattice can be defined as the work conjugate to the slip rate $(\dot{\gamma}^\alpha)$. Then, by considering the plastic power per unit volume, it can be defined as (Eq.4.3) ([150]).

$$\dot{\omega} = \boldsymbol{\tau} : \boldsymbol{D^p} = \sum_{\alpha=1}^{n} \tau^\alpha \dot{\gamma}^\alpha \tag{4.3}$$

where $\boldsymbol{\tau}$ is the Kirchhoff stress and $\boldsymbol{D^p}$ is the plastic rate of deformation tensor in the current configuration. Equation 4.3 can be written in the current configuration from Figure 4.1 U_s and Equation 4.4;

$$\tau^\alpha = \tilde{\boldsymbol{n}}^\alpha \cdot \boldsymbol{\tau} \cdot \tilde{\boldsymbol{s}}^\alpha \tag{4.4}$$

In the intermediate configuration (U_0) shown in Figure 4.1, Equation 4.4 can be written as Equation 4.5 in the n th iteration number.

$$\tilde{\boldsymbol{n}}^\alpha \cdot \boldsymbol{\tau} \cdot \tilde{\boldsymbol{s}}^\alpha = \tilde{\boldsymbol{n}}_0^\alpha \boldsymbol{F}_n^{eT} \boldsymbol{F}_n^e \boldsymbol{S}_n^{eo} \boldsymbol{F}_n^{eT} \boldsymbol{F}_n^{e-T} \tilde{\boldsymbol{s}}_0^\alpha \tag{4.5}$$

which is equal to ;

$$\tau_n^\alpha = \sum_{k=1}^{\alpha} \boldsymbol{C}_n^{eo} \boldsymbol{S}_n^{eo} \tilde{\boldsymbol{s}}_0^\alpha \otimes \tilde{\boldsymbol{n}}_0^\alpha \tag{4.6}$$

where $\boldsymbol{C}_n^{eo}$ in Equation 4.6 is the elastic right Cauchy-Green strain tensor and defined as Equation 4.7.

$$\boldsymbol{C}_n^{eo} = \boldsymbol{F}_n^{eT} \boldsymbol{F}_n^e \tag{4.7}$$

$\boldsymbol{S}_n^{eo}$ is the Piola-Second Kirchhoff stress (PK2) which can be calculated from Equation 1.36 in Chapter 1 and $\boldsymbol{C}_n^{eo} \boldsymbol{S}_n^{eo}$ is the Mandel stress ([151],[152]) on the intermediate state U_0 in Figure 4.1. $\tilde{\boldsymbol{s}}_0^\alpha \otimes \tilde{\boldsymbol{n}}_0^\alpha$ is the tensor product of the slip direction and nominal direction of initial slip system directions, which can be found by multiplying the slip system $(\boldsymbol{s}^\alpha, \boldsymbol{n}^\alpha)$ with the Bunge-formulated Euler angles (α, β, γ) from Equation 4.8. The rotation tensor $\boldsymbol{Q_0}$ can be written as Equation 4.9 ([153]).

$$\tilde{\boldsymbol{s}}_0^\alpha = \boldsymbol{Q_0} \boldsymbol{s}^\alpha, \tilde{\boldsymbol{n}}_0^\alpha = \boldsymbol{Q_0} \boldsymbol{n}^\alpha \tag{4.8}$$

$$\boldsymbol{Q_0} = \begin{bmatrix} \cos(\alpha)\cos(\gamma)- & \cos(\gamma)\sin(\alpha)+ & \\ \cos(\beta)\sin(\alpha)\sin(\gamma) & \cos(\beta)\cos(\alpha)\sin(\gamma) & \sin(\beta)\sin(\gamma) \\ -\sin(\gamma)\cos(\alpha)- & -\sin(\gamma)\sin(\alpha)+ & \\ \cos(\beta)\sin(\alpha)\cos(\gamma) & \cos(\alpha)\cos(\gamma)\cos(\beta) & \cos(\gamma)\sin(\beta) \\ \sin(\alpha)\sin(\beta) & -\cos(\alpha)\sin(\beta) & \cos(\beta) \end{bmatrix} \quad (4.9)$$

The initial orientation matrix $\boldsymbol{Q_0}$ depends on the Euler angles (α, β, γ). The transformation matrix $\boldsymbol{Q}$ according to the reference frame of the corotational lattice frame is updated by Equation 4.10 ([154],[155]). Euler angles of the single crystal during deformation can be found from $\boldsymbol{Q}$ and are used to represent the final texture.

$$\boldsymbol{Q} = \boldsymbol{R^*Q_0} \quad (4.10)$$

Slip plane directions, and normals are illustrated in Figure 1.7 and Table 1.3 in Chapter 1.

4.2.2 Power Law Type Flow Model

The slip rates and evolution of internal variables must be specified to complete the constitutive model of elastic and plastic deformation of a single crystal material. Several flow and hardening models have been proposed in the literature. A phenomenological power-law type model and another physical-based model are commonly used. The power-law type rate-dependent formulation, which relates the slip rate on each slip system to the current yield stress τ^α and the slip resistance g^α, is given in Equation 4.11 ([156]).

$$\dot{\gamma}_n^\alpha = \dot{\gamma}_0 \left| \frac{\tau_n^\alpha}{g_n^\alpha} \right|^m sign(\tau_n^\alpha) \quad (4.11)$$

where $\dot{\gamma}_0$ is the reference shearing rate, and the exponent m is the strain rate sensitivity coefficient. This flow model is straightforward and easy to implement in the user subroutine due to the simplicity of the formulation and ease of calibrating the model parameters.

4.2.3 Hardening Model

The slip resistance g^α is defined in Equation 4.12. The critical resolved shear stress τ_c^α is initially equal to g_0. The hardening moduli $h^{\alpha\beta}$ represent the rate of strain hardening on slip system α due to slip on slip system β. This occurrence of self and latent hardening is phenomenologically described by Equation 4.13 ([115]).

$$\dot{g}^\alpha = \sum_{k=1}^{12} h^{\alpha\beta}|\dot{\gamma}^\beta| \tag{4.12}$$

$$h_\alpha\beta = qh(\gamma) \tag{4.13}$$

The saturation-type model are introduced in equation 4.14.([157],[158])

$$h^{\alpha\beta} = h_0[q + (1-q)\delta^{\alpha\beta}](1 - g^\beta/g_{sat})^a sign(1 - \frac{g^\beta}{g_{sat}}) \tag{4.14}$$

where $\delta^{\alpha\beta} = 1$ for $\alpha = \beta$ and 0 otherwise; h_0, g_{sat}, and a are the material parameters, representing the reference self-hardening coefficient, the saturation values of slip resistance, and the hardening exponent, respectively. q represents the latent hardening parameter.

The hyperbolic secant formulation in Chapter 3, Equation 3.8 is an optional hardening model.

4.2.4 Plastic Component of Deformation Gradient

In the field of crystal plasticity, it is understood that the primary mechanism driving plastic deformation is the movement of dislocations through the crystal lattice. This dislocation motion is restricted to specific crystal planes and directions dictated by the material's crystallographic structure. Notably, plastic flow does not alter the underlying crystal structure of the metal. In addition to plastic deformation, elastic deformation can occur where no dislocation movement is involved. Elastic deformation results from the crystal lattice distortion without causing permanent changes to the crystal structure.

Plastic deformation is initiated by the process of shear or slip denoted as γ^α on specific slip systems. These slip systems are characterized by vectors s and n, representing

the unit vector along the slip direction and the unit normal vector to the slip plane in the intermediate configuration U_0, as illustrated in Figure 4.1. The equation provided in Equation 4.15 defines the velocity gradient.

$$L = \dot{F}F^{-1} \tag{4.15}$$

with Equation 4.1 into the above formula, straightforward differentiation using the product rule gives the following additive decomposition of the velocity gradient

$$L = L^e + F^e L^p (F^e)^{-1} \tag{4.16}$$

where L^e and L^p are, respectively, the elastic and plastic components of the velocity gradient. As defined in the above expression, the plastic component of the velocity gradient is defined in the intermediate configuration. Therefore, the second term corresponds to a pushforward to the current configuration. Plastic deformation is caused by dislocation slip along multiple slip systems. The plastic component of deformation gradient L^p can be obtained as the sum of the shear rates corresponding to each slip system, $\dot{\gamma}^\alpha$ according to Equation 4.17.

$$L^p = \sum_{k=1}^{\alpha} \dot{\gamma}_n^\alpha \tilde{s}_0^\alpha \otimes \tilde{n}_0^\alpha \tag{4.17}$$

by combining Equation 4.15 and Equation 4.17 we get Equation 4.18,

$$\dot{F}^p = (\sum_{k=1}^{\alpha} \dot{\gamma}_n^\alpha \tilde{s}_0^\alpha \otimes \tilde{n}_0^\alpha) F^p \tag{4.18}$$

Equation 4.18 defines an Ordinary Differential Equation with the unknown being the tensor function F^p. The solution of a 1st order ODE form is equal to Equation 4.19

$$F_{n+1}^p = exp(\sum_{k=1}^{\alpha} \dot{\gamma}_n^\alpha \tilde{s}_0^\alpha \otimes \tilde{n}_0^\alpha) F_n^p \tag{4.19}$$

This exponential form can be written as Equation 4.20 from series

$$F_{n+1}^p = (I + \Delta t \sum_{k=1}^{\alpha} \dot{\gamma}_n^\alpha \tilde{s}_0^\alpha \otimes \tilde{n}_0^\alpha) F_n^p \tag{4.20}$$

4.2.5 Elastic Component of Deformation Gradient

The intermediate configuration described by U_0 in Figure 4.1 is generally not uniquely determined since an arbitrary rigid body rotation can be superimposed, still leaving

it unstressed. To overcome the uniqueness problem, a total rigid body rotation can be applied to the plastic component of the deformation gradient, and the elastic left stretch tensor can be found from Equation 4.21, and the elastic component of the deformation gradient can be found from Equation 4.22.

$$V_{n+1}^e = F_{n+1}(R^* F^p)^{-1} \tag{4.21}$$

$$F_{n+1}^e = V_{n+1}^e R^* \tag{4.22}$$

4.2.6 Corotational Stress Rate

The Green-Naghdi stress rate $\sigma^{\Delta G}$ can be defined as the pushforward of the time derivative of the corotational stress σ°. One can construct objective rates by pulling back and pushing forward with the rotation tensor R only since the rotation causes the stress rates to be non-objective. To define the time derivative of the corotational Cauchy stress, we need to calculate the term $R^{*T} \dot{\sigma} R^*$, where R^* is the orthogonal rotation tensor. Whereas the Cauchy stress rate is related to the second Piola-Kirchhoff (PK2) stress, and the PK2 stress rate can be found from the multiplication of the rotated elastic modulus (Equation 4.23) according to initial orientations $\tilde{C} = Q_0^c C Q_0^{cT}$ with the material strain rate tensor, elastic Green-Lagrange strain rate from Equation 4.25, and Equation 4.26, Q_0^c is the transformed fourth order initial rotational orientation tensor. ([71],[72]) and represented in Equation 4.24.

$$C = \begin{pmatrix} C_{11} & C_{12} & C_{12} & 0 & 0 & 0 \\ C_{12} & C_{11} & C_{12} & 0 & 0 & 0 \\ C_{12} & C_{12} & C_{11} & 0 & 0 & 0 \\ 0 & 0 & 0 & C_{44} & 0 & 0 \\ 0 & 0 & 0 & 0 & C_{44} & 0 \\ 0 & 0 & 0 & 0 & 0 & C_{44} \end{pmatrix} \tag{4.23}$$

$$Q_0^c = \begin{pmatrix}
Q_0^{1I2} & Q_0^{1II2} & Q_0^{1III2} & \sqrt{2}Q_0^{1II}Q_0^{1III} & \sqrt{2}Q_0^{1I}Q_0^{1III} & \sqrt{2}Q_0^{1I}Q_0^{1II} \\
Q_0^{2I2} & Q_0^{2II2} & Q_0^{2III2} & \sqrt{2}Q_0^{2II}Q_0^{2III} & \sqrt{2}Q_0^{2I}Q_0^{2III} & \sqrt{2}Q_0^{2I}Q_0^{2II} \\
Q_0^{3I2} & Q_0^{3II2} & Q_0^{3III2} & \sqrt{2}Q_0^{3II}Q_0^{3III} & \sqrt{2}Q_0^{3I}Q_0^{3III} & \sqrt{2}Q_0^{3I}Q_0^{3II} \\
\sqrt{2}Q_0^{2I}Q_0^{3I} & \sqrt{2}Q_0^{2II}Q_0^{3II} & \sqrt{2}Q_0^{2III}Q_0^{3III} & Q_0^{2II}Q_0^{3III}+Q_0^{3II}Q_0^{2III} & Q_0^{2I}Q_0^{3III}+Q_0^{3I}Q_0^{2III} & Q_0^{2I}Q_0^{3II}+Q_0^{3I}Q_0^{2II} \\
\sqrt{2}Q_0^{1I}Q_0^{3I} & \sqrt{2}Q_0^{1II}Q_0^{3II} & \sqrt{2}Q_0^{1III}Q_0^{3III} & Q_0^{1II}Q_0^{3III}+Q_0^{3II}Q_0^{1III} & Q_0^{1I}Q_0^{3III}+Q_0^{3I}Q_0^{1III} & Q_0^{1I}Q_0^{3II}+Q_0^{3I}Q_0^{1II} \\
\sqrt{2}Q_0^{1I}Q_0^{2I} & \sqrt{2}Q_0^{1II}Q_0^{3II} & \sqrt{2}Q_0^{1III}Q_0^{2III} & Q_0^{1II}Q_0^{2III}+Q_0^{2I}Q_0^{1III} & Q_0^{1I}Q_0^{2III}+Q_0^{2I}Q_0^{1III} & Q_0^{1I}Q_0^{2II}+Q_0^{1II}Q_0^{2I}
\end{pmatrix}$$

$$\tag{4.24}$$

$$\dot{E}_{n+1}^e = \frac{1}{2}[(\dot{F}_{n+1}^e)^T F_{n+1}^e + (F_{n+1}^e)^T \dot{F}_{n+1}^e] \tag{4.25}$$

$$\dot{S}_{n+1}^{e_0} = \tilde{C} : \dot{E}_{n+1}^e \tag{4.26}$$

The corotational stress is defined on the current configuration from Fig. 4.1. The material derivative of the material PK2 stress tensor, $\dot{S}$, is objective. The corotational stress rate can be regarded as the push forward of the PK2 stress rate from the reference configuration through the elastic part of the right stretch U^e, scaled by J^{e-1}. The corotational stress can be written as Equation 4.27.

$$\sigma^\circ = R^{*T}\sigma R^* \tag{4.27}$$

The time derivative of the corotational stress can be calculated as,

$$\dot{\sigma}^\circ = \dot{R}^{*T}\sigma R^* + R^{*T}\dot{\sigma} R^* + R^{*T}\sigma \dot{R}^* \tag{4.28}$$

From the second Piola–Kirchhoff stress rate, the Kirchhoff stress rate of a push-forward operation can determine the defined current state ([159],[160]),

$$\dot{\tau}_{n+1} = F_{n+1}^e \dot{S}_{n+1}^{e_0} F_{n+1}^{eT} \tag{4.29}$$

From the Kirchhoff stress rate, the Cauchy stress can be defined on the current configuration (U_s) according to

$$\dot{\tau}_{n+1} = J^e \dot{\sigma} \tag{4.30}$$

By employing Equation 4.29, Equation 4.30, and Equation 4.2, we can derive the second term of the time derivative of the corotational stress

$$R^{*T}\dot{\sigma} R^* = \frac{1}{det F_{n+1}^e} U_{n+1}^e \dot{S}_{n+1}^{e_0} U_{n+1}^e \tag{4.31}$$

$$U_{n+1}^e = R^{*T} F_{n+1}^e \tag{4.32}$$

Rigid body rotation $\boldsymbol{R}^*$ is formulated as the Green-Naghdi rate. For a rigid body rotation, the first and third terms of Equation 4.28 are the rate caused by the rigid body spin, so the second term is that part caused by other effects (in the case of stress, the rate associated with the constitutive response), called the corotational rate of $\boldsymbol{\sigma}$ ([149]).

$$\dot{\boldsymbol{\sigma}} = \boldsymbol{\sigma}^{\triangledown} + \boldsymbol{\Omega}\boldsymbol{\sigma}_n - \boldsymbol{\sigma}_n\boldsymbol{\Omega} \tag{4.33}$$

$$\dot{\boldsymbol{\sigma}}\Delta t = \boldsymbol{\Delta\sigma}^{\triangledown} + \boldsymbol{R}\boldsymbol{\sigma}_n\boldsymbol{R}^T \tag{4.34}$$

in which $\boldsymbol{\sigma}^{\triangledown}$ is the rate of objective, corotational stress, or the rate associated with the constitutive response ([58]). Skew symmetric angular velocity tensor $\boldsymbol{\Omega}$ can be found from Equation 4.35.

$$\boldsymbol{\Omega} = \dot{\boldsymbol{R}}^*\boldsymbol{R}^{*T} \tag{4.35}$$

The Cauchy stress $\boldsymbol{\sigma}_n$, at the start of the increment, has already been rotated ([149]), so the rigid body rotation of $\boldsymbol{\sigma}_n$ is not carried out. Thus, the stress update for the spatial configuration U_s can be found as from Equation 4.36.

$$\boldsymbol{\sigma}_{n+1} = \boldsymbol{\sigma}_n + \dot{\boldsymbol{\sigma}}\Delta t \tag{4.36}$$

4.2.7 Shear Rate Evolution Procedure

The shear rates can be determined from Equation 4.11 by utilizing the initial increment values. To address this issue, the following residual equations for $\Delta\gamma$ can be formulated:

$$R^{\alpha}(\Delta\gamma^{\alpha}) = \Delta\gamma^{\alpha} - \Delta t\dot{\gamma}^{\alpha}(\tau_{n+1}^{\alpha}, g_{n+1}^{\alpha}) = 0 \tag{4.37}$$

Utilizing the full Newton-Raphson scheme in the solution process for the system of nonlinear Equation 4.37, we linearize Equation 4.37 resulting in:

$$R(\Delta\gamma^k) + J(\Delta\gamma^k)\boldsymbol{\delta\gamma} = 0 \tag{4.38}$$

93

where $\boldsymbol{\delta\gamma}$ represents the corrector vector, and J corresponds to the Jacobian matrix involved in the return-mapping procedure. Solving Equation 4.38 enables us to calculate the corrector vector:

$$\boldsymbol{\delta\gamma} = -[J(\Delta\gamma^k)]^{-1}R(\Delta\gamma^k) \tag{4.39}$$

From the Equation $\Delta\gamma^k$ is the trial values

$$\Delta\gamma^{k+1} = \Delta\gamma^k + \delta\gamma \tag{4.40}$$

The Newton-Raphson iteration continues until the residual becomes sufficiently small. Convergence of the solution is considered achieved when a specific convergence criterion involving the residual norm is satisfied.

$$||R(\Delta\gamma^{k+1})|| < Tolerance \tag{4.41}$$

The individual terms of the exact Jacobian used in the scheme for solving the residual equations are obtained by differentiating $R^\alpha(\Delta\gamma^\alpha)$ concerning each variable $\Delta\gamma^\beta$.

$$J_{\alpha\beta} = \frac{\partial R^\alpha(\Delta\gamma^\alpha)}{\partial\Delta\gamma^\beta} = \delta_{\alpha\beta} - \Delta t\frac{\partial\dot{\gamma}^\alpha}{\partial\Delta\gamma^\beta} = \delta_{\alpha\beta} - \Delta t\Big[\frac{\partial\dot{\gamma}^\alpha}{\partial\tau^\alpha}\frac{\partial\tau^\alpha}{\partial\Delta\gamma^\beta} + \frac{\partial\dot{\gamma}^\alpha}{\partial g^\alpha}\frac{\partial g^\alpha}{\partial\Delta\gamma^\beta}\Big] \tag{4.42}$$

$$\frac{\partial\dot{\gamma}^\alpha(\tau_{n+1}^\alpha, g_{n+1}^\alpha)}{\partial\tau_{n+1}^\alpha} = m\frac{\dot{\gamma}_0\Delta t}{g_{n+1}^\alpha}\Big|\frac{\tau_{n+1}^\alpha}{\gamma_{n+1}^\alpha}\Big|^{m-1} \tag{4.43}$$

$$\frac{\partial\dot{\gamma}^\alpha(\tau_{n+1}^\alpha, g_{n+1}^\alpha)}{\partial g_{n+1}^\alpha} = -sign(\tau_{n+1}^\alpha)m\frac{\dot{\gamma}_0\Delta t}{g_{n+1}^\alpha}\Big|\frac{\tau_{n+1}^\alpha}{\gamma_{n+1}^\alpha}\Big|^{m-1} \tag{4.44}$$

$$\frac{\partial g_{n+1}^\alpha}{\partial\Delta\gamma^\beta} = h_{\alpha\beta}sign(\Delta\gamma^\beta) \tag{4.45}$$

$$\frac{\partial\tau_{n+1}^\alpha}{\partial\Delta\gamma^\beta} = -\big[((\boldsymbol{m_0}\otimes\boldsymbol{s_0})^{\beta T}\boldsymbol{F_n^{p-T}}\boldsymbol{F^T}\boldsymbol{F}\boldsymbol{F^{p-1}}+$$
$$\boldsymbol{F^{p-T}}\boldsymbol{F^T}\boldsymbol{F}\boldsymbol{F_n^{p-1}}(\boldsymbol{m_0}\otimes\boldsymbol{s_0})^\beta)\boldsymbol{S_{n+1}^{e_0}}+$$
$$\frac{1}{2}\boldsymbol{C_{n+1}^{e_0}}\tilde{\boldsymbol{C}} : ((\boldsymbol{m_0}\otimes\boldsymbol{s_0})^{\beta T}\boldsymbol{F_n^{p-T}}\boldsymbol{F^T}\boldsymbol{F}\boldsymbol{F^{p-1}}+$$
$$\boldsymbol{F^{p-T}}\boldsymbol{F^T}\boldsymbol{F}\boldsymbol{F_n^{p-1}}(\boldsymbol{m_0}\otimes\boldsymbol{s_0})^\beta)\big] : (\boldsymbol{m_0}\otimes\boldsymbol{s_0})^\alpha \tag{4.46}$$

4.2.8 Algorithm of Explicit Subroutine (VUMAT)
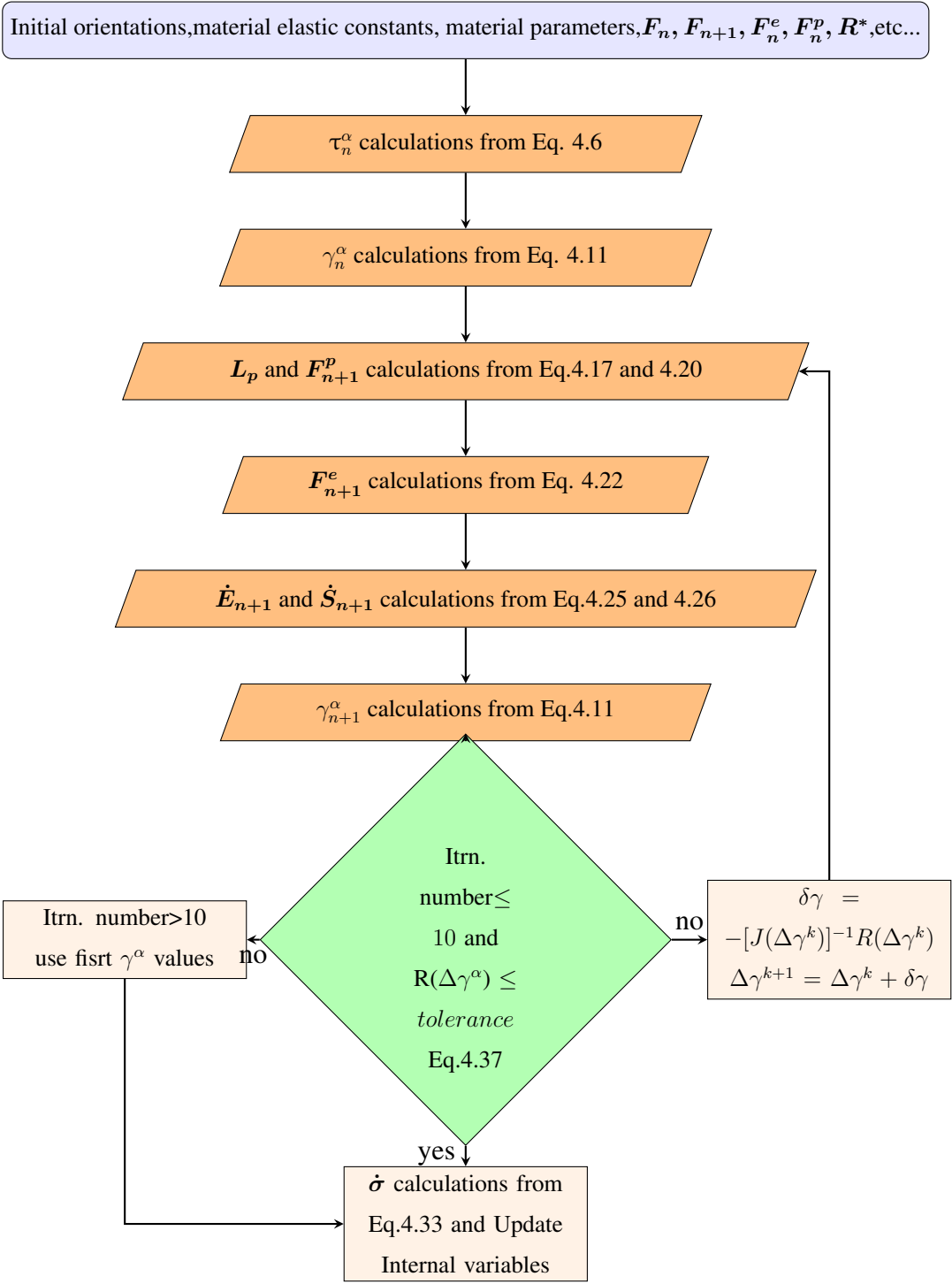
Figure 4.2: Algorithm of explicit subroutine user defined material (VUMAT)

4.3 Explicit User Defined Material (VUMAT) Code Verification Studies

4.3.1 Model Validation Under Basic Boundary Conditions

Tensile test, simple shear test, and pure shear test simulations are carried out to check the consistency of the explicit algorithm with experimental results ([161]) and the UMAT code written by Huang (see Chapter 3). The boundary conditions are treated as shown in Figure 4.3 ([162], [163]). Material parameters of single crystal copper, taken from the literature ([164]), are compared with [100] and [111] directed single copper crystal test data. Material parameters are presented in Table 4.1. The comparison of CPFEM simulations and test data curves for [100] and [111] directed single crystals are illustrated in Figure 4.4. The CPFEM results show that the test data are compatible with VUMAT and UMAT simulation results for tension and pure shear boundary conditions. However, in simple shear boundary conditions, there is inconsistency with the UMAT code. One of the main reasons for this situation is explained in Chapter 1 and illustrated in Figure 1.13.

Table 4.1: Material calibration parameters for copper single crystal.

C_{11}	C_{12}	C_{44}	τ_{cr}	h_0
170000 MPa	124000 MPa	75400 MPa	2.5 MPa	200 MPa
g_{sat}	$\dot{\gamma}_0$	m	q	a
150 MPa	$0.001\ s^{-1}$	83.333	1.4	2.25
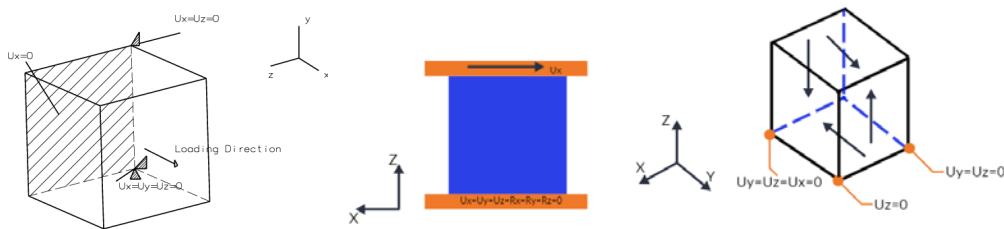
Figure 4.3: Tension boundary conditions (**left**), simple shear boundary conditions (**mid**) and pure shear boundary conditions (**right**)
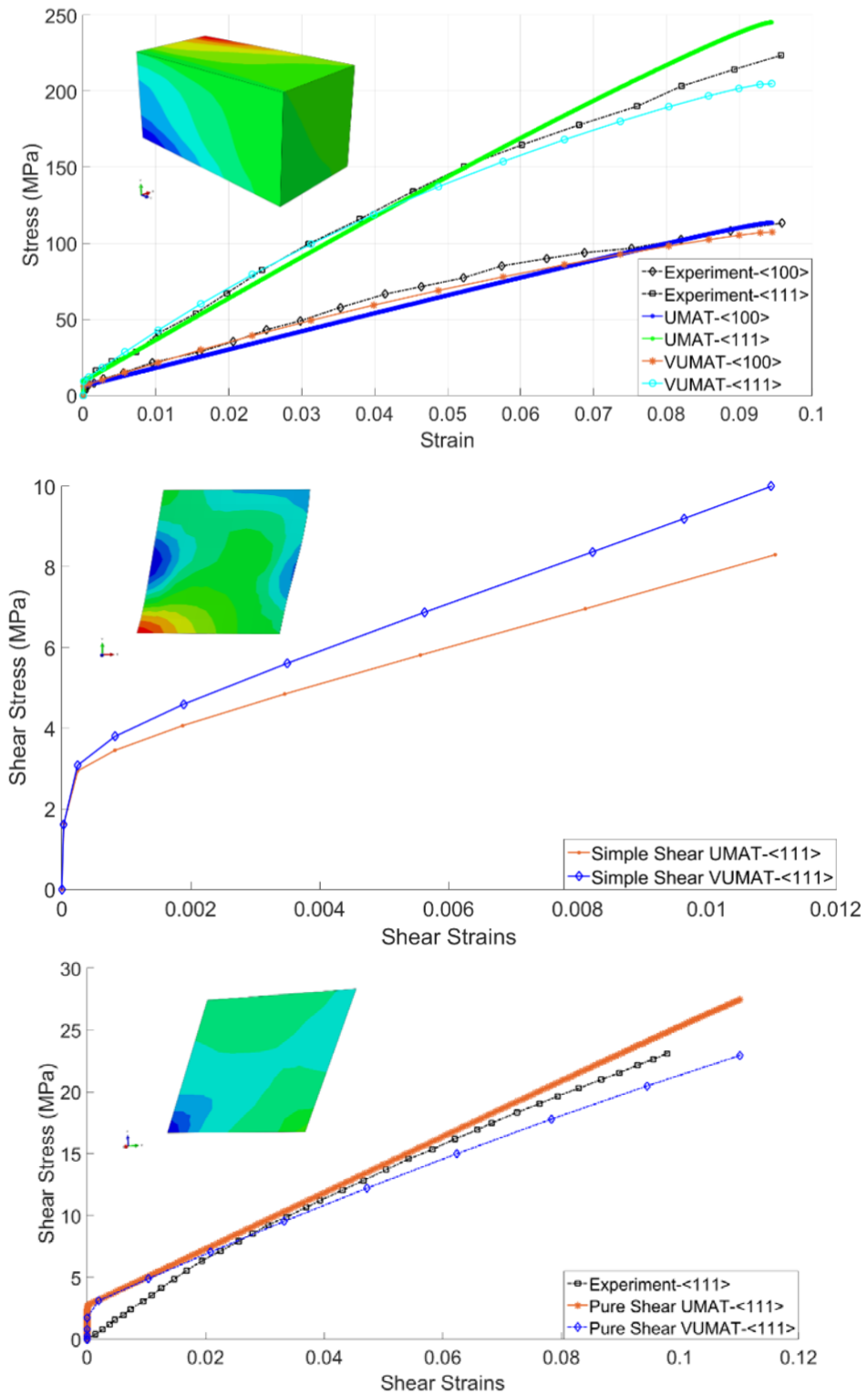
Figure 4.4: Single copper crystal UMAT and VUMAT CPFEM simulation results vs. experiment results.

4.3.2 Model Validation with Digital Image Correlation Experiments

This study explores the influence of different strain paths on polycrystalline aluminum alloy 6061-T6 deformation behavior at the microstructure scale. We aim to understand how the material responds to various loading conditions and how its behavior compares with experimental observations. We employ implicit and explicit CPFEM to simulate the deformation process to achieve this. The crystal plasticity model parameters are carefully calibrated to ensure the simulations accurately reproduce the experimental results. This involves fine-tuning the model to capture the material's response under different strain paths accurately. Through this calibration process, we aim to establish a strong correlation between the predictions of the CPFEM models and the actual experimental data.

However, the work does not stop at calibration. Once the models are tuned to match the experimental observations, we analyze the results further to identify areas for improvement. This includes investigating discrepancies between the model predictions and experimental outcomes and exploring potential refinements to the crystal plasticity model parameters or formulation.

Overall, this research contributes to a deeper understanding of how strain paths impact polycrystalline aluminum alloy 6061-T6 deformation behavior. By comparing experimental data with CPFEM simulations, we not only validate the accuracy of the models but also gain insights into the underlying mechanisms governing the material's response. This combined approach allows us to replicate experimental observations, enhance our understanding of the material's behavior, and potentially refine the crystal plasticity model for improved accuracy in future simulations.

4.3.2.1 Experimental Procedure

The Aluminum 6061-T6 material is tested using a biaxial test apparatus (see Fig. 4.5). The biaxial apparatus uses cruciform-shaped samples, which are deformed under uniaxial and equibiaxial tension conditions, to represent different strain paths. The micro-scale Digital Image Correlation (DIC) method maps strain distributions at the microstructure scale during deformation. Ncorr v1.2, an open-source MATLAB-

based software, is used for 2D-DIC analysis. The parameters are set to 80 and 8 pixels for subset size and spacing, respectively. The imaging unit for DIC consists of a Basler piA2400 - 17gm (5 MP, 2/3" Sony ICX625 CCD sensor) camera and a Navitar UltraZoom 6000 lens, including a 2X adapter, a 10X Mitutoyo objective, and coaxial LED illumination. The imaging configuration is set to 20X magnification to observe the specimen at the micro-scale, resulting in a field of view of 432 x 324 μm² and a resolution of 0.176 x 0.157 μm/pixel ([165]).

The pattern necessary for correlation is prepared by electro-etching and spraying. Etching is essential for revealing grain boundaries, while grain boundaries and other etching features provide additional contrast for correlation. However, etching alone is insufficient for successful correlation, as the interior of the grains remained featureless and lacked contrast. Subsequently, sample surfaces are sprayed with TiO2 nanoparticles, creating contrast in the grains as micron-sized dark particles. Care must be taken when applying this spraying method, as excessive particle spraying can lead to particle segregation at the grain boundaries, rendering the grain boundaries invisible and making it difficult to distinguish between grains.

In this study, aluminum alloys are stretched under uniaxial tension conditions using a biaxial tension test apparatus employing cruciform specimens. Electron Back Scatter Diffraction (EBSD) analysis is conducted to determine the texture of the samples. The specimens are deformed until a fracture occurs, and DIC, during testing, provides strain distribution maps at the microstructure scale. The Aluminum 6061 T6 alloy is also deformed under uniaxial tension up to 0.09 average equivalent strain, and the corresponding DIC and EBSD results are shown in Figure 4.6. The test is stopped before fracture to correctly identify the grains with strain localizations. Despite the relatively low average strain, some grains develop intense localizations. Under uniaxial tension conditions, the equivalent strain reaches a maximum value of 0.16 in localized regions. Adjacent to these localizations, the equivalent strain decreases to 0.04, resulting in sharp contrasts in the immediate neighbors. The minimum equivalent strain is 0.02, occurring elsewhere in the test region. Consistent with observations in the literature, strain localizes at grain boundaries and triple junctions rather than in the grain interiors. The orientations of grains neighboring the strain-localized grain boundaries differ from each other. There appears to be no preferred orientation for
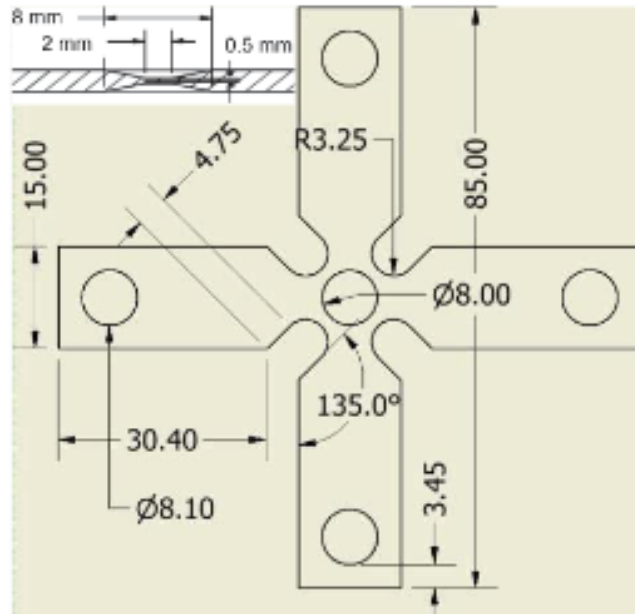
Figure 4.5: Dimensions of the cruciform sample and the dimensions of the test region (in mm)
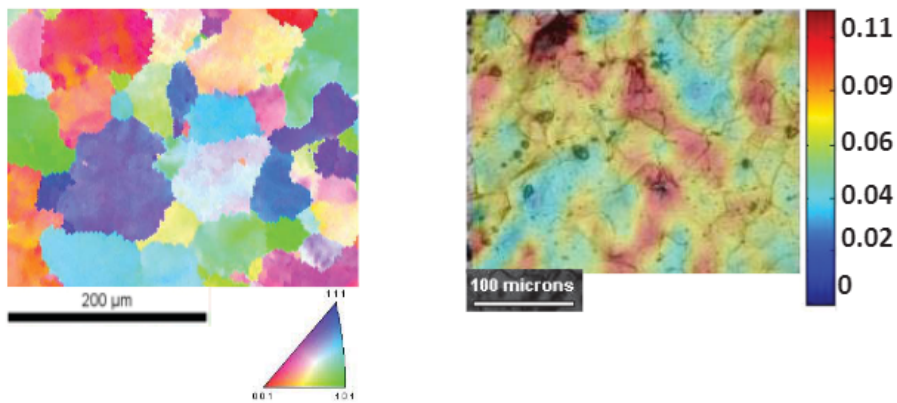
Figure 4.6: EBSD (**left**) and DIC (**right**) results of Aluminum 6061 T6 after uniaxial tension.

localizations; however, it is possible to find at least one grain with a (012) orientation near the localized regions.

4.3.2.2 Finite Element Model Definitions

The determination and modeling of microstructure follow the procedure described above. A finite element (FE) model with dimensions X, Y, and Z of 430 $\mu m \times$ 330 $\mu m \times$ 30 μm, containing nearly 150 grains, is employed to study the strain distribution in the Representative Volume Element (RVE) due to tension loading. The EBSD model is first transferred to the CATIA V5 3D design commercial program, and using the generative surface design and part design interface, the 3D microstructure model is created. Dream 3D software is also used to create the 3D microstructure model from EBSD experiment data, as shown in Figure 4.7.
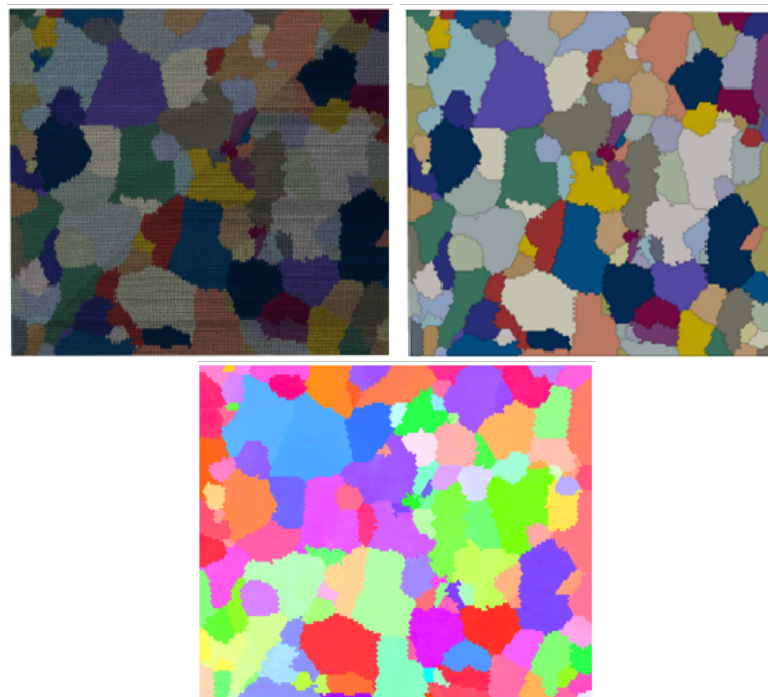
Figure 4.7: 3D Microstructural models of EBSD experiments (**bottom**) Dream 3D (**top left**) and CATIA V5 (**top right**)

Due to the mesh quality and visualization performance of Catia V5, the 3D microstructure model, which is designed in this program, is used to perform CPFEM analysis. The model is meshed with 161,956 linear C3D8R hexahedral mesh elements. The 3D mesh model of the CATIA V5 design is shown in Figure 4.8, and mesh parameters are provided in Table 4.2.

A hybrid model is created, considering that the boundary conditions are brought to the
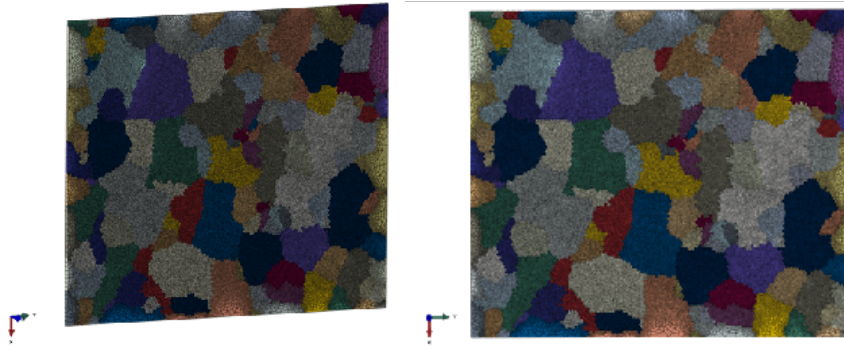
Figure 4.8: FEA model 3D mesh model of CATIA V5 microstructural design

Table 4.2: 3D microstructure mesh model parameters

Model	Element Type	Element Family	Number of Elements
Uniaxial Tension 3D Microstructure	C3D8R linear hexahedral	3D Stress	161956

same conditions as the tensile test, and the strain distribution is not homogeneously distributed on all sides of the test apparatus used. The test apparatus is created using CATIA V5, and the region observed with EBSD is modeled microstructurally in the middle of this test apparatus (Figure 4.9). Boundary conditions applied to the model are presented in Figure 4.10, and mesh parameters are shown in Table 4.3.

The polycrystalline apparatus material is modeled using von Mises Plasticity and the stress-strain curve values of Aluminum 6061 T6 material. The stress-strain curve is illustrated in Fig. 4.11. Material parameters for CPFEM analysis are obtained using a randomly distributed representative volume element (RVE) cube with 1000 orientations (Figure 4.12). Tension boundary conditions are applied to the microstructural model, with displacement as shown in Figure 4.12. The required values of the structural material parameters of the crystal plasticity (CP) model are given in Table 4.4.
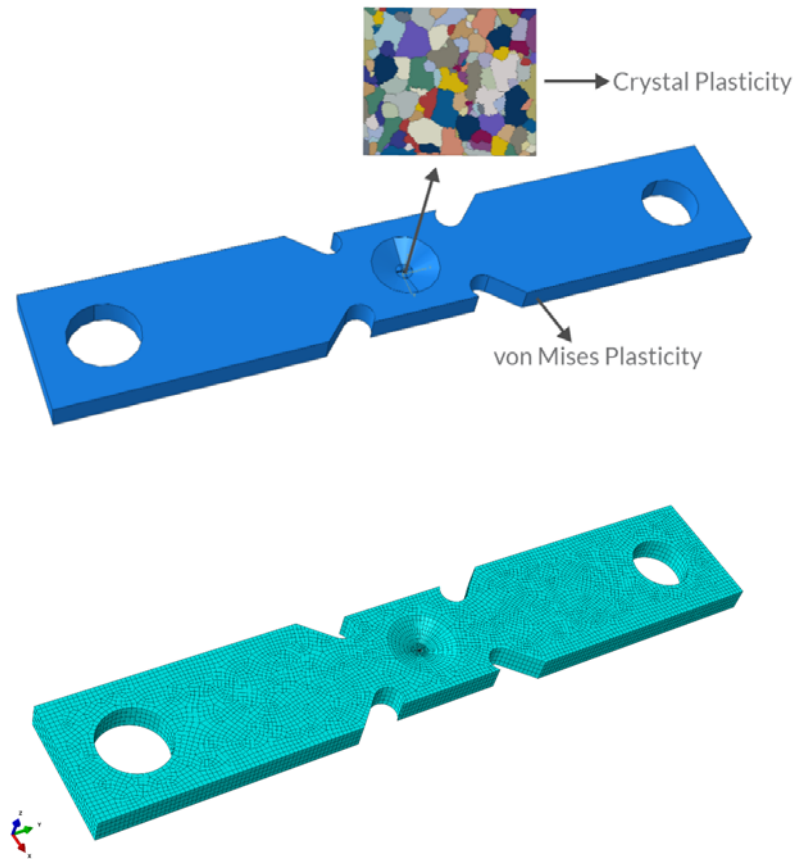
Figure 4.9: FEA 3D hybrid model (**top**) and mesh model of CATIA V5 (**bottom**) microstructural design
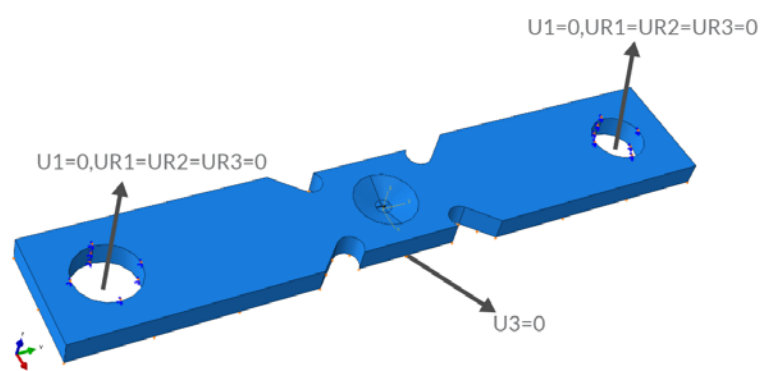
Figure 4.10: Boundary Conditions of FEA 3D hybrid model

Table 4.3: 3D Hybrid model and microstructure mesh model parameters

Model	Element Type	Element Family	Number of Elements
Tension Test Apparatus	C3D8R linear hexahedral	3D Stress	21972
Uniaxial Tension 3D Microstructure	C3D8R linear hexahedral	3D Stress	161956
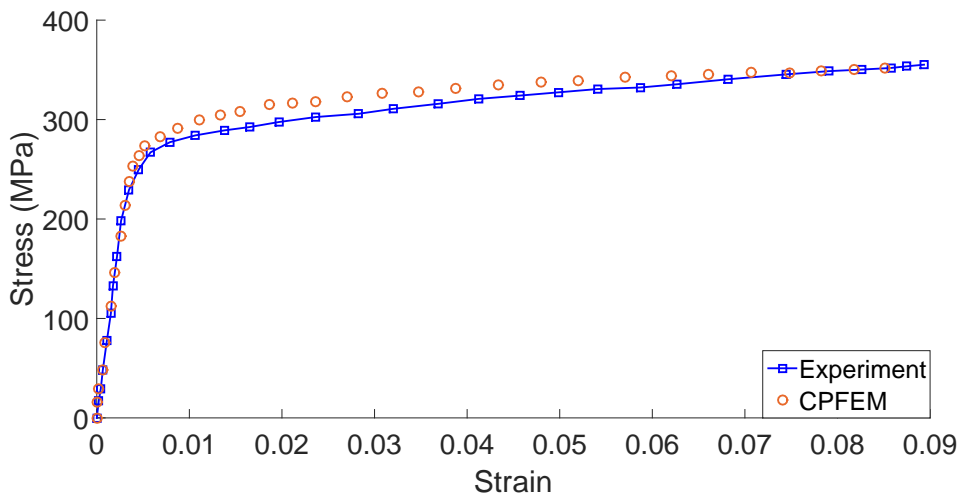
Figure 4.11: The experimental stress-strain curve of aluminum 6061 T6 and CPFEM model parameter calibration

4.3.2.3 Discussion of DIC Experiments and CPFEM Results

This study presents a comprehensive methodology for integrating microstructure morphology and texture with mechanical strain fields using implicit and explicit approaches. The foundation of this methodology lies in bridging experimental characterization of microstructures obtained through in-situ and ex-situ mechanical testing
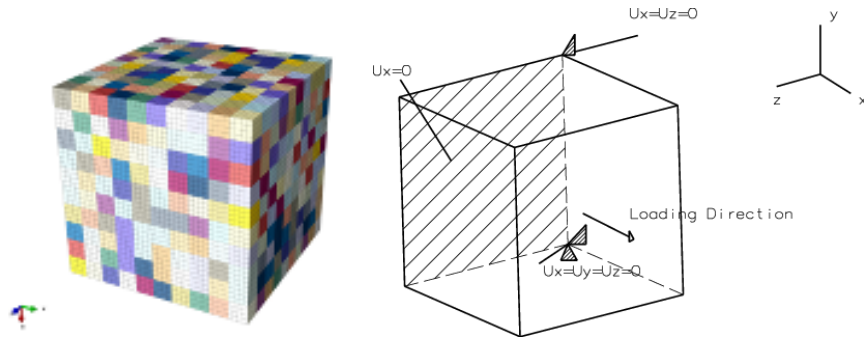
Figure 4.12: Calibration cube (RVE) (**left**) and Uniaxial Loading of Random Oriented CP Model Boundary Conditions (**right**)

Table 4.4: Single crystal aluminum 6061 T6 VUMAT model parameters

Model Aluminum 6061 T6	C_{11}	C_{12}	C_{44}	τ_0
Vumat	112850 MPa	43404 MPa	21550 MPa	125 MPa
h_0	τ_s	$\dot{\gamma}_0$	m	q
100 MPa	140 MPa	$0.1 s^{-1}$	17	1.4

with local strain field measurements and finite element simulations at the grain scale.

The workflow begins with generating a microstructure map using orientation imaging microscopy. This map is then utilized to create a meshed geometry suitable for finite element calculations. These calculations incorporate a constitutive law incorporating the crystallographic orientation of each grain, as determined by the orientation imaging microscopy.

Both implicit (UMAT) and explicit (VUMAT) crystal plasticity algorithms are utilized to obtain numerical simulation results. These results are subsequently compared to experimental strain field data obtained through digital image correlation (DIC) at the grain scale. This investigation's focus material is Aluminum 6061 T6, which is characterized by a face-centered cubic crystal lattice structure.

105

The preliminary stages involve optical microscopy and Electron Back Scatter Diffraction (EBSD) analyses to construct a microstructural map of the region under investigation for DIC measurements. DIC is then employed to measure the kinematics of the representative microstructural volume, revealing maximum strain values of approximately 0.2.

In the simulation process, the mesh employed is based on the initial mesh used for DIC analyses. However, the crystal plasticity law required for the finite element code operates in three dimensions (3D). A 2D mesh is extruded perpendicular to the observed surface to address this, effectively creating a 3D microstructure representation. This approach is chosen for its ability to provide a relatively realistic simulation of the underlying volume of the experimental microstructure, which is more accurate compared to alternative methods like Voronoi tessellations.

It's important to note that the thickness of the extruded mesh in the perpendicular direction is chosen to match the characteristic length of the microstructure. This choice is based on the observation that the mesh thickness has minimal influence on the pattern of strain localization. Therefore, by extruding the mesh to a distance equal to its characteristic length, the simulation captures the behavior of the microstructure realistically. Crystal plasticity theory accounts for the anisotropic behavior of indi-
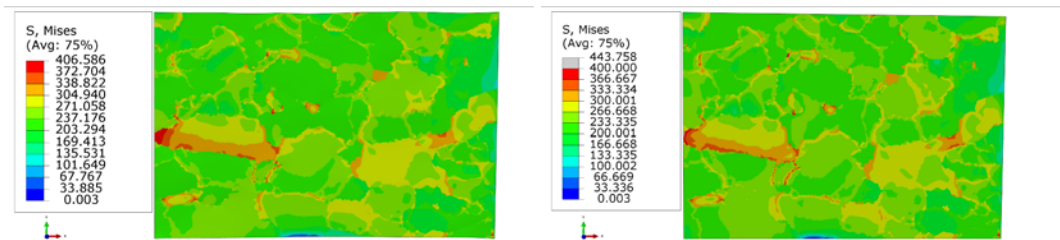
Figure 4.13: Uniaxial Experiment-1 von Mises Stress (MPa) values of microstructure for UMAT (**left**) and VUMAT CPFEM (**right**) analyses

vidual grains based on their crystallographic orientation. This enables the prediction of non-uniform stress and strain distributions, offering insights into the influence of deformation mechanisms on localized deformation and failure.

Figures 4.13 and 4.14 illustrate the stress distribution within the microstructure of uniaxially loaded experiments, as determined through implicit and explicit algorithmic

106

approaches. Remarkably, the results from these two methods exhibit good agreement.

Stress concentrations are frequently observed at grain boundaries, which can lead to various effects. In some cases, these stress concentrations trigger the activation of slip bands within the same grain, causing localized plastic deformation. Alternatively, stress concentration at grain boundaries can facilitate the slip transfer between neighboring grains, inducing plastic deformation in those adjacent grains. Consequently, the most significant stress localization often occurs at the interfaces between different grains within the microstructure. This phenomenon has profound implications for material behavior and can significantly influence various mechanical properties.
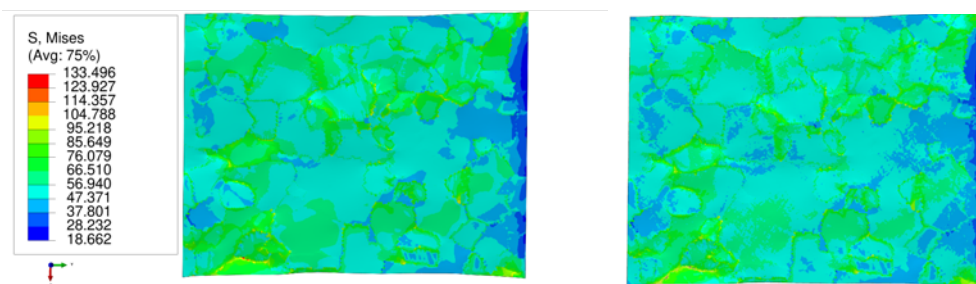
Figure 4.14: Uniaxial Experiment-2 von Mises Stress (MPa) values of microstructure for UMAT (**left**) and VUMAT CPFEM (**right**) analyses
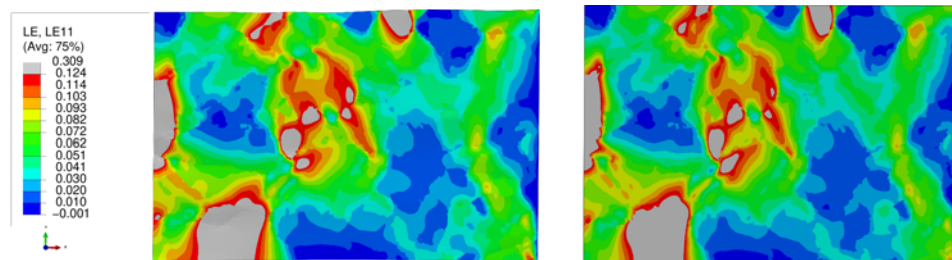
Figure 4.15: Uniaxial Experiment-1 Strain values of microstructure for UMAT (**left**) and VUMAT CPFEM (**right**) analyses

Strain localization is a widespread phenomenon observed across various loading conditions, including uniaxial and multiaxial loading, monotonic and cyclic loading, and even high-speed deformation scenarios. It occurs in diverse materials, including ductile single crystals, polycrystalline materials with different grain sizes (including nanocrystalline materials), and metallic glasses. Strain localization can manifest at

various length scales, ranging from macroscopic to mesoscale and microscale. These localizations typically take two primary forms, stationary and propagative, arising from the breakdown of uniform deformation and closely associated with non-uniform deformation patterns at the dislocation scale [166].

Figures 4.15 and 4.16 depict the phenomenon of strain localization in two distinct microstructures. Deformation is relatively uniform and low in the microstructure, characterized by grains oriented along (101) directions. However, grains with (101) orientations exhibit significant variations in deformation under uniaxial tension, with some grains accumulating substantial strain. These observations align with theoretical predictions indicating that (101) orientations are more resistant to deformation [167, 168]. Under uniaxial tension, strain tends to localize near the grain boundaries adjacent to the (012) oriented grain, with additional concentration within the grain interior. This grain possesses a (001) orientation, which is not conducive to slip in face-centered cubic materials. The explicit (VUMAT) and implicit (UMAT) results demonstrate agreement, indicating similar strain values. This study's findings offer valuable insights into the complex behavior of strain localization, its dependence on crystallographic orientations, and the compatibility of numerical simulations with experimental observations.
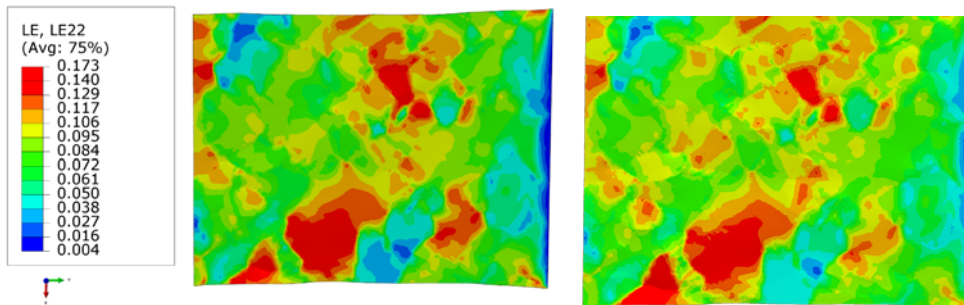
Figure 4.16: Uniaxial Experiment-2 Strain values of microstructure for UMAT (**left**) and VUMAT CPFEM (**right**) analyses

Figure 4.17 and Figure 4.18 compare experimental DIC results and predicted strain localization from CPFEM models. Initially, the modeling results demonstrate reasonable agreement in capturing the trend of strain localization observed in both the microstructure experiment and the CPFEM predictions. However, notable differences exist between the DIC results and CPFEM predictions. CPFEM predictions exhibit
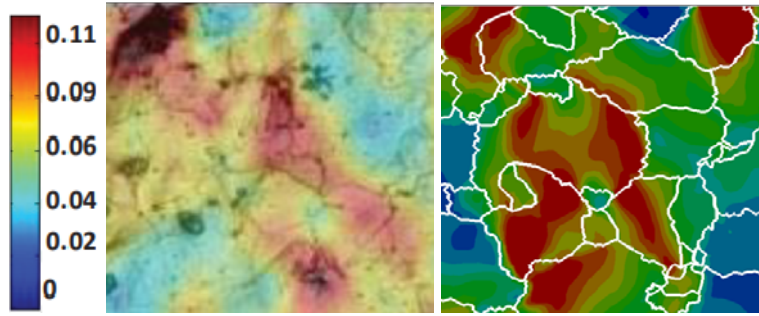
Figure 4.17: Uniaxial Experiment-1 DIC results (**left**) and CPFEM predicted results for VUMAT CPFEM (**right**) analyses

more pronounced strain localization in certain zones than the DIC results, particularly in regions with the highest localization. It's essential to acknowledge that establishing a one-to-one correspondence between experiments and simulations is challenging. Various factors contribute to the observed differences. One significant reason is the potential development of sub-grains in specific regions, which are not accounted for in the simulations. The methodology employed in this study primarily focuses on surface and near-surface behavior, neglecting finer-scale microstructural features below the surface that could influence strain localization. These findings underscore the complexity of modeling strain localization and highlight the approach's limitations in capturing all microstructural intricacies. While the initial results are promising, further refinements and adjustments in the modeling approach may be necessary to achieve closer alignment with experimental observations.
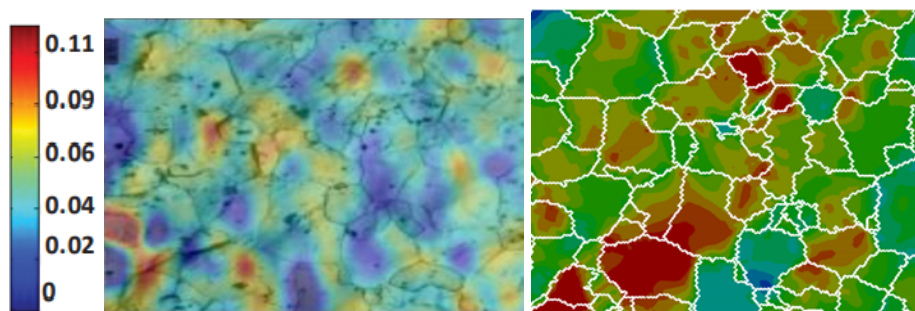
Figure 4.18: Uniaxial Experiment-2 DIC results (**left**) and CPFEM predicted results for VUMAT CPFEM (**right**) analyses

Choosing appropriate experimental boundary conditions is crucial for accurately capturing substrate effects and obtaining a valid representation of strain patterns in nu-

merical simulations ([143]). Realistic boundary conditions are essential to ensure that the simulated behavior of the material closely resembles its actual response, thereby enhancing the alignment between crystal plasticity-based numerical predictions and observed strain measurements obtained through techniques like DIC. To achieve this enhanced realism, a model of the test sample is constructed, considering the actual boundary conditions of the experimental setup. The microstructure model is positioned within the test sample, assuming that the region under investigation within the experimental conditions is aligned with the test sample's middle. Figure 4.19 compares the von Mises stress distribution of the specimen with that of the microstructure as modeled. Upon examination of the two different applied boundary conditions, differences in stress distributions become evident. In the hybrid-modeled microstructure, which considers the actual boundary conditions, more stress accumulation is observed at the grain boundaries compared to the simplified RVE model with tension boundary conditions. This disparity underscores the impact of realistic boundary conditions on stress distribution predictions. The hybrid approach, which incorporates the experimental setup and associated boundary conditions, accurately represents the material's stress and strain patterns. This enhanced modeling approach is particularly crucial when investigating strain localization and deformation behavior within complex microstructures subjected to experimental loading conditions.

A comparison of experimental strain measurements with results obtained from the hybrid numerical simulation model based on crystal plasticity reveals good agreement for most grains regarding strain patterns. The hybrid model, which considers realistic boundary conditions, provides a more accurate representation of the experimental setup, enabling it to capture strain patterns observed in most grains with similar surface grain morphology conditions. However, discrepancies are observed in some instances, particularly near grain boundaries. In certain cases, the hybrid model's predictions may not accurately capture strain localization in some grains, grain boundaries, or triple junction points. Several factors could contribute to these discrepancies, such as complex deformation interactions near grain boundaries, the presence of dislocation structures, and the influence of microstructural features not explicitly considered in the model. When comparing the results of the hybrid model to those of the simplified RVE model with the DIC experiment (Figure 4.20), it becomes evident that excessive strain localizations observed in the RVE model are re-
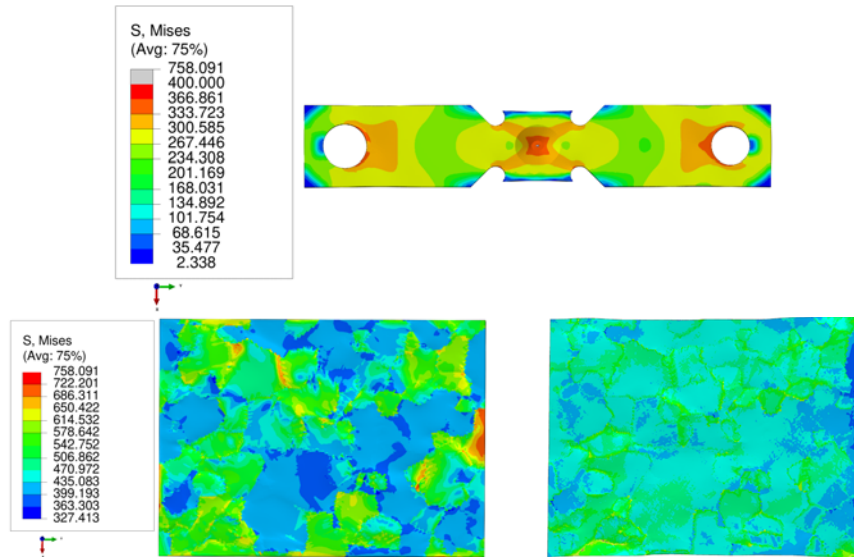
Figure 4.19: Uniaxial Experiment-2 hybrid model von Mises Stress values of VU-MAT CPFEM analyses (**left**) and tension boundary condition result (**right**)

duced in intensity in the hybrid model. This improvement suggests a closer alignment with results obtained from the DIC test, indicating that incorporating more realistic boundary conditions and experimental setup information enhances the accuracy of crystal plasticity-based numerical simulations, particularly in capturing strain localization phenomena.

4.3.3 Conclusion

Under uniaxial tension, strain localization manifests at grain boundaries and within grain interiors. Grains oriented along (012) directions are commonly found adjacent to these localized regions, accumulating significantly higher strain values up to three times more than the average. This observation aligns with the understanding that specific crystallographic orientations are predisposed to deformation localization due to their compatibility with slip systems. Importantly, CPFEM allows for predicting how strain paths influence localization behavior, offering valuable insights for assessing material formability. The comparison between experimental strain measurements and numerical simulation results from the hybrid model (considering the same surface grain morphology conditions) reveals strong agreement for individual grains. This
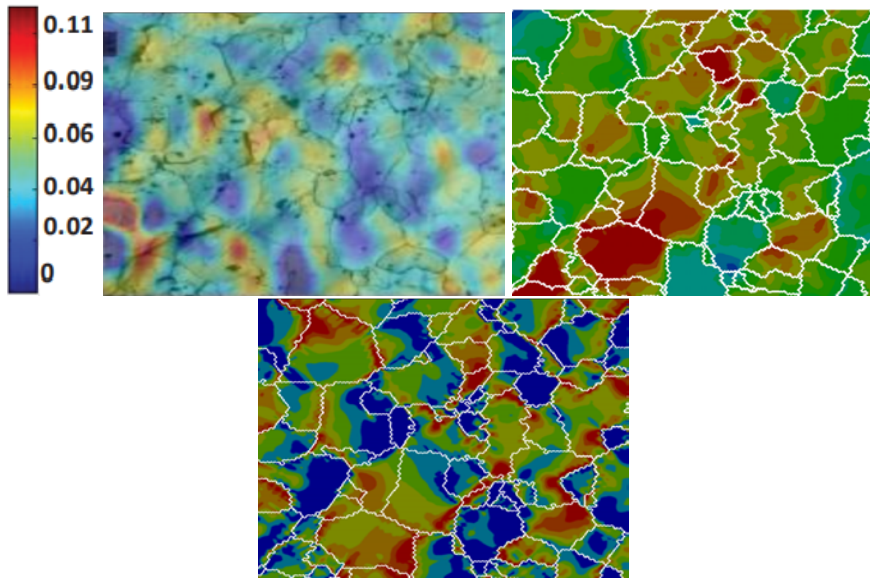
Figure 4.20: Uniaxial Experiment-2 hybrid model (**bottom**) and microstructural (**right**) model CPFEM predicted results for VUMAT CPFEM analyses vs. DIC experiment results (**left**)

highlights the importance of employing realistic experimental boundary conditions when validating CPFEM predictions against techniques like DIC. The consistency between experimental data and simulation results demonstrates the hybrid model's effectiveness in capturing the complex phenomenon of strain localization under varying conditions, including strain path dependence. In conclusion, integrating experimental characterization, crystal plasticity modeling, and realistic boundary conditions offers valuable insights into the micro-scale deformation behavior of Aluminum 6061-T6. Both implicit (UMAT) and developed explicit (VUMAT) crystal plasticity algorithms yield consistent numerical results, facilitating the understanding of strain localization, its sensitivity to strain paths, and its interaction with specific crystallographic orientations. The alignment between experimental and simulated results underscores CPFEM's potential for predicting strain localization and its dependence on various factors, thereby contributing to assessing material behavior and formability. However, it's essential to acknowledge that even with such improvements, there may still be limitations in predicting strain localization in all scenarios due to the complex and multifaceted nature of the phenomenon.

CHAPTER 5

INVESTIGATION OF NON-LINEAR TWIST EXTRUSION WITH EXPLICIT FINITE ELEMENT METHOD USING CRYSTAL PLASTICITY

5.1 Introduction

In light of material science and technology advancements, reliable experimental data on microstructural plasticity have become increasingly accessible. These data are crucial for comprehensive research into metal-forming processes, understanding local phenomena, and identifying macroscopic models. In industrial manufacturing, predicting material mechanical properties throughout the material processing phase demands improved predictive and physically-based models to influence processing. The influence of texture and anisotropy on the mechanical properties of products is a key area of investigation. Copper (Cu) has traditionally served as the primary material for thermal management and electrical conduction across diverse industrial fields owing to its superb thermal and electrical conductivity. Refining the grain size leads to a notable enhancement in hardness and mechanical characteristics ([169]). Comprehending the material's behavior throughout various processing stages facilitates the customization of mechanical properties and the creation of innovative materials adaptable for diverse applications.

Dynamic effects inherently influence the behavior of materials undergoing deformation within metal-forming conditions. Implicit finite element (FE) methods may encounter numerical challenges when simulating highly nonlinear, discontinuous, and rapidly evolving dynamic processes ([170]). The iterative nature of implicit methods can lead to convergence difficulties in analyses involving materials with pronounced nonlinear behaviors, such as the crystal plasticity (CP) constitutive models ([171]).

113

Explicit methods, on the other hand, are equipped with robust contact algorithms that simplify the resolution of dynamic effects like frictional contact and other dynamic phenomena associated with the process. This study developed a novel crystal plasticity algorithm, considering the rate-dependent behavior, to be employed in conjunction with the explicit solver of the Abaqus finite element software.

In this study, using the explicit crystal plasticity finite element method (CPFEM), which is developed in Chapter 4, the impact of dynamic friction coefficients on texture evolution following the NLTE process is meticulously investigated, and the results are compared with experimental findings to ascertain the model's accuracy and reliability. This work enhances our understanding of the NLTE process, its influence on texture evolution, and its alignment with experimental observations. The single copper crystal is produced by using the Bridgman method. The initial orientation of a single copper crystal is determined in electron backscatter diffraction (EBSD) experiments. The texture determined by the EBSD experiment is used in CPFEM analysis. The texture evolution of a single copper crystal specimen following the NLTE process is simulated and compared with the experimental results.

5.2   Finite Element Model Definition

NLTE 3D mold model inner extrusion surfaces are extracted from the geometry and converted into a 2D surface model. This conversion is done to reduce analysis time and improve the mesh quality of the mold model (Fig. 5.1). The mold model and punch are treated as rigid bodies with a $\rho = 7800 kgm^{-3}$ density. Encastre boundary conditions (u1=u2=u3=R1=R2=R3=0) are applied to the rigid body reference point (center of mass) of the mold geometry, and velocity boundary conditions are applied to the rigid body reference point of the punch geometry.

The cylindrical sample has a diameter of 10 mm and a length of 20 mm. To mitigate distortion issues, we meshed the sample using 900 linear hexahedral C3D8R elements (Table 5.1), considering the dilatational wave speed and the deformation speed ratio. The initial Euler Angle orientations of the sample are detailed in Table 5.2.
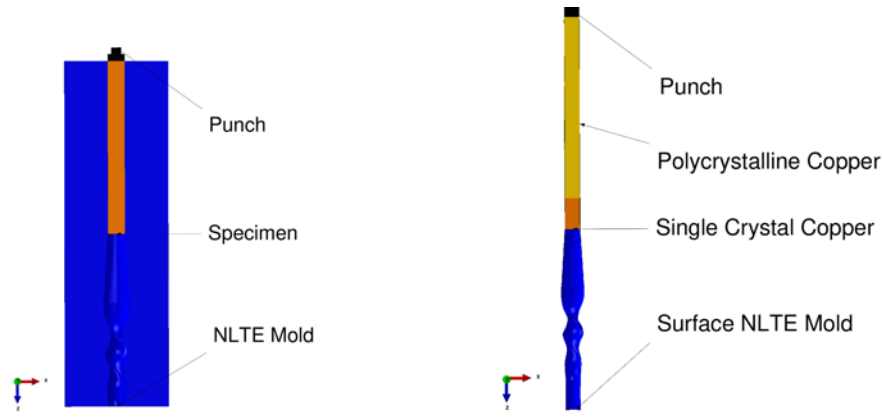
Figure 5.1: FEA model of NLTE process

A velocity boundary condition is applied to the rigid punch from its reference point, while motion is constrained by slot boundary conditions with constraints of $u_2 = u_1 = R_1 = R_2 = R_3 = 0$. The rigid punch is meshed using linear hexahedral C3D8R elements. We apply explicit general contact interaction properties and use a tangential contact algorithm for the explicit CPFEM analyses.

The simulations are conducted for three different friction coefficients: frictionless ($\mu = 0$), $\mu = 0.01$, and $\mu = 0.05$ ([172]). This investigation aims to analyze the impact of the friction coefficient on the initial orientation distribution after the NLTE process.
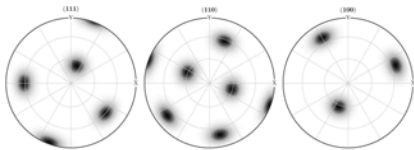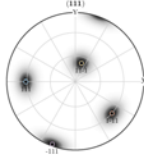
A mass scale algorithm with a quantity of four is applied to the entire model to ensure robust step increments in the NLTE explicit CPFEM simulations. A back pressure of 200 MPa is applied to the bottom surface area of the samples, opposing the extrusion direction, to maintain the billet's circular shape ([99]). Additionally, a gravity load is applied to the entire model.

Tie interaction properties are assigned to the surfaces between the polycrystalline copper and single-crystal copper models. The polycrystalline copper is modeled using von Mises Plasticity with the stress-strain curve values. (Fig. 5.2).

Table 5.1: FEM mesh model parameters of simulated NLTE process.

Model	Element Type	Element Family	Number of Elements	Model Type
NLTE Mold	Linear Triangular-S3R	2D Stress	60707	Rigid
NLTE Punch	Explicit-Hexahedral-C3D8R	3D Stress	864	Rigid
NLTE Specimen	Explicit-Hexahedral-C3D8R	3D Stress	900	Deformable (CP)

Table 5.2: Initial orientations and pole figure of single crystal copper specimen

Sample Name	Initial Orientation Bunge Euler Angles (φ_1 ϕ φ_2) and Pole Figures of Initial Orientation	Distribution of [111] symmetry planes on 111 pole figures
Single copper crystal	(110.2) (67.3) (203.5)	

5.2.1 Calibration of Crystal Plasticity Model

This section determines the material parameters for single-crystal copper through a homogenization approach. Due to inconsistent experimental data available for tensile tests on single crystal copper in the literature, stress-strain data from polycrystalline copper are used to calibrate the mechanical properties of single crystal copper, as illustrated in Figure 5.3. To achieve this, tensile boundary conditions are applied to a representative volume element (RVE) cube comprising 500 grains with random

116
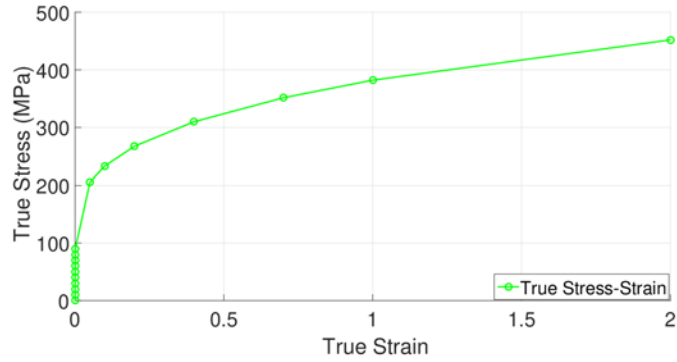
Figure 5.2: Stress-strain curve of polycrystalline copper material ([90]).

orientations, as depicted in Figure 5.4. The boundary conditions imposed on the RVE under tensile loading are shown in Figure 5.5. Table 5.3 shows the parameters of a single copper crystal. The homogenization procedure is comprehensively explained in Chapter 3.
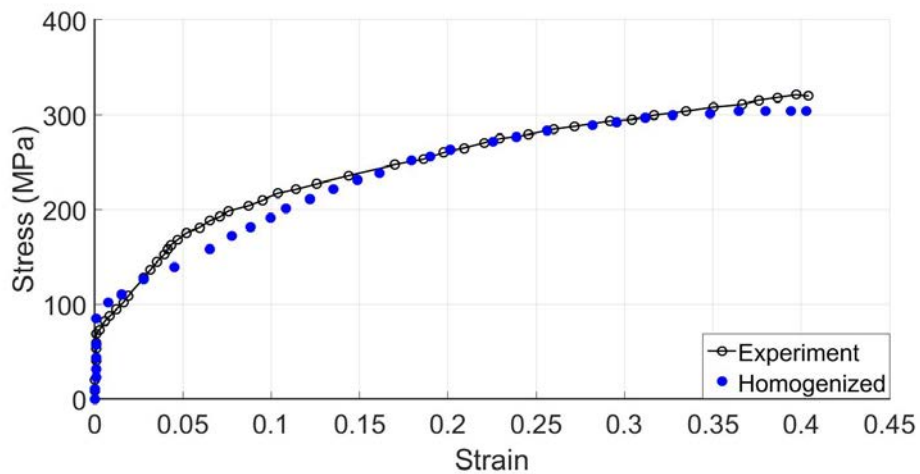
Figure 5.3: Homogenized curve vs. experiment

Table 5.3: Single crystal copper VUMAT model parameters

C_{11}	C_{12}	C_{44}	τ_{cr}	h_0
168000 MPa	121400 MPa	75400 MPa	25 MPa	147 MPa
g_{sat}	$\dot{\gamma}_0$	m	q	a
143 MPa	0.001 s^{-1}	17	1.4	1.75

117
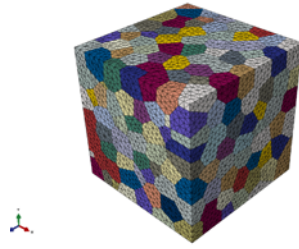
Figure 5.4: 500 grain representative volume element
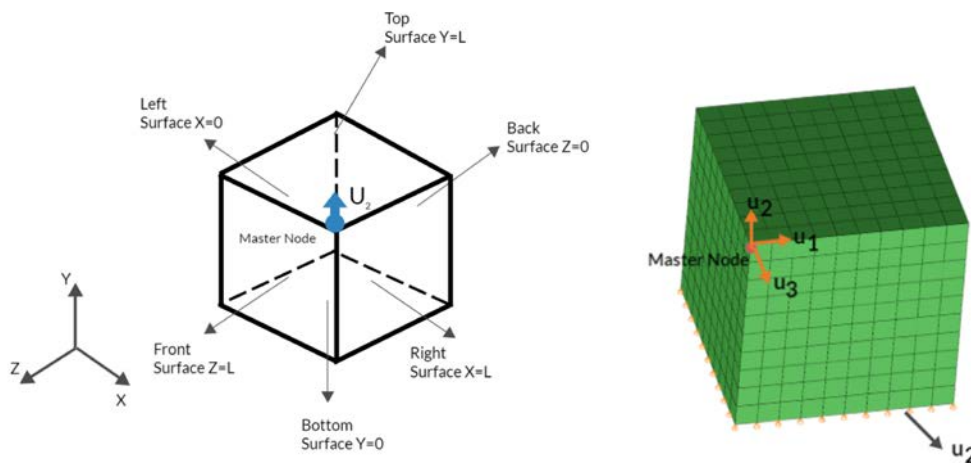
Figure 5.5: Applied boundary conditions

5.3 Experimental Procedure

The Bridgman method, designed for controlled crystal growth, is employed to produce single copper crystals. The core principle behind crystal growth using the Bridgman technique involves directional solidification, which is accomplished by transferring molten material (melt) from a hot region to a colder region within a furnace. A seed crystal is positioned at the bottom of the crucible to ensure specific crystallographic orientations.

The experimental procedure begins by placing the crucible containing the polycrystalline charge and the seed crystal into the growth chamber. Subsequently, the chamber is evacuated using a vacuum pump and refilled with an inert gas, gradually raising the furnace temperature. Throughout this stage, the melt inside the crucible undergoes homogenization, driven by natural convection and diffusion within the melt it-

self, eliminating the need for forced convection.

Fig. 5.6 presents a schematic representation of the Bridgman method for single crystal production. In this method, the furnace is heated to a temperature of 1453 K, and the pulling speed, which determines how quickly the furnace is moved, is set at approximately 10 mm/h. This carefully controlled process enables the growth of single-crystal materials with the desired properties and orientations.
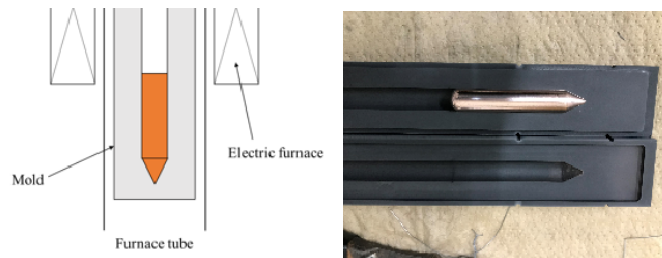
Figure 5.6: The schematic representation of the production of a single crystal with the Bridgman method (**left**) and produced single copper crystal sample (**right**).

The Markov-offline technique uses single copper crystals and a polycrystalline copper sample to determine their orientations. An NLTE experiment is conducted at room temperature with a punch speed of 1 mm/s. The experimental setup and the final state of the NLTE process are illustrated in Fig. 5.7. This technique enables the investigation and analysis of the material behavior and orientation changes resulting from the NLTE process.

The samples underwent a series of preparation steps before the Electron Backscatter Diffraction (EBSD) experiments. Initially, the samples were cut using a wire cutter and then progressively refined using fine grades of emery paper (400, 600, 800, 1000, 2400, 4200). Subsequently, they were polished using a polishing wheel with diamond paste of particle sizes 5 μm, 3 μm, and 1.5 μm to achieve a mirror-like finish. The final step involved etching the samples with an appropriate etchant. These prepared samples were then subjected to Electron Backscatter Diffraction (EBSD) experiments. The experimental procedures are summarized and depicted in Fig. 5.8. This series of
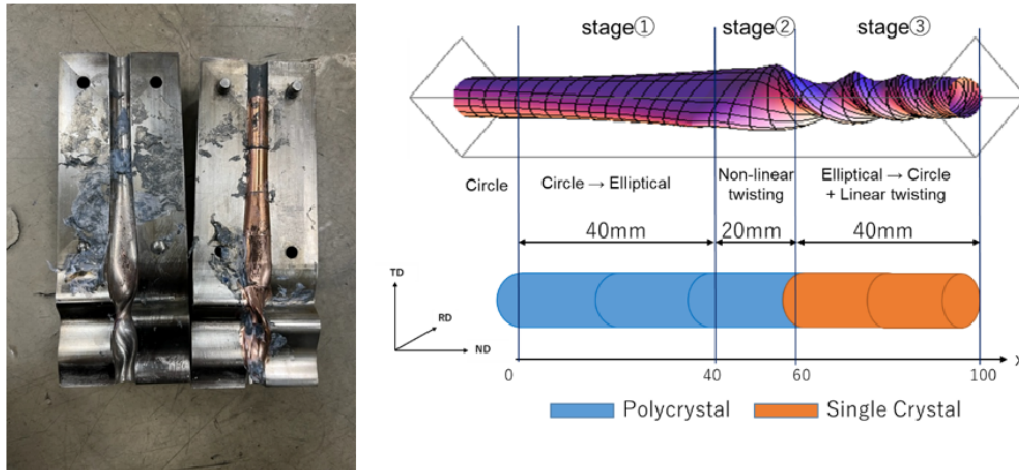
Figure 5.7: Picture of experimental NLTE process (**left**) and experiment set up (**right**).

steps ensured the preparation of samples suitable for detailed microstructural analysis.
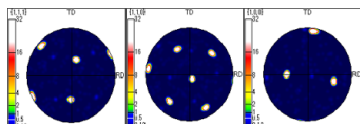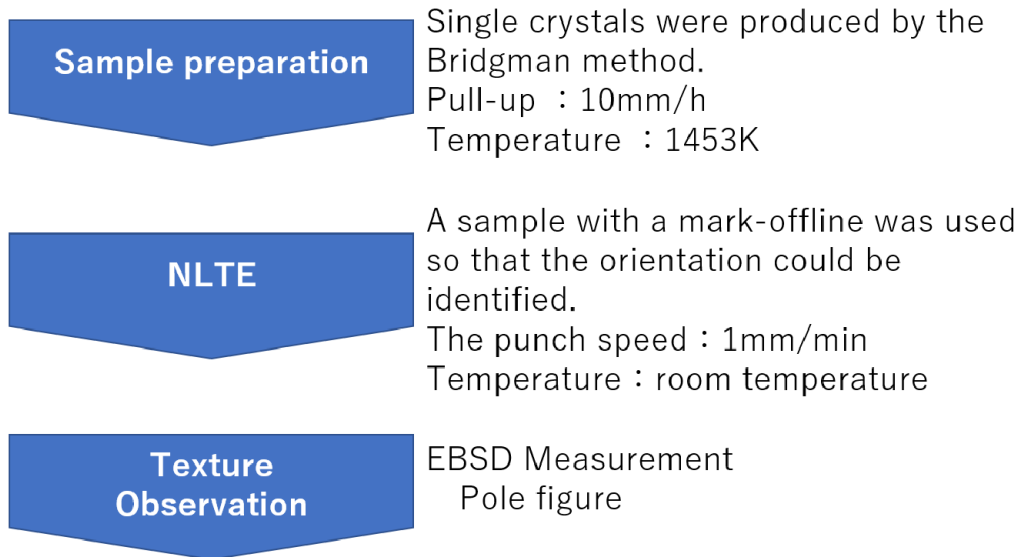
Figure 5.8: The schematic representation of experimental procedures

5.4 Results and Discussion

The simulation of the NLTE process for the single copper crystal specimen is performed using the explicit crystal plasticity model discussed earlier. The predicted results obtained through CPFEM are compared to the experimental outcomes for specimens with the same initial orientation. However, before delving into comparing results, it's essential to determine whether the explicit analysis solution is sufficiently close to quasi-static conditions to be considered acceptable. Stability is crucial in explicit dynamic analysis, especially for quasi-static metal forming processes. Time and mass scaling are introduced to reduce the computational time required for solving. However, it is imperative to exercise caution when applying these factors, as they can compromise solution accuracy. Extremely high punch speeds can yield unrealistic results. When the loading rate is increased to model a quasi-static problem efficiently, the material strain rates calculated in the simulation become artificially high due to the scaling factor applied to the loading rate. This can lead to erroneous solutions, particularly when considering strain rate sensitivity. Applying mass scaling to the finite element model can help alleviate issues related to computational time. This study uses a mass scaling factor of four to the entire model in explicit CPFEM analyses for all friction conditions. Energy balance equations can be employed to assess whether a simulation is yielding an appropriate quasi-static response. One common approach is to compare kinetic energy history with internal energy, which is widely accepted in the literature. In metal forming analyses, a significant portion of internal energy arises from plastic deformation. For an acceptable quasi-static solution, the kinetic energy should represent only a small fraction of the internal energy, typically no more than $1 - 5\%$ ([149]). The evolution of internal and kinetic energy concerning analysis time is illustrated in Fig. 5.9 for three different friction coefficients. Upon comparing Fig. 5.9, it becomes evident that the kinetic energy remains a small fraction (less than 1%) of the internal energy throughout the analysis, except at the beginning. This observation meets the criterion that kinetic energy should be significantly smaller than internal energy, indicating an acceptable quasi-static solution. Kinetic energy, much smaller than internal energy, holds for both punch speeds of 25 mm/s and 50 mm/s. Figure 5.10 illustrates this change by displaying the variations in kinetic energy (KE), internal energy (IE), and plastic dissipation energy (PD). It is worth noting that the

121

model's total energy (Etotal) remains relatively constant throughout the simulation. The completion times for the analyses are provided in Table 5.4, considering the variation in punch speeds. These considerations ensure that the explicit dynamic analysis solution is stable and quasi-static, providing a reliable basis for comparing CPFEM predictions with experimental results.
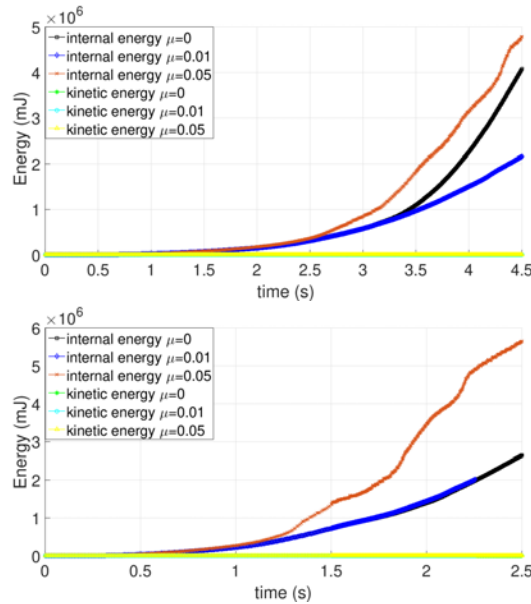
Figure 5.9: Comparison of internal and kinetic energies according to the punch speed 25 mm/s (**top**) and 50 mm/s (**bottom**)
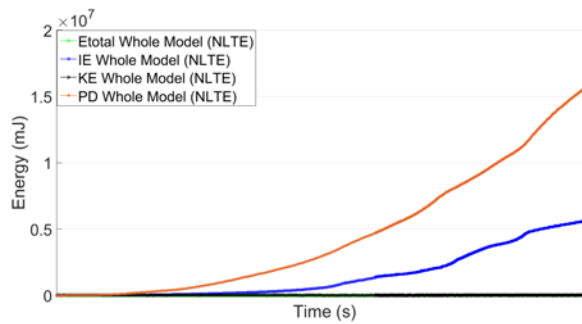
Figure 5.10: Comparison of whole model energies throughout the NLTE process

The simulation results unveil distinctive behaviors for NLTE processes with three different friction coefficients, although they all exhibit similar overall trends in NLTE processing time. Figure 5.11 illustrates the variation of punch force normalized by the cross-sectional area of the specimen, providing a clearer understanding of these

Table 5.4: NLTE processes analysis time concerning different punch speeds.

Model	Punch speed	CPU Time	Approximate analysis completion in days
VUMAT CP	25 mm/s	400 h:13 min:50 s	17 days
VUMAT CP	50 mm/s	186 h:48 min:00 s	8 days
VUMAT CP	300 mm/s	33 h:30 min:26 s	2 days

behaviors.

The analysis of the punch force evolution reveals a distinct pattern. The load is initially increased as the workpiece head enters the twist zone. Subsequently, the workpiece advances through the twist zone while maintaining a steady increase in force. This force continues to rise consistently until the conclusion of the process. These observations align with the major events discussed in a previous report ([99]).

Furthermore, the punch pressure values increase with higher friction coefficients. Specifically, there is an approximate 20% difference in the reaction forces between the frictionless state ($\mu = 0$) and $\mu = 0.01$. This difference becomes more pronounced when the friction coefficient is elevated to $\mu = 0.05$, resulting in nearly five times higher punch pressure values throughout the process. These variations underscore the substantial impact of friction on the NLTE process's overall behavior. The evolution of punch force during the NLTE process demonstrates consistent patterns across different friction coefficients. The presence of friction influences the specific behavior. The friction coefficient directly impacts the punch pressure values, resulting in significant variations in reaction forces among different friction conditions.

A comparison of von Mises stress contours in the longitudinal plane and sectional views of the workpieces for two friction conditions is shown in Figs. 5.12 and 5.13. These figures provide insight into the distribution and magnitude of Von Mises stress within the workpiece.

In the transverse section, the von Mises stress exhibits a pattern of increasing values
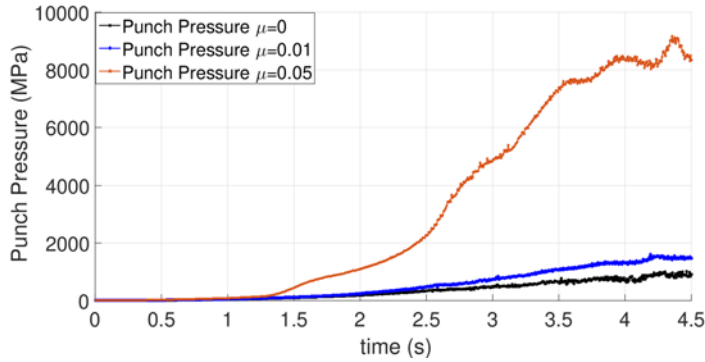
Figure 5.11: Comparison of punch pressure with respect to friction coefficients (μ=0, μ=0.01, μ=0.05)
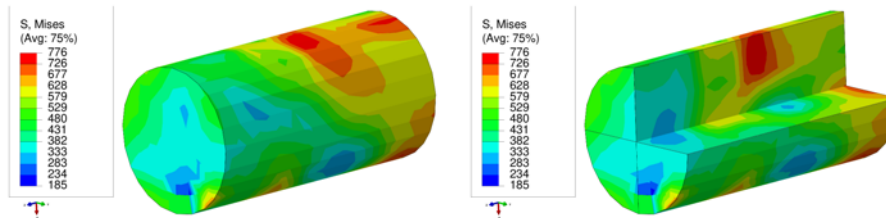
Figure 5.12: Von Mises Stress (MPa) distribution on undeformed view (**left**) and section view (**right**) for μ=0.01 friction coefficient

from the center of the billet toward the peripheral regions. In the longitudinal plane, the highest stress concentrations are observed after the completion of the NLTE processes. The frictional conditions at the contact surfaces between the mold and the workpiece notably influence stress distribution.

The contours of von Mises stress in the longitudinal plane, and the sectional views of the workpieces provide valuable insights into stress distribution and accumulation. The friction coefficient strongly influences stress patterns, with higher friction values leading to increased stress concentrations at contact surfaces and lower friction values promoting more uniform stress distribution in the specimen's central region.

Accumulated plastic strain is a critical factor in forming processes, as it represents the sum of plastic strain increments and plays a role in preventing unstable fractures or plastic collapse. Excessive accumulated plastic strain can reduce the ductility and toughness of materials. The rate of accumulated plastic strain can be linked to the rate
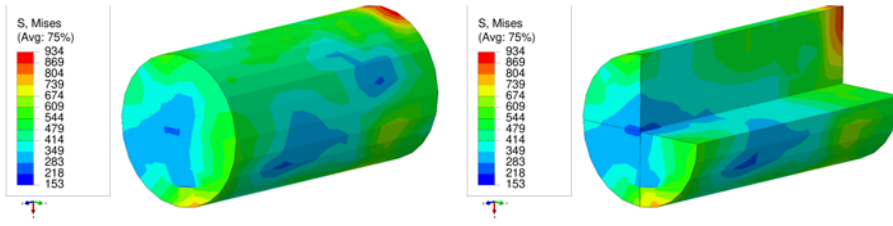
Figure 5.13: Von Mises Stress (MPa) distribution on undeformed view (**left**) and section view (**right**) for μ=0.05 friction coefficient
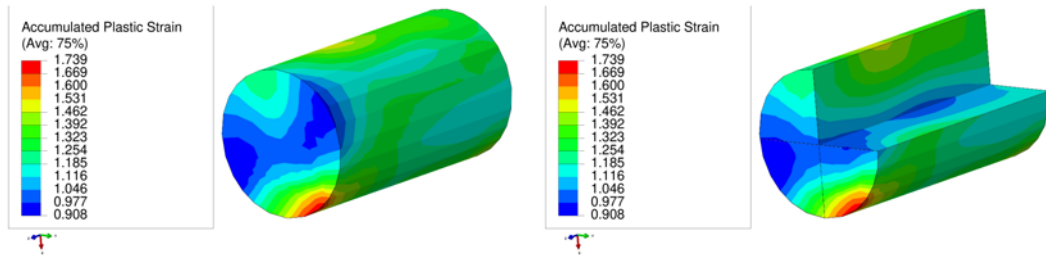
Figure 5.14: Accumulated plastic strain distribution on undeformed view (**left**) and section view (**right**) for μ=0.01 friction coefficient

of plastic deformation using the formula $\dot{\epsilon}^{ap} = \sqrt{\frac{2}{3}\left(\boldsymbol{D^p} : \boldsymbol{D^p}\right)}$, where $\boldsymbol{D^p}$ represents the rate of plastic deformation tensor ([173]).

The distribution of accumulated plastic strain within the workpiece is depicted in Fig.5.14 and Fig.5.15, along with sectional views. Typically, the area around the axis of the workpiece displays an average magnitude of accumulated plastic strain. Notably, the highest accumulation of plastic strain occurs on the contact surfaces between the mold and the workpiece. Moreover, a uniform distribution of accumulated plastic strain is observed from the center toward the periphery of the workpiece.

Comparing the two friction coefficient values, variations in the distribution of accumulated plastic strain become apparent. In particular, as the friction coefficient increases from $\mu = 0.01$ to $\mu = 0.05$, there is a noticeable increase in the amount of accumulated plastic strain. This indicates that the selection of the friction coefficient substantially impacts the development of plastic strain within the workpiece, with higher friction coefficients resulting in more significant plastic strain accumulation.

Accumulated plastic strain represents the cumulative effect of plastic deformation

125

within the workpiece, with higher strain accumulation typically observed at contact surfaces and a generally uniform distribution from the center to the periphery. The friction coefficient plays a pivotal role in determining the magnitude and distribution of accumulated plastic strain, with higher friction coefficients leading to higher levels of plastic strain accumulation.
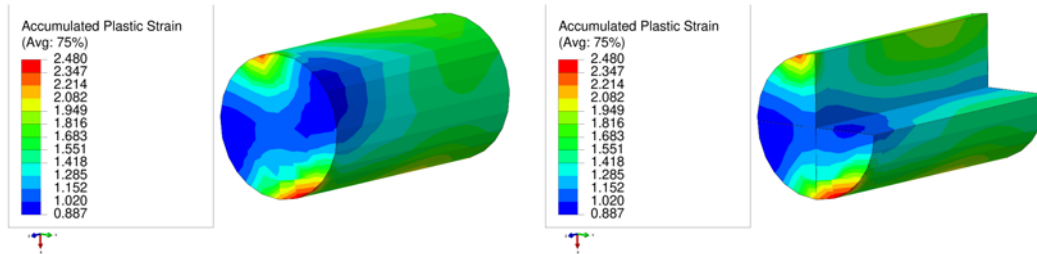
Figure 5.15: Accumulated plastic strain distribution on undeformed view (**left**) and section view (**right**) for μ=0.05 friction coefficient
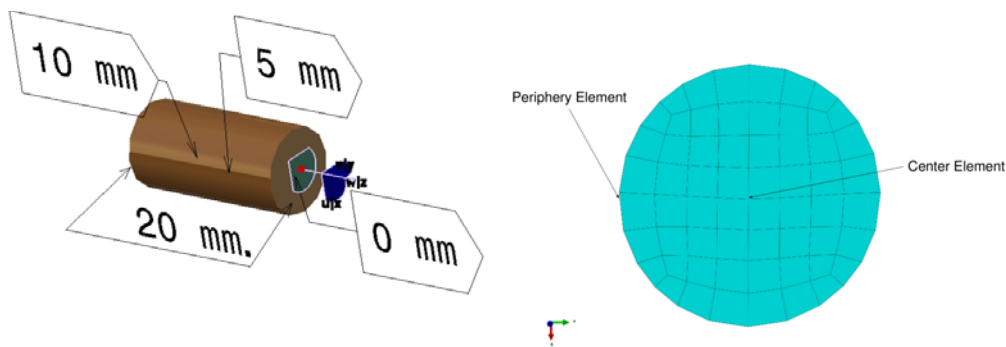
Figure 5.16: Inspection sections (**left**) and elements (**right**) of specimen

The analysis of deformation behavior and texture evolution in the single copper crystal involved examining specific regions and elements of the specimen, as shown in Fig. 5.16. Modifications were made to the mold's channel design in the twist section during the NLTE process to address challenges like strain reversal and rigid body rotation commonly associated with twist extrusion processes.

In situations involving rigid body rotation, the movement of elements can be approximated as pure rotation. This simplification leads to the time derivative of the stretch tensor ($\dot{U}$) being equal to zero ($\dot{U} = 0$). As a result, the magnitude of the time derivative of the stretch tensor should also be zero ($|\dot{U}| = 0$) when rigid body rotation is occurring.

Figure 5.17 displays the norm of the time derivative of the stretch tensor for both center and periphery elements of the specimen, considering different friction coefficients as a function of the process time. As expected under the assumption of rigid body rotation, the analyses conducted during the NLTE process period show values very close to zero for the norm of the time derivative of the stretch tensor. However, it's worth noting that while no strict rigid body rotation was observed in any case, there are instances where values very close to rigid body rotation are observed during specific time intervals. Specifically, these occurrences are observed between 1.5 to 2 seconds and 3 to 4 seconds in the simulations. The NLTE method includes adjustments to the mold's channel design to reduce unwanted effects such as strain reversal and rigid body rotation typically associated with twist extrusion. Although strict, rigid body rotation is not observed in the simulations, there are moments when values closely resembling rigid body rotation occur during specific time intervals within the NLTE process.
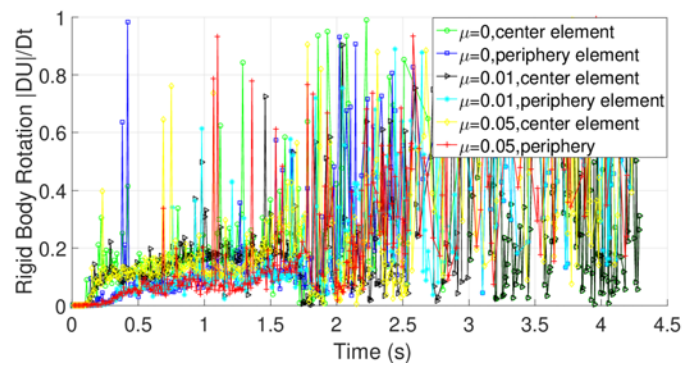
Figure 5.17: Comparison of rigid body rotation of center and periphery elements concerning friction coefficients (μ=0, μ=0.01, μ=0.05)

Twelve 111 slip systems contribute to plastic deformation in face-centered cubic metals like copper. Fig. 5.18 compares the evolution of plastic slip in all twelve slip systems for two different friction coefficients. This analysis covers both center and periphery elements for each slip system family. This analysis aims to investigate the strain reversal behavior of a single copper crystal during its initial pass and identify the most active shear systems. The evolution of plastic slip over the NLTE processing time is depicted in the figure to demonstrate this behavior visually. For both friction coefficients, it is observed that the most active slip system plane and direction for

127

both center and peripheral elements are 111 and <01-1>, respectively. As the friction coefficient increases, there is a corresponding increase in the strain values for all slip system families. Among the twelve slip systems, the least active shear system for the central element was observed to be the 111 plane. Notably, shear strain reversals are observed during the NLTE process time. These reversals are noted in the 11-1 and 111 planes between 3 to 3.5 seconds. The analysis investigates the behavior of shear strain evolution in all twelve 111 slip systems for different friction coefficients. The results reveal the most active slip systems and demonstrate the occurrence of shear strain reversals during specific time intervals in the NLTE process. The orien-
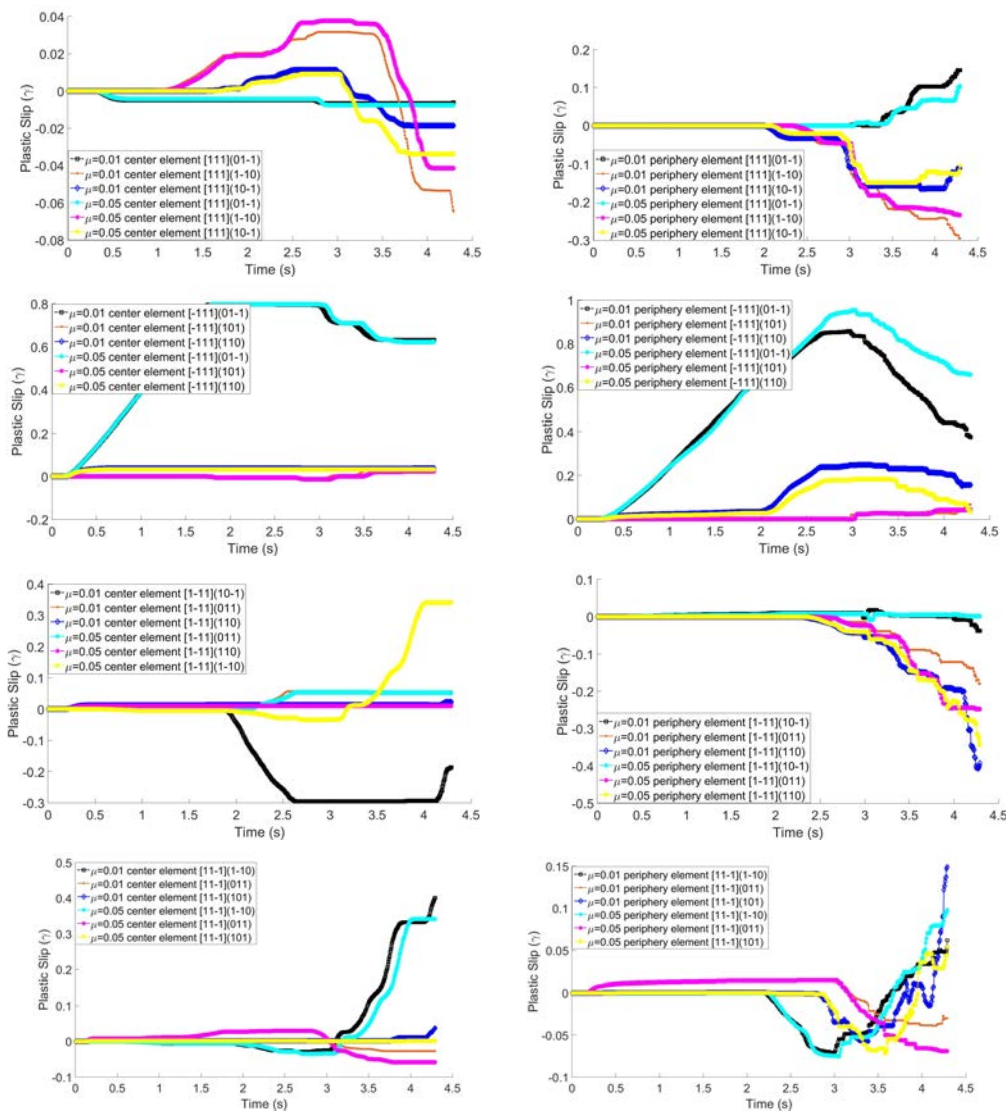
Figure 5.18: Plastic slip evolution through NLTE process time according to center element, periphery element, and friction coefficients.

tation of metallic crystals after plastic deformation is influenced by various factors, including chemical composition, working temperature, initial texture, and the deformation history. However, two dominant factors significantly affect the development of deformation textures: the crystal structure of the metal and the nature of plastic deformation, which includes the deformation mode and its magnitude. In most metals, plastic deformation at room temperature is accommodated by slip or twinning in systems that involve specific crystal planes and directions.

The stacking fault energy (SFE), particularly the specific SFE related to the partial dislocations in a dissociated perfect dislocation, strongly influences the nature of slip in face-centered cubic (FCC) metals and alloys. This energy has a substantial impact on both wire and sheet textures. The stacking fault energy plays a crucial role in determining the predominant mechanisms of plastic deformation. In metals with high SFE, such as aluminum and copper, slip becomes the dominant deformation mode. The resulting rolling texture comprises components like copper, brass, and S textures, each with nearly equal intensities.

During plastic deformation, individual grains in polycrystalline materials undergo fragmentation into regions with different orientations. This fragmentation can arise due to intrinsic grain instability or boundary conditions neighboring grains impose. Grain subdivision holds significant importance for metal-forming processes because it profoundly influences the evolution of microstructure and texture, mechanical properties, and the plastic anisotropy of the material.

Severe plastic deformation (SPD) leads to grain subdivision, which has scientific and technological implications. In scientific research, grain subdivision is studied to understand the behavior of materials under extreme plastic deformation conditions and its impact on properties. On the technological side, SPD-induced grain refinement in the nano-size scale is investigated to achieve bulk metal grain refinement, offering potential improvements in material properties and performance.

Texture in crystalline materials can often be represented by a combination of discrete texture components along with a random background component. In the case of face-centered cubic (FCC) metals, several important texture components play a significant role in shaping the overall texture, including the Cube, Brass, Goss, Copper, and S-texture components (Table.5.5). These main texture components can be characterized using Euler angles and pole figures. Euler angles describe the crystal orientation of a

reference frame. Pole figures are two-dimensional stereographic projections that depict the distribution of pole density concerning pole orientation on a selected crystal plane [hkl]. These main texture components can be used to assess the texture evolution of a single copper specimen after undergoing an NLTE process. For instance, the initial pole figure of the sample can be associated with Shear and Brass texture components (Table.5.6). After undergoing the NLTE process, both experimental and predicted pole figures indicate that the center and periphery sections of the specimen rotate in the same direction. Analyzing the distribution of the 111 planes on 111 pole figures provides a visual representation of how the orientations of the Euler angles have changed in space. The results suggest that reducing the friction coefficient between the mold and the specimen leads to a more minor rotation of the Euler angles for both sections. Conversely, increasing the friction coefficient results in more extensive rotations in orientations for both sections.

Table 5.5: Main texture components for face-centered cubic (FCC) materials ([129])
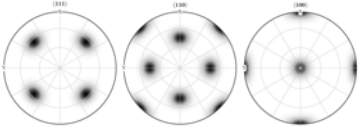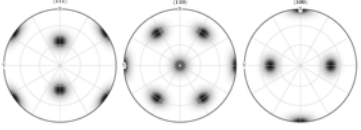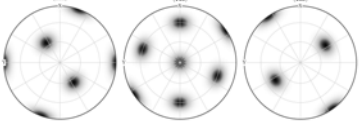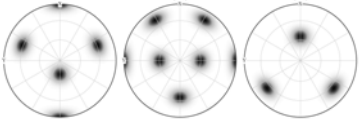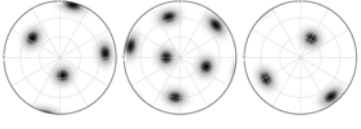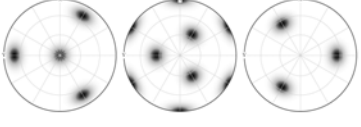
Components Name	Directions	Bunge Euler Angles($\varphi_1 \ \phi \ \varphi_2$)	Pole Figures of Components
Cube	[001]<100>	(0) (0) (0)	
Goss	[011]<100>	(0) (45) (0)	
Brass	[0$\bar{1}$1]<211>	(35) (45) (0)	
Copper	[$\bar{2}$11]<111>	(90) (35) (45)	
S	[12$\bar{3}$]<634>	(60) (32) (65)	
Shear	[111]<110>	(0) (54.74) (45)	

Table 5.6: Experiment and CPFEM results of after NLTE process for one pass final orientations and pole figure of single crystal copper specimen according to the friction coefficients μ=0.01 and μ=0.05
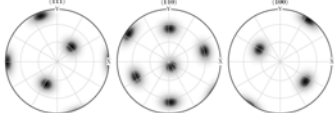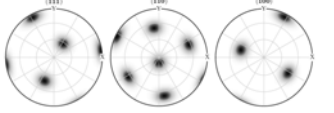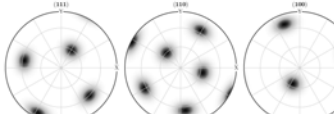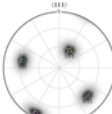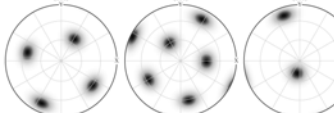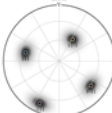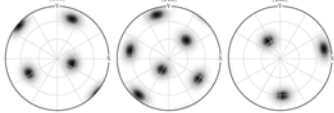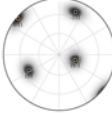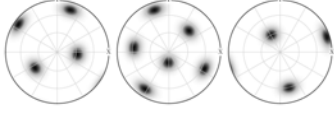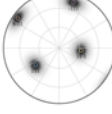
Sample Name	Final orientation represented by Bunge Euler Angles (φ_1 ϕ φ_2) and (111) (110) and (100) pole figures	Distribution of [111] symmetry planes on 111 pole figures
Single copper crystal center section experimental Pole Figure	(145.183) (85.9) (232.031)	
Single copper crystal periphery section experimental Pole Figure	(153.033) (82.3) (229.212)	
Single copper crystal center section predicted Pole Figure μ=0.01	(103.849, 74.0036, 199.886)	
Single copper crystal periphery section predicted Pole Figure μ=0.01	(106.725, 80.8892, 196.131)	
Single copper crystal center section predicted Pole Figure μ=0.05	(101.811,75.6,239.707)	
Single copper crystal periphery section predicted Pole Figure μ=0.05	(107.428,84.0542,240.637)	

Table 5.7: $\varphi_2 = 0^0$, 45^0 and 65^0 sections of ODF showing main texture components of FCC crystals

Sample Name	ODF Figures of FCC Components ($0^0, 45^0, 65^0$)
Brass ODF	
Copper ODF	
Goss ODF	
Cube ODF	
S ODF	
Shear ODF	
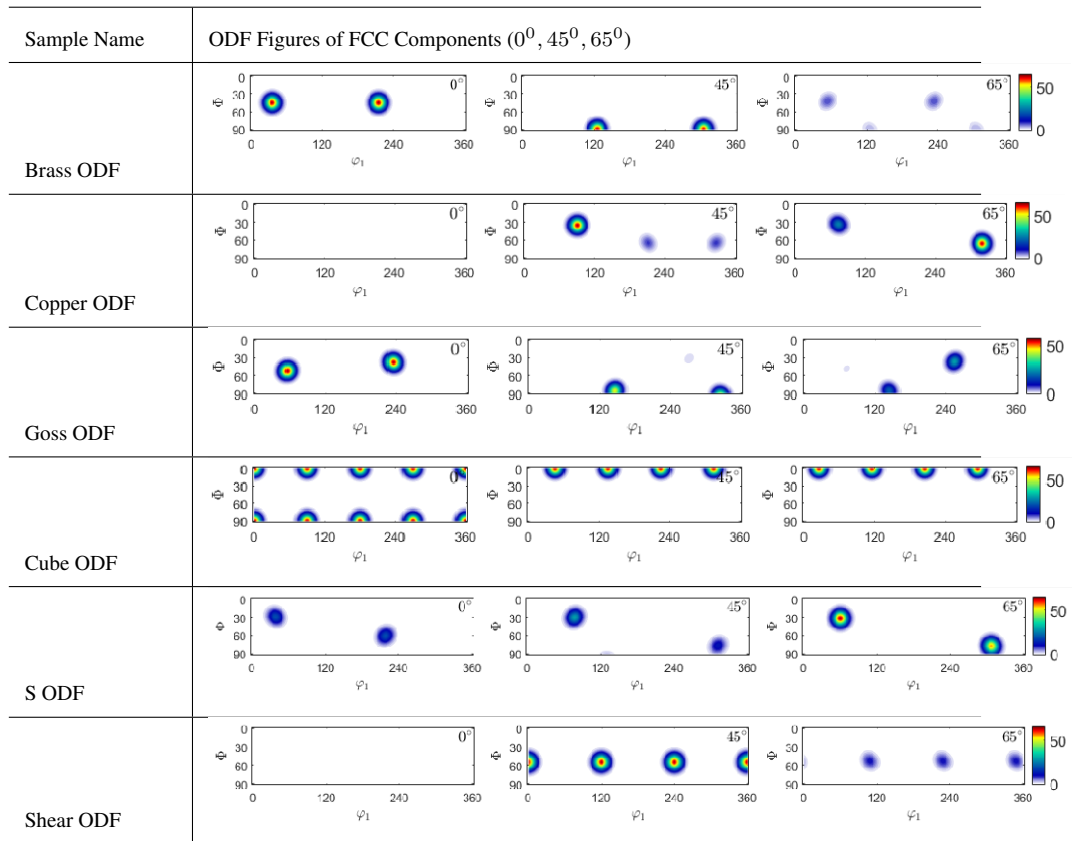
Comparing experimental results with CPFEM predicted outcomes, the final orientation can be characterized as a combination of S-texture and Copper texture after the NLTE process. The intensity of the S-type texture implies that slip was the dominant deformation mode during the NLTE process. In summary, the texture evolution in single copper specimens undergoing the NLTE process can be evaluated using main texture components, and the results reveal insights into the dominant deformation mechanisms.

Pole figures provide valuable insights into the texture of a material, but they have limitations in providing a complete and quantitative description. These limitations can be overcome by using the crystallite orientation distribution function (ODF), a three-dimensional representation describing the frequency of occurrence of particular orientations in an orientation space defined by three Euler angles. These angles represent a sequence of rotations required to align a crystallite's crystallographic axes

with the specimen axes. The ODF encompasses the rotation sets corresponding to all crystallites in the material, providing a more comprehensive description of texture. The comparison of ODFs obtained from the main FCC texture components is shown in Table 5.7. Additionally, Table 5.8 illustrates experimental and CPFEM-predicted Euler angles for the ODF, both before and after the NLTE process, categorized into ODF sections ($\phi_2 = 0^0, 45^0, 65^0$) for a single copper crystal specimen. The texture spectrum from zero to fifty defines the dominance of center and peripheral elements' texture components.

The initial texture of the sample is characterized by Goss, Brass, Shear, and Copper components, which are common rolling textures in FCC metals. These texture components' predicted volume fraction distributions and the corresponding Euler angles are displayed in Fig.5.19 and Table5.8, respectively. The copper texture exhibits the highest intensity among them. After one pass of the NLTE process, both experimental and CPFEM-predicted results indicate a weakening of the copper texture and an enhancement of the S texture. The severe plastic deformation of the copper specimen resulted in a weak Copper Cube texture and reduced orientation density values. This suggests the potential occurrence of dynamic recrystallization. The friction coefficient played a crucial role in the evolution of texture. An increase in friction leads to increased strain and a transition from Goss to Brass textures. More significant deformations result in the formation of Brass and S textures. When comparing different friction coefficients, it is observed that Shear and S textures underwent substantial changes under shear deformation. Higher friction coefficients promote the accumulated plastic strain and activated slip systems during the NLTE process, leading to changes in texture.

In Figure. 5.19, the volume fractions of the main predicted texture components after the NLTE process are displayed, along with quantitative statistics of texture evolution for two different friction coefficients: $\mu = 0.01$ and $\mu = 0.05$. Under $\mu = 0.01$ friction coefficient conditions, the content of Brass and S textures increase from low to medium, as depicted in Fig. 5.19. On the other hand, when the friction coefficient increases to $\mu = 0.05$, the Goss texture is transformed into Brass texture, while the content of the Shear texture decreases. In particular, the content of Brass and Goss textures changes, while the content of Copper and Cube textures shows less significant variations.

134

Table 5.8: Experiment and CPFEM ODF results of after one pass NLTE process for single crystal copper specimen according to the friction coefficients μ=0.01 and μ=0.05

Sample Name	ODF sections of φ_2 =0^0, 45^0 and 65^0 comparing experiments and final orientations
Single copper crystal initial ODF	
Single copper crystal after NLTE process center section experimental ODF	
Single copper crystal after NLTE process periphery section experimental ODF	
Single copper crystal center μ=0.01 predicted ODF	
Single copper crystal periphery μ=0.01 predicted ODF	
Single copper crystal center μ=0.05 predicted ODF	
Single copper crystal periphery μ=0.05 predicted ODF	

Figure 5.19: Main texture components predicted volume fractions after NLTE process according to friction coefficients μ=0.01 (**top**) μ=0.05 (**bottom**)

Notably, the texture components and their contents exhibit marked differences between the $\mu = 0.01$ and $\mu = 0.05$ friction coefficient conditions. The initial shear texture primarily decreases with slip deformation, and its intensity is transformed into S-texture content. It's essential to consider that the ratio of Goss/Brass volume fractions decreases as the friction coefficient increases. This reduction in the Goss/Brass ratio is associated with reduced crack resistance and fracture toughness of the specimen, as discussed in previous research studies ([132]). Furthermore, the main deformation texture transitions from Copper, Goss, and S textures to Brass and S textures with increased strain. These observations align with findings from previous research ([174], [175], [176]). In conclusion, the volume fractions of different texture components and their evolution provide insights into the complex interplay between friction coefficient, strain, and resulting texture transformations in the single copper crystal subjected to the NLTE process.

5.5 Conclusion

In this study, explicit simulations of single-crystal copper workpiece extrusion using NLTE processes with varying friction coefficients are conducted to investigate the impact of the friction coefficient on the NLTE process. The results revealed that the friction coefficient influences factors such as punch force, rigid body rotation of the single-crystal copper specimen, shear strain, and microstructure evolution. Furthermore, texture analysis and examination of the main texture components' contents after the NLTE process indicated that increasing the friction coefficient between the mold and workpiece decreases fracture toughness. Additionally, an increase in friction coefficient leads to higher punch forces, and a more homogeneous plastic strain distribution is observed after one pass of the single crystal copper specimen through the NLTE process. Plastic slip is expected to occur primarily in the specimen's periphery section. In contrast, on the (11-1) slip plane, there is more plastic slip in the specimen's center section. Furthermore, strain reversals mainly occur in this plane through the NLTE process. The study also identifies specific time intervals during the NLTE process (especially around 3 to 3.5 seconds) when the time derivative of stretch values decreases. This decrease in the time derivative of stretch values leads to the rotational motion of deformation approaches rigid body rotation. Consequently, strain reversals on the slip plane are observed within these time intervals. To mitigate these strain reversals, a revised NLTE mold design is proposed, where the ellipsoidal twist sections' minor and the major axis of the NLTE process coincides with the principal major and minor axes of the ellipsoidal deformed shape of the single crystal copper specimen. This design modification aims to increase the stretch value and prevent strain reversals during the NLTE process. Comparisons between experimental and CPFEM-predicted texture results show good qualitative agreement. The last orientation pole figures for the center and periphery elements are found to be the same, rotating by the same amount and direction. This suggests that the center and periphery sections of the specimen underwent homogeneous deformation. However, slight discrepancies are observed between the predicted and experimental last orientation results. To improve the quantitative accuracy of the model, finer element sizes in the RVE mesh and decreased process punch speeds in simulations can be employed. However, these adjustments will increase analysis time.

CHAPTER 6

CRYSTAL PLASTICITY FINITE ELEMENT ANALYSIS OF TEXTURE EVOLUTION AND HETEROGENEITY IN EQUAL CHANNEL ANGULAR PRESSING OF NIOBIUM SINGLE CRYSTAL

6.1 Introduction

Crystals display both plastic and elastic anisotropy. Plastic deformation predominantly occurs on particular slip systems, resulting in orientation-dependent directional strength. The Schmid and Taylor factors are commonly utilized to quantify this orientation dependence. The Schmid factor considers isostress conditions to ensure equilibrium, whereas the Taylor factor considers isostrain conditions for compatibility ([177]). Both factors connect macroscopic yield stress and critical resolved shear stress on a slip system. The directional modulus characterizes the elastic response. For a specific crystal orientation, the Taylor factor is directly proportional to the work needed for unit deformation, representing relative yield strength across different orientations. A higher Taylor factor indicates increased resistance to deformation for that particular orientation. This relationship applies to various orientations and has been confirmed through empirical measurements ([178]). The Taylor factor has a solid connection to stacking fault energy (SFE) and the ratio of critical resolved shear stresses for twinning and slipping in face-centered cubic (FCC) metals ([179]). Specifically, the Taylor factor quantifies the ratio of the sum of shear rate magnitudes of slip systems to the effective deformation rate ([180]).

Niobium (Nb) is a versatile metal with many engineering applications, often used as an alloy. Its utilization spans various industries, including producing superconducting radio frequency cavities, heat shields for space missions, and even biological applica-

tions. Nb and its alloys exhibit desirable qualities for engineering applications, such as high-temperature strength, resistance to thermal creep, formability, low neutron absorption, and compatibility with alkali metals. The advantageous combination of these properties positions niobium alloys as structural elements in nuclear reactors and makes them valuable in fields such as microelectronics, aerospace, and the automotive industry. Significantly, niobium is favored in fabricating superconducting wires, rocket boosters, sodium vapor lamps, and superconductors. Due to its pivotal role in diverse applications, its response to deformation is of utmost significance to industry researchers. Adopting the equal channel angular pressing (ECAP) technique can alter niobium's microstructure and characteristics, thus expanding its potential applications. Crystal plasticity models offer effective frameworks for predicting the stress-strain response of crystalline materials. With their twelve slip systems, FCC crystals have been extensively studied, facilitating the use of crystal plasticity models. Conversely, BCC crystals feature more slip systems (forty-eight), which complicates identifying crystal parameters for each slip system within a family. This study represents a significant advancement by conducting ECAP simulations on single crystals of Nb. It explores three diverse deformation paths to uncover the heterogeneity associated with an ECAP pass and its effects on the treated specimen. Using an explicit crystal plasticity finite element method (CPFEM) model, the investigation examines two distinct directions and three separate slip systems, investigating the mechanical response of Nb single crystals. The analysis includes evaluating shear activity to establish correlations between primary slip systems and the expected texture evolution. A crucial parameter, the Taylor factor (M), which encapsulates the average grain orientations across all grains within the specimen, is examined in conjunction with the texture analysis of Nb single crystals. This research elucidates the complex relationship between deformation properties and subsequent texture development in single niobium crystals by investigating three deformation pathways within the ECAP process.

140

6.2 Finite Element Model Definitions

CPFEM simulations for a single-pass ECAP are conducted using the commercial finite element software ABAQUS. Figure 6.1 displays the technical drawing of the conventional ECAP mold, which is simplified to a 3D 'L' shape model to reduce analysis time. Additionally, a 2D schematic cut-section drawing of the square and rounded channels of the ECAP die is presented in Figure 6.1. The ECAP mold features a channel intersection corner with a filled radius of $r = 2$ mm and an outer curvature fillet radius of $r = 0.5$ mm. The channel intersection angle is $90°$. The inlet section of the mold is a square with dimensions of 4.1 $mm \times 4.1mm$, while the outlet section of the mold has a 4 $mm \times 4mm$ cross-section.
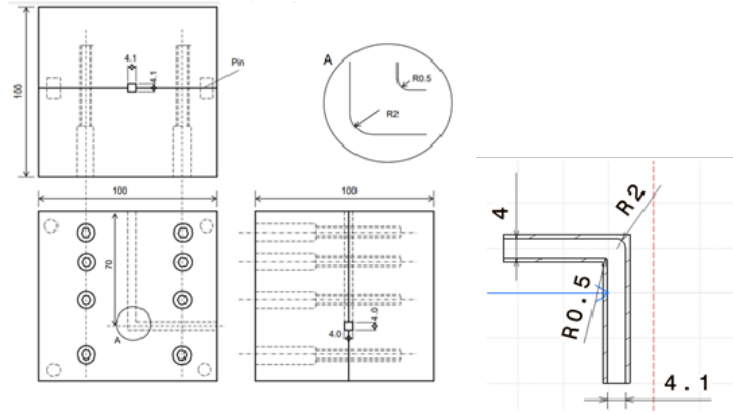
Figure 6.1: Mechanical drawing of ECAP mold

Figure 6.2 presents the 3D CAD model of the ECAP mold, along with the finite element (FE) mesh model used in the analysis. The mesh properties employed in the CPFEM model are outlined in Table 6.1. The sample is discretized using 2560 linear hexahedral C3D8R elements, chosen based on dilatational wave speed and deformation speed ratios to mitigate distortion issues. The rigid punch is meshed with 504 linear hexahedral C3D8R elements. The ECAP mold is meshed using 381,163 linear tetrahedral elements. Both the ECAP mold and punch models are treated as rigid bodies. Encastre boundary conditions ($u_1 = u_2 = u_3 = R_1 = R_2 = R_3 = 0$) are applied to the mold through a rigid body reference point. The square workpiece's cross-sectional area measures 16 mm^2 ($4mm \times 4mm$), with a length of 50 mm.
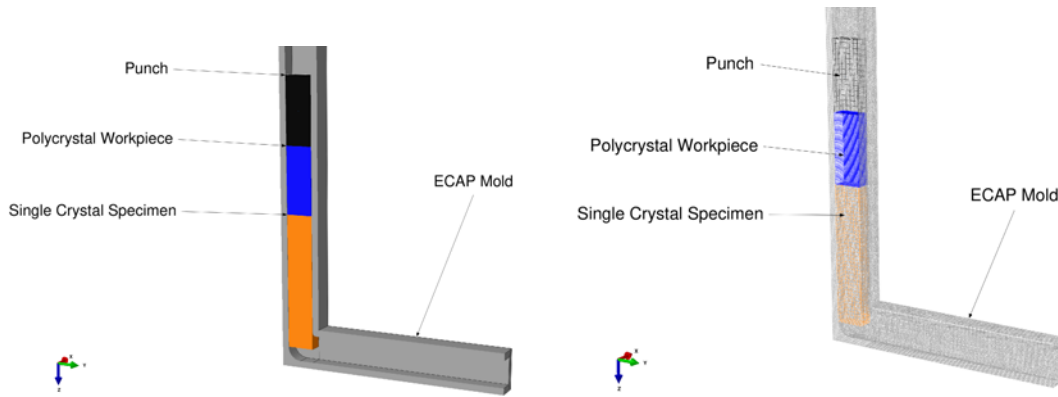
Figure 6.2: FEA model of ECAP process

Table 6.1: CPFEM mesh model parameters of simulated ECAP process.

Model	Element Type	Element Family	Number of Elements	Model Type
ECAP Mold	Linear Tetrahedral-C3D4	3D Stress	381163	Rigid
ECAP Punch	Explicit-Hexahedral-C3D8R	3D Stress	735	Rigid
ECAP Polycrystal Workpiece	Explicit-Hexahedral-C3D8R	3D Stress	758462	Deformable (von Mises Plasticity)
ECAP Specimen	Explicit-Hexahedral-C3D8R	3D Stress	2560	Deformable (CP)

In the explicit CPFEM analyses, a general contact interaction property focuses on tangential contact algorithms. The Coulomb friction coefficient ($\mu = 0.05$) describes the contact between the die and the workpiece. Additionally, a gravity load is imposed on the entire model to mimic the effect of gravity during the analysis. To ensure the va-

lidity of the analysis, the examination of the finite element results is restricted to a 25 mm section located in the middle of the deformed billets. This choice aims to mitigate potential distortions stemming from end effects. Three distinct deformation paths are employed in the simulation to investigate strain homogeneity comprehensively.

6.3 Constitutive Material Model Definitions

The polycrystalline material is modeled with von Mises Plasticity using stress-strain curve values specific to niobium (Nb) material. The stress-strain curve is illustrated in Fig. 6.3.
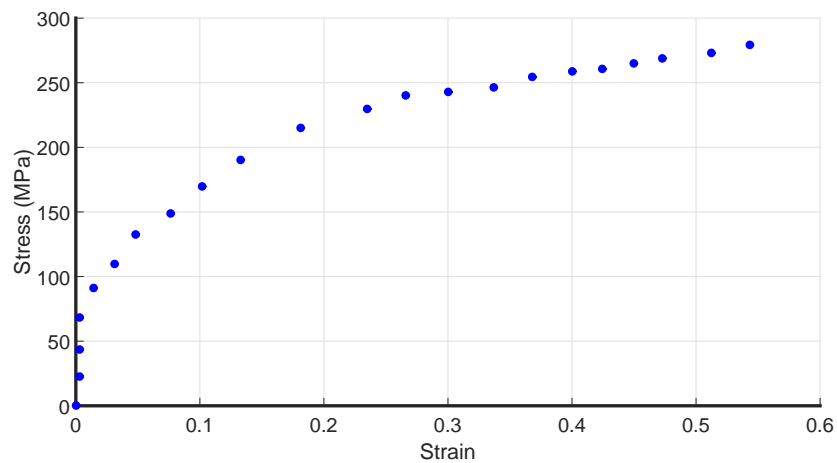
Figure 6.3: The experimental stress-strain curve of Niobium ([181])

The explicit algorithm of the CPFEM analysis is employed for performing ECAP
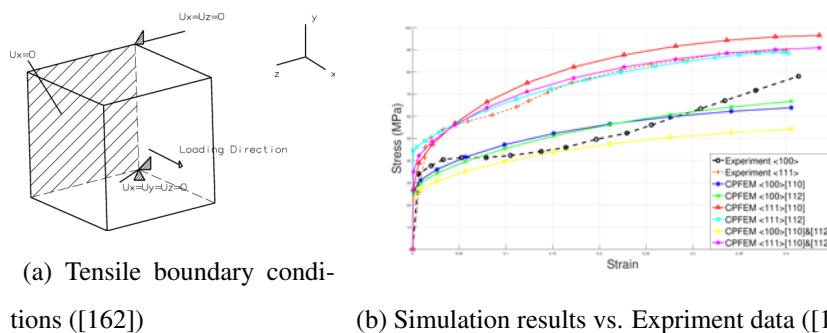
(a) Tensile boundary conditions ([162])

(b) Simulation results vs. Expriment data ([182])

Figure 6.4: Applied boundary conditions and tensile test simulations

143

simulations (Chapter 4). Tensile test simulations are conducted to assess the consistency of the explicit algorithm with experimental results. Tensile boundary conditions are applied to the boundaries, and displacement boundary conditions are imposed on the single crystal cube, as depicted in Figure 6.4a. Slip systems of BCC materials are shown in Table 1.4. Material parameters are set based on experimental data from tensile tests conducted on crystal orientations parallel to the <110> directions, and comparisons were made with test data from <100> and <111> crystal orientations of single niobium crystals. The material parameters are provided in Table 6.2 and Table 6.3. The comparison between CPFEM simulations and test data curves for <100> and <111> crystal orientations is shown in Figure 6.4b.

Table 6.2: Elastic constants of Single crystal Nb for VUMAT model parameters

Material	C_{11} (MPa)	C_{12} (MPa)	C_{44} (MPa)
Niobium (Nb)	246000	134000	28700

Table 6.3: Single crystal Nb VUMAT model parameters

Slip Systems	τ_0 (MPa)	h_0 (MPa)	τ_s (MPa)	$\dot{\gamma}_0$ (s^{-1})	m	q
(110) [111]	10	55	20	0.001	17	1.4
(112) [111]	10	43	33	0.001	17	1.4
(110)& (112) [111]	10	50	25	0.001	17	1.4

6.4 CPFEM Results and Discussion

CPFEM simulations are conducted for two distinct initial crystal orientations (parallel to <100> and parallel to <111> directions) and three different slip systems of Nb single crystals in the context of BCC materials: (110)[111], (112)[111], and (110)(112)[111]. The first two systems encompass twelve slip systems each, while the third system includes twenty-four slip systems. These two orientations are assigned separately to investigate how initial orientations impact the workpiece's kinetics, kinematics, and texture evolution during the ECAP process. A constant friction coefficient of 0.05 is maintained throughout all simulations between the workpiece and the mold. The same boundary conditions are applied to all simulations to consistently compare the effects of different initial orientations and slip systems on a single ECAP pass of the Nb single crystal specimen. Figure 6.5 shows that the kinetic energy remains a small fraction (less than 1%) of the internal energy throughout the analysis, except at the beginning. This observation meets the criterion that kinetic energy should be significantly smaller than internal energy, indicating an acceptable quasi-static solution.
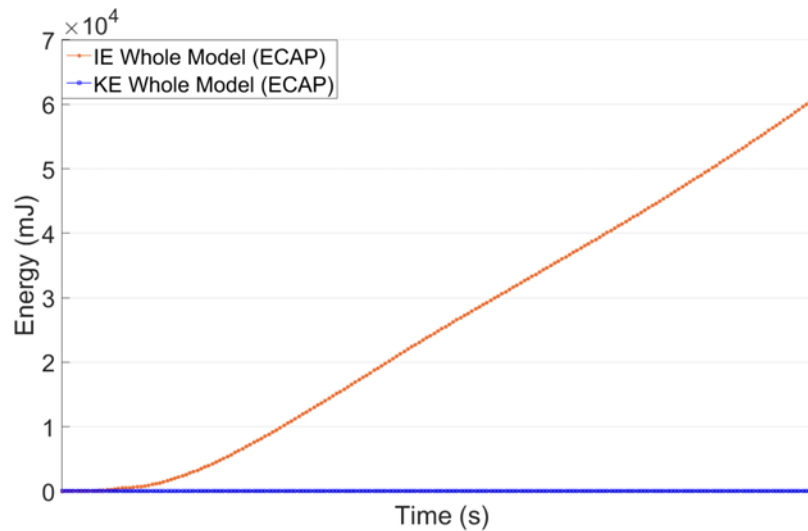
Figure 6.5: Comparison of internal and kinetic energies during ECAP process

Figure 6.6 illustrates this change by displaying the variations in strain energy (SE), and plastic dissipation energy (PD). It is worth noting that the model's total energy (Etotal) remains relatively constant throughout the simulation.
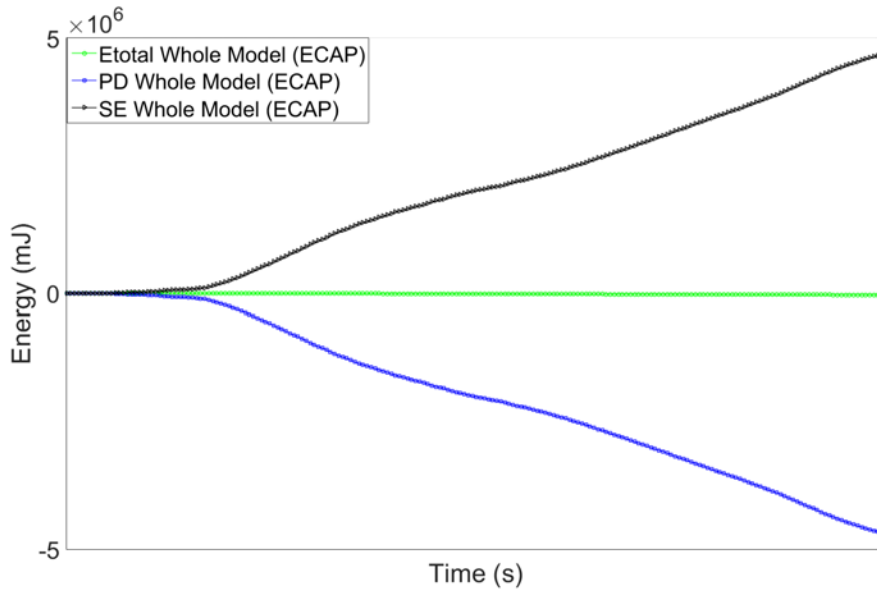
Figure 6.6: Comparison of whole model energies throughout the ECAP process
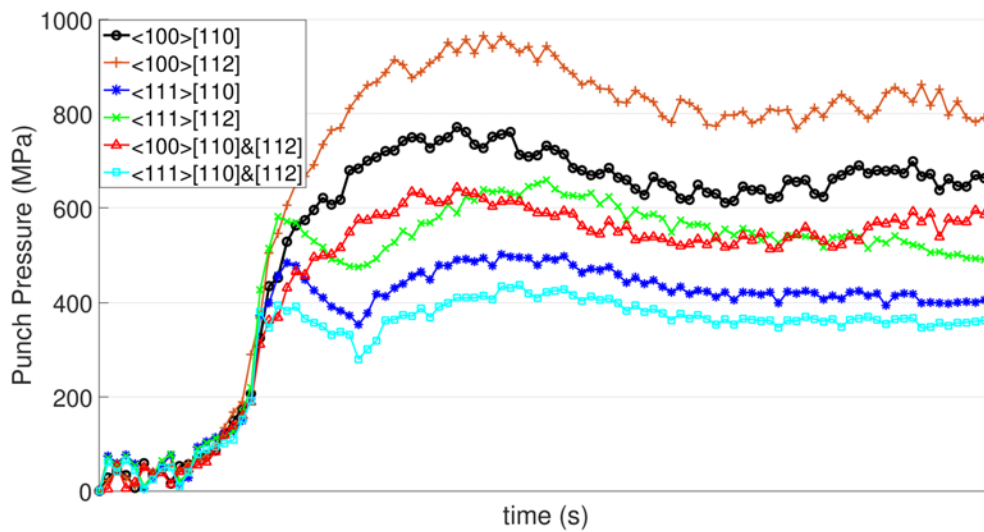
Figure 6.7: Punch Pressure (MPa) according to ECAP process time, initial orientations (<100> and<111>) and slip systems ((110)[111], (112)[111] and (110)[111]&(112)[111])

The evolution of punch pressure during the ECAP process is determined by dividing the punch force by the cross-sectional area of the sample, which is 16 mm^2. Fig. 6.7 illustrates the punch pressure versus ECAP process time curves for two distinct initial

146

orientations and three different slip systems. As depicted in the figure, the pressing force progressively increases with the movement of the punch until it stabilizes. This force level is necessary to facilitate the extrusion of the sample through the first bend, a phenomenon also observed in prior research ([183], [184]). The initial orientation is a crucial factor influencing the pressing load, significantly impacting the punching force observed when transitioning from the <100> to the <111> initial orientation for each slip system. Specifically, the maximum pressing load is 16 kN when the initial orientation is parallel to the <100> direction and the slip system is (112)[111]. In contrast, when the initial orientation is parallel to the <111> direction and involves twenty-four slip systems, the pressing load significantly drops to 4 kN, merely one-fourth of the load associated with the <100> initial orientation. Among the twelve slip systems, the [112] planes' slip system yields the highest punch force during the entire ECAP process. The CPFEM simulations yield intricate insights into the dis-
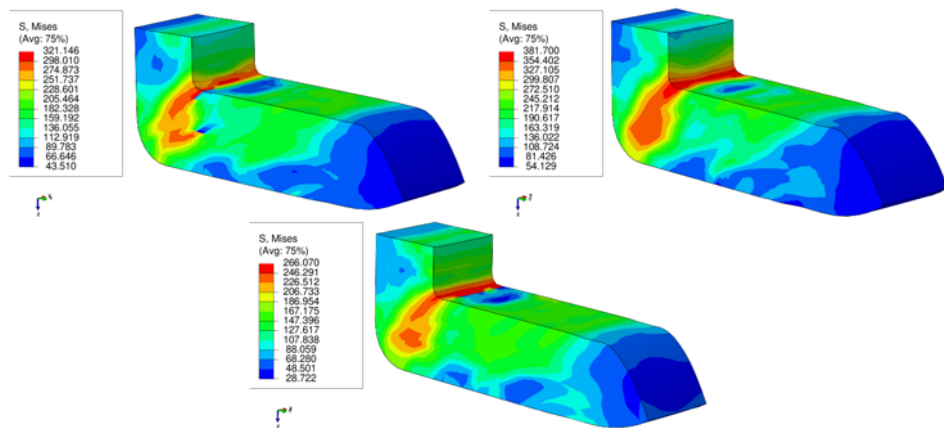
Figure 6.8: The von Mises stress (MPa) distribution after one ECAP pass of initially <100> directed single crystal Nb according to slip systems (110)[111], (112)[111] and (110)[111]&(112)[111]

tribution of stress and strain and the interactions between grains at different stages of the ECAP process. The distribution of Von Mises stress within the Nb single crystal following one ECAP pass has been visualized. Notably, the highest stress distribution occurs in the plastic deformation zone of the ECAP process for all simulation conditions, particularly when the workpiece faces simple shear boundary conditions within the ECAP mold. Conversely, the minimum Von Mises stress distribution is observed at the tip section of the workpiece. When comparing the systems with twelve and

twenty-four slip systems, it is evident that the stress distribution decreases as the number of slip systems increases. Additionally, there is a noticeable difference in stress distribution between the top and bottom surfaces of the workpiece. The top surface displays a more homogeneous stress distribution than the bottom section, indicating a possible influence of the initial orientation and slip systems on stress patterns during the ECAP process. Furthermore, the initial orientation and the number of slip
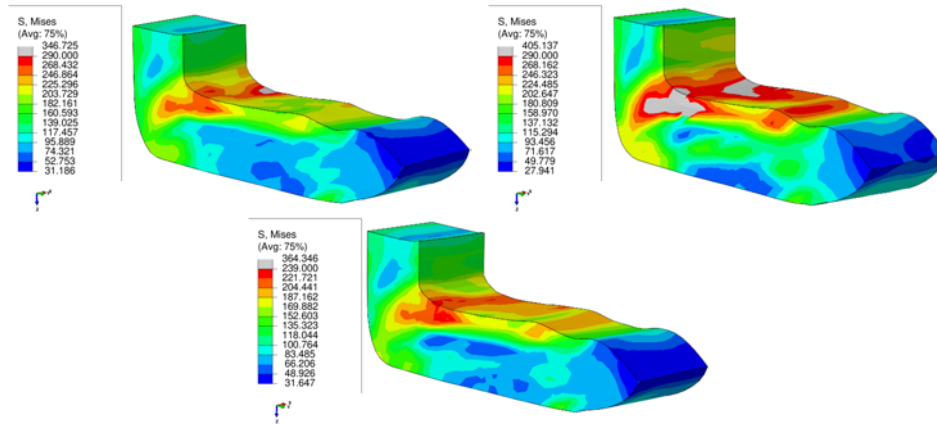
Figure 6.9: The von Mises stress (MPa) distribution after one ECAP pass of initially <111> directed single crystal Nb according to slip systems (110)[111], (112)[111] and (110)[111]&(112)[111]

systems significantly impact the stress distribution. Fig. 6.8 displays the Von Mises stress distribution after one ECAP pass for an initially <100>-oriented single crystal Nb, considering the slip systems (110)[111], (112)[111], and (110)[111]&(112)[111]. Notably, the Von Mises stress distribution decreases as the punch force increases in the ECAP process. The simulations with twenty-four slip systems exhibit lower stress values, indicating a potential benefit in terms of stress distribution. Comparatively, Fig. 6.9 illustrates the Von Mises stress distribution (in MPa) after one ECAP pass for an initially <111> oriented single crystal Nb, also considering the same slip systems. Shifting the initial orientation to <111> leads to a drastic increase in stress values compared to the <100> simulation results. The stress distribution appears more inhomogeneous for the initially <111> oriented single crystal specimen. Introducing the (112) planes' slip system increases Von Mises stress, particularly on the top and plastic deformation zone surfaces. Interestingly, the stress distribution at the tip of the workpiece appears to be more homogenous in initially <100> oriented single crystal

Nb ECAP simulations. Plastic equivalent strain (PEEQ) values were calculated as
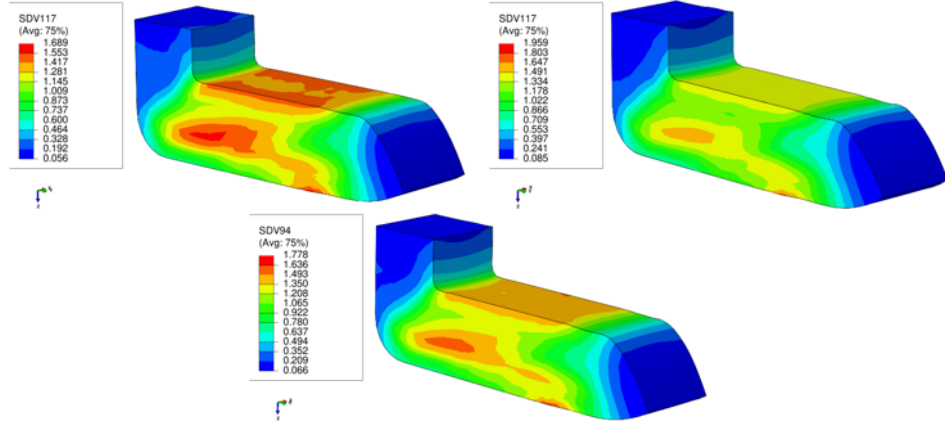
Figure 6.10: The Plastic Equivalent strain (PEEQ) distribution after one ECAP pass of initially <100> directed single crystal Nb according to slip systems (110)[111], (112)[111] and (110)[111]&(112)[111]

in Eq. 6.1([185]),

$$PEEQ = \sqrt{\frac{2}{3}(\dot{\boldsymbol{\epsilon}}^p : \dot{\boldsymbol{\epsilon}}^p)} \tag{6.1}$$

The distribution of PEEQ values in the upper region of the niobium sample reveals notable homogeneity, as these values remain approximately constant across all elements. Conversely, the strain distribution in the lower portion of the specimen exhibits heterogeneity, where each element maintains a consistent effective strain value. This trend persists along the axial direction of the billet, displaying a relatively uniform strain distribution, except for the initial section where steady-state deformation has not yet been established. Effective strain distribution along the billet height exhibits a distinct pattern commonly observed in ECAP processes that utilize dies with external curvature. A gap between the workpiece and the die introduces an external curvature effect to the process, contributing to a decrease in shear strain levels in the outer regions of the deformation zone. The material near the billet's inner corner undergoes more pronounced strains and strain gradients than the material near the outer corner. The heightened deformation near the inner corner leads to increased compressive forces acting on the material adjacent to the right-hand side interface of the entry channel. Consequently, this results in higher levels of frictional stress at the right-hand side interface and a notable plastic strain rate in that particular region. The initial orientation exerts a significant influence on the distribution of PEEQ val-

149
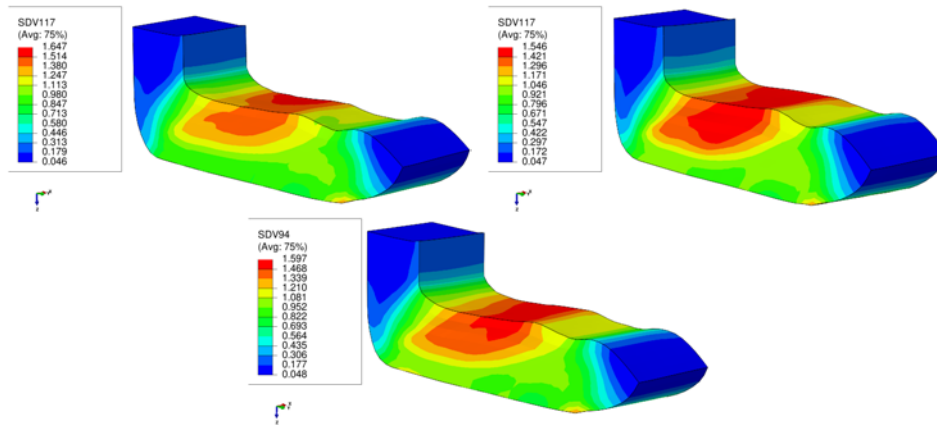
Figure 6.11: The plastic equivalent strain (PEEQ) distribution after one ECAP pass of initially <111> directed single crystal Nb according to slip systems (110)[111], (112)[111] and (110)[111]&(112)[111]

ues, and these values vary based on the initial orientation and the number of slip systems. Fig.6.10 depicts the PEEQ distribution after a single ECAP pass for an initially <100>-oriented single crystal Nb, considering slip system families (110)[111], (112)[111], and (110)[111]&(112)[111]. As the punch force increases, there is a corresponding increase in the PEEQ value for the (112) slip system family. The highest PEEQ value, reaching 1.9, is observed in this slip system family, while the lowest PEEQ value can be seen in the case of <100> orientation and the (110) slip system. The outcomes of simulations conducted on a single Nb crystal initially oriented parallel to <111> direction are illustrated in Fig.6.11. In these simulations, the crystal's orientation is such that the [111] slip direction aligns with the die's ideal shear directions, and the [111] slip direction is parallel to the shear direction. The trend in these simulations indicates a gradual decrease in PEEQ values as the punch force decreases across all the simulated scenarios. An interesting contrast to the simulations involving <100>-oriented Nb crystals is observed in simulations with <111>-oriented crystals. In these simulations, the highest PEEQ values are observed in the (110)[111] slip system, while the (112)[111] slip system exhibits the lowest PEEQ values. This observation suggests variations in plastic strain distribution and deformation behavior between the two crystal orientations. The PEEQ strain distribution along the width direction, considering the three different deformation paths, two different initial orientations, and three different slip systems, is illustrated in Figure 6.12. The PEEQ
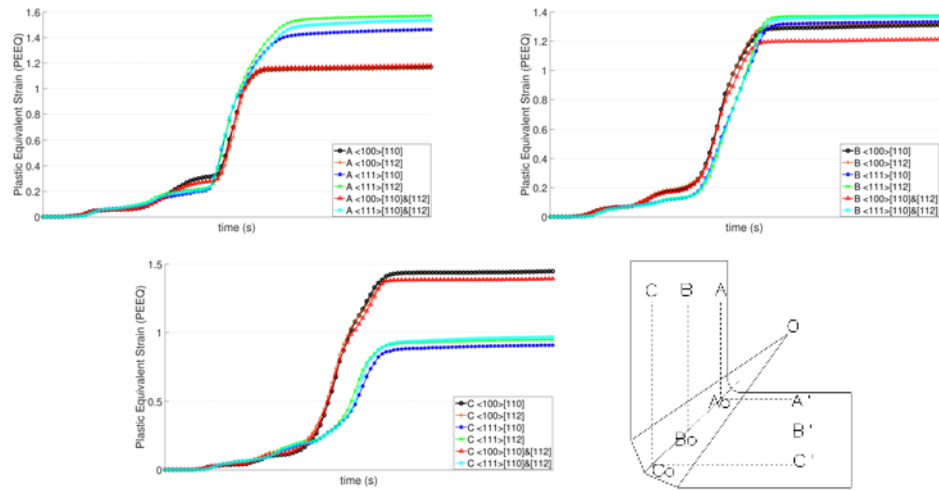
Figure 6.12: The plastic equivalent strain (PEEQ) distribution after one ECAP pass of single crystal Nb according to initial orientations (<100> and<111>), slip systems ((110)[111], (112)[111] and (110)[111]&(112)[111]) and deformation path (A,B,C)

values rapidly increase as the workpiece enters the plastic deformation zone, evolving until the turn's end. Afterward, the PEEQ values stabilize, and the strain values remain relatively constant. Among the deformation paths, point A, located near the top surface of the workpiece, exhibits the highest PEEQ values throughout the ECAP process. In contrast, the lowest PEEQ values are observed at deformation path point C, near the ECAP mold's bottom surface. The distribution of equivalent strain rates across different specimen regions is notably heterogeneous. The maximum equivalent strain rate is observed near the inner die corner, where intense deformation occurs. The central area of the specimen also shows higher strain rates than the outer die corner, where rigid rotation effects are more dominant.

The analysis of PEEQ values reveals intriguing trends in the relationship between deformation paths, slip systems, and initial orientations. In the case of deformation paths A and B, the (112) slip system exhibits the highest PEEQ values, implying that this slip system contributes significantly to plastic deformation in these paths. On the other hand, for deformation path C, the (110) slip system family demonstrates the highest PEEQ values, indicating its dominant role in this path. Interestingly, deformation path B appears less sensitive to initial orientations and slip system family variations, as evidenced by the relatively consistent PEEQ value distribution. This

151

observation implies that deformation path B may have a more consistent material response regardless of the crystal orientation and slip systems involved. These findings underscore the intricate and multifaceted nature of the deformation process, where the interplay between various factors, such as deformation path, slip systems, and initial orientations, influences the material's plastic response and distribution of plastic strain. Such insights are invaluable for understanding and optimizing material behavior in complex deformation processes like ECAP.
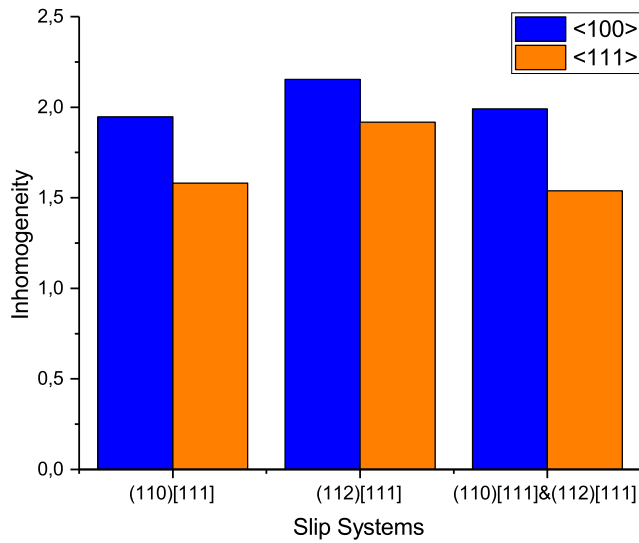
Figure 6.13: Strain inhomogeneity after one ECAP pass of single crystal Nb according to initial orientations (<100> and<111>) and slip systems ((110)[111], (112)[111] and (110)[111]&(112)[111])

The deformation modes cannot be directly measured experimentally. They are explored using a CPFEM approach, which offers the advantage of capturing the inhomogeneous distribution of strain and stress. The degree of strain inhomogeneity can be estimated using Equation 6.2, as proposed by [186].

$$SH_i = \frac{PEEQ_{max} - PEEQ_{min}}{PEEQ_{Avg}} \qquad (6.2)$$

The Equation 6.2 calculates the strain inhomogeneity index, where SH_i represents the strain inhomogeneity index, $PEEQ_{min}$ denotes the minimum equivalent plastic strain, $PEEQ_{max}$ stands for the maximum equivalent plastic strain, and $PEEQ_{Avg}$

indicates the average PEEQ. The strain inhomogeneity index and the coefficient of variation of equivalent plastic strain, according to initial orientation and slip system family predictions, are illustrated in Fig. 6.13. In the visualization, the blue color represents the initially oriented <100> crystal, while the orange color symbolizes the initially oriented <111> Nb single crystal for one ECAP pass. A lower value of the index indicates better homogeneity. The twenty-four slip system exhibits a lower inhomogeneity index for both initial orientations, with the minimum inhomogeneity index observed in the <111> initial orientation. These results suggest that the heterogeneity of through-thickness equivalent strain in the Z-direction is also orientation-dependent.

To investigate the impact of slip systems and initial orientation on the evolution of crystallographic orientation within niobium single crystals, the study focuses on three specific locations along the deformation path: Positions A, B, and C. These positions correspond to different sections within the sample, with positions A at the upper part, B in the middle, and C at the bottom. Despite undergoing a rotation in its crystallographic orientation from the initial state, the material retains its single-crystal structure throughout this analysis. The experimental results reveal distinct pole figures from positions A and B, displaying a rotated orientation compared to the initial orientation. In contrast, the initial orientation is less evident at position C. Remarkably, the simulation results closely mirror these experimental observations. The simulated pole figures exhibit the rotated and initial orientations, aligning almost perfectly with the corresponding positions on the experimental pole figures. This remarkable agreement between the simulated and experimental outcomes, consistent with previous studies ([187], [188]), validates the accuracy and reliability of the CPFEM model developed in this study for predicting texture evolution. The analysis of pole figures (Table 6.4) highlights the significant influence of the selected ECAP deformation path and the initial orientation on crystallographic orientation evolution. Pole figures indicate that orientations remain relatively stable before and after passing through the plastic deformation zone. This observation is consistent with previous research ([189]), which emphasizes the persistence of lattice orientation throughout the ECAP process. The dominance of a single primary slip mechanism reinforces the concept that lattice orientation remains largely unchanged after the material experiences plastic deformation within the defined zone ([172]). The investigation into rigid body rotation for defor-

153

Table 6.4: CPFEM predicted pole figures throughout the process of one ECAP pass of single crystal Nb according to initial orientations (<100> and<111>) , slip systems ((110)[111], (112)[111] and (110)[111]&(112)[111]) and deformation path (A,B,C)

Slip System	initial pole figure	A_0	A'	B_0	B'	C_0	C'
< 100 > [110]							
< 100 > [112]							
< 111 > [110]							
< 111 > [112]							
< 100 > [110]&[112]							
< 111 > [110]&[112]							

mation paths A, B, and C is presented in Figure 6.14. In cases where the motion of elements involves rigid body rotation, the time derivative of the stretch tensor can be assumed to be zero ($\dot{U} = 0$). Consequently, the norm of the time derivative of the stretch tensor should be zero ($|\dot{U}| = 0$) to satisfy the condition of rigid body rotation. Figure 6.14 illustrates the norm of the time derivative of the stretch tensor for different deformation path points as a function of process time, considering various initial orientations and slip systems. The Taylor factor indicates how well a crys-
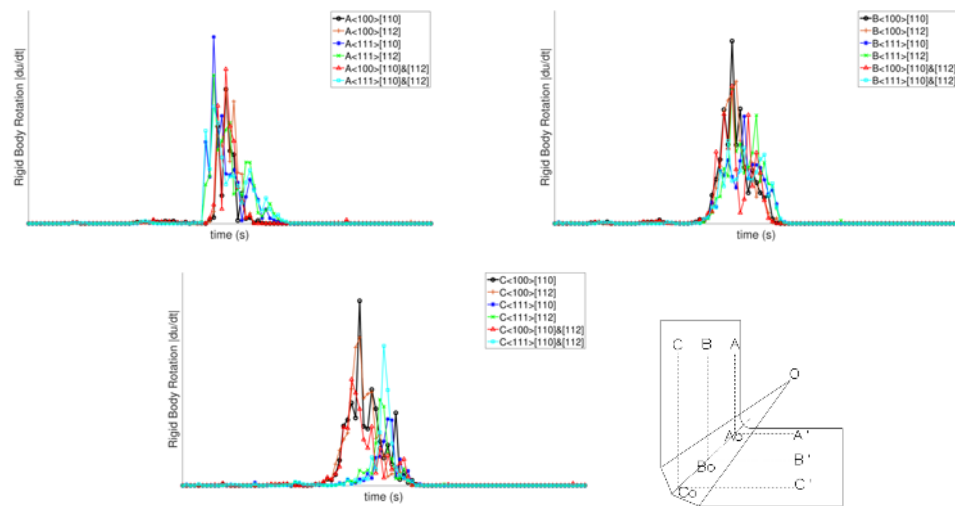
Figure 6.14: Rigid body rotation after one ECAP pass of single crystal Nb according to initial orientations (<100> and<111>), slip systems ((110)[111], (112)[111] and (110)[111]&(112)[111]) and deformation path (A,B,C)

tal's orientation aligns with the applied deformation. It is commonly used to correlate the flow stress (σ) observed in a polycrystalline material with the critical resolved shear stress (CRSS) (τ) within the constituent single crystals. This factor represents an average orientation measure influenced by the material's texture and the crystallographic characteristics of assumed slip systems. When analyzing stress-strain curves, the Taylor factor is also employed to express the macroscopic strain as the sum of crystallographic shears. Consequently, the strain hardening slope in polycrystals is proportional to M^2, making it sensitive to the assumed value of M. The strain hardening rate in single crystals, when divided by M^2, offers valuable insights into deformation mechanisms and constitutive relationships for polycrystal simulations ([190]). Moreover, the Taylor factor is closely linked to the Stacking Fault Energy (SFE) in

the twinning and slipping mechanisms of metals ([191]).

In practice, the Taylor model provides a connection between the equivalent strain rate $\dot{\epsilon}^p$ and the sum of resolved shear strain rates $\dot{\gamma}$. Here, $\dot{\gamma}$ is the algebraic sum of the determined shear strain rates $\dot{\gamma}^\alpha$ for each slip system, where α represents a specific slip system. The relationship is expressed as $\dot{\epsilon} = \dot{\gamma}/M$, where $\dot{\epsilon}$ is the equivalent strain rate, and M is the Taylor factor.

While the Taylor factor isn't directly measurable through experiments, it can be computed or estimated using crystal plasticity models. The CPFEM analysis calculates the Taylor factor using equation 6.3. This equation establishes a connection between the equivalent strain rate and the resolved shear strain rates within the crystal's slip systems, shedding light on the material's response and deformation behavior ([192]).

$$Taylor\,Factor(M) = \sum_\alpha \frac{|\dot{\gamma}^\alpha|\triangle t}{\dot{\epsilon}^p_{eff}\triangle t} \tag{6.3}$$

The evolution of the Taylor Factor in the ECAP process of single-pass single-crystal niobium is illustrated in Figure 6.15. The crystal's initial orientation influences this evolution, the chosen slip systems, and the specific deformation path employed.

As the niobium single crystal undergoes plastic deformation within the ECAP process, the Taylor Factor (M) initially experiences a gradual increase, continuing until it reaches a peak value. After getting this maximum, the Taylor Factor undergoes a sharp decrease, persisting until the end of the process, particularly within the rigid body rotation zone of the ECAP process.

The maximum values of the Taylor Factor (M) for the niobium crystal are determined based on the crystal's initial orientation and the chosen slip systems. These maximum values are summarized and presented in a tabulated form in Table 6.5. This information provides insight into the crystal's mechanical behavior and deformation characteristics throughout the ECAP process, which are influenced by slip systems, initial orientation, and the specific deformation path. In BCC structured materials, such as those encountered in conventional rolling processes, the 111 orientation is often associated with a relatively high Taylor Factor of around 3.5. This high Taylor Factor indicates a strong orientation for accommodating deformation, making the 111 orientation particularly favorable for plastic deformation. On the other hand, in BCC

structured materials undergoing plane strain compression, the rotated Goss (110) orientation tends to exhibit an even higher peak Taylor Factor of approximately 4.24 ([193]). These observed trends in Taylor Factors are consistent with the predictions made by our CPFEM simulations in this study.

It's important to clarify that reducing the Taylor or Schmid factors does not necessarily imply material softening. Instead, grains with higher Taylor Factors experience more significant stress reduction during deformation. A decrease in the Taylor Factor suggests that the grain's orientation has shifted towards more favorable slip conditions. Smaller Taylor Factor values indicate orientations more conducive to deformation, as they require lower stress levels for plastic deformation to occur. The crystals with smaller Taylor Factors tend to deform more quickly than those with larger values ([194]). Conversely, an increase in the Taylor Factor is associated with higher energy accumulation due to deformation ([195]).

These observations highlight the intricate relationship between crystal orientation, Taylor Factors, and the ease of plastic deformation in materials   The Taylor Factor
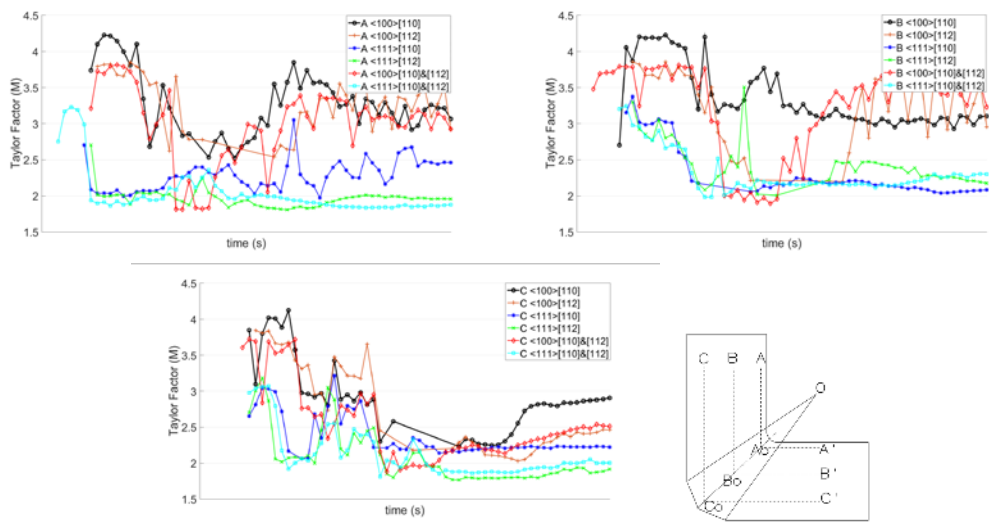
Figure 6.15: Taylor Factor distribution after one ECAP pass of single crystal Nb according to initial orientations (<100> and<111>), slip systems ((110)[111], (112)[111] and (110)[111]&(112)[111]) and deformation path (A,B,C)

values shown in Figure 6.15 demonstrate only minor fluctuations concerning various deformation paths. This observation suggests that the specific choice of deformation

path during the ECAP process has a relatively limited impact on the Taylor Factor values. In contrast, more significant variations in the Taylor Factor values are attributable to disparities in the initial orientation of the crystal and the selected slip system. These factors appear to have a more substantial influence on the Taylor Factor values than the choice of deformation path.

From Figure 6.15, it is evident that the Taylor Factor values vary based on the initial crystal orientation, the chosen slip systems, and the deformation path. Specifically, for a single crystal of niobium initially oriented along the <100> direction, the highest Taylor Factor is observed when coupled with the (110) slip plane and [111] slip direction within the plastic deformation zone. In contrast, a single crystal of niobium initially oriented along the <111> direction exhibits lower Taylor Factor values throughout the process, particularly when coupled with the [110] and [110][112] slip plane systems.

Interestingly, the trend of Taylor Factor softening is more pronounced in single crystal niobium oriented along the <111> direction. This can be attributed to the <111> direction aligning with the shear direction, leading to micro-shear banding and geometric softening effects. Additionally, the simulation results show that even towards the end of the process, a single crystal of niobium initially oriented along the <100> direction retains higher Taylor Factor values than the <111> orientation. These findings align with earlier studies that have reported similar trends in BCC structured materials, especially those with <111> oriented grains ([196], [197]). Maximum Taylor factors are also presented in Table 6.5.

Table 6.5: CPFEM predicted maximum Taylor Factor (M) trough out the process of one ECAP pass of single crystal Nb according to initial orientations (<100> and<111>) and slip systems ((110)[111], (112)[111] and (110)[111]&(112)[111])

Slip System	$<100>$ [110]	$<100>$ [112]	$<111>$ [110]	$<111>$ [112]	$<100>$ [110][112]	$<111>$ [110][112]
Taylor Factor (M)	4.21	3.87	3.58	3.47	3.82	3.45

6.5 Conclusion

The explicit CPFEM model is utilized to conduct simulations of the texture evolution and kinematics of single-crystal niobium material during a single pass of ECAP. This study involves analyses for two distinct initial crystal orientations (<100> and <111>) and three different slip systems ((110)[111], (123)[111], and (110)&(112)[111]).

The variations in initial orientation, shear systems, and deformation paths substantially influence stress distribution within the workpiece, the development of plastic equivalent strain, and the eventual formation of crystal orientation. Remarkably, the plastic strain distribution exhibits the smallest values in the bottom region of the ECAP process. This phenomenon can be attributed to the influence of the outer corner angle of the ECAP die, which induces rigid body rotations and subsequently affects the stress and strain distribution.

Regarding the Taylor factor, a more significant reduction is observed in the single crystals oriented along the <111> direction and using the 24-slip system configuration. The study also highlights that the softening degree is non-uniform and notably influenced by the grain orientation and slip system employed. Specifically, the <111> oriented crystals coupled with the 24 slip system exhibit a response with the potential for slip band formation and greater homogeneity. Deformation twinning is expected to occur in the dense direction of shear band formation and their intersections because severe plastic deformation is more localized in these directions [198]. However, the physical effects of the twinning mechanism are not included in the calculations in this study.

Nevertheless, according to the simulation results, single crystals initially parallel to the <111> direction experience more severe plastic deformation and exhibit more Taylor softening than the other simulation results. These findings also align with the results of the literature. Moreover, the predicted pole figures obtained from the simulations, which are compatible with the experimental measurements reported in the literature, underscore the accuracy and validity of the developed CPFEM model.

CHAPTER 7

CONLUSION AND SUMMARY

This thesis investigates the production of ultrafine-grained (UFG) structures within materials, allowing for the examination of the influence of mechanical properties. Severe Plastic Deformation (SPD) production methods are explored at the macro and mesoscale to determine the kinetics and kinematics of deformed metallic materials. Consequently, process parameters for metallic workpieces and SPD production methods are identified. This study uses continuum-based micromechanic approaches to cover the specimen's texture evolution, plastic deformation response, and material mechanical characteristics after deformation. It also uses experimental and simulated microstructural properties under SPD process boundary conditions to decide on scientific reviews. Chapter 2 introduces a novel torsional extrusion process called nonlinear twist extrusion (NLTE). This section addresses the initial computational study of the designed geometry for the new extrusion process. The results of the conventional extrusion process, linear twist extrusion (LTE), are discussed in detail. Secondly, in Chapter 3, implicit CPFEM user-defined material (UMAT) numerical simulations are employed to explore the extrusion process of individual single-crystal copper workpieces, encompassing the LTE and NLTE mechanisms, while considering two distinct initial orientations of the workpieces. By adopting this methodology, a thorough and intricate comparison of the effectiveness of grain refinement, utilizing crystal plasticity finite element analysis, is conducted for these two severe plastic deformation techniques, marking the first instance of such an analysis in the literature. The main parameters that impact processing, such as back pressure and friction, create convergence problems in the simulations of Chapter 3. Thus, in Chapter 4, an explicit CPFE model (VUMAT) is developed, and model verification studies are performed. Furthermore, in Chapter 5, explicit simulations of single-crystal copper workpiece

extrusion using NLTE processes with varying friction coefficients are conducted to investigate the impact of the friction coefficient on the NLTE process and compared with experimental results. Lastly, in Chapter 6, the explicit CPFEM model developed in Chapter 4 is utilized to simulate the texture evolution and kinematics of single-crystal niobium material during a single pass of ECAP. Two distinct initial crystal orientations and three different slip systems are employed to analyze the ECAP process of Nb single crystal. The main results from these studies are listed below.

- Results illustrated the advantages of the process in terms of punching force and deformation distribution, where more effective strain evolution for grain refinement had been obtained with less punch force in NLTE processes than in LTE.

- Applied back pressure substantially influences the final geometry and evolution of plastic strain.

- The NLTE process can produce more homogeneous grain refinement than the traditional LTE process.

- Both implicit (UMAT) and developed explicit (VUMAT) crystal plasticity algorithms yield consistent numerical results, facilitating the understanding of strain localization, its sensitivity to strain paths, and its interaction with specific crystallographic orientations.

- The alignment between experimental and simulated results underscores CPFEM's potential for predicting strain localization and its dependence on various factors, thereby contributing to assessing material behavior and formability.

- The friction coefficient influences factors such as punch force, rigid body rotation of the single-crystal copper specimen, shear strain, and microstructure evolution.

- Texture analysis and examination of the main texture components' contents after the NLTE process indicated that increasing the friction coefficient between the mold and workpiece decreases fracture toughness.

162

- An increase in friction coefficient leads to higher punch forces, and a more homogeneous plastic strain distribution is observed after one pass of the single crystal copper specimen through the NLTE process.

- To mitigate the strain reversals, a revised NLTE mold design is proposed, where the ellipsoidal twist sections' minor and the major axis of the NLTE process coincides with the principal major and minor axes of the ellipsoidal deformed shape of the single crystal copper specimen.

- The variations in initial orientation, shear systems, and deformation paths substantially influence stress distribution within the workpiece, the development of plastic equivalent strain, and the eventual formation of crystal orientation in ECAP process.

- The outer corner angle of the ECAP die, which induces rigid body rotations and subsequently affects the stress and strain distribution.

- Regarding the Taylor factor, a more significant reduction is observed in the single crystals oriented along the <111> direction and using the 24-slip system configuration.

- The softening degree is non-uniform and notably influenced by the grain orientation and slip system employed in ECAP process.

- Specifically, the <111> oriented crystals coupled with the 24 slip system exhibit a response with the potential for slip band formation and greater homogeneity.

- Comparisons between experimental and CPFEM-predicted texture results show good qualitative agreement.

REFERENCES

[1] A. B. B. Günther and H. Weiss, "Preparation and mechanical properties of ultrafine grained metals," *Mat. Res. Soc. Symp. Proc.*, vol. 195, no. 1, pp. 611 – 615, 1990.

[2] C. Koch, "Optimization of strength and ductility in nanocrystalline and ultrafine grained metals," *Scripta Materialia*, vol. 49, no. 1, pp. 657–662, 2003.

[3] H. Gleiter, "Nanocrystalline materials," *Prog Mater Sci*, vol. 33, no. 1, p. 223–315, 1989.

[4] M. A. Meyers, A. Mishra, and D. J. Benson, "Mechanical properties of nanocrystalline materials," *Prog Mater Sci*, vol. 51, no. 1, pp. 427–556, 2006.

[5] R. Song, D. Ponge, D. Raabe, J. Speer, and D. Matlock, "Overview of processing, microstructure and mechanical properties of ultrafine grained bcc steels," *Materials Science and Engineering*, vol. 441, no. 1, pp. 1–17, 2006.

[6] M. Kawasaki, B. Ahn, P. Kumar, J. Jang, and T. G. Langdon, "Nano- and micro-mechanical properties of ultrafine-grained materials processed by severe plastic deformation techniques," *Advanced Enginnering Materials*, vol. 1, no. 1, pp. 1–17, 2016.

[7] R. Pippan and A. Hohenwarter, "The impotrance of fracture toughness in ultrafine and nanocrystalline bulk materials," *Materials Research Letters*, vol. 1, no. 1, pp. 1–10, 2016.

[8] M. Kawasaki, R. B. Figueiredo, C. Xu, and T. G. Langdon, "Developing superplastic ductilities in ultrafine-grained metals," *Metalurgical and Materials Transactions*, vol. 38A, no. 1, pp. 1891–1897, 2007.

[9] E. G. Berdichevskij, "Use of the superplasticity effect of materials in engineering technology," *Materials Science and Engineering*, vol. 441, no. 1, pp. 1–4, 2018.

[10] H. Halfa, "Overview of processing, microstructure and mechanical properties of ultrafine grained bcc steels," *Journal of Minerals and Materials Characterization and Engineering*, vol. 2, no. 5, pp. 1–42, 2014.

[11] T. G. Langdon, "Twenty-five years of ultrafine-grained materials: achieving exceptional properties through grain refinement," *Acta Materialia*, vol. 61, no. 19, pp. 7035–7059, 2013.

[12] K. N. Kalashnikov, T. A. Kalashnikova, A. V. Chumaevski, and A. N. Ivanov, "Production of materials with ultrafine-grained structure of aluminum alloy by friction stir processing," *Journal of Physics*, vol. 1115, no. 4, pp. 42–48, 2018.

[13] G. Korznikova, "Domain structures of ultrafine grained ferromagnets achieved by severe plastic deformation or melt quenching," *Journal of Microscopy*, vol. 3, no. 239, pp. 239–244, 2010.

[14] T. Qian and M. Marx, "Mechanical properties of nanocrystalline and ultrafine-grained nickel with bimodal microstructure," *Advanced Engineering Materials*, vol. 16, no. 11, pp. 1–17, 2014.

[15] V. Ronto, L. Battezzati, A. Yavari, M. Tonegaru, N. Lupu, and G. Heunen, "Crystallization behaviour of al87ni7la6 and al87ni7sm6 amorphous alloys," *Scripta Materialia*, vol. 50, no. 6, pp. 839–843, 2004.

[16] A. Azushima, R.Kopp, A. Korhonen, and D. Yang, "Severe plastic deformation (spd) process for metals," *Manufacturing Technology*, vol. 57, no. 2, pp. 716–735, 2008.

[17] P. Newbery, B. Ahn, T. Topping, and P. Pao, "Large ufg al alloy plates from cryomilling," *Journal of Materials Processing Technology*, vol. 203, no. 3, pp. 37–45, 2008.

[18] D. Liu, Y. Xiong, P. Li, Y. Lin, F. Chen, L. Zhang, J. Schoenung, and E. J. Lavernia, "Microstructure and mechanical behavior of ns/ufg aluminum prepared by cryomilling and spark plasma sintering," *Journal of Alloys and Compounds*, vol. 679, no. 1, pp. 426–435, 2016.

[19] G. Su, V. G. Hadjiev, P. E. Loya, J. Zhang, S. Lei, S. Maharjan, P. Dong, P. M. Ajayan, J. Lou, and H. Peng, "Chemical vapor deposition of thin crystals of

layered semiconductor sns2 for fast photodetection application," *Nano Lett*, vol. 15, no. 1, pp. 506–513, 2014.

[20] D. Benetti, R. Nouar, R. Nechache, H. Pepin, F. R. A. Sarkissian, and J. M. MacLeod, "Combined magnetron sputtering and pulsed laser deposition of tio 2 and bfco thin films," *Scientific Reports*, vol. 7, no. 2503, pp. 1–9, 2017.

[21] A. Akl and H. Howari, "Nanocrystalline formation and optical properties of germanium thin films prepared by physical vapor deposition," *Journal of Physics and Chemistry of Solids*, vol. 70, no. 10, pp. 1337–1343, 2009.

[22] R. H. Kodama, A. E. Nash, F. E. Spada, and A. E. Berkowitz, "Spark erosion for production of nanocrystalline materials," *Nanophase Materials*, vol. 260, no. 10, pp. 101–108, 1994.

[23] T. Yalçınkaya, S. Çakmak, and C. Tekoglu, "A crystal plasticity based finite element framework for rve calculations of two-phase materials:void nucleation in dual-phase steels," *Finite Elements in Analysis and Design*, vol. 187, no. 1, p. 103510, 2021.

[24] T. Yalçınkaya, I. Özdemir, and I. T. Tandogan, "Misorientation and grain boundary orientation dependent grain boundary response in polycrystalline plasticity," *Computational Mechanics*, vol. 67, no. 3, pp. 937–954, 2021.

[25] S. Acar, O. Bulut, and T. Yalçinkaya, "Crystal plasticity modeling of additively manufactured metallic microstructures," *Procedia Structural Integrity*, vol. 35, no. 1, p. 219–227, 2022.

[26] T. Yalçınkaya, I. Tandogan, and I. Ozdemir, "Void growth based inter-granular ductile fracture in strain gradient polycrystalline plasticity," *International Journal of Plasticity*, vol. 147, no. 1, pp. 103–123, 2021.

[27] M. Furukawa, Z. Horita, M. Nemoto, and T. G. Langdon, "Review: Processing of metals by equal-channel angular pressing," *Journal of Materials Science*, vol. 36, no. 1, pp. 2835–2843, 2001.

[28] V. Segal, V. Reznikov, A. Drobyshevskiy, and V. Kopylov, "Plastic working of metals by simple shear," *Russian Metallurgy*, vol. 1, no. 1, pp. 99–105, 1981.

[29] M. Salleh, A. Rahman, S.H.Yahaya, M.Y.Yuhazri, and S. Akmal, "A comprehensive review on the influence of equal channel angular pressing parameters on magnesium alloys," *International Journal of Engineering Research and Technology*, vol. 13, no. 11, pp. 3855–3871, 2020.

[30] P. W. Bridgman, "On torsion combined with compression," *Journal of Applied Physics*, vol. 14, no. 1, pp. 274–283, 1943.

[31] P. A. Zhilyaev and T. G. Langdon, "Using high-pressure torsion for metal processing: Fundamentals and applications," *Progress in Materials Science*, vol. 53, no. 1, pp. 893–979, 2008.

[32] M. Evans, W. Skipper, and L. B. Johnstone, "The development of a high pressure torsion test methodology for simulating wheel/rail contacts," *Tribology International*, vol. 56, no. 1, pp. 1–30, 2021.

[33] K.Edalati, E. Akiba, and Z. Horita, "High-pressure torsion for new hydrogen storage materials," *Sci Technol Adv Mater.*, vol. 19, no. 1, pp. 185–193, 2018.

[34] A. Zhilyaev, S. Lee, G. Nurislamova, R. Valiev, and T. Langdon., "Microhardness and microstructural evolution in pure nickel during high-pressure torsion," *Scripta Mater*, vol. 44, no. 1, pp. 27–53, 2001.

[35] M. Cabibbo, "Tem kikuchi pattern study of ecap aa1200 via routes a, c, bc," *Materials Characterization*, vol. 61, pp. 613–625, 2010.

[36] N. Tsuji, Y. Saito, H. Utsunomiya, and S. Tanigawa, "Ultra-fine grained bulk stell produced by accumulative roll-bonding (arb) process," *Acta Metallurgica*, vol. 40, no. 7, pp. 795 – 800, 1999.

[37] S. M. Ghalehbandi, M. Malaki, and M. Gupta, "Accumulative roll bonding—a review," *Materials Science and Engineering*, vol. 9, no. 17, pp. 27–36, 2019.

[38] N. Hansen and D. Jensen, "Development of microstructure in fcc metals during cold work," *Phil. Trans. R. Soc. Lond.*, vol. A, no. 357, pp. 69–1447, 1999.

[39] N. Tsuji, Y. Saito, S. Lee, and Y. Minamino, "Arb(accumulated roll-bonding and other new techniques to produce bulk ultafine grained materials," *Advanced Engineering Materials*, vol. 5, no. 5, pp. 338–344, 2003.

[40] R. Imaev, V. Imaev, and G. Salischev, "Formation of submicrocrystalline microstructure in tial intermetallic compound.," *J. Mat. Sci.*, vol. A, no. 27, pp. 4465–4469, 1999.

[41] V. Segal, "Review: Modes and process of severe plastic deformation (spd)," *Materials*, vol. 11, no. 1, pp. 1–61, 2018.

[42] F. Djavanroodi, M. Ebrahimi, and J. F. Nayfeh, "Tribological and mechanical investigation of multi-directional forged nickel," *scientific reports*, vol. 11, no. 1, pp. 1–8, 2019.

[43] Y. Jin, C. Xi, P. Xue, C. Zhang, S. Wang, and J. Luo, "Microstructural morphology effects on fracture toughness and crack growth behaviors in a high strength titanium alloy," *metals*, vol. 1, no. 1, pp. 1–1, 2020.

[44] M. Odnobokova, A. Kipelova, A. Belyakov, and R. Kaibyshev, "Microstructure evolution in a 316l stainless steel subjected to multidirectional forging and unidirectional bar rolling," *IOP Conference Series: Materials Science and Engineering*, vol. 63, no. 1, pp. 12–60, 2014.

[45] Y. Beygelzimer and D. Orlov, "Metal plasticity during the twist extrusion," *Trans.Tech. Publications*, vol. 208, no. 1, pp. 311–314, 2002.

[46] Y. Beygelzimer, D. Orlov, A. Korshunov, S. Synkov, V. Varyukhin, I. Vedernikova, A. Reshetov, A. Synkov, L. Polyakov, and I. Korotchenkova, "Features of twist extrusion: Method, structures and material properties," *Trans.Tech. Publications*, vol. 114, no. 1, pp. 69–78, 2006.

[47] D. Orlov, A. Reshetov, A. Synkov, V. Varyukhin, D. Lotsko, O. Sirko, N. Zakharova, A. Sharovsky, Y. M. V. Voropaiev, S. Synkov, Y. Zhu, and V. Varyukhin, "Nanostructured materials by high pressure severe plastic deformation," *NATO Science Series, II Mathematics, Physics and Chemistry*, vol. 212, no. 1, pp. 77–85, 2006.

[48] Y. Beygelzimer, V. Varyukhin, D. Orlov, and S. Synkov, "Twist extrusion – process for strain accumulation," *Donetsk: TEAN*, vol. 1, no. 1, pp. 1–10, 2003.

[49] Y. Beygelzimer, V. Varyukhin, S. Synkov, and D. Orlov, "Useful properties of twist extrusion," *Materials Science and Engineering*, vol. A, no. 503, pp. 14–17, 2009.

[50] Y. Beygelzimer, D. Prilepoa, R. Kulagina, V. Grishaeva, O. Abramova, V. Varyukhina, and M. Kulakov, "Planar twist extrusion versus twist extrusion," *Journal of Materials Processing Technology*, vol. 201, no. 1, pp. 522–529, 2011.

[51] Y. Beygelzimer, R. Kulagin, Y. Estrin, L. S. Toth, H. S. Kim, and M. I. Latypov, "Twist extrusion as a potent tool for obtaining advanced engineering materials: A review," *Advanced Engineering Materials*, vol. 19, no. 8, pp. 1438–1656, 2017.

[52] M. Eckert, "Disputed discovery: The beginnings of x-ray diffraction in crystals in 1912 and its repercussions," *Z. Kristallogr*, vol. 227, no. 1, p. 27–35, 2011.

[53] P. Forman, "The discovery of the diffraction of x-rays by crystals; a critique of the myths," *Springer*, vol. 6, no. 1, pp. 38–71, 1969.

[54] J. Callister, *Materials science and engineering an introduction*. Wiley, 1999.

[55] L. Murr, *Interfacial Phenomena in Metals and Alloys*. Addison-Wesley, 1975.

[56] C. Wagner, "Stacking faults by low-temperature cold work in copper and alpha brass," *Acta Metallurgica*, vol. 5, no. 8, pp. 427–434, 1957.

[57] G. E. Dieter, *Mechanical Metallurgy*. Mc Graw Hill, 1988.

[58] F. Dunne and N. Petrinic, *Introduction to computational plasticity*. 2nd. Edition: Oxford University Press, 2006.

[59] C. Du, F. Maresca, M. Geers, and J. Hoefnagels, "Ferrite slip system activation investigated by uniaxial micro-tensile tests and simulations," *Acta Materialia*, vol. 146, no. 1, pp. 314–327, 2018.

[60] E. Schmid, "Contribution to the physics and metallography of magnesium," *Z. Elektrochem*, vol. 37, no. 8, pp. 447–459, 1931.

[61] H. Bunge, *Texture Analysis in Materials Science*. Butterworth-Heinemann, 1982.

[62] F. Kocks, C. Tome, and H. Wenk, *Texture and Anisotropy. Preferred Orientations in Polycrystals and Their Effect on Material Properties*. No. 1, Cambridge University Press, 2000.

[63] I. Carneiro and S. Simoes, "Recent advances in ebsd characterization of metals," *Metals*, vol. 10, no. 8, pp. 1–32, 2020.

[64] A. J. Wilkinson and T. B. Britton, "Strains, planes, and ebsd in materials science," *Materials Today*, vol. 15, no. 9, pp. 366–376, 2012.

[65] B. Inkson, *Scanning electron microscopy (SEM) and transmission electron microscopy (TEM) for materials characterization*. Woodhead Publishing, 2016.

[66] S. F. Bordin, S. Limandri, J. Ranalli, and G. Castellano, "Ebsd spatial resolution for detecting sigma phase in steels," *Ultramicroscopy*, vol. 171, pp. 177–185, 2016.

[67] D. T. Fullwood, S. Sanderson, S. Baird, J. Christensen, E. R. Homer, and O. Johnson, "Determining grain boundary position and geometry from ebsd data: Limits of accuracy," *Microscopy and Microanalysis*, vol. 28, no. 1, p. 96–108, 2022.

[68] A. Vazdirvanidis, A. Rikos, A. Toulfatzis, and A. Pantazopoulos, "Electron backscatter diffraction (ebsd) analysis of machinable lead-free brass alloys: Connecting texture with fracture," *Metals*, vol. 12, no. 4, 2022.

[69] S.Gaudet, D. K. Koen, L. M. Samuel, J. S. Jean, C. Detavernier, C. Lavoie, and P. Desjardins, "Three dimensional reciprocal space measurement by x-ray diffraction using linear and area detectors: Applications to texture and defects determination in oriented thin films and nanoprecipitates," *Journal of Vacuum Science and Technology A*, vol. 31, no. 2, pp. 1–15, 2013.

[70] R. Hielscher, C. B. Silbermann, E. Schmidl, and J. Ihlemann, "Denoising of crystal orientation maps," *Journal of Applied Crystallography*, vol. 52, no. 5, pp. 984–996, 2019.

[71] W. L. Bond, "The mathematics of the physical properties of crystals," *The Bell System Technical Journal*, vol. 22, no. 1, pp. 1–72, 1943.

[72] S.C.Cowin, *Continuum Mechanics of Anisotropic Materials.* Springer, 2013.

[73] S. Nemat-Nasser, "Decomposition of strain measures and their rates in finite deformation elastoplasticity," *International Journal of Solids and Structures*, vol. 15, no. 2, pp. 155–166, 1979.

[74] J. Simo and E. Marsden, "The hamiltonian structure of nonlinear elasticity: The material and convective representations of solids, rods, and plates," *Archive for Rational Mechanics and Analysis*, vol. 104, no. 1, pp. 125–183, 1988.

[75] R. Eve and B. Reddy, "The variational formulation and solution of problems of finite-strain elastoplasticity based on the use of a dissipation function," *International Journal for Numerical Methods in Engineering*, vol. 37, no. 1, pp. 1673 – 1695, 1994.

[76] A. R. Khoei, "Finite deformation plasticity," *Elsevier*, vol. 1, no. 8, pp. 246–293, 2005.

[77] G. Jaumann, "Geschlossenes system physikalischer und chemischer differentialgesetze," *Akad. Wiss. Wien Sitzber*, vol. 120, no. 1, pp. 385–530, 1911.

[78] J. Dienes, "On the analysis of rotation and stress rate in deformation bodies," *Acta Mechanica*, vol. 32, no. 1, pp. 217–232, 1979.

[79] J. C. Nagtegaal and J. E. D. Jong, "Some computational aspects of elastic-plastic large strain analysis," *Numerical Methods in Engineering*, vol. 17, no. 1, pp. 15–41, 1981.

[80] G. Johnson and D. Bammann, "A discussion of stress rates in finite deformation problem," *Int. J. Solids Struct.*, vol. 20, no. 8, pp. 725–737, 1984.

[81] A. E. Green and P. M. Naghdi, "A general theory of an elastic-plastic continuum," *Archive for Rational Mechanics and Analysis*, vol. 18, no. 1, pp. 251–281, 1965.

[82] B. Cotter and R. Rivlin, "Tensors associated with time-dependent stress," *Quarterly Appl. Math.*, vol. 13, no. 1, pp. 177–182, 1955.

[83] J. G. Oldroyd, "A rational formulation of the equations of plastic flow for a bingham solid," *Mathematical Proceedings of the Cambridge Philosophical Society*, vol. 43, no. 1, pp. 100–105, 1947.

[84] C. Truesdell, "Hypo-elsticity," *Rational Mechanics and Analysis*, vol. 4, no. 1, pp. 83–133, 1955.

[85] Y. Beygelzimer, V. Varyukhin, S. Synkov, and D. Orlov, "Useful properties of twist extrusion," *Mater. Sci. Eng. A*, vol. 503, no. 1, pp. 14 – 17, 2009.

[86] Y. Beygelzimer, D. Prilepo, R. Kulagin, V. Grishaev, O. Abramova, V. Varyukhin, and M. Kulakov, "Planar twist extrusion versus twist extrusion," *J. Mater. Process. Technol.*, vol. 211, no. 3, pp. 522 – 529, 2011.

[87] Y. Beygelzimer, A. Reshetov, S. Synkov, O. Prokof'eva, and R. Kulagin, "Kinematics of metal flow during twist extrusion investigated with a new experimental method," *J. Mater. Process. Technol.*, vol. 209, no. 7, pp. 3650 – 3656, 2009.

[88] M. Latypov, I. Alexandrov, Y. Beygelzimer, S. Lee, and H. Kim, "Finite element analysis of plastic deformation in twist extrusion," *Comput. Mater. Sci.*, vol. 60, pp. 194 – 200, 2012.

[89] M. Maulidi, M. H., and Y. M., "Grain refinement of pure magnesium using nonlinear twist extrusion," *Mater. Sci. Forum*, vol. 939, no. 9, pp. 54–62, 2018.

[90] N. Fang, "A new quantitative sensitivity analysis of the flow stress of 18 engineering materials in machining," *J. Eng. Mater. Technol.*, vol. 127, no. 1, pp. 192–196, 2005.

[91] S. A. Mousavi, A. Shahab, and M. Mastoori, "Computational study of ti–6al–4v flow behaviors during the twist extrusion process," *Mater. Des.*, vol. 29, no. 9, p. 1316–1329, 2008.

[92] S. A. Mousavi, S. R. Bahadori, and A. Shahab, "Numerical and experimental studies of the plastic strains distribution using subsequent direct extrusion after

three twist extrusion passes," *Mater. Sci. Eng. A*, vol. 527, no. 9, p. 3967–3974, 2010.

[93] Y. B. Marat I. Latypov and H. S. Kim, "Comparative analysis of two twist-based spd processes: Elliptical cross-section spiral equal-channel extrusion vs. twist extrusion," *(Mater. Trans.*, vol. 54, no. 9, pp. 1587–1591, 2013.

[94] Y. B. Marat I. Latypov and H. S. Kim, "Finite element analysis of the plastic deformation in tandem process of simple shear extrusion and twist extrusion," *Mater. Des.*, vol. 83, no. 9, pp. 858–865, 2015.

[95] P. Alexander and L. Langdon, "Using high-pressure torsion for metal processing:fundamentals and applications," *Progress in Materials Science*, vol. 53, pp. 893–979, 2008.

[96] S. Agnew and J. Weertman, "Cyclic softening of ultrafine grain copper," *Materials Science and Engineering: A*, vol. 244, no. 2, pp. 145–153, 1998.

[97] D. Jia, Y. M. Wang, K. T. Ramesh, E. Ma, Y. T. Zhu, and R. Z. Valiev, "Deformation behavior and plastic instabilities of ultrafine-grained titanium," *Applied Physics Letters*, vol. 79, pp. 611–613, 07 2001.

[98] M. Murashkin, I. Sabirov, D. Prosvirnin, I. Ovid'ko, V. Terentiev, R. Valiev, and S. Dobatkin, "Fatigue behavior of an ultrafine-grained al-mg-si alloy processed by high-pressure torsion," *Metals*, vol. 5, pp. 578–590, 2015.

[99] T. Yalcinkaya, U. Simsek, H. Miyamoto, and M. Yuasa, "Numerical analysis of a new nonlinear twist extrusion process," *Metals*, vol. 9, no. 15, pp. 1–15, 2019.

[100] S. R. Kalidindi, B. R. Donohue, and S. Li, "Modeling texture evolution in equal channel angular extrusion using crystal plasticity finite element models," *International Journal of Plasticity*, vol. 25, no. 12, p. 768–779, 2009.

[101] G. Denga, C. Lub, L. Sub, X. Liua, and A. Tieu, "Modeling texture evolution during ecap of copper single crystal by crystal plasticity fem," *Materials Science and Engineering A*, vol. 534, pp. 68–74, 2012.

174

[102] M. I. Latypov, M. Lee, Y. Beygelzimer, D. Prilepo, Y. Gusar, and H. S. Kim, "Modeling and characterization of texture evolution in twist extrusion," *The Minerals, Metals and Materials Society and ASM International*, vol. 1, pp. 1–13, 2015.

[103] H. Sheikh and R.Ebrahimi, "Modeling the effect of backpressure on dislocation cell structure during simple shear extrusion," *UFGSNM*, vol. 17, no. 9, pp. 1–9, 2017.

[104] Z. Xu, C. Zhang, K. Wang, K. Zhang, G. Zhao, and L. Chen, "Crystal plasticity prediction of texture evolution during helical extrusion process of aluminium alloys under three-dimensional deformation path," *Journal of Alloys and Compounds*, vol. 830, no. 16, pp. 1–16, 2020.

[105] E. Günay, T. O. Fenercioğlu, and T. Yalçinkaya, "Numerical analysis of thermo-mechanical behavior in flow forming," *Procedia Structural Integrity*, vol. 35, pp. 42–50, 2022.

[106] C. Erdogan, H. Vural, A. Karakaş, T. O. Fenercioğlu, and T. Yalçinkaya, "Ductile failure of Inconel 718 during flow forming processand its numerical investigation," *Engineering Failure Analysis*, vol. 152, no. 1, pp. 1–14, 2023.

[107] H. Vural, C. Erdoğan, T. O. Fenercioğlu, and T. Yalçinkaya, "Ductile failure prediction during the flow forming process," *Procedia Structural Integrity*, vol. 35, pp. 25–33, 2022.

[108] M. I. Latypov, E. Y. Yoon, D. J. Lee, R. Kulagin, Y. Beygelzimer, M. Seyed Salehi, and H. S. Kim, "Microstructure and mechanical properties of copper processed by twist extrusion with a reduced twist-line slope," *Metall. Mater. Trans. A*, vol. 45, pp. 2232–2241, 2014.

[109] H. Bakhtiari, M. Karimi, and S. Rezazadeh, "Modeling, analysis and multi-objective optimization of twist extrusion process using predictive models and meta-heuristic approaches, based on finite element results," *J. Intell. Manuf*, vol. 1, no. 1, pp. 1–11, 2014.

[110] F. Heydari, H. Saljoghi, and S. Nourbakhsh, "Numerical investigation of the cross-section and twist extrusion die angle on the distribution of plastic strain

and microstructure of al7050 alloy," *Journal of Stress Analysis*, vol. 1, no. 1, pp. 1–8, 2019.

[111] H. Sheikh, R. Ebrahimi, and E. Bagherpour, "Crystal plasticity finite element modeling of crystallographic textures in simple shear extrusion (sse) process," *Materilas Design*, vol. 1, no. 1, pp. 1–28, 2016.

[112] J. Alkorta and J. G. Sevillano, "A comparison of fem and upper-bound type analysis of equal-channel angular pressing (ecap)," *Journal of Materials Processing Technology*, vol. 141, no. 1, pp. 313–318, 2003.

[113] S.H.Kim, S. M. Yeon, J. H. Lee, Y. W. Kim, H. Lee, J. Park, N. K. Lee, J. P. Choi, J. C. Aranas, Y. L. Lee, S. An, K. Choi, and Y. Son, "Additive manufacturing of a shift block via laser powder bed fusion: the simultaneous utilisation of optimised topology and a lattice structure," *Virtual and Physical Prototyping*, vol. 1, no. 1, pp. 1–22, 2020.

[114] Y. Huang, "A user-material subroutine incorporating single crystal plasticity in the abaqus finite element program," *Division of Applied Sciences Harvard University*, vol. 20, no. 178, pp. 1–47, 1991.

[115] T. Yalcinkaya, W. Brekelmans, and M. Geers, "Bcc single crystal plasticity modelling and its experimental identification, modelling simul.," *Mater. Sci. Eng.*, vol. 16, no. 1, pp. 1–16, 2008.

[116] O. Bulut, S. S. Acar, and T. Yalçinkaya, "The influence of thickness/grain size ratio in microforming through crystal plasticity," *Procedia Structural Integrity*, vol. 35, pp. 228–236, 2022.

[117] C. F. Shih and J. W. Hutchinson, "Fully plastic solutions and large scale yielding estimates for plane stress crack problems," *Journal of Engineering Materials and Technology*, vol. 98, no. 10, pp. 289–295, 1976.

[118] D. Pierce, R. J. Asora, and A. Needleman, "An analysis of nonuniform and localized deformation in ductile single crystals," *Acta Metallurgica*, vol. 30, no. 6, pp. 1087–1119, 1982.

[119] C.Tekoglu, "Representative volume element calculations under constant stress triaxiality, lode parameter, and shear ratio," *International Journal of Solids and Structures*, vol. 51, no. (25-26), p. 4544–4553, 2014.

[120] T. Yalcinkaya, G. Gungor, S. O. Cakmak, and C. Tekoglu, "A micromechanics based numerical investigation of dual phase steels," *Procedia Structural Integrity*, vol. 21, no. 1, pp. 61–72, 2019.

[121] I. U. Aydiner, B. Tatli, and T. Yalçinkaya, "Investigation of failure mechanisms in dual-phase steels through cohesive zone modeling and crystal plasticity frameworks," *International Journal of Plasticity*, vol. 174, p. 103898, 2024.

[122] M. I. Latypov, Y. Beygelzimer, and H. S. Kim, "Comparative analysis of two twist-based spd processes: Elliptical cross-section spiral equal-channel extrusion vs. twist extrusion," *Metall. Mater. Trans. A*, vol. 54, pp. 1587–1591, 2013.

[123] S. V. Noor, A. Eivani, H. Jafarian, and M. Mirzaei, "Inhomogeneity in microstructure and mechanical properties during twist extrusion," *Materials Science and Engineering A*, vol. 652, no. 6, pp. 186–191, 2016.

[124] Z. Wang, I. Beyerlein, and R. LeSar, "Plastic anisotropy in fcc single crystals in high rate deformation," *International Journal of Plasticity*, vol. 25, no. 1, pp. 26–48, 2009.

[125] S. Mahesh, C. Tome, C. McCabe, G. Kaschner, I. Beyerlin, and A. Misra, "Application of a substructure-based hardening model to copper under loading path changes," *Metall. Mater.*, vol. A35, no. 1, pp. 3763–3774, 2004.

[126] Q. Xue, I. Beyerlein, D. Alexander, and G. Gray, "Mechanisms for initial grain refinement of ofhc copper during equal channel angular presssing," *Acta Mater.*, vol. 55, no. 1, pp. 665–668, 2007.

[127] N. Hansen and X. Huang, "Microstructure and flow stress of polycrystals and singlecrystals," *Acta Metall.*, vol. 46, no. 1, pp. 1827–1836, 1998.

[128] Y. Kawasaki and T. Takeuchi, "Cell structures in copper single crystals deformed in [001] and [111] axes," *Scripta Metall.*, vol. 14, no. 1, pp. 183–188, 1980.

[129] D. Raabe and F. Roters, "Using texture components in crystal plasticity finite element simulations," *International Journal of Plasticity*, vol. 20, no. 1, pp. 339–361, 2004.

[130] H. Yan, X. Zhao, N. Jia, and Y. Zheng, "Influence of shear banding on the formation of brass-type textures in polycrystalline fcc metals with low stacking fault energy," *J. Mater. Sci. Technol*, vol. 30, no. 4, pp. 408–416, 2014.

[131] L. Kestens and H. Pirgazi, "Texture formation in metal alloys with cubic crystal structures," *Materials Science and Technology*, vol. 32, no. 13, pp. 1303–1315, 2016.

[132] Q. Zhao, L. Zhiyi, T. Huang, P. Xia, and F. Li, "Enhanced fracture toughness in an annealed al-cu-mg alloy by increasing goss/brass texture ratio," *Materials Characterization*, vol. 119, no. 1, pp. 47–54, 2016.

[133] E. Cantergiani, G. Falkinger, S. Mitsche, M. Theissing, S. Klitschke, and F. Roters, "Influence of strain rate sensitivity on cube texture evolution in aluminium alloys," *Metallurgical and Materials Transactions A*, vol. 53, no. 1, pp. 18–36, 2022.

[134] A. Ridha and W. Hutchinson, "Recrystallisation mechanisms and the origin of cube texture in copper," *Acta Metall*, vol. 30, no. 1, pp. 1929–1939, 1982.

[135] R. Doherty, L. Chen, and I. Samajdar, "Cube recrystallization texture experimental results and modeling," *Materials Science and Engineering:A*, vol. 257, no. 1, pp. 18–36, 1998.

[136] S. Dumoulin, O. Hopperstad, and T. Berstad, "Investigation of integration algorithms for rate-dependent crystal plasticity using explicit finite element codes," *Computational Materials Science*, vol. 46, no. 1, pp. 785–799, 2009.

[137] F. Harewood and P. McHugh, "Comparison of the implicit and explicit finite element methods using crystal plasticity," *Computational Materials Science*, vol. 39, no. 1, pp. 481–494, 2007.

[138] D. Peirce, R. Asaro, and A. Needleman, "An analysis of nonuniform and localized deformation in ductile single crystals," *Acta Metallurgica*, vol. 30, no. 6, pp. 1087–1119, 1982.

[139] A. Zamiri, F. Pourboghrat, and F. Barlat, "An effective computational algorithm for rate-independent crystal plasticity based on a single crystal yield surface with an application to tube hydroforming," *International Journal of Plasticity*, vol. 23, no. 1, p. 1126–1147, 2007.

[140] H. Li, H. Yang, and Z. Sun, "A robust integration algorithm for implementing rate dependent crystal plasticity into explicit finite element method," *International Journal of Plasticity*, vol. 24, no. 1, pp. 267–288, 2008.

[141] J. Rossiter, A. Brahme, M. Simha, K. Inal, and R. Mishra, "A new crystal plasticity scheme for explicit time integration codes to simulate deformation in 3d microstructures: Effects of strain path, strain rate and thermal softening on localized deformation in the aluminum alloy 5754 during simple shear," *International Journal of Plasticity*, vol. 26, no. 1, p. 1702–1725, 2010.

[142] M. Grujicic and S. Batchu, "Crystal plasticity analysis of earing in deep-drawn ofhc copper cups," *Journal Of Materials Science*, vol. 37, no. 1, p. 753–764, 2002.

[143] C. Zhang, H. Li, P. Eisenlohr, W. Liu, C. Boehlert, M. Crimp, and T. Bieler, "Effect of realistic 3d microstructure in crystal plasticity finite element analysis of polycrystalline ti-5al-2.5sn," *International Journal of Plasticity*, vol. 69, pp. 21–35, 2015.

[144] S. Kuchnicki, A. Cuitino, and R. Radovitzky, "Efficient and robust constitutive integrators for single-crystal plasticity modeling," *International Journal of Plasticity*, vol. 22, no. 1, pp. 1988–2011, 2006.

[145] M. Khadyko, B. H. Frodal, and O. S. Hopperstad, "Finite element simulation of ductile fracture in polycrystalline materials using a regularized porous crystal plasticity model," *Int J Fract*, vol. 228, no. 1, pp. 15–31, 2021.

[146] R. Hill and J. Rice, "Constitutive anaylsis of elastic-plastic crystals at arbitrary strain," *J. Mech. Phys. Solids*, vol. 20, no. 1, pp. 401–413, 1972.

[147] R. Asaro and J. Rice, "Strain localization in ductile single crystals," *J. Mech. Phys. Solid*, vol. 25, no. 1, pp. 309–338, 1977.

[148] E. Lee, "Elastic-plastic deformation at finite strains," *Journal of Applied Mechanics*, vol. 36, no. 1, pp. 243–245, 1969.

[149] Abaqus Documentation, "Solid (continuum) elements," *Theory Manual*, vol. Section 14.1.1, no. 1, pp. 1–2, 2023.

[150] P. Cermelli and M. E. Gurtin, "Geometrically necessary dislocations in viscoplastic single crystals and bicrystals undergoing small deformations," *International Journal of Solids and Structures*, vol. 39, no. 1, p. 6281–6309, 2002.

[151] J. Mandel, *Plasticite classique et viscoplasticite:*. CISM International Centre for Mechanical Sciences, Springer, 1972.

[152] K. Bennett, R. Regueiro, and R. Borja, "Finite strain elastoplasticity considering the eshelby stress for materials undergoing plastic volume change," *International Journal of Plasticity*, vol. 77, pp. 214–245, 2016.

[153] K. Bowman, *Mechanical behavior of materials*. International Edition: Jhon Wiley and Sons, 2004.

[154] E. Marin, "On the formulation of a crystal plasticity model," *Sanda National Laboratories*, vol. 16, no. 1, p. 1–62, 2006.

[155] R. M. Brannon, "A review of useful theorems involving proper orthogonal matrices referenced to three dimensional physical space," *Sandia National Laboratories*, vol. 1, no. 1, pp. 1–190, 2002.

[156] J. W. Hutchinson, "Bounds and self-consistent estimates for creep of pollycrystalline materials," *Proc. R. Soc. Lond.*, vol. A, no. 348, p. 101–127, 1976.

[157] S. Kalidindi, C. Bronkhorst, and L. Anand, "Crystallographic texture evolution in bulk deformation processing of fcc metals," *J. Mech. Phys. Solids*, vol. 40, no. 3, pp. 537–569, 1992.

[158] S. B. L. Anand, "Elasto-viscoplastic constitutive equations for polycrystalline fcc materials at low homologous temperatures.," *Journal of the Mechanics and Physics of Solids*, vol. 50, no. 1, p. 101–126, 2002.

[159] O. Zienkiewicz, R. Taylor, and D.Fox, "Chapter 5 - geometrically nonlinear problems: Finite deformation," in *The Finite Element Method for Solid*

and Structural Mechanics (Seventh Edition) (O. Zienkiewicz, R. Taylor, and D. Fox, eds.), pp. 147–177, Oxford: Butterworth-Heinemann, seventh edition ed., 2014.

[160] J. Simo and J. Marsden, "On the rotated stress tensor and the material version of the doyle-ericksen formula," *Archive for Rational Mechanics and Analysis*, vol. 86, p. 213–231, 1984.

[161] T. Takeuchi, "Work hardening of copper single crystals with multiple glide orientation," *Trans. JIM*, vol. 16, no. 1, pp. 629–640, 1975.

[162] S. Wulfinghoff and T. Böhlke, "Equivalent plastic strain gradient crystal plasticity enhanced power law subroutine," *GAMM-Mitteilungen*, vol. 36, no. 2, pp. 134–138, 2013.

[163] C. S. Ha, M. E. Plesha, and R. S. Lakes, "Chiral three-dimensional isotropic lattices with negative poisson's ratio: Chiral 3d isotropic lattices with negative poisson's ratio," *Physica status solidi*, vol. 253, no. 7, p. 1243–1251, 2016.

[164] M. G. Lee, R. H. Wagoner, and S. Kim, "Comparative study of single crystal constitutive equations for crystal plasticity finite element analysis," *International Journal of Modern Physics B*, vol. 22, no. 1, pp. 5388–5393, 2008.

[165] B. Guler, U. Simsek, T. Yalcinkaya, and M. Efe, "Grain-scale investigations of deformation heterogeneities in aluminum alloys," *AIP Conference Proceedings*, vol. 1960, 2018.

[166] A. Weidner and H. Biermann, "Review on strain localization phenomena studied by high-resolution digital image correlation," *Advanced Engineering and Materials*, vol. 23, pp. 1–27, 2021.

[167] G. Zhu, X. Hu, J. Kang, R. K. Mishra, and D. S. Wilkinson, "Deformation inhomogeneity in large-grained aa5754 sheets," *Materials Science and Engineering: A*, vol. 528, no. 12, pp. 4187–4198, 2011.

[168] H. Paul, J. Driver, and W. Wajda, "Strain hardening and microstructure evolution of channel-die compressed aluminium bicrystals," *Materials Science and Engineering: A*, vol. 477, no. 1, pp. 282–294, 2008.

[169] U. Şimşek, C. Çoğun, and Z. Esen, "Effects of electrolytic copper and copper alloy electrodes on machining performance in electrical discharge machining (edm)," *Machining Science and Technology*, vol. 26, pp. 1–16, 2022.

[170] U. Şimşek, K. Davut, H. Miyamoto, and T. Yalçınkaya, "Comparison of linear and nonlinear twist extrusion processes with crystal plasticity finite element analysis," *Materials*, vol. 17, no. 5, pp. 1–24, 2024.

[171] U. Şimşek, H. Miyamoto, and T. Yalçınkaya, "Crystal plasticity finite element analysis of linear and non-linear extrusion processes," *Materials Research Proceedings*, vol. 28, no. 1, p. 553–562, 2023.

[172] G. Deng, "Crystal plasticity finite element method simulation of equal channel angular pressing," *University of Wollongong,Phd Thesis*, vol. 1, no. 1, p. 1–273, 2014.

[173] Y. Guan, B. Chen, J. Zou, B. Britton, J. Jiang, and P. Dunne, "Crystal plasticity modeling and hr-dic measurement of slip actiavation and strain localisation in single and oligo-crystal ni alloys under fatigue," *International Journal of Plasticity*, vol. 1, no. 1, pp. 1–28, 2017.

[174] T. Brown, C. Saldana, T. Murthy, J. Mann, Y. Guo, L. Allard, A. King, W. Compton, K. Trumble, and S. Chandrasekar, "A study of the interactive effects of strain, strain rate and temperature in severe plastic deformation copper," *Acta Mater*, vol. 57, no. 1, pp. 5491–5500, 2009.

[175] O. Engler, "Recrystallisation textures in copper manganese alloys," *Acta Mater*, vol. 49, no. 1, pp. 1237–1247, 2001.

[176] N. Gurao, S. Sethuraman, and S. Suwas, "Effect of strain path change on the evolution of texture and microstructure during rolling of copper and nickel," *Mater. Sci. Eng. A*, vol. 528, no. 1, pp. 7739–7750, 2011.

[177] A. C. Poshadel and P. R. Dawson, "Role of anisotropic strength and stiffness in governing the initiation and propagation of yielding in polycrystalline solids," *Cornell University*, vol. 1, no. 1, pp. 1–22, 2017.

[178] C. Zhiyong, C. Hongnian, W. F. Z. Xinming, and T. Chengwen, "Analysis for twinning and slip in face-centered cubic crystals under axisymmetric co-deformation," *Technological Sciences*, vol. 49, no. 5, pp. 521–536, 2006.

[179] Q. Li, J. Wang, and H. Wang, "Achieving strong and stable nanocrystalline al alloys through compositional design," *Journal of Materials Research*, vol. 37, no. 1, pp. 183–207, 2022.

[180] J. Bishop and R. Hill, "A theory of the plastic distortion of a polycrystalline aggregate under combined stresses.," *The London, Edinburgh, and Dublin Philosophical Magazine and Journal of Science*, vol. 42, no. 327, pp. 414–427, 1951.

[181] R. Kostin, P. Avrakhov, A. Didenko, and A. Kanareykin, "A tuner for a superconducting traveling wave cavity prototype," *Journal of Instrumentation*, vol. 10, no. 10, pp. 20–38, 2015.

[182] P. Kneisel, G. Ciovati, P. Dhakal, K. Saito, W. Singer, X. Singer, and G. Myneni, "Review of ingot niobium as a material for superconducting radiofrequency accelerating cavities," *Nuclear Instruments and Methods in Physics Research Section A: Accelerators, Spectrometers, Detectors and Associated Equipment*, vol. 774, pp. 133–150, 2015.

[183] F. Djavanroodi and M. Ebrahimi, "Effect of die parameters and material properties in ecap parallel channels," *Material Science and Engineering A*, vol. 527, no. 1, pp. 7593–7599, 2010.

[184] S. Xu, G. Zhao, X. Ma, and G. Ren, "Finite element analysis and optimization of equal channel angular pressing for producing ultra-fine grained materials," *Journal of Materials Processsing Technology*, vol. 184, no. 1, pp. 209–2106, 2007.

[185] Abaqus Documentation, "Johnson-cook plasticity," *Abaqus Users Manual*, vol. Section 23.2.7, no. 1, pp. 1–2, 2023.

[186] V. Basavaraj, U. Chakkingal, and T. Kumar, "Study of channel angle influence on material flow and strain inhomogeneity in equal channel angular pressing

using 3d finite element simulation," *Journal of Materials Processing Technology*, vol. 209, pp. 89–95, 2009.

[187] W. Skrotzki, "Deformation heterogeneities in equal channel angular pressing," *Materials Transactions*, vol. 60, no. 7, p. 1331–1343, 2019.

[188] M. Liu, S. Nambu, T. Koseki, K. A. Tieu, and K. Zhou, "Three-dimensional quantification of texture heterogeneity in single-crystal aluminium subjected to equal channel angular pressing," *Philosophical Magazine*, vol. 1, no. 1, p. 1–21, 2017.

[189] G. M. Stoica, "Equal-channel-angular processing (ecap) of materials: Experiment and theory," *University of Tennessee*, vol. 1, no. 1, pp. 1–277, 2007.

[190] H. Mecking, U. Kocks, and C. Hartig, "Taylor factors in materials with many deformation modes," *Scripta Materialia*, vol. 35, no. 4, pp. 465–471, 1996.

[191] A. Mandal, P. Modak, M. Sen, S. B. Singh, and D. Chakrabarti, "Influence of local microstructure on the dislocation transference and micro-mechanical response in metastable fcc alloy," *Journal of materials science*, vol. 57, no. 2, pp. 1390–1402, 2022.

[192] K. Zhang, B. Holmedal, T. Mánik, and A. Saai, "Assessment of advanced taylor models, the taylor factor and yield surface exponent for fcc metals," *International Journal of Plasticity*, vol. 1, no. 1, pp. 1–39, 2018.

[193] T. N.Minh1, J. Sidor1, R. Petrov, and L. Kestens, "Shear banding and its contribution to texture evolution in rotated goss orientations of bcc structured materials," *Materials Science and Engineering*, vol. 82, pp. 1–5, 2015.

[194] G. B. Sarma and P. R. Dawson, "Effects of interactions among crystals on the inhomogenous deformations of polycrystals," *Acta Metallurgica*, vol. 44, pp. 1937–1953, 1996.

[195] Y. Takayama and J. A. Szpunar, "Stored energy and taylor factor relation in an al-mg-mn alloy sheet worked by continuous cyclic bending," *Materials Transactions*, vol. 45, pp. 2316–2325, 2004.

[196] K. Ushioda and W. Hutchinson, "Role of shearbandsin annealing texture formation in 3 % si-fe (111)[112] single crystals," *ISU International*, vol. 29, pp. 862–867, 1989.

[197] M. R. Barnett, "Role of in-grain shear bands in the nucleation of <111> nd recrystallization textures in warm rolled steel," *ISIJ International*, vol. 38, no. 1, pp. 78–85, 1998.

[198] C. Huang, K. Wang, S. Wu, Z. Zhang, G. Li, and S. Li, "Deformation twinning in polycrystalline copper at room temperature and low strain rate," *Acta Materialia*, vol. 54, no. 1, pp. 655–665, 2006.

CURRICULUM VITAE

PERSONAL INFORMATION

Surname, Name: Şimşek, Ülke

Nationality: Turkish (TC)

Date and Place of Birth: ————-

Marital Status:———-

Phone: ————-

E-mail: ————

EDUCATION

Degree	Institution	Year of Graduation
M.Sc.	Gazi University Mechanical Engineering	2012
B.Sc.	Başkent University Mechanical Engineering	2009
High School	TED Ankara College Foundation High School	2003

PROFESSIONAL EXPERIENCE

Year	Place	Enrollment
2016-Present	Roketsan Missiles Inc.	Lead Engineer
2014-2016	Dassault Systemes	Technical Support Engineer

PUBLICATIONS

[1] Yalçınkaya, T., Şimşek, U., Miyamoto, H., Yuasa, M.: Numerical analysis of a new nonlinear twist extrusion process. Metals 9(15), 1–15 (2019)

[2] Şimşek, U., Çoğun, C., Esen, Z.: Effects of electrolytic copper and copper alloy electrodes on machining performance in electrical discharge machining (edm). Machining Science and Technology 26, 1–16 (2022)

[3] Şimşek, U., Davut, K., Miyamoto, H., Yalçınkaya, T.: Comparison of linear and nonlinear twist extrusion processes with crystal plasticity finite element analysis. Materials 17(5), 1–24 (2024)

International Conference Publications

[1] Şimşek, U., Çoğun, C.,: Elektrolitik ve alaşım bakır elektrotların elektroerozyon ile işleme performansına etkisi,Conference: 16th Int Conf on Machine Design and Production,2004

[2] Guler,B., Şimşek, U., Yalçınkaya, T., Efe,M.: Grain-scale investigations of deformation heterogeneities in aluminum alloys, AIP Conference Proceedings,2018

[3] Tamiaki, S., Miyamoto, H., Şimşek, U., Yalçınkaya, T.: Evolution of microstructure of copper single crystal processed by nonlinear twist extrusion, The Proceedings of Conference of Kansai Branch,2021

[4] Şimşek, U., Miyamoto, H., Yalçınkaya, T.: Crystal plasticity finite element analysis of linear and non-linear extrusion processes. Materials Research Proceedings 28(1), 553–562 (2023)